Finite Element Methods for 2D Induction Heating Problems

Katherine MacKenzie

Department of Mathematics and Statistics
University of Strathclyde

A Thesis presented for the degree of
Doctor of Philosophy

August 2025

Declaration

This Thesis is the result of the author's original research. It has been composed by the author and has not been previously submitted for examination which has led to the award of a degree.

The copyright of this Thesis belongs to the author under the terms of the United Kingdom Copyright Acts as qualified by University of Strathclyde Regulation 3.50. Due acknowledgement must always be made of the use of any material contained in, or derived from, this Thesis.

Signed:

Date: 18/12/2025

Abstract

Numerical modelling of induction heating is a challenge for many reasons. For instance, there are difficulties in defining the functional setting, resolving non-linear material properties, and capturing steep boundary layers. More specifically, for example, in a simplified 2D domain, the variational formulation is not necessarily well-defined due to a term in the heat equation belonging to $L^1(\Omega)$ only.

In this Thesis, we have two main focuses: conducting mathematical analysis on this 2D induction heating problem that deals with the irregular right-hand side, and building code to simulate realistic induction heating processes. In our analysis, by showing that the coupling leads to a right-hand side that is more regular than $L^1(\Omega)$, we prove existence of solutions in a setup that is more general than the existing literature. Under strict assumptions on the shape of the mesh, we prove convergence of the standard Galerkin finite element method. The main new result we present is a proof of convergence of a recently developed finite element method to a decoupled problem under no assumptions on the mesh. The fact that this method has no conditions on the mesh allows the resolution of boundary layers in more complicated geometries.

We also implement the standard finite element method and this new method using the `Python` software `FEniCSx`. We study two different 2D models, and show that these codes produce results that are comparable to experimental data, and also improve upon some results from finite element codes used by industry. We conclude by running the model of induction heating over an irregular mesh, and explicitly demonstrate the results we have proven, that the newly developed method is robust over irregular meshes.

Acknowledgements

First of all, I would like to express my deepest gratitude to my supervisor Dr Gabriel Barrenechea, for his guidance, patience, and generosity with his time and expertise over these last few years. His enthusiasm for mathematics is inspiring, and it has been a real pleasure to learn from him.

I would also like to thank my second supervisor Dr Aurik Andreu, whose input on all aspects of the engineering side of induction heating has been invaluable for this work.

I would also like to thank Dr Max Jensen and Professor John Mackenzie for their willingness to act as examiners for this Thesis.

Furthermore, I would like to thank Professor Tristan Pryer and Dr Eike Mueller for my enjoyable months in Bath, which was integral to the success of the numerical Chapter of this Thesis.

A large thank you goes to my colleagues in Strathclyde and in Bath for their support. My wonderful office mates Maha, Jacinta, Amani, and Alaa for our shared joys and frustrations; the NA student group with Ann, Hywel, Sam, Charlotte, Reza, and Razan for our interesting discussions and entertaining evenings; my colleagues Minhui and Anaí for our coffee study dates; and my colleagues in Bath, Jenny, Alex, Ben, Veronika, Daniel, Filipe, and Abdalaziz. I am grateful to have been able to made this journey with you all.

I would also like to thank the EPSRC and the AFRC core funding group for sponsoring this project.

Finally, I am deeply indebted to my family, friends, and partner Colm for their unconditional support, and belief in me throughout.

Contents

List of Figures

List of Tables

List of Tables

Chapter 1

Introduction

Induction heating is a non-contact method of heating electrically conductive materials. It is widely used in the metallurgical industry for forging and forming, induction hardening, brazing, welding, heat sealing, and in some cases, melting and mixing. Since it induces heat directly within the material, it can efficiently produce accurate, localised heating that is easily controlled through the setup of the system. Induction heating can be used to control the properties of the material: for example, quenching a billet above a certain temperature results in crystalline changes to the billet's microstructure and an increase in hardness. By calibrating the setup, manufacturers can produce a workpiece with optimal depth of hardened material and minimal risk of cracking. In modern times, manufacturers want these materials to be shaped and hardened to a high accuracy. Therefore, it is important to understand the temperature profile within the billet for maximum throughput, efficiency, and control, and also to avoid undesirable overheating.

However, it is difficult, time consuming, and expensive to accurately measure the evolution of the temperature profile in a billet. This is because high frequency alternating currents are typically used in induction heating, and these generate steep temperature gradients in the billet. This means that a small deviation in the placement of a thermocouple could result in a large change in temperature being recorded and, consequently, these measurements are subject to high experimental errors. Furthermore, a single experiment could take several hours and would need to be repeated if the type, shape, or placement of the billet or coils were changed, or if the current intensity or frequency was changed. These experiments are costly since expensive equipment, large quantities of materials, and professional expertise are needed to conduct these experiments safely, accurately, and to a high standard. They are also not always possible to do due to tight production schedules.

Accordingly, engineers are increasingly relying on numerical models to verify that a given setup produces the desired temperature profile within a billet. This way, different voltage setups, coil configurations, and types of materials can be accounted for in the same model. The most popular type of method used is the finite element method (FEM), since it is easily implemented on non-rectangular domains. Some commercially available FEM software includes `DEFORM` (2023), or `ANSYS` (2025).

Although there is a vast amount of work implementing FEM codes for induction heating (see, for instance, Clain et al. (1993), Chaboudez et al. (1994), Rappaz and Świerkosz (1996), Chaboudez et al. (1997), Bay et al. (2003), Hiptmair and Sterz (2005), Bermúdez et al. (2007b), Bermúdez et al. (2009), Bermúdez et al. (2010), Bermúdez et al. (2011), and Fisk et al. (2022)), there is limited analysis that proves convergence of these FEMs. Therefore, broadly, the aim of this Thesis is to bridge the gap between the limited analysis that exists for induction heating and the FEM codes that have been built.

One explanation for why the analysis is so limited is that the 3D Maxwell's equations, which describe the interactions between the magnetic and electric fields, are notoriously difficult to analyse. This is for a number of reasons, including the fact that the functional setting prevents the use of standard (nodal) finite element spaces. Hence, most papers that analyse induction heating simplify the setting by reducing the 3D problem to a 2D problem.

In this Thesis we consider two different choices of 2D models: the Solenoidal model and the Axisymmetric model. Details of these models can be found in Chapter 3. Analysis of the Axisymmetric model is minimal (Bermúdez et al. 2007b), for reasons discussed in Chapter 3, and hence the majority of the analysis focuses on the well-posedness of the weak form of the simpler Solenoidal model (see, e.g. Parietti and

Rappaz (1998), Clain and Touzani (1997a), and Clain and Touzani (1997b)). However, proving well-posedness even for this simple model is decidedly non-trivial.

The difficulty in the analysis of the Solenoidal model comes from the observation that the heat equation has a source term in $L^1(\Omega)$. To see this, let us set all material properties equal to one, let $H_\circ$ be a positive constant representing the magnetic field strength in air, let Ω be an open and bounded domain in $\mathbb{R}^2$, and let us impose Dirichlet boundary conditions for simplicity. Then the stationary Solenoidal Induction Heating Problem reads: find the magnetic field strength H, and the temperature u such that

$$-\Delta H + iH = iH_\circ \qquad \text{in } \Omega, \tag{1.1}$$

$$-\Delta u = |\nabla H|^2 \qquad \text{in } \Omega, \tag{1.2}$$

$$H = 0 \qquad \text{on } \partial\Omega, \tag{1.3}$$

$$u = 0 \qquad \text{on } \partial\Omega. \tag{1.4}$$

If we put (1.1) into a standard weak form, we look for $H \in H_0^1(\Omega;\mathbb{C})$. However, this results in the right-hand side of (1.2) belonging to $L^1(\Omega)$. This means, first of all, that the methods to prove existence and uniqueness of variational formulations, such as Lax-Milgram's Lemma (Theorem 2.4.10) or the Banach-Nečas-Babuška Theorem (Theorem 2.4.11), cannot apply to (1.2) since $L^1(\Omega)$ is not a reflexive Banach space (Ern and Guermond 2021a).

In order to tackle this problem, we take inspiration from some existing work that has been done on the Thermistor Problem. This problem has the same source term in $L^1(\Omega)$, but differs in that (1.1) is replaced by a real Poisson equation. For the Thermistor Problem, it has been shown in the literature there is additional regularity in the source term (Howison, Rodrigues, and Shillor 1993), and this additional regularity is used to prove convergence of FEMs (Jensen and Målqvist 2012). It is also seen in the literature that generally there are two methods to achieve convergence: either by having strong restrictions on the mesh (Holst et al. 2010), or by imposing some bounds within the method, i.e., by enforcing a discrete maximum principle (DMP) by using a stabilising term (Zhu, Yu, and Loula 2011) or truncation operator (Jensen and Målqvist 2012). More detail is covered in Chapter 4.

The first goal of this work is to extend some of the results found for the Thermistor Problem to the Solenoidal Induction Heating Problem. In this Thesis we apply a recently developed stabilised FEM called the Bound Preserving Method (BPM), first presented by Barrenechea et al. (2024), to the Solenoidal model. This method hardwires the bounds of the problem directly into the method so there is no restriction on the shape of the elements of the mesh, so this is an improvement on the current analysis which currently has restrictions on the mesh. This goal is achieved by proving *a-priori*, similar to the Thermistor Problem, that the source term in (1.2) is more regular than in $L^1(\Omega)$. Proofs of existence and convergence of solutions for the Solenoidal Induction Heating Problem are contained in Chapter 4.

We also considered an alternative method to prove convergence. If we consider just (1.2) as a Poisson problem with a right-hand side in $L^1(\Omega)$, it has been shown by Bénilan et al. (1995), Dall'Aglio (1996), and Dal Maso et al. (1999) that if the weak form is defined in a different way, it is possible to obtain well-posedness. This unique solution under the redefined variational form is called the *renormalised solution*. It has been shown that under very strict conditions on the mesh, a standard $\mathbb{P}_1$ Galerkin FEM for (1.2) converges to the renormalised solution (Casado-Díaz et al. 2007). We have made some progress towards proving convergence of the BPM to the renormalised solution of (1.2) under no conditions on the mesh, and a discussion on this is contained in Appendix A.1 and remains an open problem.

The second goal of this work is to implement a working numerical code of induction heating. In Chapter 5, we describe how we construct FEMs using the software `FEniCSx` to solve the Solenoidal model and the Axisymmetric model of induction heating. To properly test these methods, we compared the results from the models to experimental data and to output from a commercial industrial FEM code. The experiments were done at the Advanced Forming Research Centre (AFRC) at the University of Strathclyde. We show that the output from these codes closely matches the experimental data, and in particular, for the Solenoidal model, we see that the BPM is more accurate than the standard FEM for non-Delaunay meshes.

The structure of this Thesis is as follows: in Chapter 2, we introduce mathematical preliminaries and notation for vector calculus, functional analysis, and partial differential equations (PDEs). We review some results relating to the maximum principle and well-posedness of variational forms, and we formally introduce the FEM, the DMP, and the BPM. In Chapter 3, we derive the Solenoidal model and the Axisymmetric model from Maxwell's equations and highlight some of the features of these models. Chapter 4 contains new analysis where we prove well-posedness and additional regularity of a simplified form of the Solenoidal model. Furthermore, we prove convergence of the BPM to the solution of a coupled system and we verify our results with numerical experiments. Chapter 5 describes the numerical implementation of the Solenoidal and Axisymmetric models and the comparison to experimental data. Finally, Chapter 6 reviews this Thesis and comes to some conclusions and future questions, while the Appendix contains a discussion on the renormalised solution, an optional voltage calculation, and a copy of part of the `FEniCSx` code.

Chapter 2

Preliminaries

2.1 Abstract

In this Chapter we introduce some notation, concepts, and results for later Chapters. First, we list some notation and identities from vector calculus which will be used to define the Induction Heating Problem in Chapter 3. We introduce notation for Lebesgue, Sobolev, and dual spaces, consciously differentiating between the real and the complex case. We introduce elliptic PDEs and show that under certain conditions, they satisfy a maximum principle (i.e. the solution is bounded). We then motivate and define the variational formulation of elliptic PDEs, and discuss conditions for well-posedness in an abstract setting. In particular, we highlight that having a source term that belongs to $L^1(\Omega)$ generates problems when proving well-posedness.

We also formally introduce the FEM as a triple, define the finite element spaces used throughout this Thesis, and show how they are used in a variational framework. We pay particular attention to different types of triangulations, since it is only under strong conditions on the mesh that the DMP is satisfied. Finally, we consider how to modify the standard FEM using a stabilising form in order to guarantee satisfaction of the bounds of the problem without these strict conditions on the mesh, and under this motivation we officially introduce the BPM.

2.2 Vector Calculus

In this Section we include some differential operators from vector calculus that will be used in the derivation of the Induction Heating Problem. Let $\boldsymbol{x}$ be a generic point in $\mathbb{R}^d$, $d = 2, 3$, and let $\boldsymbol{e}_i$, $1 \leq i \leq d$ denote the Cartesian basis for $\mathbb{R}^d$.

In the case where $d = 2$, let $\varphi : \mathbb{R}^2 \to \mathbb{C}$ be a continuously differentiable scalar field and $\boldsymbol{v} : \mathbb{R}^2 \to \mathbb{C}^2$ be a continuously differentiable vector field with $\boldsymbol{v} = v_1\boldsymbol{e}_1 + v_2\boldsymbol{e}_2$. Then we denote

$$\begin{aligned}
\nabla\varphi &:= \frac{\partial\varphi}{\partial x_1}\boldsymbol{e}_1 + \frac{\partial\varphi}{\partial x_2}\boldsymbol{e}_2, \\
\operatorname{div}\, \boldsymbol{v} &:= \frac{\partial v_1}{\partial x_1} + \frac{\partial v_2}{\partial x_2}, \\
\operatorname{curl}\, \boldsymbol{v} &:= \frac{\partial v_2}{\partial x_1} - \frac{\partial v_1}{\partial x_2}, \\
\mathbf{curl}\, \varphi &:= \frac{\partial\varphi}{\partial x_1}\boldsymbol{e}_1 - \frac{\partial\varphi}{\partial x_2}\boldsymbol{e}_2.
\end{aligned}$$

Note that we make a distinction between the curl of a scalar (**curl**), which produces a vector, and the curl of a vector (curl), which produces a scalar.

In the case where $d = 3$, let $\phi : \mathbb{R}^3 \to \mathbb{C}$ be a continuously differentiable scalar field and $\boldsymbol{u} : \mathbb{R}^3 \to \mathbb{C}^3$ be a continuously differentiable vector field with $\boldsymbol{u} = u_1\boldsymbol{e}_1 + u_2\boldsymbol{e}_2 + u_3\boldsymbol{e}_3$. Then we denote

$$\begin{aligned}
\nabla\phi &:= \frac{\partial\phi}{\partial x_1}\boldsymbol{e}_1 + \frac{\partial\phi}{\partial x_2}\boldsymbol{e}_2 + \frac{\partial\phi}{\partial x_3}\boldsymbol{e}_3, \\
\operatorname{div}\, \boldsymbol{u} &:= \frac{\partial u_1}{\partial x_1} + \frac{\partial u_2}{\partial x_2} + \frac{\partial u_3}{\partial x_3}, \\
\mathbf{curl}\, \boldsymbol{u} &:= \left(\frac{\partial u_3}{\partial x_2} - \frac{\partial u_2}{\partial x_3}\right)\boldsymbol{e}_1 + \left(\frac{\partial u_1}{\partial x_3} - \frac{\partial u_3}{\partial x_1}\right)\boldsymbol{e}_2 + \left(\frac{\partial u_2}{\partial x_1} - \frac{\partial u_1}{\partial x_2}\right)\boldsymbol{e}_3.
\end{aligned}$$

2.2.1 Cylindrical Coordinates

In order to present the Axisymmetric model of induction heating, we define some notation for problems in cylindrical coordinate systems. This Section follows the presentation by Touzani and Rappaz (2014, Chapter 5). In $\mathbb{R}^3$, the cylindrical coordinates are defined by

$$\begin{aligned}&\boldsymbol{\Phi} : (r, \theta, z) \in \mathbb{R}^+ \times [0, 2\pi) \times \mathbb{R},\\&\boldsymbol{\Phi}(r, \theta, z) = r\cos(\theta)\boldsymbol{e}_1 + r\sin(\theta)\boldsymbol{e}_2 + z\boldsymbol{e}_3.\end{aligned}$$

The cylindrical basis vectors are

$$\begin{aligned}&\boldsymbol{e}_r = \cos(\theta)\boldsymbol{e}_1 + \sin(\theta)\boldsymbol{e}_2,\\&\boldsymbol{e}_\theta = -\sin(\theta)\boldsymbol{e}_1 + \cos(\theta)\boldsymbol{e}_2,\\&\boldsymbol{e}_z = \boldsymbol{e}_3.\end{aligned}$$

For any scalar field $\breve{\phi} = \breve{\phi}(r, \theta, z)$ and any vector field $\breve{\boldsymbol{u}} = \breve{u}_r(r, \theta, z)\boldsymbol{e}_r + \breve{u}_\theta(r, \theta, z)\boldsymbol{e}_\theta + \breve{u}_z(r, \theta, z)\boldsymbol{e}_z$ we state the well known vector identities:

$$\begin{aligned}\nabla\breve{\phi} &= \frac{\partial\breve{\phi}}{\partial r}\boldsymbol{e}_r + \frac{1}{r}\frac{\partial\breve{\phi}}{\partial\theta}\boldsymbol{e}_\theta + \frac{\partial\breve{\phi}}{\partial z}\boldsymbol{e}_z,\\ \operatorname{div}\,\breve{\boldsymbol{u}} &= \frac{1}{r}\left(\frac{\partial(r\breve{u}_r)}{\partial r} + \frac{\partial\breve{u}_\theta}{\partial\theta} + r\frac{\partial\breve{u}_z}{\partial z}\right),\\ \mathbf{curl}\,\breve{\boldsymbol{u}} &= \frac{1}{r}\left(\frac{\partial\breve{u}_z}{\partial\theta} - r\frac{\partial\breve{u}_\theta}{\partial z}\right)\boldsymbol{e}_r + \left(\frac{\partial\breve{u}_r}{\partial z} - \frac{\partial\breve{u}_z}{\partial r}\right)\boldsymbol{e}_\theta + \frac{1}{r}\left(\frac{\partial(r\breve{u}_\theta)}{\partial r} - \frac{\partial\breve{u}_r}{\partial\theta}\right)\boldsymbol{e}_z,\\ \Delta\breve{\phi} &= \frac{1}{r}\left(\frac{\partial}{\partial r}\left(r\frac{\partial\breve{\phi}}{\partial r}\right) + \frac{1}{r}\frac{\partial^2\breve{\phi}}{\partial\theta^2} + r\frac{\partial^2\breve{\phi}}{\partial z^2}\right).\end{aligned}$$

These identities will be used in the definition of the Axisymmetric model. Now we define an Axisymmetric field, which is a field which is rotationally symmetric around the z-axis.

Definition 2.2.1 (Axisymmetric Field)**.** A scalar field $\breve{\phi}$ (or vector field $\breve{\boldsymbol{u}}$) is called *axisymmetric* if $\breve{\phi}$ (or $\breve{\boldsymbol{u}}$) does not depend on θ. More specifically,

$$\begin{aligned}&\breve{\phi} = \breve{\phi}(r, z),\\&\breve{\boldsymbol{u}} = \breve{u}_r(r, z)\boldsymbol{e}_r + \breve{u}_\theta(r, z)\boldsymbol{e}_\theta + \breve{u}_z(r, z)\boldsymbol{e}_z.\end{aligned}$$

We also define an Axisymmetric domain, which is a domain which is rotationally symmetric around the z-axis.

Definition 2.2.2 (Axisymmetric Domain)**.** We say a set $\Omega \subset \mathbb{R}^3$ is *axisymmetric* if for any $\boldsymbol{x} = \Phi(r, \theta, z) \in \Omega$ we have

$$\begin{aligned}\breve{\Omega} &= \{(r, z) \in \mathbb{R}^+ \times \mathbb{R}; \Phi(r, \xi, z) \in \Omega, \forall\ \xi \in [0, 2\pi)\},\\ &= \{(r, z) \in \mathbb{R}^+ \times \mathbb{R}; \Phi(r, 0, z) \in \Omega\}.\end{aligned}$$

In other words, $\breve{\Omega}$ is independent of the choice of θ. Thus, in an axisymmetric setting, the axisymmetric problem reduces to solving a problem on the half-plane by setting $\theta = 0$.

2.3 Functional Analysis

In this Section we introduce notation for Lebesgue, Sobolev, and dual spaces and highlight relevant results in this topic. Let $C^0(\Omega)$ denote the space of continuous functions on Ω, and for an integer $k \geq 1$, let $C^k(\Omega)$ denote the space of functions that are k-differentiable. In a similar manner, we denote by $C^0(\Omega; \mathbb{C})$ the set of continuous complex functions, and by $C^k(\Omega; \mathbb{C})$ the set of k-differentiable complex functions. Let $\mathcal{D}(\Omega) := C_0^\infty(\Omega)$ be the set of infinitely differentiable real functions that are compactly supported in Ω, and let $\mathcal{D}(\Omega; \mathbb{C}) := C_0^\infty(\Omega; \mathbb{C})$ be the set of infinitely differentiable complex functions that are compactly supported in Ω. For a general $n \in \mathbb{N}$, we write $|\cdot|$ as the Euclidean norm over $\mathbb{R}^n$ or $\mathbb{C}^n$, write $\langle \cdot, \cdot \rangle$ to be the inner product over $\mathbb{R}^n$, and $\langle \cdot, \cdot \rangle_{\mathbb{C}}$ to be the inner product over $\mathbb{C}^n$. For a complex number z we write $\mathrm{Re}(z)$ as the real part of z and $\mathrm{Im}(z)$ as the imaginary part of z.

A fundamental characterisation of continuity is Lipschitz continuity.

Definition 2.3.1 (Lipschitz Continuous)**.** For Banach spaces $(V_1, \|\cdot\|_{V_1})$ and $(V_2, \|\cdot\|_{V_2})$, a function $A : V_1 \to V_2$ is called *Lipschitz continuous* if there exists a positive constant C_{lip} such that

$$\|A(v_1) - A(v_2)\|_{V_2} \leq C_{lip} \|v_1 - v_2\|_{V_1} \qquad \forall\ v_1, v_2 \in V_1.$$

A domain Ω is said to have *Lipschitz boundary* if the boundary can be decomposed into a finite number of open sets that can each be locally expressed as a graph of a Lipschitz function. In all of the analysis that follows, we assume that our domain has a Lipschitz boundary.

2.3.1 Lebesgue and Sobolev Spaces

We now introduce notation for Lebesgue spaces, which contain functions that can be discontinuous while requiring certain integrability properties.

Definition 2.3.2 (Lebesgue Spaces)**.** For every $p \in [1, \infty)$, we define the real Lebesgue space $L^p(\Omega)$ to be the set of real measurable functions v such that

$$L^p(\Omega) := \left\{ v : \|v\|_{0,p,\Omega} < \infty \right\}, \qquad \|v\|_{0,p,\Omega} := \left(\int_\Omega |v|^p \, \mathrm{d}\boldsymbol{x} \right)^{1/p},$$

and the complex Lebesgue space $L^p(\Omega; \mathbb{C})$ to be the set of complex measurable functions w such that

$$L^p(\Omega; \mathbb{C}) := \left\{ w : \|w\|_{0,p,\Omega,\mathbb{C}} < \infty \right\}, \qquad \|w\|_{0,p,\Omega,\mathbb{C}} := \left(\int_\Omega |w|^p \, \mathrm{d}\boldsymbol{x} \right)^{1/p}.$$

We also define the space $L^\infty(\Omega)$ (and $L^\infty(\Omega; \mathbb{C})$) to be the space of real (and complex) measurable functions v (and w) such that

$$\|v\|_{0,\infty,\Omega} := \sup_{x \in \Omega} |v(x)| < \infty, \qquad \|w\|_{0,\infty,\Omega,\mathbb{C}} := \sup_{x \in \Omega} |w(x)| < \infty.$$

When equipped with these norms, $L^p(\Omega)$ and $L^p(\Omega; \mathbb{C})$ are Banach spaces (Brezis 2011, Theorem 4.8). In the special case where $p = 2$, $L^2(\Omega)$ and $L^2(\Omega; \mathbb{C})$ are Hilbert spaces when equipped with the inner products

$$(u, v)_\Omega := \int_\Omega uv \, \mathrm{d}\boldsymbol{x} \quad \forall\, u, v \in L^2(\Omega), \qquad (w, q)_{\Omega,\mathbb{C}} := \int_\Omega w\overline{q} \, \mathrm{d}\boldsymbol{x} \quad \forall\, w, q \in L^2(\Omega; \mathbb{C}),$$

where $\overline{q}$ denotes the complex conjugate of q. In these cases, we abbreviate the norms from $\| \cdot \|_{0,2,\Omega}$ to $\| \cdot \|_{0,\Omega}$ and $\| \cdot \|_{0,2,\Omega,\mathbb{C}}$ to $\| \cdot \|_{0,\Omega,\mathbb{C}}$.

We write the inner product on the boundary $\partial\Omega$ as

$$(u, v)_{\partial\Omega} = \int_{\partial\Omega} uv \ \mathrm{d}S \qquad (w, q)_{\partial\Omega,\mathbb{C}} = \int_{\partial\Omega} w\overline{q} \ \mathrm{d}S$$

for all $u, v \in L^2(\partial\Omega)$ and all $w, q \in L^2(\partial\Omega; \mathbb{C})$.

Since we will be studying PDEs, we define Sobolev spaces where derivatives exist in a generalised sense and and have suitable integrability. The following classical definition is by Adams and Fournier (2003, Definition 3.1).

Definition 2.3.3 (Sobolev Spaces)**.** Let $p \in [1, \infty]$ and let k be a non-negative integer. Let $\boldsymbol{\alpha} = (\alpha_1, \dots, \alpha_n) \in \mathbb{N}^n$ be a multi-index, and let

$$D^\alpha := \left(\frac{\partial}{\partial x_1}\right)^{\alpha_1} \cdots \left(\frac{\partial}{\partial x_n}\right)^{\alpha_n} = \frac{\partial^{|\alpha|}}{\partial x_1^{\alpha_1} \cdots \partial x_n^{\alpha_n}}.$$

For a real function v and a complex function w, we can define the Sobolev spaces to be

$$\begin{aligned} W^{s,p}(\Omega) &:= \{v \in L^p(\Omega) : \ \|D^\alpha v\|_{0,p,\Omega} < \infty, \ |\alpha| \le s\}, \\ W^{s,p}(\Omega; \mathbb{C}) &:= \{w \in L^p(\Omega; \mathbb{C}) : \ \|D^\alpha w\|_{0,p,\Omega,\mathbb{C}} < \infty, \ |\alpha| \le s\}. \end{aligned}$$

These spaces are provided with the norms

$$\begin{aligned} \|v\|_{s,p,\Omega} &:= \left(\sum_{|\alpha| \le s} \|D^\alpha v\|^p_{L^p(\Omega)} \right)^{1/p}, \\ \|w\|_{s,p,\Omega,\mathbb{C}} &:= \left(\sum_{|\alpha| \le s} \|D^\alpha w\|^p_{L^p(\Omega)} \right)^{1/p}, \end{aligned}$$

and seminorms

$$\begin{aligned} |v|_{s,p,\Omega} &:= \left(\sum_{|\alpha| = s} \|D^\alpha v\|^p_{L^p(\Omega)} \right)^{1/p}, \\ |w|_{s,p,\Omega,\mathbb{C}} &:= \left(\sum_{|\alpha| = s} \|D^\alpha w\|^p_{L^p(\Omega)} \right)^{1/p}. \end{aligned}$$

With these norms, $W^{s,p}(\Omega)$ and $W^{s,p}(\Omega;\mathbb{C})$ are Banach spaces, and in the special case where $p=2$ these are Hilbert spaces when equipped with the inner products

$$\begin{aligned}
(u,v)_{s,\Omega} &= \sum_{|\alpha|\leq s} (D^\alpha u, D^\alpha v)_{0,\Omega} \qquad \forall\, u,v \in W^{s,2}(\Omega),\\
(w,q)_{s,\Omega,\mathbb{C}} &= \sum_{|\alpha|\leq s} (D^\alpha w, D^\alpha q)_{0,\Omega,\mathbb{C}} \qquad \forall\, w,q \in W^{s,2}(\partial\Omega;\mathbb{C}).
\end{aligned}$$

Following standard convention, we denote these Hilbert spaces by

$$H^s(\Omega) := W^{s,2}(\Omega), \qquad H^s(\Omega;\mathbb{C}) := W^{s,2}(\Omega;\mathbb{C}),$$

and abbreviate their norms and seminorms to

$$\begin{aligned}
\|v\|_{s,\Omega} &:= \|v\|_{s,2,\Omega}, & \|w\|_{s,\Omega,\mathbb{C}} &:= \|w\|_{s,2,\Omega,\mathbb{C}},\\
|v|_{s,\Omega} &:= |v|_{s,2,\Omega}, & |w|_{s,\Omega,\mathbb{C}} &:= |w|_{s,2,\Omega,\mathbb{C}}.
\end{aligned}$$

We define the space $H^s_0(\Omega)$ as the closure of $C^\infty_0(\Omega)$ in $H^s(\Omega)$, and $H^s(\Omega;\mathbb{C})$ as the closure of $C^\infty_0(\Omega;\mathbb{C})$ in $H^s(\Omega;\mathbb{C})$. This space is a Hilbert space when equipped with the norm equal to the seminorm of $H^s(\Omega)$, (or $H^s(\Omega;\mathbb{C})$).

Since we consider time-dependent PDEs in Chapter 5, we mention some notation for Bochner spaces. Let $I \subset \mathbb{R}$, where typically $I=[0,T]$ and T is the timescale of the simulation. Let $(X, \|\cdot\|_X)$ be a Banach space (e.g. $L^p(\Omega)$ or $W^{k,p}(\Omega;\mathbb{C})$). We define the Banach space

$$L^p(I;X) = \{f : I\times\Omega \to \mathbb{R} \;:\; \|f\|_{L^p(I;X)} < \infty\},$$

where

$$\|f\|_{L^p(I;X)} := \left(\int_I \|f\|^p_X\right)^{1/p}.$$

Also, for $p\in[1,\infty]$, $k\geq 1$, we define the space

$$W^{k,p}(I;X) := \{f : I\times\Omega \to \mathbb{R} \;:\; \|f\|_{W^{k,p}(I;X)} < \infty\},$$

with

$$\|f\|_{W_{k,p}(I;X)} := \left(\int_I \|f\|_{\mathcal{X}}^p\right)^{1/p}.$$

Using these spaces, we will be able to properly characterise the variational form of time-dependent PDEs.

Now that we have defined these spaces, we recap some fundamental theorems that will be referred to in later Chapters. We state the theorems in the complex setting, since that is the more general case. These first three classical results allows us to obtain inequalities for functions in $L^p(\Omega;\mathbb{C})$ and $H^1(\Omega;\mathbb{C})$, and can be found in the book by Gilbarg and Trudinger (1998, p.145 and p.164).

Theorem 2.3.4 (Cauchy-Schwarz Inequality). For all $u, v \in L^2(\Omega;\mathbb{C})$, the following holds:

$$|(u,v)_{\Omega,\mathbb{C}}| \le \|u\|_{0,\Omega,\mathbb{C}}\|v\|_{0,\Omega,\mathbb{C}}.$$

In a more general setting, we have Hölder's Inequality.

Theorem 2.3.5 (Hölder's Inequality). Let $p \ge 1$ and let q be the Hölder conjugate of p, so that $q \ge 1$ and $1/p + 1/q = 1$. Then for all $u \in L^p(\Omega;\mathbb{C})$ and all $v \in L^q(\Omega;\mathbb{C})$, the following holds:

$$|(u,v)_{\Omega,\mathbb{C}}| \le \|u\|_{0,p,\Omega,\mathbb{C}}\|v\|_{0,q,\Omega,\mathbb{C}}.$$

Finally, we have the Poincaré Inequality.

Theorem 2.3.6 (Poincaré Inequality). If Ω is bounded, there exists a positive constant C_p depending only on Ω, such that

$$\|v\|_{0,\Omega,\mathbb{C}} \le C_p|v|_{1,\Omega,\mathbb{C}} \qquad \forall\ v \in H_0^1(\Omega;\mathbb{C}).$$

Corollary 2.3.7. The norms for $H^1(\Omega;\mathbb{C})$ and $H_0^1(\Omega;\mathbb{C})$ are equivalent. That is, there exists positive constants c_{equi} and C_{equi} such that

$$c_{equi}|v|_{1,\Omega,\mathbb{C}} \le \|v\|_{1,\Omega,\mathbb{C}} \le C_{equi}|v|_{1,\Omega,\mathbb{C}} \qquad \forall\ v \in H_0^1(\Omega;\mathbb{C}).$$

Proof. By definition of a seminorm, $|v|_{1,\Omega,\mathbb{C}} \le \|v\|_{1,\Omega,\mathbb{C}}$, so we can take $c_{equi} = 1$ for the left inequality. The right inequality is satisfied is using the Poincaré inequality and taking $C_{equi} = 1 + C_p$. ☐

More generally, Sobolev spaces and Lebesgue spaces are connected by the following theorem, which is stated by Roubíček (2013, Theorem 1.20).

Theorem 2.3.8 (Sobolev Embedding). Let the exponent p^* be defined as

$$p^* = \begin{cases} \frac{dp}{d-p}, & \text{for } p < d, \\ \text{an arbitrarily large real} & \text{for } p = d, \\ +\infty & \text{for } p > d. \end{cases}$$

Then $W^{1,p}(\Omega; \mathbb{C})$ is continuously embedded in $L^{p^*}(\Omega; \mathbb{C})$ and compactly embedded in $L^{\hat{p}}(\Omega; \mathbb{C})$, where $1 \leq \hat{p} \leq p^*$.

In particular, this means that when $\Omega \subset \mathbb{R}^2$, $H^1(\Omega; \mathbb{C})$ can be continuously embedded into any $L^p(\Omega; \mathbb{C})$ for $1 \leq p < \infty$.

The following Lemma is proven using the Sobolev Embedding Theorem, and will be used when proving convergence of the Induction Heating Problem when there are coefficients that depend on temperature.

Lemma 2.3.9. Let $v_k \rightharpoonup v$ be a weakly convergent sequence in $H_0^1(\Omega; \mathbb{C})$, and let $f \in L^\infty(\Omega; \mathbb{C})$ be a Lipschitz continuous and essentially bounded function. Then $f(v_k) \to f(v)$ strongly in $L^q(\Omega; \mathbb{C})$ for any $1 \leq q < p^*$, where p^* is the constant from the Sobolev Embedding Theorem (Theorem 2.3.8).

Proof. Since $v_k \rightharpoonup v$ weakly in $H_0^1(\Omega; \mathbb{C})$, it follows from the Sobolev Embedding Theorem (Theorem 2.3.8) that $v_k \to v$ strongly in $L^p(\Omega)$, where $1 \leq p < p^*$. Since Ω is bounded, $f \in L^\infty(\Omega; \mathbb{C}) \implies f \in L^q(\Omega; \mathbb{C})$, for $1 \leq q < \infty$. Therefore, by definition of Lipschitz continuity (Definition 2.3.1)

$$\|f(v_k) - f(v)\|_{0,q,\Omega,\mathbb{C}} \leq C_{lip} \|v_k - v\|_{0,p,\Omega,\mathbb{C}} \to 0.$$

Therefore $f(v_k) \to f(v)$ strongly in $L^q(\Omega)$ for any $1 \leq q < p^*$. ☐

Finally, we formally define a projection from a Hilbert space onto a closed convex set, which will be essential in order to characterise convergence of the BPM. This definition is found in the book by (Brezis 2011, p.132).

Definition 2.3.10 (Projection onto a Closed Convex Set)**.** Let H be a Hilbert space with inner product $(\cdot,\cdot)_H$ and norm $\|\cdot\|_H$. Let $\mathcal{K} \subset H$ be a non-empty closed convex subset of H. For every $f \in H$ there exists a unique element $u \in \mathcal{K}$ such that

$$\|f-u\|_H = \min_{v \in \mathcal{K}} \|f-v\|_H = \operatorname{dist}(f,\mathcal{K}),$$

where u is characterised by the property

$$u \in \mathcal{K} \text{ and } (f-u, v-u) \leq 0 \quad \forall\, v \in \mathcal{K}.$$

The unique element u is called the *projection* of f onto $\mathcal{K}$ and is denoted by

$$u = \Pi_{\mathcal{K}} f.$$

2.3.2 Dual Spaces

In order to articulate the challenges posed by having a source term in $L^1(\Omega)$, we state some notation for dual spaces, following the presentation by Renardy and Rogers (2004).

Definition 2.3.11 (Dual Space)**.** Let X be a real (or complex) Banach space with norm $\|\cdot\|_X$. Then a *linear functional* on X is a bounded linear mapping L from X to $\mathbb{R}$ (or $\mathbb{C}$). The set of all linear functionals on X is the *dual space of* X and is denoted by X'. It is equipped with the norm

$$\|L\|_{X'} := \sup_{\|x\|_X=1} \frac{|Lx|}{\|x\|_X} = \sup_{\|x\|_X \neq 0} \frac{|Lx|}{\|x\|_X}.$$

In the special case where X is a Hilbert space, the Riesz Representation Theorem shows that X' is isomorphic to X (Renardy and Rogers 2004, Theorem 6.2).

Now we consider the case where X is a Lebesgue space $L^p(\Omega)$ with $1 < p < \infty$. Let q be the Hölder conjugate of p, so that $1/p + 1/q = 1$. Each element $v \in L^q(\Omega)$ defines a linear functional L_v on $L^p(\Omega)$ via

$$L_v(u) = \int_\Omega u(x)v(x)\ \mathrm{d}\boldsymbol{x}, \qquad u \in L^p(\Omega).$$

It is shown by Adams and Fournier (2003) that $(L^p(\Omega))'$ is isomorphic to $L^q(\Omega)$. We can write the duality product as

$$\begin{aligned} \langle u, v\rangle_{L^p\times(L^p)',\Omega} &:= \int_\Omega u(x)v(x)\ \mathrm{d}\boldsymbol{x}, \\ \langle w, q\rangle_{L^p\times(L^p)',\Omega,\mathbb{C}} &:= \int_\Omega w(x)\overline{q(x)}\ \mathrm{d}\boldsymbol{x}, \end{aligned}$$

for $u \in L^p(\Omega)$, $v \in (L^p(\Omega))'$ real, and $w \in L^p(\Omega;\mathbb{C})$, $q \in (L^p(\Omega;\mathbb{C}))'$ complex. The key point is that taking $v \in L^q(\Omega)$ and $q \in L^q(\Omega;\mathbb{C})$ is entirely equivalent taking $v \in (L^p(\Omega))'$ and $q \in (L^p(\Omega,\mathbb{C}))'$ in the duality product. If it is clear from the context, the spaces where u, v, w and q are from will be omitted.

Remark. It is more complicated in the case that $p = 1$ or $p = \infty$. In the case where $p = 1$, $(L^1(\Omega))'$ is isomorphic to $L^\infty(\Omega)$. However, it is not the case that $(L^\infty(\Omega))'$ is isomorphic to $L^1(\Omega)$. In fact, the dual of $L^\infty(\Omega)$ is much larger than $L^1(\Omega)$ (see Adams and Fournier (2003) for more details). ■

The spaces $L^p(\Omega)$ that are isomorphic to $(L^q(\Omega))'$ are characterised more formally in the following definition, presented by Roubíček (2013, p.5).

Definition 2.3.12 (Reflexive Space)**.** Let X be a Banach space. The space $X'' := (X')'$ is called the *bidual* of X. For $u \in X$, $v \in X'$, space X is embedded into the bidual X'' via the canonical embedding $i : X \to X''$ defined by $\langle i(v), u\rangle = \langle u, v\rangle$. The space X is called *reflexive* if $i : X \to X''$ is an isomorphism.

Indeed, $L^p(\Omega)$ is reflexive if and only if $1 < p < \infty$ (Adams and Fournier 2003, Theorem 2.46). We will see in Section 2.4.4 that the relationship between Hilbert spaces and their duals, and the relationship between $L^p(\Omega)$ spaces and their Hölder conjugate duals, plays a key role in proving the well-posedness of PDEs. Accordingly, we can now state a slight modification to Schauder's Fixed Point Theorem, stated by Roubíček (2013, p.65).

Theorem 2.3.13 (Tikhonov-type modification of Schauder's Fixed Point Theorem). Let V be a reflexive separable Banach space that is compactly embedded into a different Banach space V^1. Then a weakly continuous mapping $M : V \to V$ which maps a ball into V to itself has a fixed point.

This theorem will allow us to prove existence of a fixed point under a weakly continuous map in a reflexive Banach space.

We also state another fixed-point theorem, which will allow us to prove existence of a fixed point in finite-dimensional spaces. This is presented by Roubíček (2013, Theorem 1.10), and was first proven by Brouwer (1912).

Theorem 2.3.14 (Brouwer's Fixed Point Theorem). A continuous mapping on a compact convex set in $\mathbb{R}^n$ has a fixed point.

Some careful consideration should be given to the dual space of $H^s_0(\Omega)$ (or $H^s_0(\Omega;\mathbb{C})$), which is denoted by $H^{-s}(\Omega)$ with norm $\|\cdot\|_{-s,\Omega}$ (respectively denoted by $H^{-s}(\Omega;\mathbb{C})$ with norm $\|\cdot\|_{-s,\Omega,\mathbb{C}}$). Although these spaces are Hilbert spaces, and therefore should be isomorphic to their dual space, the extra derivatives make their analysis more delicate. However, the essential idea is to redefine the norm on the dual space. For more details on the definition of this norm, see Adams and Fournier (2003, p.62).

2.4 PDEs

The Induction Heating Problem can be represented as a set of coupled PDEs. In this Section, we introduce the theory for elliptic PDEs in a more general setting.

2.4.1 Elliptic PDEs

In this Section we consider a linear second order PDE with no convective term i.e. a reaction-diffusion equation. Let Ω be a bounded Lipschitz domain in $\mathbb{R}^d$, and consider the classical reaction-diffusion problem. When equipped with appropriate boundary conditions, the problem reads: find $u(\boldsymbol{x}) \in C^2(\Omega;\mathbb{C}) \cap C(\overline{\Omega};\mathbb{C})$ such that

$$-\sum_{i,j=1}^{d} \frac{\partial}{\partial \boldsymbol{x}_j}\left(a_{ij}(\boldsymbol{x})\frac{\partial u}{\partial \boldsymbol{x}_i}\right) + c(\boldsymbol{x})u = f(\boldsymbol{x}) \qquad \boldsymbol{x} \in \Omega, \tag{2.1}$$

where the coefficients $a_{ij} \in C^1(\overline{\Omega}; \mathbb{C})$, $i, j = 1, \ldots, d$, $c \in C(\overline{\Omega}; \mathbb{C})$ and $f \in C(\overline{\Omega}; \mathbb{C})$. Here, (2.1) can be written more compactly as

$$\mathcal{L}u = f \tag{2.2}$$

where

$$\mathcal{L} := -\sum_{i,j=1}^{d} \frac{\partial}{\partial \boldsymbol{x}_j} \left(a_{ij}(\boldsymbol{x}) \frac{\partial}{\partial \boldsymbol{x}_i} \right) + c(\boldsymbol{x}),$$

is a linear differential operator.

Definition 2.4.1 (Real Elliptic PDE)**.** The differential operator $\mathcal{L}$ in (2.2) is *uniformly elliptic* if $a_{ij} \in C^1(\overline{\Omega})$ and $c \in C(\overline{\Omega})$ are real, and there exists a positive constant C_{ell} such that

$$\sum_{i,j=1}^{d} a_{ij}\xi_i\xi_j \geq C_{ell} \sum_{i=1}^{d} \xi_i^2, \qquad \forall\ \xi = (\xi_1, \ldots, \xi_d) \in \mathbb{R}^d, \qquad x \in \overline{\Omega}.$$

If $f \in C(\overline{\Omega})$ is also real then the PDE (2.1) is called a *real elliptic PDE.*

When paired with appropriate boundary conditions, a function $u \in C^2(\Omega; \mathbb{C}) \cap C(\overline{\Omega}; \mathbb{C})$ satisfying (2.1) is called a classical solution. This solution is unique for real elliptic PDEs provided that a_{ij}, a and f are sufficiently smooth (Süli 2020, p. 15).

Next, we will discuss the maximum principle, which can be used to obtain *a-priori* bounds on the solution.

The Maximum Principle for Classical Elliptic Problems

The maximum principle is an essential tool to prove boundedness of classical solutions to PDEs. Here, we formally introduce the maximum principle as a way to obtain *a-priori* bounds on the solution.

For real second order elliptic PDEs, the maximum principle is well established and is stated by Gilbarg and Trudinger (1998, Theorem 3.1).

Theorem 2.4.2 (The Classical Weak Maximum Principle). Let $\mathcal{L}$ from (2.2) be real and elliptic in the bounded domain Ω, and define $u^+ = \max\{u, 0\}$, and $u^- = \min\{u, 0\}$.

Suppose that

$$\mathcal{L}u \geq 0 \; (\leq 0) \text{ in } \Omega, \qquad a(x) \leq 0 \text{ in } \Omega,$$

with $u \in C^2(\Omega) \cap C^0(\overline{\Omega})$. Then the maximum (minimum) of u is achieved on $\partial\Omega$, that is

$$\sup_{\Omega} u = \sup_{\partial\Omega} u \quad (\inf_{\Omega} u = \inf_{\partial\Omega} u).$$

Further, if $\mathcal{L}u = 0$ in Ω, then

$$\sup_{\Omega} |u| = \sup_{\partial\Omega} |u|.$$

The complex version of the maximum principle is not quite so well established. However, it has been shown by Kresin and Maz'ya (1993) that by separating the real and imaginary parts of the system and viewing the solution u as a vector and the complex PDE as a system of coupled real PDEs, we can prove the following maximum principle.

Theorem 2.4.3 (The Complex Weak Maximum Principle). Let $\mathfrak{L}$ be the complex operator defined by

$$\mathfrak{L} := -c_1(\boldsymbol{x}) \sum_{i,j=1}^{d} \frac{\partial}{\partial \boldsymbol{x}_j} \left(a_{ij}(\boldsymbol{x}) \frac{\partial}{\partial \boldsymbol{x}_i} \right) + c_0(\boldsymbol{x})$$

where a_{ij} are real functions, c_1 is a complex $d \times d$-matrix-valued function such that $\operatorname{Re}(\langle c_1(\boldsymbol{x})\eta, \eta \rangle) > 0$ for all $\eta \in \mathbb{C}^d \backslash \{0\}$, and all coefficients are bounded and smooth enough. Suppose additionally that the operator $\mathfrak{L}$ is strongly elliptic, so that for all $\boldsymbol{x} \in \overline{\Omega}$, all $\eta = (\eta_1, \ldots, \eta_d) \in \mathbb{C}^d$, and all $\xi = (\xi_1, \ldots, \xi_d) \in \mathbb{R}^d$

$$\operatorname{Re}\left(\langle \sum_{i,j=1}^{d} c_{ij}(\boldsymbol{x}) \xi_i \xi_j \eta, \eta \rangle_{\mathbb{C}} \right) > 0.$$

Then, if for all $\boldsymbol{x} \in \Omega$, and for all μ_j, $\mu \in \mathbb{C}^d$, $i = 1, \ldots, d$ with $\operatorname{Re}(\langle \mu_i, \mu \rangle) = 0$, the inequality

$$\operatorname{Re}\left(\sum_{i,j=1}^{d} a_{ij}(\boldsymbol{x}) \langle \mu_i, \mu_j \rangle + \langle c^{-1}(\boldsymbol{x}) c_1(\boldsymbol{x}) \mu, \mu) \rangle \right) \geq 0,$$

is valid, then the classical maximum modulus principle

$$\sup_{\Omega} |u| = \sup_{\partial\Omega} |u| \quad (\inf_{\Omega} |u| = \inf_{\partial\Omega} |u|)$$

is valid, where $u \in C^2(\Omega; \mathbb{C}) \cap C^0(\overline{\Omega}; \mathbb{C})$ is the solution.

These maximum principles are important to bear in mind when designing FEMs, as discrete solutions should also satisfy these bounds. Before defining discrete solutions, we first need to define weak formulations of PDEs.

2.4.2 Variational Formulation of Elliptic PDEs

The classical solution for (2.1) requires that $u \in C^2(\Omega; \mathbb{C}) \cap C(\overline{\Omega}; \mathbb{C})$, but this is too restrictive for discrete solutions. Additionally, (2.1) must have a_{ij}, a and f sufficiently smooth. Therefore, in order to weaken the regularity requirements on u and the data, we put (2.1) into its weak form by multiplying by a test function v and integrating over Ω. Then u is said to be a *weak solution* if it solves the resulting integral equation for all test functions v. The weak form of (2.1) equipped with Dirichlet boundary conditions reads: given $f \in L^2(\Omega; \mathbb{C})$, find $u \in H_0^1(\Omega; \mathbb{C})$ such that

$$\sum_{i,j}^{d} \int_{\Omega} a_{ij}(\boldsymbol{x}) \frac{\partial u}{\partial \boldsymbol{x}_i} \cdot \frac{\partial v}{\partial \boldsymbol{x}_j} \, \mathrm{d}\boldsymbol{x} + \int_{\Omega} c(\boldsymbol{x}) uv \, \mathrm{d}\boldsymbol{x} = \int_{\Omega} fv \, \mathrm{d}\boldsymbol{x} \qquad \forall \, v \in H_0^1(\Omega; \mathbb{C}). \tag{2.3}$$

Searching for $u \in H_0^1(\Omega; \mathbb{C})$ allows us to include functions that are continuous and differentiable almost everywhere (a.e.), so can be discontinuous at a finite number of points. This significantly extends the space of admissible solutions.

We can write (2.3) more compactly using inner product notation. Let $\mathbb{D}$ denote the diffusion matrix with entries a_{ij}. Then (2.3) can also read: given $f \in L^2(\Omega; \mathbb{C})$, find $u \in H_0^1(\Omega; \mathbb{C})$ such that

$$(\mathbb{D}\nabla u, \nabla v)_{\Omega,\mathbb{C}} + (cu, v)_{\Omega,\mathbb{C}} = (f, v)_{\Omega,\mathbb{C}} \qquad \forall \, v \in H_0^1(\Omega; \mathbb{C}). \tag{2.4}$$

This notation with the inner products is the one that we will use throughout this Thesis. Next, we recap some results about variational formulations in an abstract setting in order to obtain well-posedness results.

2.4.3 Abstract Variational Formulation

In this Section we follow the presentation given in Dautray and Lions (2000), and present some abstract results relating to the variational formulation. First, we give some definitions.

Definition 2.4.4 (Bounded Linear Mapping)**.** Let V and W be real vector spaces with norms $\|\cdot\|_V$ and $\|\cdot\|_W$. A *linear mapping* is a map $L : V \to W$ such that

$$L(v_1 + v_2) = L(v_1) + L(v_2) \qquad \forall\ v_1, v_2 \in V, \tag{2.5}$$

$$L(\lambda v) = \lambda L(v) \qquad \forall\ \lambda \in \mathbb{R} \text{ and all } v \in V. \tag{2.6}$$

If, instead, V and W are complex vector spaces with norms $\|\cdot\|_V$ and $\|\cdot\|_W$, and L is a map $L : V \to W$ such that

$$\begin{aligned} L(v_1 + v_2) &= L(v_1) + L(v_2) && \forall\ v_1, v_2 \in V, \\ L(\lambda v) &= \overline{\lambda} L(v) && \forall\ \lambda \in \mathbb{C} \text{ and all } v \in V, \end{aligned}$$

then L is called an *antilinear mapping.* An (anti)linear mapping is called *bounded* if there exists a positive constant $C_{lin} > 0$ such that

$$\|L(v)\|_W \leq C_{lin} \|v\|_V \qquad \forall\ v \in V.$$

The set of all bounded (anti)linear mappings from V to W is denoted $\mathcal{L}(V; W)$.

Definition 2.4.5 ((Anti)linear Form)**.** Let V be a complex vector space. An *antilinear form* on V is a bounded antilinear mapping from V to $\mathbb{C}$. If V is a real vector space and L is a linear mapping from V to $\mathbb{R}$, L is called a *linear form.*

Definition 2.4.6 (Sesquilinear Form)**.** Let V and W be complex vector spaces. A *sesquilinear form* is a map $a : V \times W \to \mathbb{C}$ such that

1. $a(v_1 + v_2, w) = a(v_1, w) + a(v_2, w)$ for all $v_1, v_2 \in V$ and all $w \in W$,

2. $a(v, w_1 + w_2) = a(v, w_1) + a(v, w_2)$ for all $v \in V$ and all $w_1, w_2 \in W$,
3. $a(\lambda v, w) = \lambda a(v, w)$ for all $\lambda \in \mathbb{C}$, all $v \in V$, and all $w \in W$,
4. $a(v, \lambda w) = \overline{\lambda} a(v, w)$ for all $\lambda \in \mathbb{C}$, all $v \in V$, and all $w \in W$.

If V and W are real and $a(\cdot, \cdot)$ maps to $\mathbb{R}$, then $a(\cdot, \cdot)$ is called a *bilinear form.*

The following definitions of bounded, continuous, and coercive sesquilinear forms also apply when $a(\cdot, \cdot)$ is a bilinear form.

Definition 2.4.7 (Continuous Sesquilinear Form)**.** Let V and W be complex vector spaces with norms $\| \cdot \|_V$ and $\| \cdot \|_W$, respectively. A sesquilinear form $a(\cdot, \cdot)$ is *bounded* if there exists a positive constant $C_{ses} > 0$ such that for all $v \in V$, $w \in W$,

$$|a(v, w)| \leq C_{ses} \|v\|_V \|w\|_W. \tag{2.7}$$

A sesquilinear form is *continuous* if and only if it is bounded.

Definition 2.4.8 (Coercive Sesquilinear Form)**.** Let V be a complex vector space with norm $\| \cdot \|_V$. A sesquilinear for $a(\cdot, \cdot)$ is *coercive* if there exists a positive constant $\alpha > 0$ such that for every $v \in V$,

$$|a(v, v)| \geq \alpha \|v\|_V^2. \tag{2.8}$$

If we write (2.4) in a more abstract form by defining

$$a(u, v) := (\mathbb{D} \nabla u, \nabla v)_{\Omega, \mathbb{C}} + (cu, v)_{\Omega, \mathbb{C}}, \tag{2.9}$$

$$L(v) := (f, v)_{\Omega, \mathbb{C}}, \tag{2.10}$$

then is straightforward to show that (2.9) is a bounded and coercive sesquilinear form and that (2.10) is a bounded antilinear form.

In addition to having a maximum principle for classical solutions, we also have a similar maximum principle for variational formulations. Here we state the result presented by Barrenechea, John, and Knobloch (2025, Theorem 2.21).

Theorem 2.4.9 (Maximum Principle for Weak Solutions). Let $a(\cdot,\cdot)$ be a real, coercive, elliptic bilinear form representing the weak form of the reaction diffusion equation (2.9) and let $c \geq 0$ a.e. in Ω. If $a(\cdot,\cdot)$ is equipped with Dirichlet boundary conditions, then for any $u \in H^1(\Omega)$, it follows that

$$\begin{aligned} a(u,v) \leq 0 \quad \forall\, v \in H_0^1(\Omega),\ v \geq 0 &\implies \operatorname*{ess\,sup}_{\Omega} u \leq \operatorname*{ess\,sup}_{\partial\Omega} u^+, \\ a(u,v) \geq 0 \quad \forall\, v \in H_0^1(\Omega),\ v \geq 0 &\implies \operatorname*{ess\,inf}_{\Omega} u \geq \operatorname*{ess\,inf}_{\partial\Omega} u^-. \end{aligned}$$

In particular,

$$a(u,v) = 0 \quad \forall\, v \in H_0^1(\Omega) \qquad \implies \qquad \operatorname*{ess\,sup}_{\Omega} |u| = \operatorname*{ess\,sup}_{\partial\Omega} |u|.$$

Moreover, if $c = 0$ a.e. in Ω, then

$$\begin{aligned} a(u,v) \leq 0 \quad \forall\, v \in H_0^1(\Omega),\ v \geq 0 &\implies \operatorname*{ess\,sup}_{\Omega} u = \operatorname*{ess\,sup}_{\partial\Omega} u, \\ a(u,v) \geq 0 \quad \forall\, v \in H_0^1(\Omega),\ v \geq 0 &\implies \operatorname*{ess\,inf}_{\Omega} u = \operatorname*{ess\,inf}_{\partial\Omega} u. \end{aligned}$$

This result will be used in Chapter 4.

2.4.4 Well-Posedness Results

Using the abstract variational definitions from Section 2.4.3, in this Section we state some well known well-posedness results and discuss their application to problems with data in $L^1(\Omega)$.

The most widely used result is the following, whose proof for the real case can be found in Raviart and Thomas (1992, Theorem 2.2-1, p.37), and for the complex case can be found in Dautray and Lions (2000, Theorem 7, p.368).

Theorem 2.4.10 (Lax-Milgram). Let H be a Hilbert space over $\mathbb{R}$ (or $\mathbb{C}$). Let $a(\cdot,\cdot)$ be a continuous, coercive bilinear (or sesquilinear) form, and let $L(\cdot)$ be a continuous (anti)linear form. Then the problem: find $v \in H$ such that

$$a(v,w) = L(w) \quad \forall\, w \in H \tag{2.11}$$

has a unique solution.

Theorem 2.4.10 guarantees the existence of a unique solution if v and w belong to a Hilbert space, for example $H_0^1(\Omega)$, as in (2.4). However, in order for the right-hand side in (2.4) to be well-defined, we require $f \in L^2(\Omega)$. So, in order to possibly consider the case where $f \in L^1(\Omega)$ only, we mention an extension of Theorem 2.4.10 to reflexive Banach spaces, which can be found in the book by Ern and Guermond (2021a, Theorem 25.9).

Theorem 2.4.11 (Banach-Nečas-Babuška (BNB) Theorem). Let V be a complex Banach space and let W be a complex reflexive Banach space. Let $a(\cdot,\cdot)$ be a bounded sesquilinear form on $V \times W$ and let $L \in W'$ be a bounded antilinear form. Then the problem: find $v \in V$ such that

$$a(v,w) = L(w) \qquad \forall\, w \in W$$

is well-posed if and only if, for $v, w \neq 0$

$$\inf_{v\in V}\sup_{w\in W}\frac{|a(v,w)|}{\|v\|_V\|w\|_W} =: \alpha > 0, \text{ and} \tag{2.12}$$

$$\forall\, w \in W, \quad [\forall\, v \in V,\ a(v,w) = 0] \implies [w = 0]. \tag{2.13}$$

Condition (2.12) is known as the *inf-sup condition*. In particular, Theorem 2.4.11 shows that if $V = L^p(\Omega)$ and $W = L^q(\Omega)$ where q is the Hölder conjugate of p, then the problem is well-posed when $1 < p < \infty$. Since $L^1(\Omega)$ is not a reflexive Banach space, we cannot use Theorem 2.4.11 to prove well-posedness when $f \in L^1(\Omega)$.

One possible solution could be to take test functions $w \in H_0^1(\Omega) \cap L^\infty(\Omega)$, as this would make the term $(f,w)_\Omega$ well-defined for $f \in L^1(\Omega)$. However, $H_0^1(\Omega) \cap L^\infty(\Omega)$ is not a Banach space under the $H_0^1(\Omega)$ norm. In order to prove well-posedness, we would have to prove an inf-sup condition under a different norm, for instance with the norm $\|w\|_* := |w|_{1,\Omega} + \|w\|_{0,\infty,\Omega}$, and it is not clear how to justify the inf-sup condition under this norm. We are not aware of any results on the inf-sup stability of the discrete problem for this norm. In fact, if such a stability were to hold, then this would imply that the solution of the discrete problem satisfies bounds in $L^\infty(\Omega)$, which is known to only hold under certain mesh conditions.

A reformulation of the weak Poisson problem with a right-hand side in $L^1(\Omega)$ has been proposed in the literature for which well-posedness has been proven (Bénilan et al. 1995; Dall'Aglio 1996; Dal Maso et al. 1999). Details of this reformulation are shown in Appendix A.1. For the Induction Heating Problem studied in this Thesis, in Section 4.4.3 we prove existence of solutions by showing that there is additional regularity on the source term.

Once well-posedness has been established, the main focus of this Thesis is to prove convergence of FEMs to a weak solution. Hence, in the next Section, we introduce the FEM.

2.5 FEMs

There are actually numerous methods (e.g. finite difference method, finite volume, spectral method, etc.) that could be used to solve the Induction Heating Problem. However, the FEM is particularly well suited to general meshes, in comparison to other methods, that require structured quadrilateral meshes. Hence, we only consider the FEM.

2.5.1 Triangulations

First, we give some definitions. Let $\Omega \subset \mathbb{R}^d$ be an open, bounded, polygonal or polyhedral domain with Lipschitz boundary $\partial\Omega$.

Definition 2.5.1 (Conforming Triangulation). We say that $\mathcal{T}_h$ is a *simplicial conforming triangulation* or a *simplicial conforming mesh* if it is a finite set such that

1. $K \in \mathcal{T}_h$ is a open simplex contained in Ω,

2. $\overline{\cup\{K : K \in \mathcal{T}_h\}} = \overline{\Omega}$,

3. for $K_1, K_2 \in \mathcal{T}$, if $K_1 \neq K_2$ then $K_1 \cap K_2 = \emptyset$,

4. for $K_1, K_2 \in \mathcal{T}$, $\overline{K_1} \cap \overline{K_2}$ is either $\emptyset$, a common edge to K_1 and K_2, or $\overline{K_1} = \overline{K_2}$.

The vertices of the simplices in the triangulation are denoted by $\boldsymbol{x}_i$, $i = 1, \ldots, N+M$. The interior nodes are $\boldsymbol{x}_i$, $i = 1, \ldots, N$, and the boundary nodes are $\boldsymbol{x}_i$, $i = N+1, \ldots, N+M$.

For every $K \in \mathcal{T}_h$, we define $h_K := \operatorname{diam}(K)$ and denote ρ_K as the diameter of the ball inscribed in K. We denote by E_j the edge opposite the node $\boldsymbol{x}_j$ and denote by $\theta^K_{E_j}$ the interior angle opposite E_j on the element K. An illustration is shown in Figure 2.1.

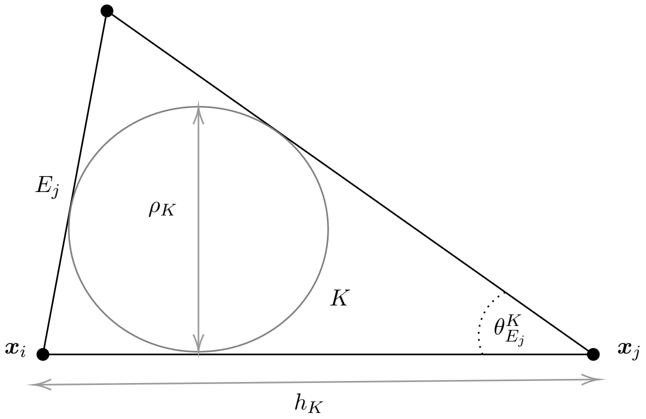

Figure 2.1: Example finite element K with maximum diameter h_K and inscribed ball with diameter ρ_K. Here E_j, is the edge opposite the node $\boldsymbol{x}_j$ and $\theta^K_{E_j}$ is the interior angle opposite E_j on the element K.

We set

$$h = \max\{h_K \ : \ K \in \mathcal{T}_h\}.$$

The prescribed index h in $\mathcal{T}_h$ corresponds to this value of h. A family $\{\mathcal{T}_h\}_h$ with $h \to 0$ corresponds to a sequence of meshes becoming increasingly refined. Now we give some definitions of different types of mesh families.

Definition 2.5.2 (Affine Triangulation)**.** A triangulation $\mathcal{T}_h$ is called *affine* if every $K \in \mathcal{T}$ is an affine map from a fixed reference element.

Definition 2.5.3 (Shape-Regular Triangulation)**.** A family of conforming triangulations $\{\mathcal{T}_h\}_h$ is *shape-regular* if there exists a constant $C_{reg} > 0$ independent of h such that

$$\frac{h_K}{\sigma_K} \leq C_{reg}, \qquad \forall\, K \in \mathcal{T}_h, \quad \forall\, \mathcal{T}_h \in \{\mathcal{T}_h\}_h.$$

The geometric interpretation of a shape-regular triangulation is that the elements do not get arbitrarily long and thin. This means that a shape-regular mesh also satisfies a minimum angle condition, i.e. there exists a constant $\theta_\circ > 0$ independent from h that for any $\mathcal{T}_h \in \{\mathcal{T}_h\}_h$ and any $K \in \mathcal{T}_h$, the minimal dihedral angle θ_E^K of K satisfies $\theta_E^K \geq \theta_\circ$ (Barrenechea, John, and Knobloch 2025, p.113).

Another useful characterisation of families of meshes is the following:

Definition 2.5.4 (Quasi-Uniform Triangulation)**.** A conforming family of triangulations $\{\mathcal{T}_h\}_h$ is *quasi-uniform* if there exists a constant $C_{qu} > 0$ independent of h such that

$$\frac{\max_{K\in\mathcal{T}_h} h_K}{\min_{K\in\mathcal{T}_h} h_K} \leq C_{qu} \qquad \forall\, \mathcal{T}_h \in \{\mathcal{T}_h\}_h.$$

The geometrical interpretation of this condition is that the ratio between the largest element on the mesh and the smallest element on the mesh cannot get arbitrarily large.

One of the main focuses of this Thesis is on proving results with no conditions on the mesh. For example, if we wanted to use the maximum principle to prove that a discrete function is bounded in the $L^\infty(\Omega)$ norm, the size and shape of the underlying mesh has to satisfy certain conditions. So, in order to understand these, we define some common conditions on mesh shapes. Some of the notation varies in the literature, so to be clear we explicitly say what we mean here.

Definition 2.5.5 (Properties of Meshes)**.** A simplicial triangulation $\mathcal{T}_h$ is said to be

- *strongly acute* if there exists an $\epsilon > 0$ such that every internal angle in each element $K \in \mathcal{T}_h$ satisfies $\theta \leq \frac{\pi}{2} - \epsilon$,
- *weakly acute* if every internal angle in each element $K \in \mathcal{T}_h$ satisfies $\theta \leq \frac{\pi}{2}$,
- of *Delaunay type* if the interior of the circumscribed sphere of any simplex of the mesh $\mathcal{T}_h$ does not contain any node of $\mathcal{T}_h$.

Generally, a strongly acute mesh is weakly acute, and a weakly acute mesh is Delaunay. So strongly acute is the strictest condition, and Delaunay is the weakest condition. In two dimensions, a triangulation is Delaunay if and only if the sum of the dihedral angles opposite E is smaller or equal to π (Barrenechea, John, and Knobloch 2025, Theorem 4.8).

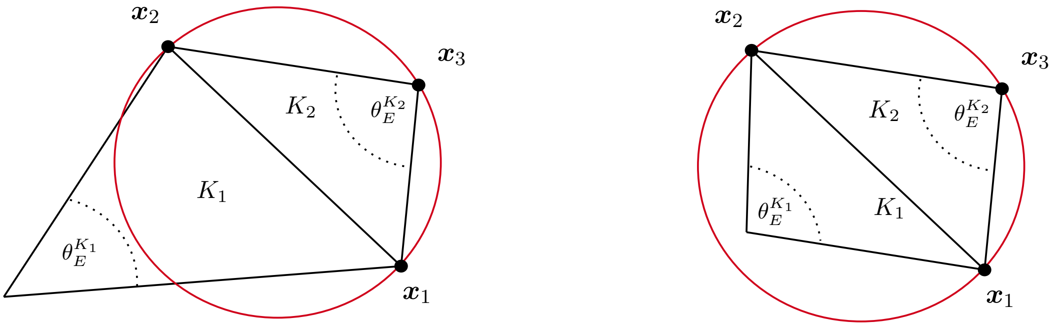

(a) Delaunay condition satisfied.

(b) Delaunay condition not satisfied.

Figure 2.2: Example of part of a mesh that satisfies the Delaunay condition, and part of a mesh that does not.

2.5.2 Finite Element Spaces

Now we have defined simplicial triangulations, we can define finite element spaces. The following definition is by Raviart and Thomas (1992).

Definition 2.5.6 (Finite Element as a Triple)**.** Consider the triple (K, Σ, P), where

1. K is a closed, connected, compact, non-empty subset of $\mathbb{R}^d$,
2. $\Sigma = \{\boldsymbol{a}_i\}_{i=1}^n$ is a collection of distinct points in K, called *degrees of freedom*, and
3. P is a finite dimensional vector space of polynomials composed of functions defined on K.

We say that the set Σ is *P-unisolvent* if and only if for n (complex) scalars α_j, $j = 1, \dots, n$, there exists a unique function P in the space K such that

$$P(\boldsymbol{a_j}) = \alpha_j, \quad j = 1, \dots, n.$$

If the set Σ is P-unisolvent, the triple (K, Σ, P) is called a *Lagrangian Finite Element.*

Let us denote $\mathbb{P}_k(K)$ or $(\mathbb{P}_{k;\mathbb{C}}(K))$ as the set of real (or complex)-valued polynomials with degree k defined on K. For example, when $K \subset \mathbb{R}^2$ is a simplex, the standard degrees of freedom defined on K are:

- when $P(K) = \mathbb{P}_0(K)$, $\Sigma = \{\boldsymbol{x}_0\}$, the centre of the simplex,
- when $P(K) = \mathbb{P}_1(K)$, $\Sigma = \{\boldsymbol{x}_1, \boldsymbol{x}_2, \boldsymbol{x}_3\}$, the vertices of the simplex, and
- when $P(K) = \mathbb{P}_2(K)$, $\Sigma = \{\boldsymbol{x}_1, \boldsymbol{x}_2, \boldsymbol{x}_3, \boldsymbol{x}_{12}, \boldsymbol{x}_{23}, \boldsymbol{x}_{13}\}$, the vertices and midpoints of the edges of the simplex.

This is illustrated in Figure 2.3.

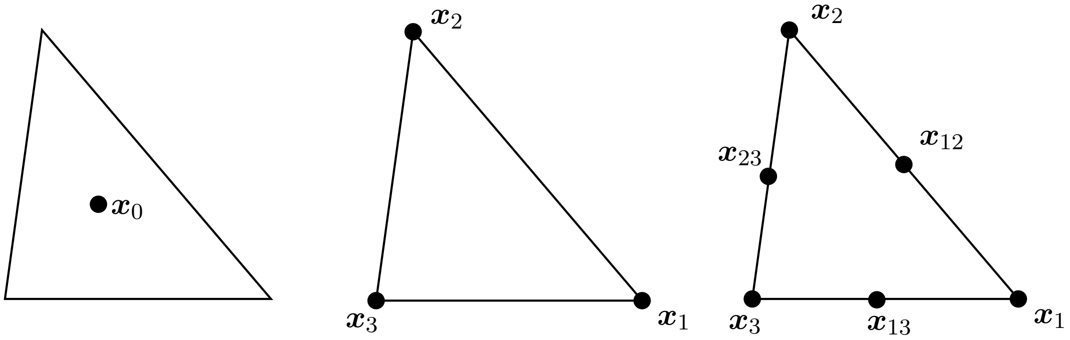

Figure 2.3: Degrees of freedom for $\mathbb{P}_0$, $\mathbb{P}_1$ and $\mathbb{P}_2$, respectively.

Here k is referred to as the *degree* of the finite element, corresponding to the degree of the polynomial space. It is possible to obtain finite elements with degree higher than 2, in fact, they can get much higher, and the details of this are in Raviart and Thomas (1992). However, in this Thesis, we only consider the case where $P(K) = \mathbb{P}_1(K)$ or $P(K) = \mathbb{P}_{1;\mathbb{C}}(K)$.

Definition 2.5.7 ($\mathbb{P}_1$ Finite Element Space)**.** Over the real numbers, the *finite element space* is defined as the set of continuous piecewise affine polynomial functions:

$$W_h := \{v_h \in C^0(\overline{\Omega}) : v_h|_K \in \mathbb{P}_1(K) \text{ for all } K \in \mathcal{T}_h\} \cap H^1(\Omega), \tag{2.14}$$

and

$$V_h := W_h \cap H_0^1(\Omega). \tag{2.15}$$

Over the complex numbers as, for P complex,

$$W_{h,\mathbb{C}} := \{v_h \in C^0(\overline{\Omega}) : v_h|_K \in \mathbb{P}_{1;\mathbb{C}}(K) \text{ for all } K \in \mathcal{T}_h\} \cap H^1(\Omega;\mathbb{C}), \tag{2.16}$$

and

$$V_{h,\mathbb{C}} := W_{h,\mathbb{C}} \cap H_0^1(\Omega;\mathbb{C}). \tag{2.17}$$

We remark here that V_h and $V_{h,\mathbb{C}}$ are subspaces of $H^1(\Omega)$ and $H^1(\Omega;\mathbb{C})$, respectively, and functions in V_h or $V_{h,\mathbb{C}}$ are fully determined by their degrees of freedom, that is, in the case of linear polynomials, their values at the nodes of the mesh. In this case, the degrees of freedom on for this space correspond to the vertices on the mesh.

Let $\phi_1, \ldots, \phi_{N+M}$ be the set of Lagrangian basis functions defined by the unique element in V_h (or $V_{h,\mathbb{C}}$) such that

$$\phi_i(\boldsymbol{x}_j) = \begin{cases} 1 & \text{if } i = j \\ 0 & \text{otherwise.} \end{cases}$$

Then

$$\begin{aligned} W_h &= \operatorname{span}\{\phi_1, \ldots, \phi_{N+M}\} \quad \text{over } \mathbb{R}, & W_{h,\mathbb{C}} &= \operatorname{span}\{\phi_1, \ldots, \phi_{N+M}\} \quad \text{over } \mathbb{C}, \\ V_h &= \operatorname{span}\{\phi_1, \ldots, \phi_N\} \quad \text{over } \mathbb{R}, & V_{h,\mathbb{C}} &= \operatorname{span}\{\phi_1, \ldots, \phi_N\} \quad \text{over } \mathbb{C}. \end{aligned}$$

Now we can define the Lagrange Interpolant, which is one method of projecting functions into the finite element space.

Definition 2.5.8 (Lagrange Interpolant)**.** Let V be a Sobolev space that can be continuously embedded onto $C^0(\overline{\Omega})$ (or $C^0(\overline{\Omega};\mathbb{C})$). Then for any $v \in V$, we denote by $\mathcal{I}_h v$ the unique element in V_h (or $V_{h,\mathbb{C}}$) such that

$$\mathcal{I}_h v = \sum_{i=1}^{N+M} v(\boldsymbol{x}_i)\phi_i.$$

The function $\mathcal{I}_h v$ is called the *Lagrange interpolant* of v onto V_h (or $V_{h,\mathbb{C}}$).

We now show some convergence results for the Lagrange Interpolant on $\mathbb{P}_{1;\mathbb{C}}$ elements, presented by Barrenechea, John, and Knobloch (2025, Theorem 5.8) and Ern and Guermond (2021b, Section 11.5).

Theorem 2.5.9 (Convergence Results for Lagrange Interpolant). Let $\{\mathcal{T}_h\}_h$ be a shape-regular family of affine meshes. Let $p \in [1, \infty]$, let $l = d$ if $p = 1$ and let l be the smallest integer such that $l > d/p$ if $p > 1$. Then there exists a positive constant C_{int} depending only on p, Ω, and the shape-regularity of the mesh, such that for all $v \in W^{r+1,p}(\Omega; \mathbb{C})$:

$$\|v - \mathcal{I}_h v\|_{m,p,\Omega,\mathbb{C}} \leq C_{int} h^{r+1-m} |v|_{r+1,p,\Omega,\mathbb{C}}$$

for $0 \leq m \leq r+1$, $l - 1 \leq r \leq 1$.

Corollary 2.5.10. If $\varphi \in \mathcal{D}(\Omega; \mathbb{C})$, then $\mathcal{I}_h \varphi \to \varphi$ a.e. as $h \to 0$.

Proof. By Theorem 2.5.9,

$$\|\varphi - \mathcal{I}_h \varphi\|_{0,\infty,\Omega,\mathbb{C}} \to 0 \quad \text{as } h \to 0$$

and since convergence in $L^\infty(\Omega; \mathbb{C})$ implies convergence a.e., we have the required result.

□

The Lagrange interpolant is useful enough in many cases. However, in Chapter 4 we require convergence results for functions that belong to $H_0^1(\Omega)$. For this we use the Scott-Zhang interpolant, and the full definition can be found in the book by Brenner and Scott (2008, Section 4.8). For our purposes we simply state the following result, which comes from Brenner and Scott (2008, Corollary 4.8.15).

Theorem 2.5.11. Let $\tilde{\mathcal{I}}_h$ denote the Scott-Zhang interpolant, as presented by Brenner and Scott (2008, Section 4.8), and first defined by Scott and Zhang (1990). Then, this interpolant is continuous with respect to the $H^1(\Omega)$-norm. Furthermore, there exists a positive constant C_{SZ} such that for all $v \in H^1(\Omega)$

$$\|v - \tilde{I}_h v\|_{0,\Omega} \leq C_{SZ} h \|v\|_{1,\Omega}, \tag{2.18}$$

and

$$\lim_{h\to 0} \|v - \tilde{I}_h v\|_{1,\Omega} = 0, \tag{2.19}$$

for all $v \in H^1(\Omega)$.

2.5.3 Finite Element Approximation of PDEs

Consider the variational formulation for the elliptic reaction-diffusion equation defined in (2.9). The problem reads: given $f \in L^2(\Omega;\mathbb{C})$: find $u \in H_0^1(\Omega;\mathbb{C})$, such that

$$a(u,v) = (f,v)_{\Omega,\mathbb{C}} \qquad \forall\ v \in H_0^1(\Omega;\mathbb{C}). \tag{2.20}$$

We seek an approximate solution in the finite dimensional subspace $V_{h,\mathbb{C}} \subset H_0^1(\Omega;\mathbb{C})$. Therefore, in finite dimensions the problem becomes: find $u_h \in V_{h,\mathbb{C}}$ such that

$$a(u_h,v_h) = (f,v_h)_{\Omega,\mathbb{C}} \qquad \forall\ v_h \in V_{h,\mathbb{C}}. \tag{2.21}$$

In fact, we can show that u_h is the best approximation for u in this subspace. Setting $v = v_h$ in (2.20), and subtracting (2.21) from (2.20) it follows that

$$a(u-u_h,v_h) = 0 \qquad \forall\ v_h \in V_{h,\mathbb{C}}.$$

This property is called *Galerkin orthogonality*; the error between u and u_h is orthogonal to $V_{h,\mathbb{C}}$. Using the boundedness condition (2.7) and the coercivity condition (2.8), it follows that

$$\alpha\|u-u_h\|^2_{1,\Omega,\mathbb{C}} \leq a(u-u_h,u-u_h) = a(u-u_h,u-v_h) \leq C_{ses}\|u-u_h\|_{1,\Omega,\mathbb{C}}\|u-v_h\|_{1,\Omega,\mathbb{C}},$$

and dividing through by $\|u-u_h\|_{1,\Omega,\mathbb{C}}$, we get

$$\|u-u_h\|_{1,\Omega,\mathbb{C}} \leq \inf_{v_h\in V_h} \frac{C_{ses}}{\alpha}\|u-v_h\|_{1,\Omega,\mathbb{C}}.$$

This shows that of all $v_h \in V_{h,\mathbb{C}}$, u_h is our best choice for approximating u, and this result is known as *Céa's lemma* (Céa 1964).

Since (2.21) holds for all v_h, it also holds for all basis functions ϕ_i. Since the basis functions span V_h, (2.21) is equivalent to the problem: find $u_h \in V_{h,\mathbb{C}}$ such that

$$a(u_h, \phi_i) = (f, \phi_i)_{\Omega,\mathbb{C}} \qquad i = 1, \dots, N. \tag{2.22}$$

We also know that u_h can be expressed as $\sum_{j=1}^{N} u_j \phi_j$, where $u_j = u_h(\boldsymbol{x}_j)$. Hence (2.22) is equivalent to saying: find u_j, $j = 1, \dots, N$ such that

$$\sum_{j=1}^{N} a(u_j \phi_j, \phi_i) = (f, \phi_i) \qquad i = 1, \dots, N,$$

or equivalently

$$\sum_{j=1}^{N} a(\phi_j, \phi_i) u_j = (f, \phi_i) \qquad i = 1, \dots, N.$$

We have thus reduced the discrete problem (2.21) to a linear system. Let $\mathbf{u}$ be the vector $(u_1, \dots, u_N)$, $\mathbb{A}$ be the $N \times N$ matrix with entries $a_{ij} = a(\phi_j, \phi_i)$, and let $\mathbf{f}$ be the vector $\mathbf{f} := ((f, \phi_i)_{\Omega,\mathbb{C}})_{i=1}^{N}$. Then the problem (2.22) finally becomes: find $u \in \mathbb{C}^N$ such that

$$\mathbb{A}\mathbf{u} = \mathbf{f}.$$

The matrix $\mathbb{A}$ is sometimes called the *stiffness* matrix. Since the basis functions are defined locally, this leads to a sparse matrix, which can be easily solved using an appropriate linear solver.

2.6 Stabilised FEMs

We have shown in Section 2.4.1 that certain elliptic PDEs can be shown *a-priori* to have solutions that attain their maximum (or minimum) on the boundary. However, it is not necessarily guaranteed that a numerical solution to a PDE satisfies these bounds. For example, for solutions with a boundary layer or for PDEs with a dominant reactive term, spurious oscillations - points that violate the physical bounds - can appear in the discrete solution if the mesh is not refined enough, or is not regular enough. This can lead to physically unrealistic values appearing in the solution, for example: negative concentrations, negative temperature (Kelvin), or increased mass or momentum. Additionally, since many problems are systems of two or more coupled problems (such as the Induction Heating Problem), where the solution of one PDE is used as data for another, physically inconsistent solutions in one variable can accumulate to large errors in all variables, and can lead to loss of stability. Therefore, in these scenarios, it is important to ensure that the numerical solution stays within the bounds of the continuous problem.

A numerical discretisation of a PDE is bound-preserving if the discrete solution does not violate the $L^\infty(\Omega)$ bounds of the continuous problem. The way to prove that a discretisation is bound-preserving is usually by proving a stronger requirement, namely, by proving that it satisfies the DMP. There are, in general, two ways to guarantee this: either by ensuring that the triangulation $\mathcal{T}_h$ satisfies certain properties, or by including a stabilising term in the numerical method. We will briefly discuss both here.

Conditions on the Mesh

We show in this Section that a discrete solution satisfies the DMP if the mesh $\mathcal{T}_h$ has certain regularity conditions. These conditions are established from properties of the problem's stiffness matrix. Therefore, first, we begin with a definition.

Definition 2.6.1 (Matrix of Non-Negative Type)**.** A matrix $(a_{ij})_{j=1,\dots,N}^{i=1,\dots,M} \in \mathbb{R}^{M\times N}$ is of *non-negative type* if

$$a_{ij} \le 0 \qquad \forall\ i \ne j, 1 \le i \le M, 1 \le j \le N, \tag{2.23}$$

$$\sum_{j=1}^{N} a_{ij} \ge 0 \qquad \forall\ 1 \le i \le M. \tag{2.24}$$

It was first shown by Ciarlet and Raviart (1973) that for the Poisson problem, if the stiffness matrix was of non-negative type, then the numerical solution satisfied the DMP. In particular, for (2.23) to be satisfied, a sufficient condition is that the normal direction from two different edges on the same element form an obtuse angle. This corresponds to the condition that the mesh $\mathcal{T}_h$ must be weakly acute. It is explained by Barrenechea, John, and Knobloch (2024) that for the Poisson problem, these conditions are sufficient, but not necessary. Indeed, it is shown that a Delaunay mesh is strict enough for the method to satisfy the DMP.

For the reaction-diffusion equation (2.4), stronger conditions are needed on the mesh. It was shown by Ciarlet and Raviart (1973) that the mesh $\mathcal{T}_h$ has to be strongly acute and h has to be small enough. Therefore, the reaction term imposes tighter restrictions on the meshes $\mathcal{T}_h$ in order to satisfy the DMP.

Stabilised Mass Lumping

We can relax the conditions on the mesh required for (2.4) to satisfy the DMP if we apply a mass-lumping strategy to the discretisation. Since this method guarantees the stability of the solution (i.e. guarantees no spurious oscillations), this method is called a *stabilised method.*

The stabilised mass-lumping method modifies the mass matrix of the reaction term (Barrenechea, John, and Knobloch 2024, Section 4.2). For $\mathbb{P}_1$ finite elements, let the mass matrix for the reaction term be the $N \times N$ matrix $\mathbb{M}$ and be defined in the usual way, with entries m_{ij} defined by

$$m_{ij} = (c\phi_j, \phi_i)_\Omega.$$

Then the stabilised mass-lumping form of the mass matrix is the diagonal matrix $\mathbb{M}_s$ with diagonal entries $\tilde{m}_{ii}$ defined by

$$\tilde{m}_{ii} = \sum_{j=1}^{N} m_{ij}.$$

In other words, the lumped mass matrix $\mathbb{M}_s$ is a diagonal matrix with entries equal to the row sums of the mass matrix $\mathbb{M}$. By writing it in this way, the reaction term does not contribute positive terms to the off-diagonals of the stiffness matrix, and thus the stiffness matrix is guaranteed to be of non-negative type under the same conditions as the Poisson problem. Therefore, this method removes the restriction on the size of h for the reaction-diffusion equation, although it converges at a lower rate than the standard FEM (Barrenechea, John, and Knobloch 2025, Theorem 7.12).

The Bound Preserving Method (BPM)

Here we introduce the main new method that is used in this Thesis: the BPM, first described by Barrenechea et al. (2024). Chapter 4 presents new FEM analysis of the BPM for the stationary Solenoidal Induction Heating Problem, and Chapter 5 presents a novel application of this method to a realistic induction heating problem combined with external data.

The appeal of this method is that it ensures bound preservation by constraining the solution *a-priori*. This is a property needed to obtain results in Chapter 4 that prove convergence without conditions on the mesh.

This Section follows the presentation by Barrenechea, John, and Knobloch (2025). Here, the BPM is presented for the reaction-diffusion equation in a real setting with homogeneous Dirichlet boundary conditions. The weak problem reads: given $f \in L^2(\Omega)$, find $u \in H_0^1(\Omega)$ such that

$$a(u, v) = (f, v)_\Omega \quad \forall\, v \in H_0^1(\Omega), \tag{2.25}$$

where $a(\cdot,\cdot) : H_0^1(\Omega) \times H_0^1(\Omega) \to \mathbb{R}$ is the bilinear form defined by

$$a(u, v) := (\mathbb{D}\nabla u, \nabla v)_\Omega + (cu, v)_\Omega$$

for $\mathbb{D} = (d_{i,j})_{i,j=1}^d \in L^\infty(\Omega)^{d\times d}$ and $a(\cdot) \in L^\infty(\Omega)$. We assume that $a(\boldsymbol{x}) \geq a_\circ > 0$ a.e. in Ω, and that $\mathbb{D}$ is symmetric and strictly positive definite.

The main assumption of this method is that the solution of the strong form of (2.25) satisfies

$$0 \leq u(\boldsymbol{x}) \leq k \quad \text{ for almost all } \boldsymbol{x} \in \Omega,$$

where k is a known positive constant. With this in mind, we define the set V^k as

$$V^k := \{v \in H_0^1(\Omega) : 0 \leq v(\boldsymbol{x}) \leq k \text{ a.e. in } \Omega\}, \tag{2.26}$$

and the set V_h^k as

$$V_h^k := \{v_h \in V_h : v_h(\boldsymbol{x}_i) \in [0,k] \text{ for all } \boldsymbol{x}_i = 1, \dots N\}. \tag{2.27}$$

If V_h consists of $\mathbb{P}_1$ Lagrange finite elements, then $V_h^k \subset V^k$ and every function $v_h^k \in V_h^k$ is bounded everywhere by k. However, if V_h consists of Lagrange finite elements with higher order, then $V_h^k \not\subset V^k$ and v_h^k is only bounded by k at the nodes. For the proofs in Chapter 4 we need $L^\infty(\Omega)$ bounds, so we only consider $\mathbb{P}_1$ Lagrange finite elements.

Every function $v_h \in V_h$ can be decomposed as $v_h = v_h^k + v_h^{-k}$ where $v_h^k \in V_h^k$ is defined as

$$v_h^k := \sum_{i=1}^{n} \max\{0, \min\{v_h(\boldsymbol{x}_i), k\}\}\phi_i,$$

and $v_h^{-k} := v_h - v_h^k$. We refer to v_h^k and v_h^{-k} as the *constrained* and *complementary* parts of v_h, respectively.

With these notations, the non-linear method proposed by Barrenechea et al. (2024) reads: find $u_h \in V_h$ such that

$$a(u_h^k, v_h) + s(u_h^{-k}, v_h) = (f, v_h)_\Omega \quad \text{for all } v_h \in V_h. \tag{2.28}$$

We take u_h^k to be the solution of (2.28).

In (2.28), the term $s(\cdot,\cdot) : C(\overline{\Omega}) \times C(\overline{\Omega}) \to \mathbb{R}$ is a stabilising bilinear mass-lumping form. In order to formulate it explicitly, we need to introduce the function $\mathfrak{h}$, which is a continuous, piecewise linear function which 'averages' the mesh widths of surrounding elements. More precisely, let ω_i be the vertex neighbourhood around the node $\boldsymbol{x}_i$, i.e., $w_i := \cup_{K \in \mathcal{T}_h : \overline{K} \cap \overline{K}_{\boldsymbol{x}_i} \neq \emptyset} K$, where $K_{\boldsymbol{x}_i}$ are the elements such that $\boldsymbol{x}_i \in \overline{K}_{\boldsymbol{x}_i}$. Then $\mathfrak{h}$ is defined as

$$\mathfrak{h}(\boldsymbol{x}_i) := \frac{\sum_{K \subset \omega_i} h_K}{\operatorname{card}\{K : K \subset \omega_i\}}, \qquad i = 1, \dots, N.$$

Using this mesh function, $s(\cdot,\cdot)$ is defined as

$$s(v_h, w_h) := \alpha \sum_{i=1}^{N} \left(\|\mathbb{D}\|_{0,\infty,\omega_i} \mathfrak{h}(\boldsymbol{x}_i)^{d-2} + \|c\|_{0,\infty,\omega_i} \mathfrak{h}(\boldsymbol{x}_i)^{d} \right) v_h(\boldsymbol{x}_i) w_h(\boldsymbol{x}_i), \qquad (2.29)$$

where α is a non-dimensional positive constant.

The stabilising bilinear mass lumping form (2.29) is designed to be monotone and to scale with the energy norm in order to guarantee existence and uniqueness of solutions to the method. However, there are other ways we could define $s(\cdot,\cdot)$. For example, we could choose

$$\mathfrak{h}(\boldsymbol{x}_i) := \max\{h_K : \boldsymbol{x}_i \in K\} \quad \text{or} \quad \mathfrak{h}(\boldsymbol{x}_i) := \min\{h_K : \boldsymbol{x}_i \in K\},$$

or even, if the mesh is quasi-uniform, we could choose

$$\mathfrak{h}(\boldsymbol{x}_i) := \max\{h_K : K \in \mathcal{T}_h\} \quad \text{or} \quad \mathfrak{h}(\boldsymbol{x}_i) := \min\{h_K : K \in \mathcal{T}_h\}.$$

We could also consider a h-independent stabilisation form like

$$s(v_h, w_h) := \alpha \sum_{i=1}^{N} v_h(\boldsymbol{x}_i) w_h(\boldsymbol{x}_i), \qquad (2.30)$$

but since this does not scale like the energy norm, it is not clear whether existence and uniqueness of solutions for the BPM can be proven, since this proof relies of the equivalence of these norms. In addition, it has been observed in some numerical experiments that for certain problems the non-linear solver behaves better with $\mathfrak{h}$ present.

In a similar vein, the proof of existence and uniqueness of solutions to the BPM relies on α being a positive constant. Allowing α to be any positive constant gives a degree of flexibility in the method. We highlight that the constrained part u_h^k does not depend on α, but the choice of α affects the scaling of the complementary part u_h^{-k}. More explicitly,

$$s(u_h^{-k}, v_h) = \alpha s\left(u_h^{-k}/\alpha, v_h\right). \qquad (2.31)$$

Within our numerical experiments, $\alpha = 1$ has been sufficient in all cases.

The BPM has also been designed to be monotone in order to guarantee existence and uniqueness of solutions. More specifically, it has been shown by Barrenechea et al. (2024) that

$$\begin{aligned} s(v_h^k - w_h^k, v_h^{-k} - w_h^{-k}) &\geq 0 \quad \forall\, v_h, w_h \in V_h, \\ s(v_h^{-k}, w_h - v_h^k) &\leq 0 \quad \forall\, v_h \in V_h, w_h \in V_h^k. \end{aligned}$$

The key argument used to prove well-posedness is that, crucially, since $s(\cdot,\cdot)$ is monotone, (2.28) implies the variational inequality

$$a(u_h^k, v_h - u_h^k) \geq (f, v_h - u_h^k)_\Omega \quad \forall\, v_h \in V_h^k. \tag{2.32}$$

This can be shown to have a unique solution due to Stampacchia's Theorem (see (Kinderlehrer and Stampacchia 2000, Theorem 2.1), quoted by Barrenechea, John, and Knobloch (2025, p.219)). In particular, (2.32) directly implies that u_h^k is the projection of u onto V_h^k using the inner product $a(\cdot,\cdot)$. This shows that u_h^k is the best approximation of u in the space V_h^k in the energy norm. This, in particular, implies that u_h^k converges to u regardless of the geometry of the mesh.

We could also solve (2.32) using a variational inequality solver (see, e.g., Facchinei (2003)). However, posing the problem as an equation opens the door to solving more general problems where there is no underlying variational inequality at the discrete level. For example, the recent work by Amiri et al. (2025) solves elliptic problems on polytopic meshes, where the discrete form cannot be formulated as an inequality. Additionally, the BPM was chosen for the Induction Heating Problem since it has all the desirable properties needed for the theoretical results in Chapter 4 (such as monotonicity, well-posedness, boundedness in $L^\infty(\Omega)$, and no mesh conditions), whilst at the same time also being straightforward to implement in a time-dependent and realistic simulation of induction heating in Chapter 5.

Remark. At first, it is unclear what $\lim_{h\to 0} u_h^k$ corresponds to when k is not assumed to be the physical bound of the problem. We might be interested in this problem if the physical bounds are *a-priori* unknown, or if we want to artificially constrain the solution space, for example in an optimal control problem. However, we prove in Chapter 4, Lemma 4.6.1 that if k is smaller than the physical bound of the problem, then $u_h^k \to \Pi_{V^k}(u)$ as $h \to 0$, where Π_{V^k} is the projection from V onto V^k, as characterised in Definition 2.3.10. This new result might have applications that extend beyond the scope of this Thesis. ■

Chapter 3

Description of the Induction Heating Problem

3.1 Abstract

In this Chapter we derive the Solenoidal model and the Axisymmetric model for induction heating directly from Maxwell's equations. We highlight the assumptions and considerations that we have made in these derivations.

3.2 Physical Interpretation and Full 3D Problem

Induction heating is a process commonly used in industrial settings to heat conductive materials using a magnetic field. The magnetic field is produced by passing an alternating current through an inductor. Generally, these currents have a very high frequency in order to maximise the heat transferred into the material. When a conductive material, such as a billet, is placed within the coil, the magnetic field induces eddy currents near the surface of the billet, and these currents generate heat due to the Joule effect. For more details on the setup see the book by Rudnev et al. (1997).

Let us consider a 3D model of an induction heating system. Let Σ_0 denote an open and bounded subset of $\mathbb{R}^3$ representing the billet, and let Σ_1 be a open, bounded, simply connected, non-convex subset of $\mathbb{R}^3$, disjoint from Σ_0, representing the inductor, which is usually a copper wire coil. Note that in industrial applications, this wire can be hollow, but for simplicity we assume that it is solid. Let $\Sigma_a = \mathbb{R}^3 \backslash (\overline{\Sigma_0} \cup \overline{\Sigma_1})$ be the air domain so that $\Sigma = \overline{\Sigma_0} \cup \overline{\Sigma_1} \cup \overline{\Sigma_a} = \mathbb{R}^3$. The boundaries of Σ_0 and Σ_1 are assumed to be Lipschitz continuous. An example configuration is illustrated in Figure 3.1.

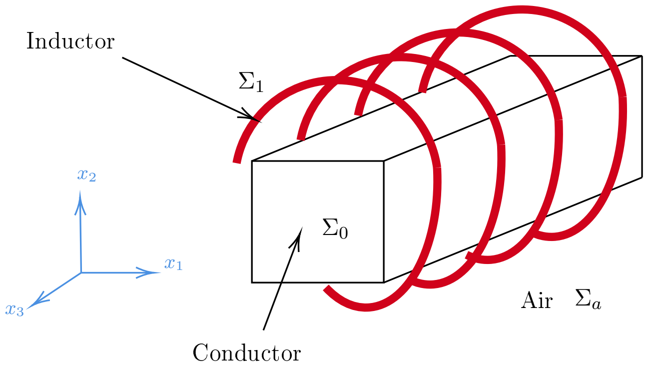

Figure 3.1: Illustration of the three dimensional induction heating domain.

The process of induction heating can be fully described by Maxwell's equations coupled with the heat equation. We now show how this is done by deriving the Eddy Current approximation of Maxwell's equations, which is the used to define the Induction Heating Problem.

3.2.1 Eddy Current Approximation of Maxwell's Equations

Let $\mathcal{B}(\boldsymbol{x}, t)$, $\mathcal{H}(\boldsymbol{x}, t)$, $\mathcal{D}(\boldsymbol{x}, t)$, $\mathcal{E}(\boldsymbol{x}, t)$, and $\mathcal{J}(\boldsymbol{x}, t)$ denote the magnetic induction field, magnetic field, electric displacement current field, electric field, and electric current density field, respectively. Additionally, let ρ_q denote the charge density, and $\mu_0 \approx 2\pi \times 10^{-7}\,\mathrm{H\,m^{-1}}$ and $\epsilon_0 \approx 8.854 \times 10^{-12}\,\mathrm{F\,m^{-1}}$ denote the physical constants for the permeability and permittivity of free space, respectively. Then Maxwell's equations read as follows:

$$
\begin{aligned}
\mu_0 \left(\mathcal{J} + \epsilon_0 \frac{\partial \mathcal{E}}{\partial t} \right) &= \mathbf{curl}\ \mathcal{H}, && \text{(Ampère's circuital law)} \\
\frac{\partial \mathcal{B}}{\partial t} + \mathbf{curl}\ \mathcal{E} &= \mathbf{0}, && \text{(Faraday's law of induction)} \\
\operatorname{div} \mathcal{B} &= 0, && \text{(Gauss's law for magnetism)} \\
\operatorname{div} \mathcal{E} &= \frac{\rho_q}{\epsilon_0}. && \text{(Gauss's law)}
\end{aligned}
$$

We introduce the functions μ and ϵ that stand for magnetic permeability and electrical permittivity, respectively, in order to be able to characterise the behaviour of the magnetic and electric fields. Assuming that all materials are linear and isotropic, we can write the constitutive equations

$$\mathcal{B} = \mu \mathcal{H}, \tag{3.1}$$

$$\mathcal{D} = \epsilon \mathcal{E}. \tag{3.2}$$

In (3.1) - (3.2), $\mathcal{B}$ and $\mathcal{D}$ are fields that describe the magnetic and electric behaviour observed in the system, whereas $\mathcal{H}$ and $\mathcal{D}$ are auxiliary fields that only account for free charges or currents. Any changes due to the material properties are described by μ and ϵ.

In general, μ and ϵ are functions depending on temperature, and μ can also depend on $|\mathcal{H}|$ to account for magnetic saturation. The function μ can also depend on the history of the system as some materials experience magnetic hysteresis. However, in this work we neglect hysteresis since the associated heat losses are only $\approx 7\%$ of the total eddy current losses (Rudnev et al. 1997).

An essential component to complete the system is Ohm's law. If we denote by σ the electrical conductivity, which is a function depending on temperature, then

$$\mathcal{J} = \begin{cases} \sigma \mathcal{E} & \text{in } \Sigma_0 \cup \Sigma_1, \\ 0 & \text{in } \Sigma_a. \end{cases} \tag{3.3}$$

In the materials that we study, σ is relatively high over a range of temperatures, i.e. $\approx 10^6\,\mathrm{S\,m^{-1}}$. For a constant temperature, a reasonable approximation to Ampère's circuital law is the following:

$$\mu_0 \left(\mathcal{J} + \epsilon_0 \sigma^{-1} \frac{\partial \mathcal{J}}{\partial t} \right) = \textbf{curl}\ \mathcal{H}.$$

Since ϵ_0 and σ^{-1} are small, the second term in Ampére's circuital law is negligible unless the current has an extremely high frequency, e.g. 10MHz (see Develey (2000)), which is not the case in induction heating applications. Therefore, we neglect this term; this is called the Low Frequency Approximation of Maxwell's equations.

Additionally, if we assume that the alternating current is sinusoidal, we can decouple the time dependence from the spatial dependence and write all fields in Maxwell's equations in the form

$$\mathcal{F}(\boldsymbol{x}, t) = \mathrm{Re}(\mathbf{F}(\boldsymbol{x}) e^{i\omega t}).$$

Here $\omega > 0$ is the angular frequency of the current and $\mathbf{F}(\boldsymbol{x}) = \hat{F}(\boldsymbol{x}) e^{i\phi}$ is a phasor: $\hat{F}(\boldsymbol{x})$ is a real function representing the maximum amplitude of the field and ϕ is the phase. Therefore, we can distinguish between $\mathcal{F}(\boldsymbol{x}, t)$, which is a real function depending on time that fully describes the evolution of the system; and $\mathbf{F}(\boldsymbol{x})$, which is a complex function independent of time that describes the amplitude of the field over the spatial domain, taking into account the phase of the system. In this case, we can rewrite Maxwell's equations to be in terms of these complex functions, which is called the Eddy Current approximation of Maxwell's equations. So, the Eddy Current equations are:

$$\textbf{curl}\ \mathbf{H} = \mathbf{J}, \tag{3.4}$$

$$-i\omega \mathbf{B} + \textbf{curl}\ \mathbf{E} = \mathbf{0}, \tag{3.5}$$

$$\mathrm{div}\ \mathbf{B} = 0, \tag{3.6}$$

$$\mathrm{div}\ \mathbf{E} = \frac{\rho_q}{\epsilon_0}. \tag{3.7}$$

Note that these equations are now quasi-static in time, since we removed the time-dependency. If μ is a function the justification of this approximation is more subtle than if μ is a constant (see Chapter 4.2.1 for a detailed discussion on this topic), but for now we consider it justified.

It is a well understood electromagnetic phenomenon that alternating currents in a wire are concentrated near the surface of the wire, and that this effect is more pronounced for higher frequencies. As might be expected, eddy currents induced in the billet exhibit the same behaviour: the eddy currents are concentrated near the surface of the billet and the current density decreases exponentially towards the centre. This is known as the *skin-effect*. We define the *skin-depth* δ to be the perpendicular distance between the boundary of the billet and the point where the current density is equal to '$1/e$', of its value at the boundary, where e is Euler's number. The power density decreases to '$1/e^2$' of its value at the boundary. This means that 63% of the current and 86% of the power is concentrated within this layer. For a constant temperature, using the formula by Develey (2000), the skin-depth can be approximated by

$$\delta = 503.1\sqrt{\frac{2\pi}{\sigma\mu_r\omega}},$$

where $\mu_r = \mu/\mu_0$ is the relative magnetic permeability. Crucially, this implies that a current with a very high frequency induces an extremely small skin-depth, e.g., in common steels, a typical alternating current of 100 kHz induces a skin-depth $\delta \approx 5 \times 10^{-5}$ m. See Figure 3.2 for magnetic field intensity for different frequencies.

As we will see in Section 3.2.2, heat is generated by the equivalent of the gradient of the magnetic field in the billet, so a smaller skin-depth induces more heat. Thus, to maximise the heating in the billet, the skin-effect is unavoidable. Rather, in many industrial applications the skin-effect is a desirable consequence, for example in induction hardening, it is used to create a very thin hot layer which is rapidly quenched to induce crystalline changes near the surface of the billet. This creates a very hard surface layer (i.e. martensite) but does not modify the inner material, minimising the risk of cracking (Rudnev et al. 1997).

However, the skin-effect means that there is a boundary layer in the magnetic field term $\mathbf{H}$. This is challenging to model with a FEM due to the computational cost of requiring a fine mesh refinement near the boundary in order to both avoid instabilities

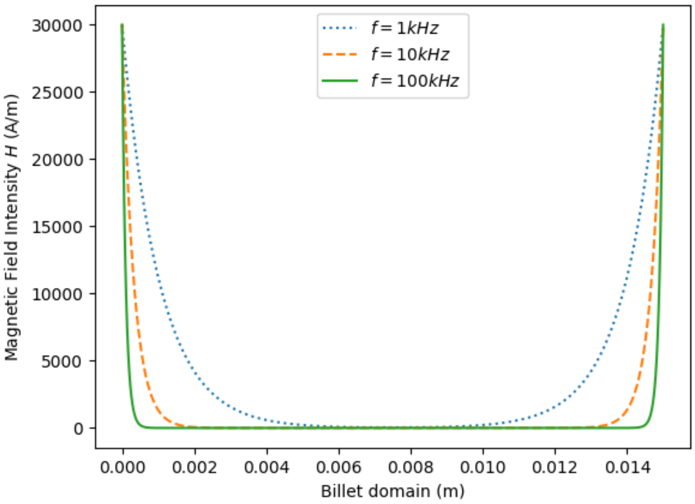

Figure 3.2: Calculation of the magnetic field strength along the x_1-axis of a 15 mm C42-MOD micro-alloyed steel billet for different frequencies. A frequency of 100 kHz is within the range of frequencies commonly used in induction heating processes.

in the method and to accurately capture the behaviour of $\mathbf{H}$.

The skin-depth can also vary throughout the induction heating process. In most magnetic materials, there is a temperature where the material becomes completely demagnetised. This is called the Curie point. At this point, μ decreases sharply and thus δ increases. As we will see more clearly in (3.15), larger skin-depths lead to a weaker heat source, so we can expect a sharp decrease in power to the source term in the heat equation (3.15) when the Curie point is reached. This perhaps presents an opportunity to use an adaptive algorithm to optimise an FEM.

The well-posedness of some variational formulations of the 3D Eddy Current Problem are discussed in detail by Touzani and Rappaz (2014, Chapter 4). Since the problem is posed in an infinite domain, all of these formulations involve boundary integrals. Numerical approximation of these formulations leads to non-local problems in the whole domain resulting in a dense matrix, and so solving the numerical approximation is exceedingly restrictive in terms of computational time.

The use of integral equations is avoided by Bermúdez, Rodríguez, and Salgado (2002), who prove well-posedness of the 3D Eddy Current problem in a bounded domain. Moreover, they propose and construct a finite element scheme using Nédélec edge finite element. However, for the analysis and the numerics, there are many extra conditions needed for this model, such as: a curl-free magnetic field in the air domain, cuts on the domain to make it simply connected, jump conditions on the cuts, and boundary conditions satisfying a curl condition. These additional constraints lead to very complicated variational formulations. So, even without considering temperature, the Eddy Current problem is challenging to solve.

Now we consider the heat equation, which will complete the Induction Heating Problem.

3.2.2 Heat Equation

The heat equation in induction heating reads: find the temperature u such that

$$\rho(u)C_p(u)\frac{\partial u}{\partial t} - \operatorname{div}(\kappa(u)\nabla(u)) = f_{\text{joule}} \qquad \text{in } \Omega,$$

where $\rho(\cdot)$ is the material density, $C_p(\cdot)$ is the specific heat capacity, $k(\cdot)$ is the thermal conductivity, and f_{joule} is the source term due to Joule heating. Joule heating is defined mathematically, as shown by Touzani and Rappaz (2014), as

$$f_{\text{joule}} = \mathcal{J}(\boldsymbol{x},t) \cdot \mathcal{E}(\boldsymbol{x},t).$$

Physically, this corresponds to heating a conductive material due to the flow of a current.

When ω is large, the time frequency domain of $\mathcal{J}(\boldsymbol{x},t)$ is much smaller than the rate of change of the temperature. For example, a typical frequency of 100 kHz has a period of 10^{-6} s but this only induces noticeable temperature change after about 10^{-2} s. Thus, if we were to model this using an FEM, even using two different time-scales, this would require computing the current density thousands of times for each temperature step, which is rather inefficient.

We can avoid the restrictive time-step by noticing that the heat source does not depend on the the direction of the current, only its magnitude. Therefore, we can take an average to get an approximation of the Joule heating power. Under the assumption that $\mathcal{J}$ and $\mathcal{E}$ are sinusoidal, it is common to take an averaged approximation f^*_{joule} of f_{joule} (see Touzani and Rappaz (2014, Section 8.1)). This can be defined as

$$\begin{aligned} f^*_{\text{joule}} &:= \frac{\omega}{2\pi}\int_0^{\frac{2\pi}{\omega}} \operatorname{Re}(e^{i\omega t}\mathcal{J}(\cdot,t)) \cdot \operatorname{Re}(e^{i\omega t}\mathcal{E}(\cdot,t))\,\mathrm{d}t \\ &= \frac{1}{2}\operatorname{Re}(\mathbf{J}\cdot\overline{\mathbf{E}}) \\ &= \frac{1}{2\sigma(u)}\mathbf{curl}\ \mathbf{H}\cdot\mathbf{curl}\ \overline{\mathbf{H}}. \end{aligned} \tag{3.8}$$

Therefore, the heat equation in three dimensions with the averaged source term is

$$\rho(u)C_p(u)\frac{\partial u}{\partial t} - \operatorname{div}(\kappa(u)\nabla(u)) = \frac{1}{2\sigma(u)}\mathbf{curl}\ \mathbf{H}\cdot\mathbf{curl}\ \overline{\mathbf{H}} \qquad \text{in } \Omega. \tag{3.9}$$

The ambient air u_{amb} is assumed to be constant at 298.15 K (25 °C). Physically, this can be justified by using water-cooling agents in the coils and allowing air flow over the billet. The temperature difference between the billet and the surrounding ambient air induces convective heat loss, which is written as a Robin boundary condition. Additionally, at higher temperatures (say 700 °C or ≈ 950 K) heat loss due to radiation must also be considered, and so the Stefan Boltzmann law should be included. Combining both terms, the boundary condition for (3.9) is

$$-\kappa(u)\frac{\partial u}{\partial n} = \alpha(|u|^3 u - u_{\text{amb}}^4) + \beta(u - u_{\text{amb}}) \qquad \text{on } \partial\Omega, \tag{3.10}$$

where β is the convective heat transfer coefficient, $\alpha = \varepsilon\sigma_s$ is the radiative heat transfer coefficient, ε is the material emissivity coefficient, and $\sigma_s \approx 5.67 \times 10^{-8}\,\mathrm{W\,m^{-2}\,K^{-4}}$ is the Stefan-Boltzmann constant. Since α is usually small, radiative heat loss is relatively small for lower temperatures, but will come to dominate as u increases.

The exact value of α can differ between billets made from the same material, and can depend on the shape of the billet, whether the surface has been polished, or if the surface has been oxidised from a previous heat treatment. In particular, if Σ is non-convex, and the normal vector to the surface intersects with the Σ, then we can have non-local heat transfer due to radiative heat loss (see, for instance, Tiihonen (1997) for analysis of the heat equation with radiation boundary conditions in non-convex domains). For modelling purposes we assume that Σ is allowed to be non-convex, but that the normal vector on every surface does not intersect with Σ.

3.3 The 2D Solenoidal Induction Heating Problem

In order to simplify the 3D problem, we can assume that the billet is symmetric in the x_3 direction. This way, the 3D problem can be reduced to a 2D problem. To this end, we assume that the billet domain Σ_0 is an infinite cylinder, in the sense that $\Sigma_0 = \Omega_0 \times \mathbb{R}$, where Ω_0 is a bounded open subset in $\mathbb{R}^2$ representing a perpendicular cross-section of the billet. The domain Ω_0 is surrounded by an annulus Ω_1, representing the induction coil, which is is also assumed to be an infinite cylinder in the x_3 direction. The assumption here is that the coil can be accurately represented as an infinitely long coil with no air gaps between each turn. The annulus splits the air domain into two disjoint subsets: Ω_a^+, which lies between the billet and the coil, and Ω_a^-, which is an infinite domain outside the inductor. Let the boundary between Ω_0 and Ω_a^+ be denoted by γ_0, and let the inside and outside boundaries of Ω_1 be respectively be noted by γ_1^+ and γ_0^+. We call this the Solenoidal domain; illustration of an example configuration is shown in Figure 3.3.

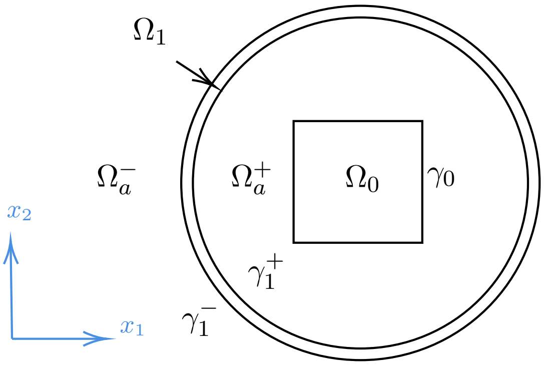

Figure 3.3: Illustration of the Solenoidal domain.

The Solenoidal configuration is a useful approximation when modelling a very long billet and a tightly wound coil, and we are interested in the general temperature profile in a cross-section of the centre of the billet. It is not so useful if we are interested in temperature distributions within short billets, around corners, or if there are air gaps in the coils. For these interests, an Axisymmetric model is better suited. For us, the Solenoidal model is useful as it provides the simplest realistic model of induction heating that can be analysed within a numerical analysis framework.

3.3.1 The Magnetic Field Equations

With this in mind, we can now simplify the Eddy Current equations by searching for solutions in the Solenoidal domain. Following Touzani and Rappaz (2014, Chapter 3.2), the current density in the coil $\mathbf{J}(\boldsymbol{x})$ does not depend on x_3 and is a vector field in the $x_1 - x_2$ plane. It follows that we can define

$$\mathbf{J}(x_1, x_2, x_3) = J_1(x_1, x_2)\boldsymbol{e}_1 + J_2(x_1, x_2)\boldsymbol{e}_2 =: \tilde{\mathbf{J}}.$$

Under this assumption, then by (3.4), it follows that

$$\mathbf{H}(\boldsymbol{x}) = H(x_1, x_2)\boldsymbol{e}_3 =: H.$$

Therefore, the magnetic field can be fully described by a scalar field. By rewriting (3.4) as

$$\mathbf{curl}\ H = \tilde{\mathbf{J}}, \tag{3.11}$$

we can use (3.5), some vector calculus identities, and the fact that div $H = 0$ to get

$$\begin{aligned} & i\omega\mu H + \mathrm{curl}(\sigma^{-1}\mathbf{curl}\ H) = 0 \\ \Rightarrow\quad & i\omega\mu H - \mathrm{div}(\sigma^{-1}\nabla H) = 0. \end{aligned} \tag{3.12}$$

We have now arrived at the magnetic field equation for the Solenoidal model. The full behaviour of the Eddy Current Problem has been condensed into a PDE of a single variable. We remark that when ω is large, we can see the skin-effect at the PDE level.

Since air is a dielectric, (3.11) implies that $\tilde{\mathbf{J}} = 0$ in the air domain, so $\mathbf{curl}\ H = 0$ in the air domain. This implies that $\nabla H = 0$ in the air domain, hence the magnetic field has a constant value which we denote $H_\circ$. If we assume there are no surface currents, then (3.11) also implies that H is continuous across the boundaries between the coil, air, and billet domains.

To complete the model, we need to prescribe the data for the current within the model. Here we consider two models commonly used in the literature. In reality, the transfer of current intensity to numerical input data is one of the most complex tasks in induction heating numerical modelling (Bay et al. 2003, Section 2.1.3), so it is worth mentioning.

Total Current Data

By applying Ampère's Law to the coil, we can calculate

$$H_\circ = \frac{nI}{L}, \tag{3.13}$$

where n is the number of turns in the coil, I is the total current flowing in the coil, and L is the working length of the coil. Therefore, if we know the total current I, we can calculate $H_\circ$ directly. This way, we can reduce the domain of the problem to the billet domain Ω_0, and prescribe $H_\circ$ as a Dirichlet boundary condition. We write $\Omega := \Omega_0$ as the billet domain, and we write the boundary as $\partial\Omega := \gamma_0$. See Figure 3.4 for the simplified domain.

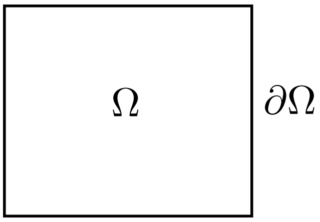

Figure 3.4: Illustration of the simplified Solenoidal domain when using total current data.

In practice, it is difficult to measure the total current I, as it requires breaking the circuit to measure the current flow. It is much easier to measure the voltage, which does not require breaking the circuit, so another approach is to incorporate the voltage data into the PDE.

Voltage Data

The voltage data is incorporated to a weak formulation of (3.12) over a modified Hilbert space. To define this, let $\tilde{\Omega} := \Omega_0 \cup \Omega_1$ be the union of the billet and the coil domain, and $\hat{\Omega} := \Omega_0 \cup \Omega_1 \cup \overline{\Omega}_a^+$ be the union of the billet, coil and inner air domain. Then we define the Hilbert space as

$$\mathcal{H} := \{v \in H_0^1(\hat{\Omega}; \mathbb{C}) : v|_{\Omega_a^+} = \text{ constant}\}. \tag{3.14}$$

Then the variational form of the magnetic field equation reads: given a voltage $v \in \mathbb{C}$, find $H \in \mathcal{H}$ such that

$$(\sigma^{-1}(u)\nabla H, \nabla Q)_{\tilde{\Omega},\mathbb{C}} + (i\omega\mu(u)H, Q)_{\hat{\Omega},\mathbb{C}} = v\overline{Q}|_{\Omega_a^+} \qquad \forall\, Q \in \mathcal{H}.$$

This formulation has a unique solution (Touzani and Rappaz 2014, Theorem 3.2.4). Since this model needs to include the coil and the air domain (Chaboudez et al. 1994; Clain 1994), and needs to use a specially designed Hilbert space, for simplicity, we elect to use the total current model for the purposes of our analysis. That being said, voltage measurements can still be incorporated into the total current model by manually calculating the current from the voltage (see Chapter A.2 for an example of this calculation).

3.3.2 The Heat Equation

The source term for the heat equation for the Solenoidal model can be further reduced from (3.8). We can calculate

$$\begin{aligned} f^*_{\text{joule}} &= \frac{1}{2\sigma(u)}\mathrm{Re}\left(\mathbf{curl}\ H \cdot \mathbf{curl}\ \overline{H}\right) \\ &= \frac{1}{2\sigma(u)}\nabla H \cdot \nabla\overline{H} \\ &= \frac{1}{2\sigma(u)}|\nabla H|^2. \end{aligned}$$

Therefore, the Solenoidal heat equation reads: given H, find u such that

$$\rho(u)C_p(u)\frac{\partial u}{\partial t} - \operatorname{div}(\kappa(u)\nabla(u)) = \frac{1}{2\sigma(u)}|\nabla H|^2 \qquad \text{in } \Omega, \tag{3.15}$$

$$-\kappa(u)\frac{\partial u}{\partial n} = \alpha(|u|^3 u - u_{\text{amb}}^4) + \beta(u - u_{\text{amb}}) \qquad \text{on } \partial\Omega. \tag{3.16}$$

Note that in this framework we can clearly see how the source term depends on the gradient of H, and thus shallower skin-depths produce more heat.

3.3.3 Weak Formulation

We can now state a formal 'naïve' weak formulation for the Solenoidal Induction Heating Problem using (3.12), (3.13), (3.15), and (3.16). We call it 'naïve' because it is not clear exactly which Sobolev spaces are needed to make the formulation well-posed, so for now we just assume that they are 'regular enough'. Therefore, we state the weak formulation of the Solenoidal Induction Heating Problem as the following:

Problem. Let u_0 be a sufficiently regular initial temperature, and let $[0,T] \subset \mathbb{R}$ be a time interval. The problem reads: find (H,u) 'regular enough' such that $\tilde{H} = H - H_\circ$, $\tilde{H}|_{\partial\Omega} = 0$ and for all $t \in (0,T)$,

$$(\sigma^{-1}(u)\nabla\tilde{H}, \nabla Q)_{\Omega,\mathbb{C}} + (i\omega\mu(u,|H|)H, Q)_{\Omega,\mathbb{C}} = (i\omega\mu(u,|H|)H_\circ, Q)_{\Omega,\mathbb{C}}, \tag{3.17a}$$

and

$$\begin{aligned}(\rho(u)C_p(u)u_t, v)_\Omega + (\kappa(u)\nabla u, \nabla v)_\Omega + \left(\alpha|u|^3u + \beta u, v\right)_{\partial\Omega} \\ = \left(\frac{|\nabla H|^2}{2\sigma(u)}, v\right)_\Omega + \left(\alpha u_{\text{amb}}^4 + \beta u_{\text{amb}}, v\right)_{\partial\Omega},\end{aligned} \tag{3.17b}$$

and

$$(u(0), z)_\Omega = (u_0, z)_\Omega, \tag{3.17c}$$

for all (Q,v) and z 'regular enough'.

If we search for a solution to (3.17a) in $H^1(\Omega;\mathbb{C})$, as is standard in the weak formulation, *a-priori* we have $|\nabla H|^2 \in L^1(\Omega)$ only, and thus (3.17b) is not fully justified.

Indeed, if this is this case, the heat equation cannot be analysed using Lax-Milgram's Lemma (Theorem 2.4.10), or the BNB Theorem (Theorem 2.4.11) and we are not guaranteed a unique solution to the heat equation. A rigorous justification of the weak formulation of the Solenoidal Induction Heating Problem with Dirichlet boundary condition is contained in Chapter 4. Note that we call this problem the 'Solenoidal Induction Heating Problem' when in the context of numerical analysis, but shorten this to the 'Solenoidal model' when in the context of numerical modelling.

It is worth remarking that the non-linearity in the radiation boundary term adds additional constraints on the solution space. Since $|u|^3 u$ appears in the boundary conditions, in order for the weak form to be well-defined, we must have

$$\int_{\partial\Omega} |u|^3 uv \, \mathrm{d}S < \infty \qquad \forall \, v.$$

Taking $v = u$ it follows that we must have $u \in L^5(\partial\Omega)$. Therefore, in order to define a well-posed problem, we would need to look for solutions in the space

$$V := \{v \in H^1(\Omega) : v|_{\partial\Omega} \in L^5(\partial\Omega)\}.$$

However, this is outwith the scope of this Thesis. For the analysis presented in Chapter 4, for simplicity we choose to equip the problem Dirichlet boundary conditions, and we mention the radiation boundary conditions as a possible extension.

3.4 The 2D Axisymmetric Induction Heating Problem

If the induction heating setup has a symmetry of rotation around the x_3 axis, then another possible reduction of the 3D model is the 2D Axisymmetric model. This way, we can reduce the model to a two dimensional of cylindrical system in the (r, z) half plane. Axisymmetric models are sometimes preferred in industrial settings because they can capture temperature differences at corners and due to air gaps between the coils.

In this Section, we follow the presentation by Bermúdez et al. (2007b). Let us represent the billet $\breve{\Omega}_0$ as an open, bounded and convex domain in $\breve{\Omega} := \mathbb{R}^+ \times \mathbb{R}$, with one boundary $\breve{\Gamma}_n^u$ on the z axis, and the second boundary $\breve{\Gamma}_u^n$ within the domain. Let the m induction coils $\breve{\Omega}_1, \ldots, \breve{\Omega}_m$ be represented by disjoint, open, bounded convex subsets of $\breve{\Omega}$. Finally let the air domain $\breve{\Omega}_a = \breve{\Omega} \backslash (\overline{\breve{\Omega}_0} \cup \ldots \cup \overline{\breve{\Omega}_m})$. An example configuration of the Axisymmetric domain is shown in Figure 3.5.

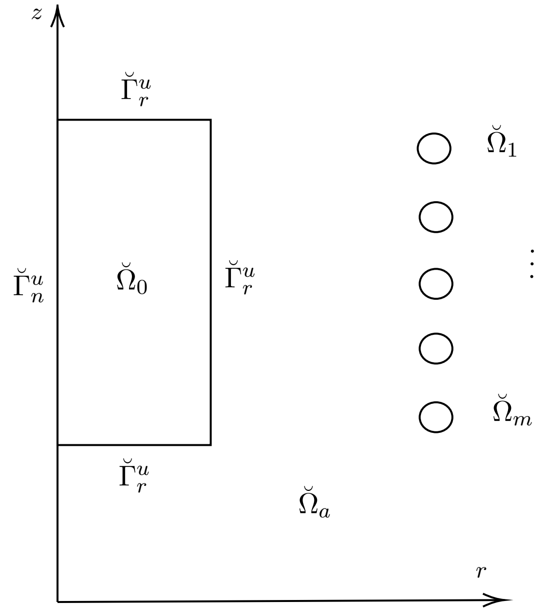

Figure 3.5: Example unbounded Axisymmetric domain.

Notice that in the 3D representation of the Axisymmetric domain, the coil is modelled as disjoint rings around the billet. Additionally, the Axisymmetric air domain is not simply connected.

3.4.1 The Magnetic Potential Equations

As an analogue of Section 3.3, we seek solutions where the current in the coils has a non-zero component only in the $\boldsymbol{e}_\theta$ direction (Touzani and Rappaz 2014, Chapter 5.1). We can therefore write

$$\breve{\boldsymbol{J}}(r, z) = J_\theta(r, z)\boldsymbol{e}_\theta,$$

which means that current density can be represented as a scalar field. It follows from Ohm's law (3.3) and the Eddy Current equations (3.4)-(3.7) that the electric field can also be represented as a scalar field, and the magnetic field can be fully described by a vector field lying within the (r, z) plane; that is,

$$\breve{\mathbf{E}}(r, z) = E_\theta(r, z)\boldsymbol{e}_\theta, \tag{3.18}$$

$$\breve{\mathbf{H}}(r, z) = H_r(r, z)\boldsymbol{e}_r + H_z(r, z)\boldsymbol{e}_z, \tag{3.19}$$

$$\breve{\mathbf{B}}(r, z) = B_r(r, z)\boldsymbol{e}_r + B_z(r, z)\boldsymbol{e}_z. \tag{3.20}$$

It is possible to design a well-posed model where the solution variable is the vector field $\breve{\mathbf{H}}$, as shown by Touzani and Rappaz (2014, Theorem 5.2.2). However, similar to the 3D case, this method involves boundary integral methods, requiring that $\breve{\mathbf{H}}$ satisfies a curl condition, and creating 'cuts' in the domain to make the air domain simply connected. Therefore, we choose to formulate the problem in terms of a vector potential, as under axisymmetric assumptions, this problem is scalar. This is a fairly popular formulation due to these simplifications (see, e.g. Chaboudez et al. (1997), Bermúdez et al. (2007b), and Fisk et al. (2022)).

The vector potential $\mathbf{A}$ is a vector field satisfying

$$\breve{\mathbf{B}} = \mathbf{curl}\ \mathbf{A}. \tag{3.21}$$

This is only unique up to a constant, so for uniqueness we take $\mathbf{A}$ to be divergence free (also called taking the Coloumb gauge). It has been shown by Touzani and Rappaz (2014, Theorem 5.3.1) that $\mathbf{A}$ is a scalar in an Axisymmetric domain, so

$$\mathbf{A}(r, \theta, z) = A_\theta(r, z)\boldsymbol{e}_\theta. \tag{3.22}$$

We call A_θ the *scalar potential*, and to simplify the notation we write $A := A_\theta$. With the same spirit as the Solenoidal model in Section 3.3, we reduce the Eddy Current equations to be formulated entirely in terms of A. Then, the magnetic vector field $\breve{\mathbf{H}}$ can be recovered from A. By definition of the axisymmetric **curl**, it follows that

$$B_r(r, z) = -\frac{\partial A}{\partial z}, \qquad B_z(r, z) = \frac{1}{r}\frac{\partial (rA)}{\partial r}.$$

Substituting (3.21) into (3.5), we get

$$\begin{aligned} & \mathbf{curl}(i\omega\mathbf{A}+\mathbf{E})=\mathbf{0}, \\ \Rightarrow\quad & \mathbf{curl}(i\omega A+\sigma^{-1}J_\theta)\boldsymbol{e}_\theta=\mathbf{0}, \end{aligned}$$

which implies that

$$\frac{\partial}{\partial z}(i\omega A+\sigma^{-1}J_\theta)=0 \quad\text{and}\quad \frac{\partial}{\partial r}\left\{r(i\omega A+\sigma^{-1}J_\theta)\right\}.$$

Therefore, there exist constants $C_k\in\mathbb{C}$, $k=0,\dots,m$, and $C_{air}\in\mathbb{C}$ such that

$$i\omega A+\sigma^{-1}J_\theta=\frac{C_k}{r} \qquad \text{in } \Omega_k,\quad k=0,\dots,m, \tag{3.23}$$

$$i\omega A+\sigma^{-1}J_\theta=\frac{C_{air}}{r} \qquad \text{in } \Omega_{air}. \tag{3.24}$$

In particular, it is shown by Bermúdez et al. (2007b) that $C_0=0$ in the billet domain $\breve{\Omega}_0$ is necessary to avoid a singularity when $r=0$. Finally, combining (3.4), and (3.23), over the entire domain A satisfies

$$\mathbf{curl}\left(-\frac{1}{\mu}\frac{\partial A}{\partial z}\boldsymbol{e}_r+\frac{1}{\mu r}\frac{\partial rA}{\partial r}\boldsymbol{e}_z\right)=\sigma\left(-i\omega A+\frac{C_k}{r}\right)\boldsymbol{e}_\theta. \tag{3.25}$$

Using the expression for **curl** in cylindrical coordinates from Section 2.2.1, we get for $k=0,\dots,m$,

$$-\left(\frac{\partial}{\partial r}\left(\frac{1}{\mu r}\frac{\partial(rA)}{\partial r}\right)+\frac{\partial}{\partial z}\left(\frac{1}{\mu}\frac{\partial A}{\partial z}\right)\right)+i\omega\sigma A=\frac{\sigma}{r}C_k \quad \text{in } \Omega_k.$$

Since $\sigma=0$ in air, it follows that

$$-\left(\frac{\partial}{\partial r}\left(\frac{1}{\mu r}\frac{\partial(rA)}{\partial r}\right)+\frac{\partial}{\partial z}\left(\frac{1}{\mu}\frac{\partial A}{\partial z}\right)\right)=0 \quad \text{in } \Omega_{air}.$$

The constants C_k depend on the current intensity and can be thought of as Lagrange multipliers. A method to determine these constants explicitly is shown in Section 5.4.1.

Boundary Conditions

In order to apply a standard FEM to this problem, we take a sufficiently large rectangular box in the (r, z) plane and impose conditions on the boundary of this box. The bounded geometry is shown in Figure 3.6. We now set $\breve{\Omega} := \overline{\breve{\Omega}}_a \cup \overline{\breve{\Omega}}_0 \cup \ldots \cup \overline{\breve{\Omega}}_m$ to be this box rather than the entire half-plane.

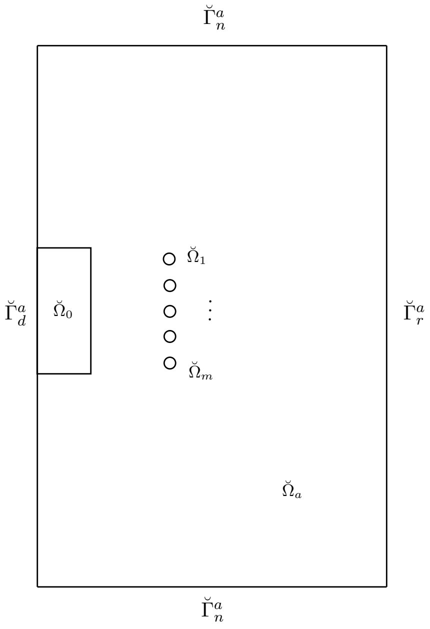

Figure 3.6: Example bounded Axisymmetric domain.

The Biot-Savart law implies that the field $\breve{\mathbf{B}}$ behaves like $1/(r^3 + z^3)$ far from the conductors (see Chaboudez et al. (1997)). For large values of r, the behaviour of A can be considered to be similar to $1/r^2$. Therefore, on the boundary $\breve{\Gamma}_r^a$ parallel to the axis of symmetry, we impose the Robin boundary condition

$$\frac{\partial(rA)}{\partial r} + A = 0. \tag{3.26}$$

For the boundaries perpendicular to the symmetry axis, by assuming that the radial component of the magnetic field is close to zero, we set homogeneous Neumann boundary conditions on $\breve{\Gamma}_n^a$

$$\frac{\partial(rA)}{\partial z} = 0. \tag{3.27}$$

On the axis of symmetry $\breve{\Gamma}^a_d$, we set the natural symmetry condition

$$A = 0. \tag{3.28}$$

For these boundary conditions, the box has to be 'large enough'. In most practical applications, setting the air domain to be four times the billet length in the z direction and four times the distance from the axis of symmetry to the outer edges of the coils is considered enough.

We should also consider interface conditions on the conduction. Following the presentation by Rappaz and Świerkosz (1996), let $[f]$ denote the jump of a function f, and let $\boldsymbol{n} = n_r \boldsymbol{e}_r + n_z \boldsymbol{e}_z$ denote the unit vector normal to the boundary of the conductors. We assume there are no surface currents so

$$[\breve{\mathbf{H}} \times \boldsymbol{n}] = \mathbf{0},$$

on the boundary between domains. As $\breve{\mathbf{H}} \times \boldsymbol{n} = (H_z n_r - H_z n_z)\boldsymbol{e}_\theta$, this implies that

$$[H_r n_z - H_z n_r] = 0,$$

and it follows that

$$\left[\frac{1}{\mu r}\left(\frac{\partial(rA)}{\partial z} n_z + \frac{\partial(rA)}{\partial r} n_r\right)\right] = 0,$$

and hence

$$[A] = \left[\frac{1}{r}\frac{\partial(rA)}{\partial \boldsymbol{n}}\right] = 0.$$

We will enforce this continuity across the boundary by using a piecewise continuous Galerkin method.

3.4.2 The Heat Equation

In a similar manner to the Solenoidal model in Section 3.3.2, the heat equation can be written as

$$\rho(u)C_p(u)\frac{\partial u}{\partial t} - \frac{1}{r}\frac{\partial}{\partial r}\left(r\kappa(u)\frac{\partial(ru)}{\partial r}\right) - \frac{\partial}{\partial z}\left(\kappa(u)\frac{\partial u}{\partial z}\right) = \frac{|J_\theta|^2}{2\sigma(u)}, \tag{3.29}$$

where the source term $|J_\theta|^2/2\sigma(u)$ has been calculated using the same averaging process as (3.8). It follows from (3.23) that

$$J_\theta = -i\omega\sigma(u)A \quad \text{in } \breve{\Omega}_0,$$

since $C_0 = 0$ in $\breve{\Omega}_0$.

Along $\breve{\Gamma}_r^u$, the boundary condition for (3.29) describing radiative heat loss into the air domain is

$$-\kappa(u)\frac{\partial u}{\partial \boldsymbol{n}} = \alpha(|u|^3 u - u_{\text{amb}}^4) + \beta(u - u_{\text{amb}}) \qquad \text{on } \breve{\Gamma}_r^u.$$

Along the axis of symmetry $\breve{\Gamma}_n^u$, we set the homogeneous Neumann condition

$$\kappa(u)\frac{\partial u}{\partial \boldsymbol{n}} = 0 \qquad \text{on } \breve{\Gamma}_n^u,$$

which specifies that there is to be no heat flux across the axis of symmetry.

3.4.3 Weak Formulation

In order to define a variational formulation for the Axisymmetric model, we need to introduce weighted Sobolev spaces in order to resolve the singularity around the axis of symmetry. Here, we follow the presentation given by Bermúdez et al. (2010).

We define the weighted Lebesgue space $L_r^2(\breve{\Omega})$ as the space of all measurable functions v such that

$$\|v\|_{L_r^2(\breve{\Omega})}^2 := \int_{\breve{\Omega}} |v|^2 \, r \,\mathrm{d}r \,\mathrm{d}z < \infty.$$

The space $H_r^1(\breve{\Omega})$ consists of all functions in $L_r^2(\breve{\Omega})$ with finite derivatives in the

$L^2_r(\breve{\Omega})$ norm. We define $\tilde{H}^1_r(\breve{\Omega}) := H^1_r(\breve{\Omega}) \cap L^2_{1/r}(\breve{\Omega})$, which is a Hilbert space when equipped with the norm

$$\|v\|_{\tilde{H}^1_r(\breve{\Omega})} := \left(\|v\|^2_{H^1_r(\breve{\Omega})} + \|v\|^2_{L^2_{1/r}(\breve{\Omega})} \right)^{1/2}.$$

The spaces $L^2_r(\breve{\Omega};\mathbb{C})$, $H^1_r(\breve{\Omega};\mathbb{C})$, and $\tilde{H}^1_r(\breve{\Omega};\mathbb{C})$ are defined analogously for complex functions. Here we state a 'naïve' weak formulation of the Axisymmetric model, which has not yet been rigorously justified. However, since the source term of (3.29) is more regular than $L^1(\breve{\Omega})$, we do not have the difficulty with the regularity that we see in the Solenoidal Induction Heating Problem. This is because A is related to the gradient of H by

$$\mu \mathbf{H} = \mathbf{curl}\ \mathbf{A}. \tag{3.30}$$

Therefore, a right-hand side of $|A|^2$ with $A \in H^1_r(\breve{\Omega})$ gives $|A|^2 \in W^{1,1}_r(\breve{\Omega})$, which by Sobolov embedding is contained in $L^2_r(\breve{\Omega})$.

Therefore, we state the weak formulation of the Axisymmetric Induction Heating Problem as the following, which is well-defined:

Problem. Given constants $C_k \in \mathbb{C}$, an initial condition $u_0 \in L^2_r(\Omega)$, and a time interval $[0,T] \subset \mathbb{R}$, find $(A,u) \in L^2([0,T];\tilde{H}^1_r(\Omega;\mathbb{C})) \times L^2([0,T];\tilde{H}^1_r(\Omega) \cap L^5(\breve{\Gamma}^u_r))$ such that $A = 0$ on Γ^a_d and for all $t \in (0,T]$:

$$\begin{aligned} \int_{\breve{\Omega}} \left(\frac{1}{\mu(u,A,r,z)r} \frac{\partial(rA)}{\partial r} \frac{1}{r} \frac{\partial(r\overline{Q})}{\partial r} + \frac{1}{\mu(u,A,r,z)} \frac{\partial A}{\partial z} \frac{\partial \overline{Q}}{\partial z} \right) r \, \mathrm{d}r \, \mathrm{d}z& \\ + \int_{\breve{\Omega}} i\omega\sigma(u,r,z) A\overline{Q}\, r \, \mathrm{d}r \, \mathrm{d}z + \int_{\breve{\Gamma}^a_r} \frac{1}{\mu(u,A,r,z)} A\overline{Q} \, \mathrm{d}z& \\ = \sum_{k=1}^{m} \int_{\breve{\Omega}_k} \sigma(u,r,z) C_k \overline{Q} z \, \mathrm{d}r \, \mathrm{d}z,& \end{aligned} \tag{3.31}$$

for all $Q \in \tilde{H}^1_r(\Omega;\mathbb{C})$, and

$$\int_{\breve{\Omega}_0} \rho(u) C_p(u) \frac{\partial u}{\partial t} v \, r \, \mathrm{d}r \, \mathrm{d}z + \int_{\breve{\Omega}_0} \kappa(u) \nabla u \cdot \nabla v \, r \, \mathrm{d}r \, \mathrm{d}z + \int_{\breve{\Gamma}^u_r} (\alpha |u|^3 u + \beta u) v \, r \, \mathrm{d}z \\ = \int_{\breve{\Omega}_0} \frac{|\omega \sigma(u) A|^2}{2\sigma(u)} v \, r \, \mathrm{d}r \, \mathrm{d}z + \int_{\breve{\Gamma}^u_r} (\alpha u^4_{\text{amb}} + \beta u_{\text{amb}}) v \, r \, \mathrm{d}z \quad (3.32)$$

$$(3.33)$$

for all $v \in \tilde{H}^1_r(\Omega) \cap L^5(\breve{\Gamma}^u_r)$, and

$$\int_{\breve{\Omega}_0} u(0) w \, r \, \mathrm{d}r \, \mathrm{d}z = \int_{\breve{\Omega}_0} u_0 w \, r \, \mathrm{d}r \, \mathrm{d}z,$$

for all $w \in L^2_r(\Omega)$.

It has been proven by Bermúdez et al. (2010) that (3.31) is well-posed when μ is constant in each subdomain. We also briefly mention some extensions by the same authors proving well-posedness for transient magnetic potential formulations (Bermúdez et al. 2013; Bermúdez et al. 2015). However, it is not clear that that the coupling of (3.31) with (3.32) constitutes a well-defined or well-posed problem. Indeed, analysis of the Axisymmetric Induction Heating Problem seems to be minimal, perhaps due to the compounded complications from the magnetic potential formulation and coupling with a heat equation. We therefore only concern ourselves with the numerical implementation of the Axisymmetric model, and focus our analysis on the Solenoidal Induction Heating Problem.

Chapter 4

A FEM for the 2D Steady-State Problem

4.1 Abstract

In this Chapter, we analyse a steady-state version of the Solenoidal Induction Heating Problem, where we impose Dirichlet boundary conditions and simplify some coefficients. By showing that the source term is more regular than $L^1(\Omega)$, we rigorously prove existence of solutions using a fixed-point argument, and improve on the current literature by allowing a non-convex domain. Then, we study the finite element approximation and prove that the standard Galerkin FEM converges in convex domains and under strict conditions on the mesh. We improve on this result by applying the BPM to the heat equation, and show that this method converges to a solution of a one-directional coupled problem under no conditions on the domain or the mesh. Additionally, we prove that when imposing non-physical bounds on the discrete heat solution in the BPM, the method converges to a projection of the continuous solution onto a constrained convex set. This result allows us to prove convergence of the one-directional system.

4.1.1 Statement of Problem

Let us define the steady-state Solenoidal Induction Heating Problem. Let $\Omega \in \mathbb{R}^2$ be an open, bounded, and potentially non-convex polygon with boundary $\partial\Omega$. Then the steady-state Solenoidal Induction Heating Problem reads: find the magnetic field H and temperature u such that

$$
\begin{aligned}
-\Delta H + i\omega\mu(u)H &= 0 && \text{in } \Omega, && (4.1a)\\
H &= H_\circ && \text{on } \partial\Omega, && (4.1b)\\
-\Delta u &= |\nabla H|^2 && \text{in } \Omega, && (4.1c)\\
u &= 0 && \text{on } \partial\Omega. && (4.1d)
\end{aligned}
$$

Here:

- ω is a positive constant representing the angular frequency of the alternating current,
- $H_\circ$ is a positive constant representing the magnetic field strength in the surrounding air, and
- $\mu(\cdot)$ is a function depending on temperature representing the magnetic permeability of the material. We assume that $\mu(\cdot)$ is Lipschitz continuous and that there exist positive constants $\mu_\circ$ and μ° such that

  $$0 < \mu_\circ \le \mu(s) \le \mu^\circ \qquad \forall\, s \in \mathbb{R}.$$

The main difficulty with the Solenoidal Induction Heating Problem is the source term in (4.1c). Following standard practices, if we assume that the weak form of (4.1a) is imposed in $H^1(\Omega;\mathbb{C})$, then the source term of (4.1c) appears to belong only to $L^1(\Omega)$. If this is the case, (4.1c) cannot be written as a weak problem with the trial and test functions belonging only to $H^1_0(\Omega)$, so we cannot apply Lax-Milgram's Lemma (Theorem 2.4.10). Additionally, since $L^1(\Omega)$ is not reflexive, we cannot apply the BNB Theorem (Theorem 2.4.11) either. In this Chapter, we resolve this issue by showing that $|\nabla H|^2 \in L^2(\Omega)$, and thus has additional regularity that allows the application of Lax-Milgram's Lemma.

We have chosen to consider a simplified coupled system by setting the electrical conductivity $\sigma(\cdot)$ from (3.12) and thermal conductivity $\kappa(\cdot)$ from (3.15) equal to one. This is because including $\sigma(\cdot)$ and $\kappa(\cdot)$ will not qualitatively change our argument but will make the calculations more involved, and these cases have already been considered in the literature, see, e.g., the work by Clain and Touzani (1997a) and Clain and Touzani (1997b) where they use a Kirchoff transformation to prove existence of solutions where $\kappa(\cdot)$ and $\sigma(\cdot)$ are allowed to be functions, but $\mu(\cdot)$ is set to be a constant and Ω is required to be convex and smooth. Indeed, $\mu(\cdot)$ requires careful consideration; a detailed discussion of $\mu(\cdot)$ and how we choose to handle it is presented in Section 4.2.1.

Other technical aspects of the analysis of the full system (3.17), such as the non-linear boundary term $|u|^3u$ from (3.10) are considered to be beyond the scope of this research: for the analysis of a scalar problem with radiation boundary conditions, interested readers are directed to the book by Roubíček (2013). For simplicity we take homogeneous Dirichlet boundary conditions.

4.2 Literature Review

In this Section, we give an overview of the literature relevant to the Solenoidal Induction Heating Problem. We discuss some different methods to handle the term $\mu(\cdot)$, how these can affect the validity and efficiency of the model, and justify our choice of method. We outline the literature that exists on the Solenoidal Induction Heating Problem, of which there is surprisingly little due to the challenges arising from the irregular heat source term. Accordingly, we mention some work that has been done on elliptic problems with a right-hand side in $L^1(\Omega)$. We also discuss some existing results for the Thermistor Problem, which is a simpler, related problem containing the same irregular right-hand side. In this problem, it has been shown that the coupled system implies that, in fact, there is additional regularity on the irregular source term. There is a wealth of literature on this problem, so we discuss how the methods used could be extended to the Solenoidal Induction Heating Problem.

4.2.1 The Coupling Term

The first aspect of the Solenoidal Induction Heating Problem we discuss is the term $\mu(\cdot)$. In practical applications, this term depends on both u and $|H|$, so (4.1a) becomes a non-linear equation. Furthermore, as is commonly seen in magnetic systems, $\mu(\cdot)$ also depends on the history of the system. This is a phenomenon known as *hysteresis*, where there is a lag between the H and the corresponding output $\mu(\cdot)$. However, it is rather complicated to model (see, e.g., Jiles and Atherton (1986)) and in any case, variations due to hysteresis in most applications can be regarded as negligible (Rudnev et al. 1997, p.782). Therefore, like the majority of models, we choose to neglect hysteresis. We also choose to let $\mu(\cdot)$ only depend on u, not on H, because this is beyond the scope of the analysis. Dependence on H will be included in the numerical modelling in Chapter 5.

However, even if $\mu(\cdot)$ depends only on temperature, some subtleties still remain to be considered. Specifically, if $\mu(\cdot)$ is not constant, then even if the alternating current is a sine wave, the magnetic field is not necessarily also a sine wave. More specifically, notice that since u depends on time, this implies that

$$\frac{\partial\left(\mu(u)He^{i\omega t}\right)}{\partial t} \neq i\omega\mu(u)He^{i\omega t}.$$

One solution is to skip the Eddy Current approximation and consider an evolutive magnetic field equation. In this case, we solve for $\mathcal{H}$, where $\mathcal{H}(\boldsymbol{x},t)$ depends on $\boldsymbol{x}$ and t, and (4.1a) is replaced by

$$-\Delta\mathcal{H} + \omega\frac{\partial}{\partial t}(\mu(u)\mathcal{H}). \tag{4.2}$$

Thus, instead of solving a complex quasi-static equation, we solve a real parabolic equation for $\mathcal{H}(\boldsymbol{x},t)$.

The time-dependent formulation was studied in the Thesis of Clain (1994), where existence and uniqueness of continuous solutions was proven when $\sigma(\cdot)$ and $\kappa(\cdot)$ were Lipschitz functions and when $\mu(\cdot)$ was a constant. Convergence of finite element solutions was proven by imposing an $L^\infty(\Omega)$ bound on the discrete source term in the heat equation. This FEM was implemented by Clain et al. (1993) and obtained moderately good results when compared to experimental data. However, since the time-step for the model needs be small enough to capture the sinusoidal behaviour of the oscillating magnetic field, the authors noted that the model was prohibitively computationally expensive. More recent time-dependent formulations that exhibit the same restriction on the time-step are primarily focused on the Axisymmetric model due to its relevance in industry (see, e.g., Fisk et al. (2022)). For high frequencies, an extremely small time-step was needed to solve (4.2) e.g. $\Delta t < 10^{-6}$. Therefore, it would be desirable not to have such a strict restriction on the time-step.

In the quasi-static approximation, H in (4.1a) is a complex function representing the amplitude of the oscillating magnetic field that does not depend on time. Thus, there is no restriction on the time-step when numerically solving a quasi-static approximation. If $\mu(\cdot)$ is a constant, it is clear that the time-dependent formulation and the quasi-static formulation are equivalent.

If $\mu(\cdot)$ is not constant, then the argument for the quasi-static approximation is more subtle. Notice that since

$$\frac{\partial}{\partial t}\left(\mu(u(t))e^{i\omega t}H(\boldsymbol{x})\right) = \left(i\omega\mu(u(t)) + \mu'(u(t))u'(t)\right)e^{i\omega t}H(\boldsymbol{x}),$$

if $\mu(\cdot)$ is 'relatively smooth', and ω is large, the first term will dominate and the second term can be neglected. In practice, $\mu(\cdot)$ has a boundary layer at the Curie point, so $\mu'(\cdot)$ will be very large. However, for the sake of the analysis, we assume that $\mu(\cdot)$ is 'smooth enough' for the quasi-static approximation to be valid, so we take $\mu(\cdot)$ to be Lipschitz continuous. This is similar to arguments made by Chaboudez et al. (1997), who make the case that including $\mu'(u(t))u'(t)$ has limited effect on the size of the source term in (4.1c), while the savings in computational cost are significant compared to solving a time-dependent magnetic field equation.

4.2.2 Analysis of the Solenoidal Induction Heating Problem

Now that we have justified the quasi-static approximation, we discuss the available literature on this problem, bearing in mind that, we found that there was a limited amount of analysis on the steady-state quasi-static Solenoidal Induction Heating Problem, possibly due to the irregular source term in the heat equation.

In all papers mentioned here, $\mu(\cdot)$ is assumed to be a positive constant, the coefficients $\kappa(\cdot)$ and $\sigma(\cdot)$ are assumed to be Lipschitz continuous, and the problem is rewritten using a Kirchoff transformation.

The main paper that analyses the steady-state quasi-static Solenoidal Induction Heating Problem is by Clain and Touzani (1997a), where they prove existence of solutions in $W^{1,p}(\Omega)$ Sobolev spaces, for $2 < p < \infty$. In Section 4.4, we obtain similar results to Clain and Touzani (1997a), however, their proof is formulated slightly differently to ours, as they argue using the compactness of mappings while we argue using weak convergence of subsequences. Additionally, they use a regularity lemma by Meyers (Bensoussan, Lions, and Papanicolau 1978), which requires that Ω has a C^2 boundary, whereas we prove existence for polygonal non-convex domains.

The analysis by Clain and Touzani (1997a) was extended to the case of unbounded material coefficients by Clain and Touzani (1997b). The analysis with a time-dependent heat equation was considered by Parietti and Rappaz (1998), which also required a smooth boundary. Under additional regularity assumptions, uniqueness of solutions was also found. The paper by Parietti and Rappaz (1999) extended the results from Parietti and Rappaz (1998) and showed that under even stronger regularity assumptions, there exists a unique Galerkin finite element solution that converges to the continuous solution, assuming that the mesh is quasi-uniform and shape-regular. To our knowledge, the work by Parietti and Rappaz (1999) is the only paper analysing the FEM for this quasi-static Solenoidal Induction Heating Problem.

All of these papers discuss the difficulties of having a term belonging only to $L^1(\Omega)$. This term can probably explain the noticeable absence of analysis on the steady-state quasi-static Solenoidal Induction Heating Problem. Therefore, we mention some work that considers the heat equation alone with a right-hand side that belongs to $L^1(\Omega)$, to see where the difficulties lie. Note from now on, the Solenoidal Induction Heating Problem refers to the steady-state quasi-static problem.

4.2.3 Elliptic Problems

In the literature, elliptic problems with right-hand sides in $L^1(\Omega)$ do not have well-defined weak formulations when posed in standard Sobolev spaces. Therefore, a solution suggested in the literature is to completely redefine the weak formulation, and look for a so-called *renormalised solution* to the problem. This formulation is more complicated than a standard variational formulation, as it involves a limiting sequence of truncated test functions to ensure that the formulation is well-defined. More information about the formulation can be found in Appendix A.1. Some results for existence, uniqueness, and continuity of renormalised solutions are found by Boccardo and Gallouët (1989), Gallouët and Herbin (1994), and Bénilan et al. (1995).

It should be noted that in standard finite element spaces, a discrete problem with a right-hand side in $L^1(\Omega)$ is well-defined, since each element in the test function space belongs to $L^\infty(\Omega)$. Therefore, the difficulty lies in proving that the discrete FEM solution converges to the renormalised solution. For a Poisson problem, under very strict conditions on the mesh, convergence of the standard Galerkin approximation to the renormalised solution has been proven by Casado-Díaz et al. (2007). Unfortunately, these conditions are too restrictive for the Solenoidal Induction Heating Problem, where ideally, we want no conditions on the mesh, to allow for anisotropic meshes on complicated domains in order to capture the skin-effect. One idea that we had was to prove convergence of the BPM to the renormalised solution, and thus avoid strict conditions on the mesh since the BPM is mesh-independent. This remains an open problem, but some comments and numerical experiments are detailed in Appendix A.1.

For now, we turn our attention to a problem that is similar to the Solenoidal Induction Heating Problem and show another way in which the complications due to the irregular source term can be resolved.

4.2.4 The Thermistor Problem

The Thermistor Problem (also called the Joule Heating Problem) models a simpler physical system that contains the same $L^1(\Omega)$ term in the heat equation. It models the temperature and electric potential generated by a current in a conductive material, where heat is generated via Joule heating in proportion to the resistivity of the material. Let u be the temperature, ϕ be the electric potential, $\rho(\cdot)$ be the electrical resistivity, and $\kappa(\cdot)$ be the thermal conductivity. Then the Thermistor Problem, coupled with Dirichlet boundary conditions, reads: find u and ϕ such that

$$\begin{aligned}
\operatorname{div}(\rho(u)\nabla\phi) &= 0 && \text{in } \Omega, && \text{(4.3a)}\\
\frac{\partial u}{\partial t} - \operatorname{div}(\kappa(u)\nabla u) &= \rho(u)|\nabla\phi|^2 && \text{in } \Omega, && \text{(4.3b)}\\
\phi &= \phi_\circ && \text{on } \partial\Omega, && \text{(4.3c)}\\
u &= u_\circ && \text{on } \partial\Omega. && \text{(4.3d)}
\end{aligned}$$

The main difference between the Thermistor Problem and the Solenoidal Induction Heating Problem is that the electric potential is represented by a real (non-linear) Poisson equation rather than a complex quasi-static equation. The key argument used in the analysis of the Thermistor Problem is to show explicitly that $|\nabla\phi|^2$ is more regular than only $L^1(\Omega)$. Our aim in later Sections of this Chapter is to extend some of the arguments used for this problem to the Solenoidal Induction Heating Problem.

Crucially for the Thermistor Problem, the irregular heat source term in (4.3b) can be rewritten using a vector identity that uses (4.3a). Let $v \in C_0^\infty(\Omega)$ be a test function. An identity by Howison, Rodrigues, and Shillor (1993) shows us that, taking a test function $(\phi - \phi_\circ)v$ in the weak form of (4.3a),

$$\begin{aligned}
&(\rho(u)\nabla\phi, \nabla\left((\phi-\phi_\circ)v\right))_\Omega = 0\\
\Rightarrow \qquad &(\rho(u)|\nabla\phi|^2, v)_\Omega = (\rho(u)(\phi_\circ - \phi)\nabla\phi, \nabla v)_\Omega. \qquad \text{(4.4)}
\end{aligned}$$

By substituting (4.4) into the right-hand side of (4.3b), it is evident that this term is more regular than in $L^1(\Omega)$, and thus the problem becomes much easier to analyse. This method was employed by Howison, Rodrigues, and Shillor (1993) to prove existence of solutions to the steady-state problem for general boundary conditions. Additionally, uniqueness was proven by assuming that the data $|\nabla\phi|$ was sufficiently small and that it was bounded in $L^p(\Omega)$ for some $p > 2$.

There are also older results proving existence of solutions for the Thermistor Problem using different methods. Under strict assumptions on the smoothness of the domain, and smoothness and boundedness of coefficients, Cimatti and Prodi (1987) proved existence of solutions using a maximum principle. This was extended to the case including a non-constant heat diffusion coefficient by Cimatti (1988), and then further extended to mixed boundary conditions by Cimatti (1989), where even stricter smoothness conditions for uniqueness were found. A paper by Gallouët and Herbin (1994) proved existence of solutions using an equivalent definition of renormalised solutions for $L^1(\Omega)$ problems (see Boccardo and Gallouët (1989) for this formulation). The Meyers Lemma used by Clain and Touzani (1997a) for the Solenoidal Induction Heating Problem was used by Cimatti (1992) to prove existence of solutions to the time-dependent Thermistor Problem. It was also used by Loula and Zhu (2001) to prove existence and uniqueness of solutions for a problem where (4.3a) had non-zero right-hand side.

An argument that has been used in some of the above works is that a solution of (4.3a) belongs to $H^2(\Omega)$, and thus is bounded in $L^\infty(\Omega)$. However, although we have some additional regularity in the continuous solution, this does not necessarily imply that there is more regularity in the discrete solution. Indeed, if we take the standard piecewise linear finite element space, by definition, this is a subspace of $H^1(\Omega)$ and not of $H^2(\Omega)$. This means, ideally, we would like to somehow guarantee that the discrete solution ϕ_h has uniform bounds and hence satisfies the bounds of the continuous problem.

Indeed, this is what we see in the literature for FEMs for the Thermistor Problem; FEMs are designed to respect the bounds of the solution. One way this is done is by having strict conditions on the mesh so that the discrete problem satisfies the DMP. This is done by Akrivis and Larsson (2005), where convergence of a discrete solution to a solution of a time-dependent problem was proven, assuming quasi-uniformity of the mesh and additional regularity on the solutions. This was extended to three dimensions by Holst et al. (2010) with similar strict conditions on the mesh discretisation. Convergence estimates for the 3D viscoelastic case were found by Målqvist and Stillfjord (2017) with quasi-uniform meshes. Convergence with non-linear thermal conductivity was proven with regular meshes in 3D by Mbehou (2018). Convergence of a finite element solution of a mixed method was studied by Loula and Zhu (2006) assuming a regular mesh, and similar results for a stabilised mixed discontinuous Galerkin method were found by Zhu, Yu, and Loula (2011) under the same assumptions.

Another method of guaranteeing that bounds of the solution are satisfied is to incorporate the bound into the method. This technique was showcased by Jensen and Målqvist (2012), where the bound was explicitly hardwired in the FEM through a truncation operator, and so restrictions on the mesh were avoided. This was necessary to ensure that the triple product in (4.4) had a term in $L^\infty(\Omega)$. They proved strong convergence of conforming finite element approximations to a weak solution in three dimensions with mixed boundary conditions. This study was extended to a time dependent case by Jensen, Målqvist, and Persson (2022).

It is worth highlighting that the homogeneous Poisson equation (4.3a) implies that ϕ satisfies a maximum principle, and this fact is used in all the proofs of existence and uniqueness for the Thermistor Problem. For the Solenoidal Induction Heating Problem, it is less straightforward to show that H satisfies a maximum principle, although it can be shown by adapting arguments from Kresin and Maz'ya (1993). However, we did not need to use the maximum principle in order to obtain our results, so we do not expand on this further.

In this Chapter, we propose to solve the Solenoidal Induction Heating Problem using the BPM as described in Section 2.6. This method is designed to have the bounds hardwired explicitly into the method, and so it will always respect bounds with no restriction on the shape of the mesh. This means, in particular, that this method can be used for meshes that are potentially non-Delaunay, such as anisotropic meshes on complex geometries that are needed to resolve the skin-effect in induction heating. First, we prove that there is additional regularity on the source term, similar to the Thermistor Problem, which means that the heat equation satisfies Lax-Milgram's Lemma (Theorem 2.4.10) and so there exists a unique solution. For a fixed bound, we prove convergence of the BPM to an orthogonal projection of the solution of the bounded space, and thus if we choose a bound large enough, we show that the BPM solution converges to the exact solution.

The rest of the Chapter is as follows: In Section 4.3 we introduce some bounded spaces and prove their closure. In Section 4.4, we prove existence of solutions of the weak form of (4.1) by applying Schauder's fixed-point lemma. In Section 4.5, we prove existence and convergence of solutions of the standard Galerkin FEM to a solution of the Solenoidal Induction Heating Problem under strict conditions on the domain and the mesh. Then, in Section 4.6 we introduce the BPM obtain some preliminary lemmas, and state and prove our main convergence result for the one-directional coupled problem. Finally, in Section 4.7 we demonstrate some numerical experiments.

4.3 General Setting

Let Ω be an open, bounded, polyhedral, Lipschitz, and potentially non-convex domain. We use notation for Sobolev spaces as presented in Section 2.3.1. In addition, we explicitly define the sets that are bounded a.e. by a positive real number k. We define

$$\mathcal{D}_k(\Omega) := \{f \in \mathcal{D}(\Omega) : 0 \leq f(\boldsymbol{x}) \leq k \text{ a.e. in } \Omega\},$$

and

$$V^k := \{v \in H_0^1(\Omega) : 0 \leq v(\boldsymbol{x}) \leq k \text{ a.e. in } \Omega\}.$$

These closed convex sets will be used to prove convergence of the BPM to a solution of the Solenoidal Induction Heating Problem.

First, we show that V^k is closed in $H_0^1(\Omega)$, in order to show that a sequence in V^k converges to a limit in V^k.

Lemma 4.3.1. The closure of $\mathcal{D}_k(\Omega)$ with respect to the $H_0^1(\Omega)$ norm is V^k.

Proof. Let $v \in V^k$ and let $\rho : \mathbb{R}^2 \to \mathbb{R}$ be a mollifier such that $\rho \in C^\infty(\mathbb{R}^2)$, and

$$\begin{cases} \rho \geq 0, \ \rho(\boldsymbol{x}) = 0, \quad |\boldsymbol{x}| \geq 1, \\ \int_\Omega \rho(\boldsymbol{x}) \ \ \mathrm{d}\boldsymbol{x} = 1. \end{cases}$$

For all $\epsilon > 0$, let ρ_ϵ be the function defined by

$$\rho_\epsilon(\boldsymbol{x}) = \frac{1}{\epsilon}\rho\left(\frac{\boldsymbol{x}}{\epsilon}\right).$$

Consider the regularised function $v_\epsilon = \rho_\epsilon * v$, i.e.,

$$v_\epsilon := \int_\Omega \rho_\epsilon(\boldsymbol{x}-\boldsymbol{y})v(\boldsymbol{y})\ \mathrm{d}\boldsymbol{y} = \int_\Omega \rho_\epsilon(\boldsymbol{y})v(\boldsymbol{x}-\boldsymbol{y})\ \mathrm{d}\boldsymbol{y} \geq 0.$$

Since Ω is open and bounded, it is immediate that $v_\epsilon \in \mathcal{D}(\Omega)$, and it has been proven by Raviart and Thomas (1992, Lemma 1.2-1) that $v_\epsilon \to v$ strongly in $H_0^1(\Omega)$. Furthermore,

$$\begin{aligned} \|v_\epsilon\|_{\infty,\Omega} &= \left\| \int_\Omega \rho_\epsilon(\boldsymbol{y})v(\boldsymbol{x}-\boldsymbol{y})\ \mathrm{d}\boldsymbol{y} \right\|_{\infty,\Omega} \\ &\leq \|v\|_{\infty,\Omega} \left\| \int_\Omega \rho_\epsilon(\boldsymbol{y})\ \mathrm{d}\boldsymbol{y} \right\|_{\infty,\Omega} \\ &= \|v\|_{\infty,\Omega}. \end{aligned}$$

It follows that since $\|v\|_{\infty,\Omega} \leq k$, $v_\epsilon \in \mathcal{D}_k(\Omega)$. Since v was arbitrary, we have shown that the closure of $\mathcal{D}_k(\Omega)$ is V^k. □

4.4 Existence Results

In this Section we prove existence of solutions to the coupled Solenoidal Induction Heating Problem (4.1) by applying a modified version of Schauder's Fixed-Point Theorem. In order to do this, we first show that the solutions H and u are bounded in appropriate Sobolev spaces.

4.4.1 Bounds on H

Let us first consider the magnetic field equation (4.1a)-(4.1b). Let $u \in H_0^1(\Omega)$ be arbitrary and fixed, and let $\mu(\cdot)$ be positive and Lipschitz with upper bound μ°. We define the change of variables $\tilde{H} = H - H_\circ$. Then the weak problem reads: find H such that $H = \tilde{H} + H_\circ$, $\tilde{H} \in H_0^1(\Omega;\mathbb{C})$, and

$$\left(\nabla\tilde{H}, \nabla Q\right)_{\Omega,\mathbb{C}} + \left(i\omega\mu(u)\tilde{H}, Q\right)_{\Omega,\mathbb{C}} = (i\omega\mu(u)H_\circ, Q)_{\Omega,\mathbb{C}}\,, \tag{4.5}$$

for all $Q \in H_0^1(\Omega;\mathbb{C})$. This weak formulation has a unique solution thanks to Lax-Milgram's Lemma (Theorem 2.4.10). We now show that any solution of (4.5) in uniformly bounded in $H^1(\Omega)$ independent from the choice of u.

Lemma 4.4.1 (Bound of H in $H^1(\Omega)$). Let $u \in H_0^1(\Omega)$ be arbitrary and let H solve (4.5). Then there exists a positive constant C_1 depending only on Ω, ω, and μ°, and $H_\circ$ such that

$$\|H\|_{1,\Omega,\mathbb{C}} \le C_1 \tag{4.6}$$

Proof. Fix $u \in H_0^1(\Omega)$. Taking $Q = \tilde{H}$ as a test function in (4.5), writing C_p as the Poincaré inequality constant from Theorem 2.3.6, writing C_{equi} as the equivalence constant between $H_0^1(\Omega)$ and $H^1(\Omega)$ from Corollary 2.3.7, and using the Cauchy-Schwarz inequality from Theorem 2.3.4, it follows that

$$\begin{aligned}
& \|\nabla\tilde{H}\|_{0,\Omega,\mathbb{C}}^2 + \left(i\omega\mu(u)\tilde{H}, \tilde{H}\right)_{\Omega,\mathbb{C}} = \left(i\omega\mu(u)H_\circ, \tilde{H}\right)_{\Omega,\mathbb{C}} \\
\Rightarrow \quad & \mathrm{Re}\left(\|\nabla\tilde{H}\|_{0,\Omega,\mathbb{C}}^2 + i\omega\|\sqrt{\mu(u)}\tilde{H}\|_{0,\Omega,\mathbb{C}}^2\right) = \mathrm{Re}\left(\left(i\omega\mu(u)H_\circ, \tilde{H}\right)_{\Omega,\mathbb{C}}\right) \\
\Rightarrow \quad & \|\nabla\tilde{H}\|_{0,\Omega,\mathbb{C}}^2 = \mathrm{Re}\left(\left(i\omega\mu(u)H_\circ, \tilde{H}\right)_{\Omega,\mathbb{C}}\right) \\
& \le \omega\mu^\circ\|H_\circ\|_{0,\Omega,\mathbb{C}}\|\tilde{H}\|_{0,\Omega,\mathbb{C}} \\
& \le \omega\mu^\circ C_p\|H_\circ\|_{0,\Omega,\mathbb{C}}\|\nabla\tilde{H}\|_{0,\Omega,\mathbb{C}} \\
\Rightarrow \quad & \|\nabla\tilde{H}\|_{0,\Omega,\mathbb{C}} \le \omega\mu^\circ C_p\|H_\circ\|_{0,\Omega,\mathbb{C}} \\
\Rightarrow \quad & \|\tilde{H}\|_{1,\Omega,\mathbb{C}} \le \omega\mu^\circ C_{equi}C_p\|H_\circ\|_{0,\Omega,\mathbb{C}}.
\end{aligned}$$

Finally, notice that since $H_\circ$ is a constant, $\|H_\circ\|_{1,\Omega,\mathbb{C}} = \|H_\circ\|_{0,\Omega,\mathbb{C}}$, and so

$$\begin{aligned}
\|H\|_{1,\Omega,\mathbb{C}} &= \|\tilde{H} + H_\circ\|_{1,\Omega,\mathbb{C}} \\
&\leq \|\tilde{H}\|_{1,\Omega,\mathbb{C}} + \|H_\circ\|_{1,\Omega,\mathbb{C}} \\
&\leq \omega\mu^\circ C_{equi} C_p \|H_\circ\|_{0,\Omega,\mathbb{C}} + \|H_\circ\|_{0,\Omega,\mathbb{C}} \\
&= (\omega\mu^\circ C_{equi} C_p + 1)|\Omega|^{1/2}|H_\circ| \\
&=: C_1,
\end{aligned}$$

which proves the result. $\square$

We will use this result to construct a fixed-point mapping to prove existence. However, in order to prove that the right-hand side of the heat equation (4.1c) is well defined, we require a stronger result, and so next we will prove that the solution of (4.5) belongs to $W^{1,4}(\Omega;\mathbb{C})$.

Lemma 4.4.2 (Regularity of H). Let $u \in H_0^1(\Omega)$ be arbitrary and let H be the corresponding unique solution of (4.5). Then $H \in W^{1,4}(\Omega;\mathbb{C})$. Additionally, there exists a constant C_2 depending only on Ω, ω, μ°, and $H_\circ$ such that

$$\|H\|_{1,4,\Omega,\mathbb{C}} \leq C_2.$$

Proof. We first split equation (4.1a) into real and complex parts. Writing $\tilde{H} = H - H_\circ$ and $\tilde{H} = H_r + iH_c$, where $H_r, H_c \in H_0^1(\Omega)$ are real functions, and writing $H_\circ = H_{\circ,r} + iH_{\circ,c}$ it follows that

$$-\Delta H_r - \omega\mu(u)H_c + i(-\Delta H_c + \omega\mu(u)H_r) = -\omega\mu(u)H_{\circ,c} + i\omega\mu(u)H_{\circ,r},$$

which implies that the following system of equations is satisfied:

$$-\Delta H_r = \omega\mu(u)(H_c - H_{\circ,c}), \tag{4.7}$$

$$-\Delta H_c = -\omega\mu(u)(H_r - H_{\circ,r}). \tag{4.8}$$

Additionally, since $\tilde{H} \in H_0^1(\Omega;\mathbb{C})$, it follows that

$$H_r = H_c = 0 \qquad \text{on } \partial\Omega. \tag{4.9}$$

For a fixed $u \in H_0^1(\Omega)$ there exists a unique solution for (4.5), and so there exists a unique solution for the system (4.7) - (4.9). Since $\mu(\cdot) \in L^\infty(\Omega)$, it follows from Lemma 4.4.1 that

$$\|\omega\mu(u)(H_c - H_{\circ,c})\|_{0,\Omega} \leq \omega\mu^\circ(\|H_c\|_{1,\Omega} + \|H_{\circ,c}\|_{1,\Omega}) \leq \omega\mu^\circ(C_1 + \|H_\circ\|_{0,\Omega}), \tag{4.10}$$

hence $\omega\mu(u)(H_c - H_{\circ,c}) \in L^2(\Omega)$. Using analogous arguments, it can be shown that $-\omega\mu(u)(H_r - H_{\circ,r}) \in L^2(\Omega)$. Hence (4.7) and (4.8) are two real Poisson problems with right-hand sides in $L^2(\Omega)$; these right-hand sides are regarded as given data.

Consider just (4.7): the argument for (4.8) follows in an identical manner. Since Ω is Lipschitz and bounded, and (4.7) is a Poisson equation with a right-hand side in $L^2(\Omega)$, we can apply Theorem 0.5 from Jerison and Kenig (1995), which allows us to state that there exists a positive constant C_j depending on Ω such that

$$\|H_r\|_{1,4,\Omega} \leq C_j\|\omega\mu(u)(H_c - H_{\circ,c})\|_{-1,4,\Omega}.$$

Now, since $L^2(\Omega) \subset W^{-1,4}(\Omega)$ and this injection is continuous (see Brezis, p.291), there exists a constant C_i such that for every $v \in L^2(\Omega)$, we have that $\|v\|_{-1,4,\Omega} \leq C_i\|v\|_{0,\Omega}$. Therefore, using (4.10), we have that

$$\|H_r\|_{1,4,\Omega} \leq C_jC_i\|\omega\mu(u)(H_c - H_{\circ,c})\|_{0,\Omega} =: C_r(\Omega, \omega, \mu^\circ, H_\circ). \tag{4.11}$$

An identical argument shows that there exists a positive constant C_c such that $\|H_c\|_{1,4,\Omega} \leq C_c(\Omega, \omega, \mu^\circ, H_\circ)$. Finally, using the triangle inequality, it follows that

$$\begin{aligned} \|H\|_{1,4,\Omega,\mathbb{C}} &\leq \|\tilde{H}\|_{1,4,\Omega,\mathbb{C}} + \|H_\circ\|_{1,4,\Omega,\mathbb{C}} \\ &\leq \|H_r\|_{1,4,\Omega} + \|H_c\|_{1,4,\Omega} + \|H_\circ\|_{1,4,\Omega,\mathbb{C}} \leq C_r + C_c + \|H_\circ\|_{1,4,\Omega,\mathbb{C}} =: C_2, \end{aligned}$$

which finishes the proof. □

More specifically, Lemma 4.4.2 implies that $\nabla H \in L^4(\Omega;\mathbb{C})^2$ and that $\|\nabla H\|_{0,4,\Omega,\mathbb{C}} \leq C_2$. This is the key step used to prove that the right-hand side of the heat equation (4.1c) belongs to $L^2(\Omega)$.

Remark. An alternative way to prove that $\nabla H \in L^4(\Omega;\mathbb{C})^2$ is to use a version of the Sobolev Embedding Theorem. By splitting $\tilde{H}$ into $H_r + iH_c$ again, we can apply Corollary 4.4.4.14 from the book by Grisvard (2011), which shows that for a constant $\epsilon \in (0, \frac{1}{2}]$ depending on the interior angles of the domain,

$$H_r \in H^{\frac{3}{2}+\epsilon}(\Omega).$$

This implies that $\nabla H_r \in H^{\frac{1}{2}+\epsilon}(\Omega)^2$. The Sobolev Embedding Theorem from Grisvard (2011, Theorem 1.4.4.1) shows that $H^{\frac{1}{2}+\epsilon}(\Omega)$ is continuously embedded in $L^4(\Omega)$, and hence $\nabla H_r \in L^4(\Omega)^2$. Identical arguments show that $\nabla H_c \in L^4(\Omega)^2$, and hence by the triangle inequality again, $\nabla H \in L^4(\Omega;\mathbb{C})^2$. ■

Now we show that this additional regularity on ∇H is enough to prove that the right-hand side of (4.1c) is in $L^2(\Omega)$ independent from the choice of u. This will enable us to prove existence of solutions of the heat equation for a fixed $H \in W^{1,4}(\Omega;\mathbb{C})$ via Lax-Milgram's Lemma.

Lemma 4.4.3 (Source term of (4.1c) belongs to $L^2(\Omega)$). *Let H be the unique solution of (4.5) for any fixed $u \in H^1_0(\Omega)$. Then $|\nabla H|^2 \in L^2(\Omega)$.*

Proof. Since $\|H\|_{1,4,\Omega,\mathbb{C}} \leq C_2$ by Lemma 4.4.2, by definition of Lebesgue and Sobolev norms it follows that

$$\||\nabla H|^2\|_{0,\Omega} = \|\nabla H\|^2_{0,4,\Omega,\mathbb{C}} \leq C_2^2.$$

Hence $|\nabla H|^2 \in L^2(\Omega)$ and $\||\nabla H|^2\|_{0,\Omega} \leq C_2^2$. □

As a consequence, we can now consider the heat equation (4.1c), and prove *a-priori* estimates with the right-hand side in $L^2(\Omega)$.

4.4.2 Bounds on u

Due to Lemma 4.4.3, any solution of (4.1a) - (4.1b) satisfies $|\nabla H|^2 \in L^2(\Omega)$. Then the standard weak formulation for (4.1c) - (4.1d) with test functions in $H_0^1(\Omega)$ is well-defined. For a fixed $H \in W^{1,4}(\Omega;\mathbb{C})$, the weak form of (4.1c) reads: find $u \in H_0^1(\Omega)$ such that

$$(\nabla u, \nabla v)_\Omega = \left(|\nabla H|^2, v\right)_\Omega \qquad \forall\ v \in H_0^1(\Omega). \tag{4.12}$$

By Lax-Milgram's Lemma (Theorem 2.4.10), this weak formulation has a unique solution.

In this analysis we consider (4.1c) equipped with homogeneous Dirichlet boundary conditions. We anticipate that extending this analysis to inhomogeneous Dirichlet, Neumann or mixed boundary conditions will be fairly straightforward. However, we also anticipate that extending this analysis to realistic boundary conditions for induction heating, such as the Robin and radiation boundary conditions, will be decidedly non-trivial due to singularities at the corners of the domain and due to the need to use more specialised Sobolev spaces, as discussed at the end of Section 3.3.3. For now, we focus on the Dirichlet problem.

As was done with H in Lemma 4.4.1, we now find some *a-priori* bounds for u, which will be used to prove existence of solutions using a fixed-point method.

Lemma 4.4.4. Let u be the unique solution to (4.12) for a fixed $H \in W^{1,4}(\Omega;\mathbb{C})$ with the condition that $\|H\|_{1,4,\Omega,\mathbb{C}} \leq C_2$. Then there exists a constant C_3 depending only on Ω, ω, μ°, and $H_\circ$, such that

$$|u|_{1,\Omega} \leq C_3. \tag{4.13}$$

Proof. Taking u as a test function in (4.12), using the Cauchy-Schwarz inequality from Theorem 2.3.4, the equivalence of the $H^1(\Omega)$ and $H_0^1(\Omega)$ norms from Corollary 2.3.7, and the constant C_2^2 from Lemma 4.4.3, it follows that

$$\begin{aligned} |u|_{1,\Omega}^2 &= (|\nabla H|^2, u)_\Omega \\ &\le \||\nabla H|^2\|_{0,\Omega}\|u\|_{0,\Omega} \\ &\le C_2^2 C_{equi}|u|_{1,\Omega} \\ \Rightarrow |u|_{1,\Omega} &\le C_2^2 C_{equi} =: C_3. \end{aligned}$$

Therefore, u is uniformly bounded in $H_0^1(\Omega)$, as required. $\square$

In particular, we have established that H is uniformly bounded in $H^1(\Omega;\mathbb{C})$ and in $W^{1,4}(\Omega;\mathbb{C})$ *independently* from the choice of $u \in H_0^1(\Omega)$. Additionally, we have shown that u is uniformly bounded in $H_0^1(\Omega)$ as long as $\|H\|_{1,4,\Omega,\mathbb{C}} \le C_2$.

4.4.3 Existence Theorem

Now that we have established these *a-priori* bounds we will use them to prove existence of weak solutions to the Solenoidal Induction Heating Problem (4.1). Consider the full weak form: find $(H,u) \in H^1(\Omega;\mathbb{C}) \times H_0^1(\Omega)$ such that $H = \tilde{H} + H_\circ$, $\tilde{H} \in H_0^1(\Omega;\mathbb{C})$, and

$$(\nabla\tilde{H}, \nabla Q)_{\Omega,\mathbb{C}} + \left(i\omega\mu(u)\tilde{H}, Q\right)_{\Omega,\mathbb{C}} = (i\omega\mu(u)H_\circ, Q)_{\Omega,\mathbb{C}}, \tag{4.14a}$$

$$(\nabla u, \nabla v)_\Omega = \left(|\nabla\tilde{H}|^2, v\right)_\Omega, \tag{4.14b}$$

for every $(Q,v) \in H_0^1(\Omega;\mathbb{C}) \times H_0^1(\Omega)$.

Theorem 4.4.5. There exists a solution to (4.14).

Proof. For this proof we use a Tikhonov-type modification of Schauder's Fixed Point Theorem, stated in Theorem 2.3.13, where $V = H_0^1(\Omega)$ is our reflexive separable Banach space that is compactly embedded in $V^1 = L^2(\Omega)$. This Theorem allows us to prove existence of a fixed point under a weakly continuous map. We follow the strategy presented by Roubíček (2013, p. 189). Let B be the closed ball in $H_0^1(\Omega)$ defined by

$$B := \{v \in H_0^1(\Omega) : |v|_{1,\Omega} \leq C_3\},$$

where C_3 is the constant from Lemma 4.4.4. Now, given $\hat{w} \in B$, consider the following problem: find $(\varphi, w) \in H^1(\Omega; \mathbb{C}) \times H_0^1(\Omega)$ such that $\tilde{\varphi} = \varphi - H_\circ$, $\tilde{\varphi} \in H_0^1(\Omega; \mathbb{C})$, and

$$(\nabla\tilde{\varphi}, \nabla\psi)_{\Omega,\mathbb{C}} + (i\omega\mu(\hat{w})\tilde{\varphi}, \psi)_{\Omega,\mathbb{C}} = (i\omega\mu(\hat{w})H_\circ, \psi)_{\Omega,\mathbb{C}}, \tag{4.15}$$

$$(\nabla w, \nabla v)_\Omega = \left(|\nabla\varphi|^2, v\right)_\Omega, \tag{4.16}$$

for all $(\psi, v) \in H_0^1(\Omega; \mathbb{C}) \times H_0^1(\Omega)$. Then we can define the mapping

$$M := M_2 \circ M_1 : \hat{w} \mapsto w, \qquad \text{where} \qquad M_1 : \hat{w} \mapsto \varphi, \qquad M_2 : \varphi \mapsto w.$$

For a fixed $\hat{w} \in H_0^1(\Omega)$, φ is a solution of (4.15), and for a fixed $\varphi \in W^{1,4}(\Omega, \mathbb{C})$ with $\|\varphi\|_{1,4,\Omega,\mathbb{C}} \leq C_2$, w is a solution of (4.16). These types of decoupled equations, considered on their own, are well known to have unique solutions by Lax-Milgram's Lemma (Theorem 2.4.10).

From Lemma 4.4.2, for any $\hat{w} \in H_0^1(\Omega)$, the solution φ of (4.15) is bounded by C_2 in $W^{1,4}(\Omega; \mathbb{C})$, and so $\|M_1(\hat{w})\|_{1,4,\Omega,\mathbb{C}} \leq C_2$. Additionally, from Lemma 4.4.4, it follows that since $\varphi \in W^{1,4}(\Omega; \mathbb{C})$ with $\|\varphi\|_{1,4,\Omega,\mathbb{C}} \leq C_2$, w is bounded by C_3 in $H_0^1(\Omega)$ and $|M_2(\varphi)|_{1,\Omega} \leq C_3$. It follows that $M(B) \subseteq B$. Hence, to prove that M has a fixed point, it suffices to show that M is weakly continuous.

By the Sobolev Embedding Theorem shown in Theorem 2.3.8, $H_0^1(\Omega)$ is compactly embedded in $L^2(\Omega)$, so weak convergence in $H_0^1(\Omega)$ implies strong convergence in $L^2(\Omega)$. First, suppose that $\{\hat{w}_k\}_k$ is a sequence in B such that $\hat{w}_k \rightharpoonup \hat{w}$ weakly in $H_0^1(\Omega)$. Then $\hat{w}_k \to \hat{w}$ strongly in $L^2(\Omega)$. For each $\hat{w}_k$, we define the image under the mapping M_1 to be $M_1(\hat{w}_k) =: \varphi_k \in H^1(\Omega; \mathbb{C})$, and define $\tilde{\varphi}_k = \varphi_k - H_\circ$. We have established that the sequence $\{\varphi_k\}_k$ is uniformly bounded in $H^1(\Omega; \mathbb{C})$ by Lemma 4.4.1, and therefore, up to a subsequence $\varphi_k \rightharpoonup \varphi$ weakly in $H^1(\Omega; \mathbb{C})$. It follows that the sequence $\{\tilde{\varphi}_k\}_k$ is uniformly bounded in $H_0^1(\Omega; \mathbb{C})$, and therefore, up to a subsequence $\tilde{\varphi}_k \rightharpoonup \tilde{\varphi}$ weakly in

$H^1_0(\Omega;\mathbb{C})$, and $\varphi = \tilde{\varphi} + H_\circ$.

Next, since $\tilde{\varphi}_k \rightharpoonup \tilde{\varphi}$ weakly in $H^1_0(\Omega;\mathbb{C})$, hence $\tilde{\varphi}_k \to \tilde{\varphi}$ strongly in $L^2(\Omega;\mathbb{C})$ and since we can apply Lemma 2.3.9 because $\mu(\cdot)$ is Lipschitz, it follows that for all $\psi \in \mathcal{D}(\Omega;\mathbb{C})$,

$$\begin{aligned}(\nabla\tilde{\varphi}_k, \nabla\psi)_{\Omega,\mathbb{C}} &\to (\nabla\tilde{\varphi}, \nabla\psi)_{\Omega,\mathbb{C}},\\ (i\omega\mu(\hat{w}_k)\tilde{\varphi}_k, \psi)_{\Omega,\mathbb{C}} &\to (i\omega\mu(\hat{w})\tilde{\varphi}, \psi)_{\Omega,\mathbb{C}},\\ (i\omega\mu(\hat{w}_k)H_\circ, \psi)_{\Omega,\mathbb{C}} &\to (i\omega\mu(\hat{w})H_\circ, \psi)_{\Omega,\mathbb{C}}.\end{aligned}$$

So, $\varphi = \tilde{\varphi} - H_\circ$ and $\tilde{\varphi} \in H^1_0(\Omega;\mathbb{C})$ satisfies

$$(\nabla\tilde{\varphi}, \nabla\psi)_{\Omega,\mathbb{C}} + (i\omega\mu(\hat{w})\tilde{\varphi}, \psi)_{\Omega,\mathbb{C}} = (i\omega\mu(\hat{w})H_\circ, \psi). \tag{4.17}$$

This problem has a unique solution thanks to Lax-Milgram's lemma from Theorem 2.4.10, so the whole sequence φ_k converges weakly to φ in $H^1(\Omega;\mathbb{C})$. Hence, $\varphi = M_1(\hat{w})$ and this mapping is weakly continuous. Since φ is a solution of (4.15), φ also belongs to $W^{1,4}(\Omega;\mathbb{C})$ and $\|\varphi\|_{1,4,\Omega,\mathbb{C}} \le C_2$.

In a similar way, define the image of φ_k under the mapping M_2 to be $M_2(\varphi_k) =: w_k \in H^1_0(\Omega)$. This sequence $\{w_k\}_k$ is bounded in $H^1_0(\Omega)$ by Lemma 4.4.4 and consequently $w_k \in B$ for any $\varphi_k \in W^{1,4}(\Omega;\mathbb{C})$ with $\|\varphi_k\|_{1,4,\Omega,\mathbb{C}} \le C_2$. It follows that there is a subsequence of $\{w_k\}_k$ such that $w_k \rightharpoonup w$ weakly in $H^1_0(\Omega)$. Now, for all $v \in \mathcal{D}(\Omega)$, it follows from the definition of weak convergence in $H^1_0(\Omega)$ that

$$(\nabla w_k, \nabla v)_\Omega \to (\nabla w, \nabla v)_\Omega.$$

It remains to prove that $(|\nabla\varphi_k|^2, v)_\Omega \to (|\nabla\varphi|^2, v)_\Omega$. In order to do this, it is enough to show that $(|\nabla\tilde{\varphi}_k|^2, v)_\Omega \to (|\nabla\tilde{\varphi}|^2, v)_\Omega$, since $\nabla\varphi = \nabla\tilde{\varphi}$ and $\nabla\varphi_k = \nabla\tilde{\varphi}_k$. We use the fact that $\tilde{\varphi}_k \rightharpoonup \tilde{\varphi}$ weakly in $H^1_0(\Omega;\mathbb{C})$, and that $\tilde{\varphi}_k \to \tilde{\varphi}$ strongly in $L^2(\Omega;\mathbb{C})$.

First, note that taking $\tilde{\varphi}v$ as a test function in (4.15), $\tilde{\varphi}$ satisfies the identity

$$(|\nabla\tilde{\varphi}|^2, v)_{\Omega,\mathbb{C}} = (i\omega\mu(\hat{w})H_\circ, \tilde{\varphi}v)_{\Omega,\mathbb{C}} - (i\omega\mu(\hat{w})|\tilde{\varphi}|^2, v)_{\Omega,\mathbb{C}} - (\overline{\tilde{\varphi}}\nabla\tilde{\varphi}, \nabla v)_{\Omega,\mathbb{C}}.$$

In a similar way, taking $\tilde{\varphi}_k$ as a test function, every $\tilde{\varphi}_k$ in the sequence $\{\tilde{\varphi}_k\}_k$ solving (4.15) satisfies that identity

$$\begin{aligned}(|\nabla\tilde{\varphi}_k|^2, v)_{\Omega,\mathbb{C}} &= (i\omega\mu(\hat{w}_k)H_\circ, \tilde{\varphi}_k v)_{\Omega,\mathbb{C}} - (i\omega\mu(\hat{w}_k)|\tilde{\varphi}_k|^2, v)_{\Omega,\mathbb{C}} - (\overline{\tilde{\varphi}_k}\nabla\tilde{\varphi}_k, \nabla v)_{\Omega,\mathbb{C}} \\ &= (A) + (B) + (C).\end{aligned}$$

Now we prove convergence of the individual terms. Since $\tilde{\varphi}_k \to \tilde{\varphi}$ strongly in $L^2(\Omega;\mathbb{C})$, and since $\mu(\hat{w}_k)$ converges a.e. to $\mu(\hat{w})$,

$$(A) \to (i\omega\mu(\hat{w})H_\circ, \tilde{\varphi}v)_{\Omega,\mathbb{C}} \qquad \text{as } k \to \infty.$$

Next, since $\tilde{\varphi}_k \rightharpoonup \tilde{\varphi}$ weakly in $W^{1,4}(\Omega;\mathbb{C})$ and is uniformly bounded in $W^{1,4}(\Omega;\mathbb{C})$, and since $\mu(\hat{w}_k)$ converges a.e. to $\mu(\hat{w})$,

$$(B) \to (i\omega\mu(\hat{w})|\tilde{\varphi}|^2, v)_{\Omega,\mathbb{C}} \qquad \text{as } k \to \infty.$$

Finally, since $\tilde{\varphi}_k \to \tilde{\varphi}$ strongly in $L^2(\Omega;\mathbb{C})$ and $\tilde{\varphi}_k \rightharpoonup \tilde{\varphi}$ weakly in $H^1_0(\Omega;\mathbb{C})$

$$(C) \to (\overline{\tilde{\varphi}}\nabla\tilde{\varphi}, \nabla v)_{\Omega,\mathbb{C}} \qquad \text{as } k \to \infty.$$

Putting this all together, we get that

$$\begin{aligned}\lim_{k\to\infty}(|\nabla\tilde{\varphi}_k|^2, v)_{\Omega,\mathbb{C}} &= \lim_{k\to\infty}((A) + (B) + (C)) \\ &= (|\nabla\tilde{\varphi}|^2, v)_{\Omega,\mathbb{C}}.\end{aligned}$$

Therefore, since $\nabla\varphi = \nabla\tilde{\varphi}$ and $\nabla\varphi_k = \nabla\tilde{\varphi}_k$, it holds for all $v \in \mathcal{D}(\Omega)$ that

$$0 = (\nabla w_k, \nabla v)_\Omega - (|\nabla\varphi_k|^2, v)_\Omega \to (\nabla w, \nabla v)_\Omega - (|\nabla\varphi|^2, v)_\Omega = 0.$$

Then, it follows that the limit of the sequence is $w \in H^1_0(\Omega)$ and this limit satisfies

$$(\nabla w, \nabla v)_\Omega = (|\nabla\varphi|^2, v)_\Omega,$$

for all $v \in \mathcal{D}(\Omega)$. But, again, this problem has a unique solution thanks to Lax-Milgram's Lemma (Theorem 2.4.10) so the whole sequence $w_k \rightharpoonup w$ converges weakly in $H_0^1(\Omega)$. Hence $w = M_2(\varphi)$ and this mapping is weakly continuous.

Therefore, $M = M_2 \circ M_1 : B \to B$, $\hat{w} \mapsto w$, is a weakly continuous mapping, so by Schauder's Fixed Point Theorem for weakly continuous mappings (Theorem 2.3.13), M has a fixed point. Hence, a weak solution to the system (4.1) exists and is defined by the fixed point (u, H), where $H = M_1(u)$. $\square$

4.5 The Standard FEM

In this Section we show that under strict conditions on the domain and the mesh, we can prove existence of standard Galerkin finite element solutions and convergence of these solutions to that of the coupled problem (4.14).

We use the finite element notation introduced in Chapter 2.5. Let $\{\mathcal{T}_h\}_h$ be a family of simplicial triangulations of Ω, and for each triangulation $\mathcal{T}_h$, let W_h and V_h denote the real $\mathbb{P}_1$ finite element subspaces of $H^1(\Omega)$ and $H_0^1(\Omega)$, respectively, as defined in (2.14) and (2.15). Similarly, let $W_{h,\mathbb{C}}$ and $V_{h,\mathbb{C}}$ denote the complex $\mathbb{P}_{1;\mathbb{C}}$ finite element subspaces of $H^1(\Omega;\mathbb{C})$ and $H_0^1(\Omega;\mathbb{C})$, respectively, as defined in (2.17) and (2.16).

The standard Galerkin approximation of (4.14) reads: find $(H_h, u_h) \in W_{h,\mathbb{C}} \times V_h$ such that $\tilde{H}_h = H_h - H_\circ \in V_{h,\mathbb{C}}$ and

$$(\nabla \tilde{H}_h, \nabla Q_h)_{\Omega,\mathbb{C}} + (i\omega\mu(u_h)\tilde{H}_h, Q_h)_{\Omega,\mathbb{C}} = (i\omega\mu(u_h)H_\circ, Q_h)_{\Omega,\mathbb{C}}, \tag{4.18a}$$

$$(\nabla u_h, \nabla v_h)_\Omega = \left(|\nabla H_h|^2, v_h\right)_\Omega, \tag{4.18b}$$

for all $(Q_h, v_h) \in V_{h,\mathbb{C}} \times V_h$. First, we prove some *a-priori* bounds on H_h and u_h.

4.5.1 Bounds on H_h

Lemma 4.5.1. Let $u_h \in V_h$ be fixed. Consider the problem: find $H_h \in W_{h,\mathbb{C}}$ such that $H_h - H_\circ = \tilde{H}_h \in V_{h,\mathbb{C}}$, and

$$(\nabla \tilde{H}_h, \nabla Q_h)_{\Omega,\mathbb{C}} + (i\omega\mu(u_h)\tilde{H}_h, Q_h)_{\Omega,\mathbb{C}} = (i\omega\mu(u_h)H_\circ, Q_h)_{\Omega,\mathbb{C}},$$

for all $Q_h \in V_{h,c}$. Then $\|H_h\|_{1,\Omega,\mathbb{C}} \leq C_1$, where C_1 is the constant from Lemma 4.4.1 that depends only on $\Omega, \omega, \mu^\circ$, and $H_\circ$.

Proof. This proof is identical to the proof of Lemma 4.4.1, except we take $\tilde{H}_h$ as a test function instead of $\tilde{H}$. □

Now, we show that ∇H_h is bounded in $L^4(\Omega; \mathbb{C})$, which is needed to show that the right-hand side of the heat equation is well-defined.

Lemma 4.5.2. Assume that Ω is convex with a smooth boundary, the family of meshes $\{\mathcal{T}_h\}_h$ is quasi-uniform, and h is small enough. Let $u_h \in V_h$ be fixed, and let H_h be the solution of (4.18a). Then there exists a constant C_4 depending only on Ω, ω, μ, and $H_\circ$ such that

$$\|\nabla H_h\|_{0,4,\Omega,\mathbb{C}} \leq C_4. \tag{4.19}$$

Proof. First, note that writing $\tilde{H}_h = \tilde{H}_{h,r} + i\tilde{H}_{h,c}$ and $H_\circ = H_{\circ,r} + iH_{\circ,c}$, (4.18a) satisfies

$$\begin{aligned} (\nabla \tilde{H}_{h,r}, \nabla v_h)_\Omega - (\omega\mu(u_h)\tilde{H}_{h,c}, v_h)_\Omega &= -(\omega\mu(u_h)H_{\circ,c}, v_h)_\omega, \\ i\left[(\nabla \tilde{H}_{h,c}, \nabla v_h)_\Omega + (\omega\mu(u_h)\tilde{H}_{h,r}, v_h)_\Omega\right] &= i\left[(\omega\mu(u_h)H_{\circ,r}, v_h)_\omega\right], \end{aligned}$$

for all $v_h \in V_h$. By definition of the Dual norm in for Lebesgue spaces on bounded domains, there there exists an α_1 such that

$$\alpha_1 \|\nabla \tilde{H}_{h,r}\|_{0,4,\Omega} \leq \sup_{w \in W_0^{1,4/3}(\Omega)} \frac{(\nabla \tilde{H}_{h,r}, \nabla w)_\Omega}{\|\nabla w\|_{0,4/3,\Omega}}. \tag{4.20}$$

By definition of the Ritz projection from Rannacher and Scott (1982), $(\nabla \tilde{H}_{h,r}, \nabla w)_\Omega = (\nabla \tilde{H}_{h,r}, \nabla R_h w)_\Omega$. Additionally, another result from Rannacher and Scott (1982) states that under the assumption that Ω is convex, the family of triangulations $\{\mathcal{T}_h\}_h$ is quasi-uniform, h is small enough, and the boundary $\partial\Omega$ is smooth, there exists a positive constant C_{ritz} such that for all $1 \leq p \leq \infty$, and all $w \in W^{1,p}(\Omega)$,

$$\|\nabla R_h w\|_{0,p,\Omega} \leq C_{ritz} \|\nabla w\|_{0,p,\Omega}. \tag{4.21}$$

Therefore, including (4.21) and the definition of Ritz projection in (4.20), we get

$$\alpha_1\|\nabla\tilde{H}_{h,r}\|_{0,4,\Omega} \le \sup_{w\in W_0^{1,4/3}(\Omega)} \frac{1}{C_{ritz}} \frac{(\nabla\tilde{H}_{h,r}, \nabla R_h w)_\Omega}{\|\nabla R_h w\|_{0,4/3,\Omega}}. \tag{4.22}$$

Since $R_h w \in V_h$, it follows that (4.22) is equivalent to

$$\alpha_1\|\nabla\tilde{H}_{h,r}\|_{0,4,\Omega} \le \sup_{v_h\in V_h} \frac{1}{C_{ritz}} \frac{(\nabla\tilde{H}_{h,r}, \nabla v_h)_\Omega}{\|\nabla v_h\|_{0,4/3,\Omega}}.$$

Finally, using (4.18a), Hölder's Inequality, and the Poincaré Inequality, it follows that

$$\begin{aligned}
\alpha_1 C_{ritz}\|\nabla\tilde{H}_{h,r}\|_{0,4,\Omega,\mathbb{C}} &\le \sup_{0\neq v_h\in V_h,} \frac{(\nabla\tilde{H}_{h,r}\nabla v_h)_\Omega}{\|\nabla v_h\|_{0,4/3,\Omega}} \\
&\le \sup_{0\neq v_h\in V_h} \frac{(\omega\mu(u_h)\tilde{H}_{h,c}, v_h)_\Omega - (\omega\mu(u_h)H_{\circ,c}, v_h)_\Omega}{\|\nabla v_h\|_{0,4/3,\Omega}} \\
&\le \sup_{0\neq v_h\in V_h} \frac{\omega\mu^\circ(\|\tilde{H}_{h,c}\|_{0,4,\Omega}\|v_h\|_{0,4/3,\Omega} + \|H_{\circ,c}\|_{0,4,\Omega}\|v_h\|_{0,4/3,\Omega})}{\|\nabla v_h\|_{0,4/3,\Omega}} \\
&\le \sup_{0\neq v_h\in V_h} \frac{\omega\mu^\circ C_p(\|\tilde{H}_{h,c}\|_{0,4,\Omega} + \|H_{\circ,c}\|_{0,4,\Omega})\|\nabla v_h\|_{0,4/3,\Omega}}{\|\nabla v_h\|_{0,4/3,\Omega,}} \\
&\le \omega\mu^\circ C_p(\|\tilde{H}_{h,c}\|_{0,4,\Omega} + \|H_\circ\|_{0,4,\Omega,}).
\end{aligned}$$

By the Sobolev Embedding Theorem, $H_0^1(\Omega)$ is continuously embedded in $L^4(\Omega)$, and so there exists a positive constant C_{emb} such that $\|\tilde{H}_{h,c}\|_{0,4,\Omega} \le C_{emb}\|\tilde{H}_{h,c}\|_{1,\Omega}$. It has been shown in Lemma 4.5.1 that $\|\tilde{H}_h\|_{1,\Omega,\mathbb{C}} \le C_1$, and since $\|\tilde{H}_{h,c}\|_{1,\Omega} \le \|\tilde{H}_h\|_{1,\Omega,\mathbb{C}}$ it follows that

$$C_{ritz}\alpha_1\|\nabla\tilde{H}_{h,c}\|_{0,4,\Omega} \le \omega\mu^\circ C_p(\|H_\circ\|_{0,4,\Omega,\mathbb{C}} + C_{emb}C_1). \tag{4.23}$$

It can be shown in an identical manner that for some $\alpha_2 > 0$,

$$\alpha_2 C_{ritz}\|\nabla\tilde{H}_{h,c}\|_{0,4,\Omega} \le \omega\mu^\circ C_p(\|H_\circ\|_{0,4,\Omega,\mathbb{C}} + C_{emb}C_1).$$

It follows that

$$\begin{aligned}\|\nabla\tilde{H}_h\|_{0,4,\Omega,\mathbb{C}} &\leq \frac{1}{C_{ritz}\min(\alpha_1,\alpha_2)}\Big(\alpha_1\|\nabla\tilde{H}_{h,c}\|_{0,4,\Omega}+\alpha_2\|\nabla\tilde{H}_{h,c}\|_{0,4,\Omega}\Big)\\ &\leq \frac{2\omega\mu^\circ C_p(\|H_\circ\|_{0,4,\Omega,\mathbb{C}}+C_{emb}C_1)}{C_{ritz}\min(\alpha_1,\alpha_2)} =: C_4.\end{aligned}$$

This shows that $\nabla\tilde{H}_h$ is bounded in $L^4(\Omega,\mathbb{C})$ by a positive constant C_4 depending only on Ω,ω,μ°, and $H_\circ$. □

Remark. It should be highlighted that Lemma 4.5.2 only holds if h is small enough. In practice, this is very difficult to quantify as it depends on various embedding constants. Therefore, this is quite a restrictive assumption. ■

Lemma 4.5.2 immediately shows that $|\nabla H_h|^2$ is uniformly bounded in $L^2(\Omega)$, so next we apply Brouwer's Fixed Point Theorem (Theorem 2.3.14) to prove existence of solutions. However, first, we prove an *a-priori* bound for u_h.

4.5.2 Bounds on u_h

Lemma 4.5.3. There exists a positive constant C_5 independent of h such that for any $H_h \in V_{h,\mathbb{C}}$ with $\|\nabla H_h\|_{0,4,\Omega,\mathbb{C}} \leq C_4$, the solution to u_h to (4.18b) satisfies

$$|u_h|_{1,\Omega} \leq C_5. \tag{4.24}$$

Proof. This analogous to the proof of Lemma 4.4.4 using C_4 from Lemma 4.5.2. □

Now we prove existence of discrete solutions using a fixed-point argument.

4.5.3 Existence and Convergence of Solutions

Theorem 4.5.4. There exist a solution (H_h, u_h) to (4.18).

Proof. Since V_h is a finite-dimensional subspace, we can apply Brouwer's Fixed Point Theorem (Theorem 2.3.14) to prove existence of solutions of (4.18). Consider the decoupled problem: given $\hat{w}_h \in V_h$, find $(\varphi_h, w_h) \in W_{h,\mathbb{C}} \times V_h$ such that $\tilde{\varphi}_h = \varphi_h - H_\circ$,

$\tilde{\varphi}_h \in V_{h,\mathbb{C}}$ and

$$(\nabla\tilde{\varphi}_h, \nabla Q_h)_{\Omega,\mathbb{C}} + (i\omega\mu(\hat{w}_h)\tilde{\varphi}_h, Q_h)_{\Omega,\mathbb{C}} = (i\omega\mu(\hat{w}_h)H_\circ, Q_h)_{\Omega,\mathbb{C}}, \tag{4.25}$$

$$(\nabla w_h, \nabla v_h)_\Omega = \left(|\nabla\varphi_h|^2, v_h\right)_\Omega, \tag{4.26}$$

for all $(Q_h, v_h) \in V_{h,\mathbb{C}} \times V_h$. These define the mapping

$$M_h : V_h \to V_h : \hat{w}_h \mapsto w_h, \qquad \text{where } M_{1,h} : \hat{w}_h \mapsto \varphi_h, \qquad M_{2,h} : \varphi_h \mapsto w_h.$$

As it was proven in Theorem 4.4.5, we can show using Lemma 4.5.2 that

$$\|\nabla(M_{2,h} \circ M_{1,h})(w_h)\|_{0,\Omega} \leq M_h \qquad \forall\ w_h \in V_h.$$

Let $\{\hat{w}_k\}_k$ be a sequence in V_h. Define $\varphi_k =: M_{1,h}(\hat{w}_k)$, which defines another sequence $\{\varphi_k\}_k$, which is uniformly bounded by a constant C_1 in $H^1(\Omega;\mathbb{C})$. It follows that the sequence $\{\tilde{\varphi}_k\}_k$, where $\tilde{\varphi} = \varphi - H_\circ$ is also uniformly bounded in $H_0^1(\Omega;\mathbb{C})$. Similarly, the map the $w_k =: M_{2,h}(\varphi_k)$ defines a sequence $\{w_k\}_k$, which is uniformly bounded by a constant C_5 in $H_0^1(\Omega)$. Therefore if we show that the map M_h is continuous, we can apply Brouwer's Fixed Point Theorem (Theorem 2.3.14) and show that there exists a solution to the discrete problem. Let $\tilde{\varphi}_k$ and $\tilde{\varphi}_j$ be elements of the sequence $\{\tilde{\varphi}_k\}_k$. Then for all test functions $Q_h \in V_{h,\mathbb{C}}$,

$$(\nabla\tilde{\varphi}_k, \nabla Q_h)_{\Omega,\mathbb{C}} + (i\omega\mu(\hat{w}_k)\tilde{\varphi}_k, Q_h)_{\Omega,\mathbb{C}} = (i\omega\mu(\hat{w}_k)H_\circ, Q_h)_{\Omega,\mathbb{C}},$$
$$(\nabla\tilde{\varphi}_j, \nabla Q_h)_{\Omega,\mathbb{C}} + (i\omega\mu(\hat{w}_j)\tilde{\varphi}_j, Q_h)_{\Omega,\mathbb{C}} = (i\omega\mu(\hat{w}_j)H_\circ, Q_h)_{\Omega,\mathbb{C}},$$

which implies that

$$\begin{aligned}(\nabla(\tilde{\varphi}_k - \tilde{\varphi}_j), \nabla Q_h)_{\Omega,\mathbb{C}} = {} & (i\omega\mu(\hat{w}_k)H_\circ - i\omega\mu(\hat{w}_j)H_\circ, Q_h)_{\Omega,\mathbb{C}} \\ & - (i\omega\mu(\hat{w}_k)\tilde{\varphi}_k - i\omega\mu(\hat{w}_j)\tilde{\varphi}_j, Q_h)_{\Omega,\mathbb{C}}.\end{aligned}$$

Taking $\tilde{\varphi}_k - \tilde{\varphi}_j$ as a test function, it follows that

$$\begin{aligned}\|\nabla(\tilde{\varphi}_k - \tilde{\varphi}_j)\|^2_{0,\Omega,\mathbb{C}} &= (i\omega H_\circ(\mu(\hat{w}_k) - \mu(\hat{w}_j)), \tilde{\varphi}_k - \tilde{\varphi}_j)_{\Omega,\mathbb{C}} \\ &\quad - (i\omega\mu(\hat{w}_k)\tilde{\varphi}_k - i\omega\mu(\hat{w}_j)\tilde{\varphi}_j, \tilde{\varphi}_k - \tilde{\varphi}_j)_{\Omega,\mathbb{C}}.\end{aligned}$$

Now, it follows that

$$\begin{aligned}&(i\omega\mu(\hat{w}_k)\tilde{\varphi}_k - i\omega\mu(\hat{w}_j)\tilde{\varphi}_j, \tilde{\varphi}_k - \tilde{\varphi}_j)_{\Omega,\mathbb{C}} \\ &\qquad = (i\omega\mu(w_k)\tilde{\varphi}_k - i\omega\mu(\hat{w}_j)\tilde{\varphi}_k + i\omega\mu(\hat{w}_j)\tilde{\varphi}_k - i\omega\mu(\hat{w}_j)\tilde{\varphi}_j, \tilde{\varphi}_k - \tilde{\varphi}_j)_{\Omega,\mathbb{C}} \\ &\qquad = (i\omega(\mu(\hat{w}_k) - \mu(\hat{w}_j))\tilde{\varphi}_k, \tilde{\varphi}_k - \tilde{\varphi}_j)_{\Omega,\mathbb{C}} \\ &\qquad + \underbrace{(i\omega\mu(\hat{w}_j)(\tilde{\varphi}_k - \tilde{\varphi}_j), \tilde{\varphi}_k - \tilde{\varphi}_j)_{\Omega,\mathbb{C}}}_{\text{purely imaginary}}.\end{aligned}$$

It also follows that from the Cauchy-Schwarz inequality, the Poincaré inequality, and the definition of a Lipschitz function, that

$$\begin{aligned}|(i\omega H_\circ(\mu(\hat{w}_k) - \mu(\hat{w}_j)), \tilde{\varphi}_k - \tilde{\varphi}_j)_{\Omega,\mathbb{C}}| &\le \omega|H_\circ|\|\mu(\hat{w}_k) - \mu(\hat{w}_j)\|_{0,\Omega,\mathbb{C}}\|\tilde{\varphi}_k - \tilde{\varphi}_j\|_{0,\Omega,\mathbb{C}} \\ &\le \omega|H_\circ|C_{lip}C_p\|\hat{w}_k - \hat{w}_j\|_{0,\Omega}\|\nabla(\tilde{\varphi}_k - \tilde{\varphi}_j)\|_{0,\Omega,\mathbb{C}}.\end{aligned}$$

Therefore, since $\|\nabla(\tilde{\varphi}_k - \tilde{\varphi}_j)\|_{0,\Omega,\mathbb{C}}$ is real, and using the embedding constant C_{emb} from (4.23), it follows that

$$\begin{aligned}\|\nabla(\tilde{\varphi}_k - \tilde{\varphi}_j)\|^2_{0,\Omega,\mathbb{C}} &= \operatorname{Re}\big((i\omega H_\circ(\mu(\hat{w}_k) - \mu(\hat{w}_j)), \tilde{\varphi}_k - \tilde{\varphi}_j)_{\Omega,\mathbb{C}} \\ &\qquad + (i\omega(\mu(\hat{w}_k) - \mu(\hat{w}_j))\tilde{\varphi}_k, \tilde{\varphi}_k - \tilde{\varphi}_j)_{\Omega,\mathbb{C}}\big) \\ &\le \omega|H_\circ|C_{lip}C_p\|\hat{w}_k - \hat{w}_j\|_{0,\Omega}\|\nabla(\tilde{\varphi}_k - \tilde{\varphi}_j)\|_{0,\Omega,\mathbb{C}} \\ &\qquad + \omega C_{lip}C_pC_4\|\hat{w}_k - \hat{w}_j\|_{0,\Omega}\|\tilde{\varphi}_k - \tilde{\varphi}_j\|_{0,4,\Omega,\mathbb{C}} \\ &\le \omega C_{lip}C_p(|H_\circ| + C_4C_{emb}C_{equi})\|\hat{w}_k - \hat{w}_j\|_{0,\Omega}\|\nabla(\tilde{\varphi}_k - \tilde{\varphi}_j)\|_{0,\Omega,\mathbb{C}} \\ \Rightarrow \|\nabla(\tilde{\varphi}_k - \tilde{\varphi}_j)\|_{0,\Omega,\mathbb{C}} &\le \omega C_{lip}C_p(|H_\circ| + C_4C_{emb}C_{equi})\|\hat{w}_k - \hat{w}_j\|_{0,\Omega}.\end{aligned}$$

By the equivalence of the $H^1_0(\Omega;\mathbb{C})$ and $H^1(\Omega;\mathbb{C})$ norms, and since $\varphi_k - \varphi_k = (\tilde{\varphi}_k +$

$H_\circ) - (\tilde{\varphi}_j + H_\circ) = \tilde{\varphi}_k - \tilde{\varphi}_j$, it follows that

$$\|\varphi_k - \varphi_j\|_{1,\Omega,\mathbb{C}} \leq \omega C_{equi} C_{lip} C_p^2 (|H_\circ| + C_4 C_{emb}) \|\nabla(\hat{w}_k - \hat{w}_j)\|_{0,\Omega},$$

which proves that $M_{1,h}$ is continuous.

Now to prove that $M_{2,h}$ is continuous, let w_j and w_k be the results from the maps $M_{2,h}(\varphi_j)$ and $M_{2,h}(\varphi_k)$ respectively. Then for all $v_h \in V_h$,

$$(\nabla(w_k - w_j), \nabla v_h)_\Omega = (|\nabla\varphi_k|^2 - |\nabla\varphi_j|^2, v_h)_\Omega.$$

Taking $w_k - w_j$ as a test function in the above equality, we have that

$$\begin{aligned}
\|\nabla(w_k - w_j)\|_{0,\Omega}^2 &= (|\nabla\varphi_k|^2 - |\nabla\varphi_j|^2, w_k - w_j)_\Omega \\
&= (\nabla\varphi_k \cdot \overline{\nabla\varphi_k} - \nabla\varphi_k \cdot \overline{\nabla\varphi_j} + \nabla\varphi_k \cdot \overline{\nabla\varphi_j} - \nabla\varphi_j \cdot \overline{\nabla\varphi_j}, w_k - w_j)_\Omega \\
&= (\nabla\varphi_k \cdot (\overline{\nabla\varphi_k} - \overline{\nabla\varphi_j}), w_k - w_j)_\Omega + ((\nabla\varphi_k - \nabla\varphi_j) \cdot \overline{\nabla\varphi_j}, w_k - w_j)_\Omega \\
&\leq \|\nabla\varphi_k\|_{0,4,\Omega,\mathbb{C}} \|\overline{\nabla\varphi_k} - \overline{\nabla\varphi_j}\|_{0,\Omega,\mathbb{C}} \|w_k - w_j\|_{0,4,\Omega,\mathbb{C}} \\
&\qquad + \|\nabla\varphi_k - \nabla\varphi_j\|_{0,\Omega,\mathbb{C}} \|\overline{\nabla\varphi_j}\|_{0,4,\Omega,\mathbb{C}} \|w_k - w_j\|_{0,4,\Omega,\mathbb{C}} \\
&\leq 2C_4 C_{emb} C_{equi} \|\varphi_k - \varphi_j\|_{1,\Omega,\mathbb{C}} \|\nabla(w_k - w_j)\|_{0,\Omega} \\
\Rightarrow \|\nabla(w_k - w_j)\|_{0,\Omega} &\leq 2C_4 C_{emb} C_{equi} \|\varphi_k - \varphi_j\|_{1,\Omega,\mathbb{C}}.
\end{aligned}$$

Therefore $M_{1,h}$ and $M_{2,h}$ are continuous, so $M_h = M_{2,h} \circ M_{1,h}$ is also continuous and it follows that the mapping M_h has a fixed point. By Brouwer's Fixed Point Theorem (Theorem 2.3.14), there exists a solution for (4.18), and we denote this solution (H_h, u_h). □

Remark. We can apply Brouwer's Fixed Point Theorem (Theorem 2.3.14) here because V_h and $V_{h,c}$ are finite dimensional spaces. ■

Now that we have proven the existence of a discrete solution, we prove that the discrete solution converges to a continuous solution.

Theorem 4.5.5. Let $\{(H_h, u_h)\}_h$ be a sequence of solutions of (4.18). Then, up to a subsequence, $H_h \rightharpoonup H$ weakly in $H^1(\Omega; \mathbb{C})$ and $u_h \rightharpoonup u$ weakly in $H_0^1(\Omega)$ and (H, u) is a solution of (4.14).

Proof. Convergence of solutions can be shown using a method similar to the proof of existence in Theorem 4.4.5. The sequence $\{H_h\}_h$ is uniformly bounded in $H^1(\Omega, \mathbb{C})$ and therefore $H_h \rightharpoonup H$ weakly in $H^1(\Omega, \mathbb{C})$. Additionally, there is a subsequence such that $\nabla H_h \rightharpoonup \nabla H$ weakly in $L^4(\Omega; \mathbb{C})^2$. Since we have shown that ∇H_h is uniformly bounded in $L^4(\Omega; \mathbb{C})$, we also have a subsequence $\{u_h\}_h$ such that $u_h \rightharpoonup u$ weakly in $H_0^1(\Omega)$ since $\{u_h\}_h$ is uniformly bounded in $H_0^1(\Omega)$. Let $Q \in \mathcal{D}(\Omega; \mathbb{C})$ and let $Q_h := \mathcal{I}_h(Q) \in V_{h,\mathbb{C}}$, where $\mathcal{I}_h$ is the Lagrange interpolant from Definition 2.5.8. Since $Q_h \to Q$ strongly in $W^{1,\infty}(\Omega; \mathbb{C})$ as $h \to 0$, as shown in Theorem 2.5.9, and defining $\tilde{H}_h = H_h - H_\circ$ and $\tilde{H} = H - H_\circ$, it follows that

$$\begin{aligned}(\nabla \tilde{H}_h, \nabla Q_h)_{\Omega,\mathbb{C}} &= (\nabla \tilde{H}_h, \nabla(Q_h - Q))_{\Omega,\mathbb{C}} + (\nabla \tilde{H}_h, \nabla Q)_{\Omega,\mathbb{C}} \\ &\to (\nabla \tilde{H}, \nabla Q)_{\Omega,\mathbb{C}} \text{ as } h \to 0.\end{aligned}$$

Since $\mu(\cdot)$ is Lipschitz, and since $u_h \to u$ strongly in $L^2(\Omega)$, $\mu(u_h) \to \mu(u)$ a.e., and therefore

$$(i\omega\mu(u_h)\tilde{H}_h, Q_h)_{\Omega,\mathbb{C}} \to (i\omega\mu(u)\tilde{H}, Q)_{\Omega,\mathbb{C}},$$

and

$$(i\omega\mu(u_h)H_\circ, Q_h)_{\Omega,\mathbb{C}} \to (i\omega\mu(u)H_\circ, Q)_{\Omega,\mathbb{C}}.$$

This shows that (H, u) satisfies (4.18a).

Now let $v \in \mathcal{D}(\Omega)$, and let $v_h =: \tilde{\mathcal{I}}_h(v)$ be the Scott-Zhang interpolant of v (see Theorem 2.5.11) so that $v_h \to v$ strongly in $H_0^1(\Omega)$. Then by definition of weak convergence in $H_0^1(\Omega)$,

$$(\nabla u_h, \nabla v_h)_\Omega \to (\nabla u, \nabla v)_\Omega \text{ as } h \to 0.$$

Now, we can write the right-hand side as

$$(|\nabla H_h|^2, v_h)_\Omega = (|\nabla H_h|^2, v_h - v)_\Omega + (|\nabla H_h|^2, v)_\Omega = (1) + (2).$$

Since $|\nabla H_h|^2$ is bounded in $L^2(\Omega)$ for all h, (1) $\to 0$, so it remains to consider (2). First note that if we take $\tilde{H}v$ as a test function in (4.14a), the exact solution (H, u) satisfies for all $v \in \mathcal{D}(\Omega)$, $H - H_\circ = \tilde{H} \in H_0^1(\Omega, \mathbb{C})$, and

$$(|\nabla \tilde{H}|^2, v)_{\Omega,\mathbb{C}} = (i\omega\mu(u)H_\circ\overline{\tilde{H}}, v)_{\Omega,\mathbb{C}} - (i\omega\mu(u)|\tilde{H}|^2, v)_{\Omega,\mathbb{C}} - (\overline{\tilde{H}}\nabla\tilde{H}, \nabla v)_{\Omega,\mathbb{C}}. \quad (4.27)$$

Now, take the discrete form (4.18a) with $Q_h = \mathcal{I}_h(\tilde{H}_h v) \in V_{h,\mathbb{C}}$. Then we get

$$\begin{aligned}(\nabla\tilde{H}_h, \nabla(\mathcal{I}_h(\tilde{H}_h v))_{\Omega,\mathbb{C}} + (i\omega\mu(u_h)\tilde{H}_h, \mathcal{I}_h(\tilde{H}_h v))_{\Omega,\mathbb{C}} &= (i\omega\mu(u_h)H_\circ, \mathcal{I}_h(\tilde{H}_h v))_{\Omega,\mathbb{C}} \\ &=: (3) + (4) = (5).\end{aligned}$$

Now,

$$(4) = (i\omega\mu(u_h)\tilde{H}_h, \mathcal{I}_h(\tilde{H}_h v) - \tilde{H}_h v)_{\Omega,\mathbb{C}} + (i\omega\mu(u_h)\tilde{H}_h, \tilde{H}_h v)_{\Omega,\mathbb{C}} = (4a) + (4b)$$

and $(4a) \to 0$ as $h \to 0$ by the discrete commutator property (see Ern and Guermond (2004, Lemma 1.137)), and

$$(4b) \to (i\omega\mu(u)|\tilde{H}|^2, v)_{\Omega,\mathbb{C}}.$$

We also have that

$$\begin{aligned}(5) &= (i\omega\mu(u_h)H_\circ, \mathcal{I}_h(\tilde{H}_h v) - \tilde{H}_h v)_{\Omega,\mathbb{C}} + (i\omega\mu(u_h)H_\circ, \tilde{H}_h v)_{\Omega,\mathbb{C}} \\ &\to (i\omega\mu(u)H_\circ\overline{\tilde{H}}, v)_{\Omega,\mathbb{C}} \text{ as } h \to 0,\end{aligned}$$

by, again, using the discrete commutator property. Finally, we have

$$(3) = (\nabla\tilde{H}_h, \nabla(\mathcal{I}_h(\tilde{H}_h v) - \tilde{H}_h v))_{\Omega,\mathbb{C}} + (\nabla\tilde{H}_h, \nabla(\tilde{H}_h v))_{\Omega,\mathbb{C}} = (3a) + (3b).$$

Again, $(3a) \to 0$ as $h \to 0$ by the discrete commutator property. It follows by the product rule that

$$(3b) = (|\nabla\tilde{H}_h|^2, v)_{\Omega,\mathbb{C}} + (\overline{\tilde{H}_h}\nabla\tilde{H}_h, \nabla v)_{\Omega,\mathbb{C}} = (3bi) + (3bii)$$

and

$$(3bii) \to (\overline{\tilde{H}}\nabla\tilde{H}, \nabla v)_{\Omega,\mathbb{C}} \text{ as } h \to 0.$$

Therefore, using the the fact that the exact solution satisfies (4.27), it follows that

$$\begin{aligned}\lim_{h\to 0}\left((|\nabla\tilde{H}_h|^2, v)_{\Omega,\mathbb{C}}\right) &= \lim_{h\to 0}\left(-(3bii) + (5) - (4)\right)\\ &= -(\overline{\tilde{H}}\nabla\tilde{H}, \nabla v)_{\Omega,\mathbb{C}} + (i\omega\mu(u)H_\circ\overline{\tilde{H}}, v)_{\Omega,\mathbb{C}} - (i\omega\mu(u)|\tilde{H}|^2, v)_{\Omega,\mathbb{C}}\\ &= (|\nabla\tilde{H}|^2, v)_{\Omega,\mathbb{C}}\end{aligned}$$

and hence, since $|\nabla H|^2 = |\nabla\tilde{H}|^2$,

$$(\nabla u_h, \nabla\mathcal{I}_h(v))_\Omega - (|\nabla\tilde{H}_h|^2, \mathcal{I}_h(v))_\Omega \to (\nabla u, \nabla v)_\Omega - (|\nabla H|^2, v)_\Omega \text{ as } h \to 0,$$

which shows that $(H_h, u_h) \to (H, u)$ as $h \to 0$ if there are strict conditions on the mesh. This shows that the limits (H, u) satisfies the continuous problem. □

4.6 The Bound Preserving Method

In this Section, for a simplified problem, we circumvent the restrictions on the mesh and the assumption of convexity on the domain by using the Bound Preserving Method (BPM).

For this Section we consider the finite element approximation of a simplified problem, which reads: find $(H, u) \in H^1(\Omega;\mathbb{C}) \times H^1_0(\Omega)$ such that $\tilde{H} = H - H_\circ$, $\tilde{H} \in H^1_0(\Omega;\mathbb{C})$ and

$$(\nabla\tilde{H}, \nabla Q)_{\Omega,\mathbb{C}} + (i\omega\tilde{H}, Q)_{\Omega,\mathbb{C}} = (i\omega H_\circ, Q)_{\Omega,\mathbb{C}}, \tag{4.28a}$$

$$(\nabla u, \nabla v)_\Omega = \left(|\nabla\tilde{H}|^2, v\right)_\Omega, \tag{4.28b}$$

for all $(Q, v) \in H^1_0(\Omega;\mathbb{C}) \times H^1_0(\Omega)$. In particular, this is (4.5) but with $\mu(\cdot) = 1$.

The FEM considered here reads: given a positive real constant k, find $(H_h, u_h) \in$

$W_{h,\mathbb{C}} \times V_h$ such that $\tilde{H}_h = H_h - H_\circ$, $\tilde{H}_h \in V_{h,\mathbb{C}}$ and

$$(\nabla \tilde{H}_h, \nabla Q_h)_{\Omega,\mathbb{C}} + (i\omega \tilde{H}_h, Q_h)_{\Omega,\mathbb{C}} = (i\omega H_\circ, Q_h)_{\Omega,\mathbb{C}}, \tag{4.29a}$$

$$(\nabla u_h^k, \nabla v_h)_\Omega + s(u_h^{-k}, v_h) = (|\nabla \tilde{H}_h|^2, v_h)_\Omega, \tag{4.29b}$$

for all $(Q_h, v_h) \in V_{h,\mathbb{C}} \times V_h$. Here, (4.29a) is solved using the standard Galerkin FEM, and (4.29b) is solved using the BPM posed by Barrenechea et al. (2024), presented in Section 2.6. Here, u_h^k is the constrained part of u_h, in the sense that $u_h^k \in V_h^k$, where V_h^k is the finite element subset of V^k defined in (2.27), and

$$u_h^k := \sum_{i=1}^{n} \max\{0, \min\{u_h(\boldsymbol{x}_i), k\}\}\phi_i.$$

The term $u_h^{-k} := u_h - u_h^k$ is the complementary part of u_h. This method guarantees that the bounds of the solution (here taken to be $[0, k]$) are satisfied by explicitly hardwiring the bounds into the method and searching for a solution in V_h^k. Thus, we will show that we can prove convergence for non-convex domains and with no restrictions on the mesh.

Following the definition for the stabilising mass lumping term (2.29), the term $s(\cdot,\cdot)$ for (4.29b) is defined as

$$s(v_h, w_h) := \alpha \sum_{i=1}^{N} v_h(\boldsymbol{x}_i) w_h(\boldsymbol{x}_i),$$

where α is a non-dimensional constant.

Remark. Since the weak systems (4.28) and (4.28) are only coupled in one direction, these systems have unique solutions. ■

4.6.1 Convergence Results for H_h

Since (4.29a) does not depend on u_h, we can use standard convergence results for the standard Galerkin FEM. It it follows that

$$H_h \to H \qquad \text{strongly in } H^1(\Omega;\mathbb{C}). \tag{4.30}$$

This implies from the Sobolev Embedding Theorem (Theorem 2.3.8) that

$$|\nabla H_h| \to |\nabla H| \qquad \text{strongly in } L^2(\Omega),$$

and also that

$$|\nabla H_h|^2 \to |\nabla H|^2 \qquad \text{strongly in } L^1(\Omega). \tag{4.31}$$

Finally, it can be shown in an identical manner to Lemma 4.4.1 that the solution H_h satisfies

$$\|H_h\|_{1,\Omega,\mathbb{C}} \leq C_1, \tag{4.32}$$

where C_1 is the same constant form Lemma 4.4.1 that depends only on Ω, ω, μ°, and $H_\circ$. In particular, it does not depend on h.

4.6.2 Convergence Results for u_h^k

Here, we find some convergence results for u_h^k for a fixed k. Taking the test function $v_h = u_h^k$ in (4.29b), using the bound in (4.32), and the fact that $s(\cdot,\cdot)$ is monotone as shown in Chapter 2.6, we can obtain a bound for u_h^k in $H_0^1(\Omega)$. Using Hölder's inequality and the fact that $\|u_h^k\|_{0,\infty,\Omega} \leq k$, it follows that

$$\begin{aligned} \|\nabla u_h^k\|_{0,\Omega}^2 + \underbrace{s(u_h^{-k}, u_h^k)}_{\geq 0} &= \Big(|\nabla H_h|^2, u_h^k\Big)_\Omega \\ \Rightarrow |u_h^k|_{1,\Omega}^2 \leq k|H_h|_{1,\Omega,\mathbb{C}}^2 &\leq C_1^2 k. \end{aligned} \tag{4.33}$$

Therefore, there exists a subsequence (still denoted u_h^k) depending on k such that

$$u_h^k \rightharpoonup \hat{u}^k \qquad \text{weakly in } H_0^1(\Omega). \tag{4.34}$$

By Sobolev Embedding (Theorem 2.3.8), this implies that

$$u_h^k \to \hat{u}^k \qquad \text{strongly in } L^2(\Omega). \tag{4.35}$$

Moreover, using Sobolev Embedding again, the following stronger result holds:

$$u_h^k \to \hat{u}^k \qquad \text{in } L^p(\Omega) \quad \text{for all } 1 \leq p < \infty.$$

As a consequence, there exists a subsequence still denoted by u_h^k such that

$$u_h^k \to \hat{u}^k \qquad \text{a.e. in } \Omega. \tag{4.36}$$

Finally, convergence a.e. and the fact that $\|u_h^k\|_{0,\infty} \leq k$ for all h, implies that

$$\|\hat{u}^k\|_{0,\infty,\Omega} \leq k, \tag{4.37}$$

and so $\hat{u}^k \in V^k$.

In the following Section we use these results to take the limit as $h \to 0$ in the term u_h^k. This way, we show that the limit $\hat{u}^k$ defined in (4.34) is the projection of the exact solution u onto the space V^k.

4.6.3 Convergence of Solutions

In this Section we prove convergence of a subsequence of the finite element solutions (H_h, u_h^k) to an exact solution (H, u) as $h \to 0$ and $k \to \infty$. First, we prove a variational inequality for the heat equation, which shows that if we take $h \to 0$, the resulting limit $\hat{u}^k$ defined in (4.34) is the projection of the exact solution u into the space V^k with respect to the $H_0^1(\Omega)$ norm.

Lemma 4.6.1. The function $\hat{u}^k$ satisfies the inequality

$$(\nabla \hat{u}^k, \nabla(\varphi - \hat{u}^k))_\Omega \geq (|\nabla H|^2, \varphi - \hat{u}^k)_\Omega \qquad \forall\, \varphi \in V^k.$$

Proof. Let $\varphi \in D_k(\Omega)$ and let $\varphi_h := \mathcal{I}_h(\varphi) \in V_h^k$, where $\mathcal{I}_h$ is the Lagrange interpolant from Definition 2.5.8. It is well known that $\varphi_h \to \varphi$ a.e. in Ω (see Corollary 2.5.10). Taking $\varphi_h - u_h^k$ as a test function in (4.29b) and using the monotonicity of $s(\cdot,\cdot)$, we get

$$\begin{aligned} (\nabla u_h^k, \nabla(\varphi_h - u_h^k))_\Omega + \underbrace{s(u_h^{-k}, \varphi_h - u_h^k)}_{\leq 0} &= (|\nabla H_h|^2, \varphi_h - u_h^k)_\Omega \\ \Rightarrow (\nabla u_h^k, \nabla(\varphi_h - u_h^k))_\Omega &\geq (|\nabla H_h|^2, \varphi_h - u_h^k)_\Omega. \end{aligned}$$

Now let us consider the limit as $h \to 0$ for the right-hand side (RHS) and left-hand side (LHS) above in turn.

RHS

The sum of two sequences converging a.e. is also converging a.e.. Therefore, using (4.36) we have $\varphi_h - u_h^k \to \varphi - \hat{u}^k$ a.e.. The product of a sequence that converges weakly in $L^1(\Omega)$ and a bounded sequence that converges pointwise a.e. also converges weakly in $L^1(\Omega)$ (Fonseca and Leoni 2007, Proposition 2.61). Since $\|\varphi_h - u_h^k\|_{0,\infty,\Omega} \leq 2k$ is bounded and converges pointwise a.e., and (4.31) shows strong convergence in $L^1(\Omega)$, it follows that

$$(|\nabla H_h|^2, \varphi_h - u_h^k)_\Omega \to (|\nabla H|^2, \varphi - \hat{u}^k)_\Omega. \tag{4.38}$$

LHS

We split the LHS into three parts,

$$\begin{aligned}(\nabla u_h^k, \nabla(\varphi_h - u_h^k))_\Omega &= (\nabla u_h^k, \nabla(\varphi_h - \varphi))_\Omega + (\nabla u_h^k, \nabla(\varphi - \hat{u}^k))_\Omega \\ &\quad + (\nabla u_h^k, \nabla(\hat{u}^k - u_h^k))_\Omega \\ &= \text{(A)} + \text{(B)} + \text{(C)}.\end{aligned}$$

We consider each of these parts separately.

(A) Using (4.33) and the fact that $\varphi_h \to \varphi$ strongly in $H^1(\Omega)$, we apply the Cauchy-Schwarz Inequality from Theorem 2.3.4, and get for a fixed k,

$$\left|(\nabla u_h^k, \nabla(\varphi_h - \varphi))_\Omega\right| \leq \|\nabla u_h^k\|_{0,\Omega} \|\varphi_h - \varphi\|_{0,\Omega} \to 0 \text{ as } h \to 0.$$

Therefore,

$$(A) \to 0 \text{ as } h \to 0.$$

(B) Since $\varphi - \hat{u}^k$ is a fixed test function in $H_0^1(\Omega)$, and since $u_h^k \rightharpoonup \hat{u}^k$ weakly in $H_0^1(\Omega)$ by (4.34), we have

$$(B) \to (\nabla \hat{u}^k, \nabla(\varphi - \hat{u}^k))_\Omega \quad \text{ as } h \to 0.$$

(C) For the final term, by splitting the inner product again, we get

$$\begin{aligned}(C) &= (\nabla u_h^k, \nabla(\hat{u}^k - u_h^k))_\Omega \\ &= (\nabla(u_h^k - \hat{u}^k), \nabla(\hat{u}^k - u_h^k))_\Omega + (\nabla \hat{u}^k, \nabla(\hat{u}^k - u_h^k))_\Omega \\ &= -\|\nabla(u_h^k - \hat{u}^k)\|_{0,\Omega}^2 + (\nabla \hat{u}^k, \nabla(\hat{u}^k - u_h^k))_\Omega \\ &\leq (\nabla \hat{u}^k, \nabla(\hat{u}^k - u_h^k))_\Omega =: (\tilde{C}).\end{aligned}$$

Since $u_h^k \rightharpoonup \hat{u}^k$ weakly in $H_0^1(\Omega)$, it follows that $\tilde{C} \to 0$ as $h \to 0$.

Therefore,

$$\begin{aligned} & (A) + (B) + (C) \geq (|\nabla H_h|^2, \varphi_h - u_h^k)_\Omega \\ \Rightarrow \quad & (A) + (B) + (\tilde{C}) \geq (|\nabla H_h|^2, \varphi_h - u_h^k)_\Omega. \end{aligned}$$

Taking the limit as $h \to 0$, we have shown that $\hat{u}^k$ satisfies

$$(\nabla \hat{u}^k, \nabla(\varphi - \hat{u}^k))_\Omega \geq (|\nabla H|^2, \varphi - \hat{u}^k)_\Omega,$$

for all $\varphi \in D_k(\Omega)$. Since $\overline{D_k(\Omega)} = V^k$ from Lemma 4.3.1, then $\hat{u}^k \in V^k$ satisfies

$$(\nabla \hat{u}^k, \nabla(v - \hat{u}^k))_\Omega \geq (|\nabla H|^2, v - \hat{u}^k)_\Omega \qquad \forall\ v \in V^k.$$

It follows from Definition 2.3.10 that

$$\hat{u}^k = \Pi_{V^k}(u)$$

where $\Pi_{V^k}(u)$ is the projection of u, the solution of (4.28b), from $H_0^1(\Omega)$ onto V^k with respect to the $H_0^1(\Omega)$ norm. □

Lemma 4.6.1 has significant implications as, most importantly, it shows that if we choose k large enough, and u is bounded, then $\hat{u}^k$ and u coincide.

The following result is used to show strong convergence of u_h^k to $\hat{u}^k$.

Lemma 4.6.2. Let $f \in L^2(\Omega)$ and and f_h be a sequence such that $f_h \to f$ strongly in $L^1(\Omega)$. Let $w_h \in V_h^k$ be a sequence such that $w_h \rightharpoonup w$ weakly in $H_0^1(\Omega)$ as $h \to 0$ and $w \in V^k$. Suppose $w_h \in V_h^k$ and $w \in V^k$ satisfy the variational inequalities:

$$\begin{aligned} (\nabla w_h, \nabla(v_h - w_h))_\Omega &\geq (f_h, v_h - w_h)_\Omega \qquad && \forall\ v_h \in V_h^k, \\ (\nabla w, \nabla(v - w))_\Omega &\geq (f, v - w)_\Omega && \forall\ v \in V^k. \end{aligned}$$

Then $|w_h - w|_{1,\Omega} \to 0$ as $h \to 0$.

Proof. First note that the inequalities imply that:

$$\begin{aligned} -(\nabla w_h, \nabla(v_h - w_h))_\Omega &\le -(f_h, v_h - w_h)_\Omega \qquad && \forall\, v_h \in V_h^k, \\ -(\nabla w, \nabla(v - w))_\Omega &\le -(f, v - w)_\Omega && \forall\, v \in V^k. \end{aligned}$$

For this proof, let $\tilde{\mathcal{I}}_h$ be the Scott-Zhang interpolant (see Theorem 2.5.11). It follows that

$$\begin{aligned} 0 &\le (\nabla(w - w_h), \nabla(w - w_h))_\Omega \\ &= (\nabla w, \nabla(w - w_h))_\Omega - (\nabla w_h, \nabla(w - w_h)))_\Omega \\ &= (\nabla w, \nabla(w - w_h))_\Omega - (\nabla w_h, \nabla(w - \tilde{\mathcal{I}}_h(w) + \tilde{\mathcal{I}}_h(w) - w_h))_\Omega \\ &= -(\nabla w, \nabla(w_h - w))_\Omega - (\nabla w_h, \nabla(\tilde{\mathcal{I}}_h(w) - w_h)))_\Omega - (\nabla w_h, \nabla(w - \tilde{\mathcal{I}}_h(w))_\Omega \\ &\le -(f, w_h - w)_\Omega - (f_h, \tilde{\mathcal{I}}_h(w) - w_h)_\Omega - (\nabla w_h, \nabla(w - \tilde{\mathcal{I}}_h(w)))_\Omega. \end{aligned}$$

Now, notice that

$$\begin{aligned} -(f, w_h - w)_\Omega - (f_h, \tilde{\mathcal{I}}_h(w) - w_h)_\Omega &= -(f, w_h)_\Omega + (f, w)_\Omega - (f_h, \tilde{\mathcal{I}}_h(w))_\Omega + (f_h, w_h)_\Omega \\ &= (f_h - f, w_h)_\Omega + (f - f_h + f_h, w)_\Omega - (f_h, \tilde{\mathcal{I}}_h(w))_\Omega \\ &= (f_h - f, w_h)_\Omega + (f - f_h, w)_\Omega + (f_h, w - \tilde{\mathcal{I}}_h(w))_\Omega. \end{aligned}$$

The first two terms converge to zero as $h \to 0$ since $f_h \to f$ strongly in $L^1(\Omega)$. Since $\tilde{\mathcal{I}}_h(w) \to w$ strongly in $H_0^1(\Omega)$ and $w_h \rightharpoonup w$ weakly, it follows that

$$0 \le \lim_{h \to 0} |w - w_h|_{1,\Omega} \le \lim_{h \to 0} -(\nabla w_h, \nabla(w - \tilde{\mathcal{I}}_h(w)))_\Omega = 0.$$

Hence $|w - w_h|_{1,\Omega} \to 0$ as $h \to 0$. □

Now we present the main result of this Section, which proves convergence of discrete BPM system (4.29) to the exact solution (4.28). Note that this exact solution is unique, which follows from the one-directional coupling of the equations.

Theorem 4.6.3. Let $(H, u) \in H^1(\Omega; \mathbb{C}) \times H_0^1(\Omega)$ be the unique solution of the simplified

Induction Heating Problem (4.28), and let $(H_h, u_h^k) \in W_{h,\mathbb{C}} \times V_h$ be the solution of the BPM (4.29). Then

$$(H_h, u_h^k) \to (H, u) \quad \text{strongly in } H^1(\Omega;\mathbb{C}) \times H_0^1(\Omega),$$

as $h \to 0$ and $k \to \infty$.

Proof. Since (4.29a) has no dependence on u_h, it has already been established in (4.30) that $H_h \to H$ strongly in $H^1(\Omega;\mathbb{C})$. Therefore, it remains to show that $u_h^k \to u$ strongly in $H_0^1(\Omega)$ as $h \to 0$ and $k \to \infty$.

First, taking the limit as $h \to 0$, we have established that $u_h^k \rightharpoonup \hat{u}^k$ weakly in $H_0^1(\Omega)$ in (4.34). We have shown in Lemma 4.6.1 that $\hat{u}^k$ satisfies

$$(\nabla \hat{u}^k, \nabla(v - \hat{u}^k))_\Omega \geq (|\nabla H|^2, v - \hat{u}^k)_\Omega \qquad \forall\, v \in V^k.$$

By definition of the BPM, and using the fact that $s(\cdot,\cdot)$ is monotone, the BPM solution u_h^k satisfies

$$(\nabla u_h^k, \nabla(v_h - u_h^k))_\Omega \geq (|\nabla H_h|^2, v_h - u_h^k)_\Omega \qquad \forall\, v_h \in V_h^k.$$

Since $|\nabla H_h|^2 \to |\nabla H|^2$ strongly in $L^1(\Omega)$, as established in (4.31), we can apply Lemma 4.6.2 with $w = \hat{u}^k$ and $w_h = u_h^k$. This gives us that $u_h^k \to \hat{u}^k$ strongly in $H_0^1(\Omega)$ as $h \to 0$.

Since (4.28b) is a Poisson problem, the Maximum Principle for Weak solutions in Theorem 2.4.9 implies that if Ω is bounded, there exists a positive constant C_{mp} such that $|u(\boldsymbol{x})| \leq C_{mp}$ for all $\boldsymbol{x} \in \Omega$. Therefore, for $k > C_{mp}$, the projection operator from $H_0^1(\Omega)$ onto V^k defined by $\Pi_{V^k}(\cdot)$ is simply the identity mapping. In Lemma 4.6.1, we showed that $\hat{u}^k = \Pi_{V^k}(u)$, so for $k > C_{mp}$, we have $\hat{u}^k = \Pi_{V^k}(u) = u$. Taking the limit as $k \to \infty$ we eventually have $k > C_{mp}$, and so

$$\lim_{k\to\infty} \left(\lim_{h\to 0} u_h^k \right) = \lim_{k\to\infty} \left(\Pi_{V^k}(u) \right) = u.$$

Thus

$$(H_h, u_h^k) \to (H, u) \quad \text{strongly in } H^1(\Omega;\mathbb{C}) \times H_0^1(\Omega),$$

as $h \to 0$ and $k \to \infty$. □

4.7 Numerical Experiments

In this Section we describe some numerical experiments that showcase orders of convergence for the BPM for certain problems. We illustrate the main result found in Lemma 4.6.1, and show that when truncating at a non-physical height, the BPM converges to the $H_0^1(\Omega)$ projection of the unique solution into the closed convex set V^k. We also show that the BPM is more accurate than the standard Galerkin method when resolving boundary layers on coarse non-Delaunay meshes. This is particularly relevant to induction heating as boundary layers are present, and the use of Delaunay meshes is not always optimal in complicated domains. Finally, we implement the BPM for the fully coupled non-linear Solenoidal Induction Heating Problem (4.14) and show convergence numerically.

We implement the BPM by using a Richardson style iteration: given an initial guess $u_h^0 \in V_h$ and $\omega_r \in (0, 1]$, we iteratively solve

$$\begin{aligned}(\nabla u_h^{n+1}, \nabla v_h)_\Omega &= (\nabla (u_h^n)^k, \nabla v_h)_\Omega \\ &\quad + \omega_r((f, v_h)_\Omega - (\nabla (u_h^n)^k, \nabla v_h)_\Omega - s((u_h^n)^{-k}, v_h)), \quad (4.39)\end{aligned}$$

for all $v_h \in V_h$. The algorithm is terminated when $\|u_h^{n+1} - u_h^n\|_{0,\Omega} \le 10^{-12}$, and we say $u_h^k := (u_h^{n+1})^k$ is the resulting numerical solution. We take the initial condition $u_h^0 := u_h^{GAL}$ to be the solution of the standard Galerkin problem:

$$(\nabla u_h^{GAL}, \nabla v_h)_\Omega = (f, v_h)_\Omega. \quad (4.40)$$

The BPM has been implemented using `Python` code with the software package `FEniCSx v.0.9.0` (Baratta et al. 2023). The resulting linear systems are solved using an LU solver within the `petsc` module of `FEniCSx`. In all tests we take $\alpha = 1$ and

$\omega_r = 0.5$. The full code for the BPM and these experiments can be found in the GitHub repository by MacKenzie (2025).

4.7.1 Convergence when Truncating at a Non-Physical Bound

Let Ω be the unit square, and consider the problem

$$\begin{aligned} -\Delta u &= f \quad \text{in } \Omega, \\ u &= 0 \quad \text{on } \partial\Omega. \end{aligned} \tag{4.41}$$

The function $u = \sin(\pi x)\sin(\pi y)$ is a known analytical solution for (4.41) when $f = 2\pi^2 \sin(\pi x)\sin(\pi y)$. Additionally, $u(x, y) \in (0, 1]$ for all $(x, y) \in \Omega$. For this experiment, we truncate at $k = 1/2$, and show that the numerical solution converges to the best approximation of the $H_0^1(\Omega)$ projection onto the subset

$$V^{1/2} := \{v \in H_0^1(\Omega) : |v(x)| \leq 1/2\}.$$

This is done by comparing to a numerical solution computed on an extremely fine mesh ($\approx 2.88 \times 10^6$ elements). A visualisation of the numerical solution u_h^k for $h = 0.00625$, and corresponding convergence results over a sequence of uniformly refined meshes are shown in Figure 4.1a and 4.1b respectively.

h size	N. elements	$\|u_h^k - u\|_{0,\Omega}$	$\|u_h^k - u\|_{1,\Omega}$	Time (s)	Iterations
0.10000	200	0.004408	0.066594	2.943357	7
0.05000	800	0.001223	0.023105	2.892834	7
0.02500	3200	0.000313	0.008143	3.271738	24
0.01250	12800	0.000079	0.002824	3.778616	26
0.00625	51200	0.000021	0.003189	4.850676	26

Table 4.1: Numerical results when solving for u_h^k using (4.39).

The results support the findings in Lemma 4.6.1, which states that u_h^k is the best approximation of u in the space $V_h^{1/2}$, and as $h \to 0$, u_h^k converges to the projection of u onto $V^{1/2}$. We see in Table 4.1 that the algorithm seems fairly robust in time, and the number of iterations in the Richardson algorithm seems consistent once the mesh

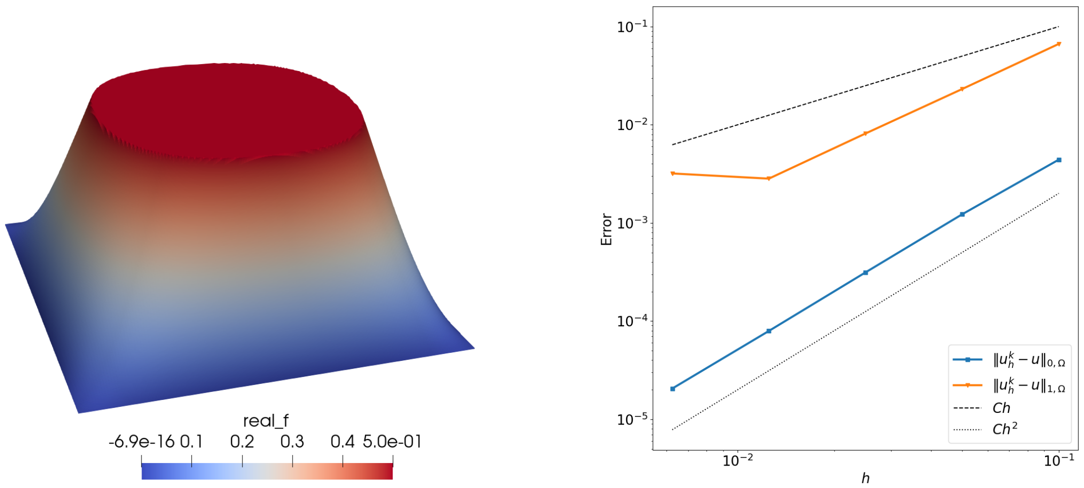

(a) Plot of u_h^k over a uniform mesh with $h = 0.00625$.

(b) Convergence in the L^2 and H^1 norms.

Figure 4.1: The numerical solution u_h^k over a sequence of increasingly refined uniform meshes.

is refined enough.

4.7.2 Convergence on a Non-Delaunay Mesh for Solutions with a Boundary Layer

In this experiment, we consider a problem where the solution has a boundary layer. We compare convergence rates over a sequence of non-Delaunay meshes for the BPM and the standard Galerkin method. The meshes are generated using `GMSH` (Geuzaine and Remacle 2009) and then manually edited. These meshes are designed to have severely obtuse angles to generate numerical solutions of the standard FEM that violate the DMP.

Let Ω be the unit square. We choose our exact solution to be $u_{ex}(x, y) = e^{-dx} + e^{-dy}$ where $d > 0$ (see Figure 4.3). For d large enough, $u(x, y)$ will have a boundary layer. Indeed, the magnetic field distribution in a Solenoidal Induction Heating Problem will typically contain an exponential boundary layer, so this type of problem is expected in

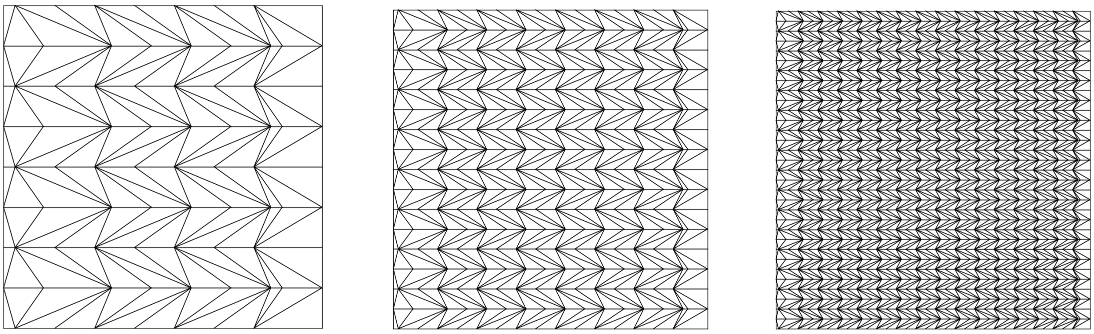

(a) Iteration 1. (b) Iteration 2. (c) Iteration 3.

Figure 4.2: A sequence of increasingly refined non-Delaunay meshes.

realistic applications. Letting $f = -d^2(e^{-dx} + e^{-dy})$, we solve the problem

$$\begin{aligned} -\Delta u &= f && \text{in } \Omega, \\ u &= u_{ex}|_{\partial\Omega} && \text{on } \partial\Omega, \end{aligned} \tag{4.42}$$

using the BPM with the Richardson iteration (4.39). We denote our solution by u_h^k, where $k = 2$ is the natural bound for this problem. We compare to the solution of the standard Galerkin method u_h^{GAL}. Figure 4.4 shows the convergence rates for different values of d.

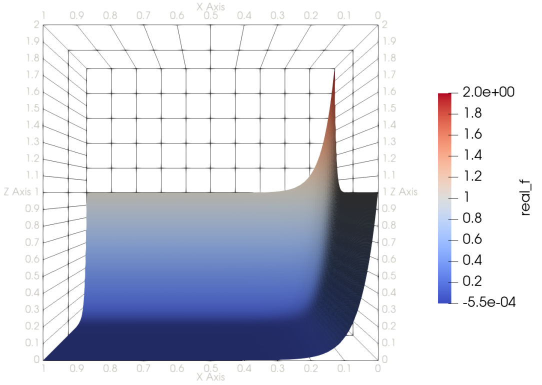

Figure 4.3: The function $u(x, y) = e^{-dx} + e^{-dy}$ for $d = 20$.

The results from Figure 4.4 show that u_h^k is more accurate or equivalent to u_h^{GAL} in all cases. However, the advantage of the BPM is most clearly seen when the mesh is coarse, or the boundary layer is more prominent. In the most extreme case, with $d = 40$

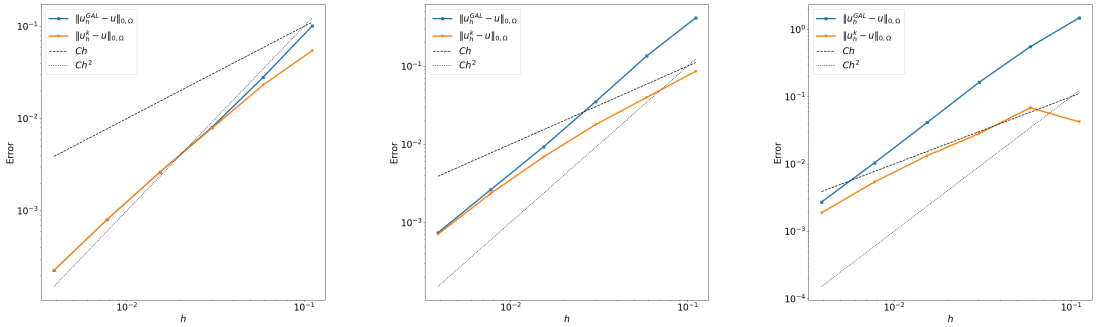

(a) $d = 10$ (b) $d = 20$ (c) $d = 40$

Figure 4.4: Comparison between $L^2(\Omega)$ errors of u_h^k and u_h^{GAL} for different values of d over a sequence of increasingly refined non-Delaunay meshes.

on the coarsest grid, u_h^k is significantly more accurate than u_h^{GAL}. The reason for this is illustrated in Figure 4.5. Since the mesh does not guarantee that the DMP holds for the Galerkin solution, we obtain undershoots in the solution. These undershoots are most significant in the coarsest mesh, where the numerical solution obtains a minimum of -3.3, and a maximum of 2, where the solution should be strictly positive. This illustrates a significant advantage of the BPM over the Galerkin solution for coarse non-Delaunay meshes, as it preserves positivity.

4.7.3 Convergence of the Non-Linear Solenoidal Induction Heating Problem

Finally, we test for convergence for the fully coupled Solenoidal Induction Heating Problem (4.1). We let the domain Ω be the unit square and we choose the exact solution (H_{ex}, u_{ex}) and the non-linear, strictly positive function $\mu(\cdot)$ to be

- $u_{ex} := \sin(\pi x)\sin(\pi y)$,
- $H_{ex} := 2 + \sin(\pi x)\sin(\pi y)$,
- $\mu(u) := u^2 + 1$.

Thus, $u_{ex}(x, y) \in (0, 1]$ for all $(x, y) \in \Omega$, so we set $k = 1$ in the BPM. Then, we create a manufactured solution by defining the source terms to be

- $f_H := -\Delta H_{ex} + i\omega\mu(u_{ex})H_{ex}$,

(a) u_h^{GAL} with $n = 9$ (b) u_h^{GAL} with $n = 17$ (c) u_h^{GAL} with $n = 65$

(d) u_h^k with $n = 9$ (e) u_h^k with $n = 17$ (f) u_h^k with $n = 65$

Figure 4.5: Visualisation of u_h^{GAL} and u_h^k for different non-Delaunay meshes for $d = 40$.

- $f_u := -\Delta u_{ex} - |\nabla H_{ex}|^2$.

The Richardson iteration in (4.39) is used to solve the heat equation (4.1c), then the coupled system (4.1) is solved using Algorithm 1. We denote the output from Algorithm 1 by $(H_h^{m^*}, u_h^{m^*})$.

Convergence results for Algorithm 1 are shown in Figure 4.6, where we tested the convergence rates over a sequence of uniform meshes and a sequence of non-Delaunay meshes, where we use non-Delaunay sequence of meshes illustrated in Figure 4.2. The results show that we have second order $L^2(\Omega)$ convergence and first order $H^1(\Omega)$ convergence in both the magnetic field H and the temperature u when using the BPM within the coupled fixed point method, regardless of the shape of the mesh. This result presents numerical evidence that the BPM could be could be used to solve the coupled system.

More detailed results about Algorithm 1 are shown in Table 4.2. We can see that the time increases because the mesh gets refined, but M stays fairly consistent, and so

Algorithm 1 A fixed-point algorithm to solve the coupled Solenoidal Induction Heating Problem.

```
Require: $\delta = 10^{-6}$, $M = 100$, $\omega_d \in (0, 1]$.
  Step 1: Find the initial guess $H_h^0 \in V_{h,\mathbb{C}}$ by solving the linear system:
      $(\nabla H_h^0, \nabla Q_h)_{\Omega,\mathbb{C}} + (i\omega H_h^0, Q_h)_{\Omega,\mathbb{C}} = (f_H, Q_h)_{\Omega,\mathbb{C}}, \qquad \forall\, Q_h \in V_{h,\mathbb{C}}.$
  Set $H_h^m = H_h^0$.
  Step 2: Find the initial guess $u_h^0 \in V_h^k$ using the Richardson iteration to solve:
      $(\nabla (u_h^0)^k, \nabla v_h)_\Omega + s((u_h^0)^{-k}, v_h) = (|\nabla H_h^m|^2 + f_u, v_h)_\Omega \qquad \forall\, v_h \in V_h.$
  Set $u_h^m = u_h^0$.
  while ($\|u_h^m - u_h^{m+1}\|_{0,\Omega} > \delta$ or $\|H_h^m - H_h^{m+1}\|_{0,\Omega,\mathbb{C}} > \delta$) and $m < M$ do
    Step 3: Find $\tilde{H}_h^m \in V_{h,\mathbb{C}}$ such that:
        $(\nabla \tilde{H}_h^m, \nabla Q_h)_{\Omega,\mathbb{C}} + (i\omega\mu(u_h^m)\tilde{H}_h^m, Q_h)_{\Omega,\mathbb{C}} = (f_H, Q_h)_{\Omega,\mathbb{C}}, \qquad \forall\, Q_h \in V_{h,\mathbb{C}}$
    Step 4: Set $H_h^{m+1} = H_h^m + \omega_d(\tilde{H}_h^m - H_h^m)$
    Step 5: Find $\tilde{u}_h^m \in V_h^k$ by using the Richardson iteration to solve:
        $(\nabla (\tilde{u}_h^m)^k, \nabla v_h)_\Omega + s((\tilde{u}_h^m)^{-k}, v_h) = (|\nabla H_h^{m+1}|^2 + f_u, v_h)_\Omega \qquad \forall\, v_h \in V_h.$
    Step 6: Set $u_h^{m+1} = u_h^m + \omega_d\,(\tilde{u}_h^m - u_h^m)$
    Step 7: Check the tolerance criteria, then set $u_h^m = u_h^{m+1}$ and $H_h^m = H_h^{m+1}$.
  end while
  return ($H_h^{m+1}$, $u_h^{m+1}$) as ($H_h^{m^*}$, $u_h^{m^*}$) .
```

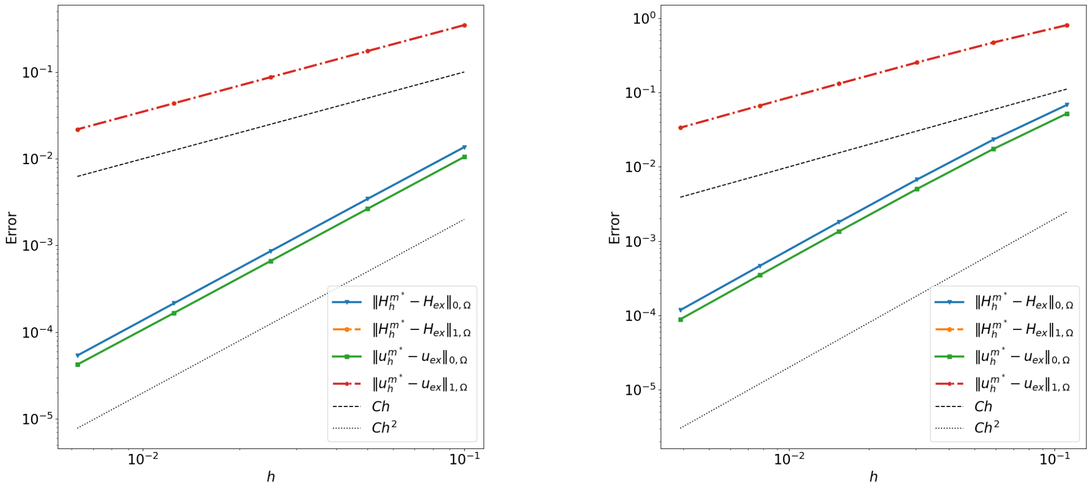

(a) Uniform meshes.

(b) Non-Delaunay meshes.

Figure 4.6: Convergence plot comparing the output of Algorithm 1 $(H_h^{m^*}, u_h^{m^*})$ to the exact solution (H_{ex}, u_{ex}) over a sequence of increasingly refined uniform meshes and also over non-Delaunay meshes. Plot contains the $L^2(\Omega)$ and $H^1(\Omega)$ errors.

do the number of Richardson iterations N in the inner BPM algorithm.

h size	N. elems	$\|u_h^{m^*} - u_{ex}\|_{0,\Omega}$	$\|H_h^{m^*} - H_{ex}\|_{0,\Omega}$	Time (s)	M	N
0.10000	200	0.010496	0.013608	0.629598	19	1
0.05000	800	0.002646	0.003440	0.766960	19	1
0.02500	3200	0.000664	0.000862	1.245891	19	1
0.01250	12800	0.000167	0.000216	3.424925	19	1
0.00625	51200	0.000042	0.000054	16.220433	19	1

Table 4.2: Results from Algorithm 1 for uniform meshes. Here M is the number of outer iterations of the fixed point method and N is the number of iterations of the inner Richardson algorithm.

4.8 Conclusions and Discussion

In this Chapter we analysed the stationary Solenoidal Induction Heating Problem with Dirichlet boundary conditions on non-convex polygonal domains. By proving that H and u were bounded in appropriate Sobolev norms, and in particular that $|\nabla H|^2$ belongs to $L^2(\Omega)$, we were able to prove, using a fixed-point argument, that a solution of (4.14) exists when Ω is non-convex. We proved that under strict conditions on the mesh, the coupled problem (H_h, u_h) converged (H, u) as $h \to 0$ when u_h is the standard Galerkin solution. We then proved that without any conditions on the mesh, the one-directional coupled system (H_h, u_h^k) converged to (H, u) as $h \to 0$ and $k \to \infty$, where u_h^k was the BPM solution of the heat equation. Moreover, we proved that for a fixed k, u_h^k converged to a projection of u onto the closed convex subset V^k. These results were verified using numerical experiments on convergence when truncating at a non-physical bound, convergence on non-Delaunay meshes with boundary layers, and convergence of the coupled system.

These results present a development from the current literature. The existence results presented in Section 4.4 extend results by Clain and Touzani (1997a) by allowing non-convex and polygonal domains. Convergence of FEMs for this problem is similarly limited to convex domains in the paper by Parietti and Rappaz (1999) for the time-dependent problem. Therefore, by applying the BPM, and removing the requirements on the mesh and on the domain, we have presented a relaxation on the requirements for convergence for the one-directional coupled problem. We would hope, in the future, to extend this to the coupled problem.

Furthermore, we proved that the solution of the BPM satisfied a variational inequality for any k in Lemma 4.6.1. This proved that u_h^k converged $\hat{u}^k$, which is a projection of u onto the closed convex subset V^k in the $H_0^1(\Omega)$ norm. We used this result to prove convergence of the simplified one-directional coupled problem, but this result might also have applications in cases not covered in this Thesis. For example, if we were interested in a problem where the physical bounds are *a-priori* unknown, or if we want to artificially constrain the solution as is often required in optimal control problems. This presents another potential useful application of the BPM.

Chapter 5

Numerical Results and Experimental Validation

5.1 Abstract

In this final Chapter, we discuss the numerical implementation of the Solenoidal model and the Axisymmetric model for realistic scenarios. We have built three different codes using FEM software `FEniCSx`: a standard Galerkin code for the Solenoidal model, a new BPM code for the Solenoidal model, and a standard Galerkin code for the Axisymmetric model. Numerical tests for all of these variants have been implemented and show convergence to manufactured and analytical solutions. The culmination of this Chapter is a comparison to experimental data and to industrial software. The results show that the implementation here produces accurate results compared to experimental data and that the BPM is more accurate over non-Delaunay meshes.

5.2 Introduction and Literature Review

First, we restate the PDEs for the Solenoidal model and the Axisymmetric model and give a brief overview of the current literature on numerical implementation of these models.

5.2.1 Solenoidal 2D Model

First, we consider the numerical approximation of the Solenoidal model. As already discussed in Chapter 3, this model is well suited to problems where we are interested in the average temperature distribution in the centre of a long workpiece with a long tightly wound coil.

To define the Solenoidal model, let Ω be an open and bounded domain in $\mathbb{R}^2$ representing a two-dimensional cross-section of the billet. Let $H : \Omega \times [0,T] \to \mathbb{C}$ denote the magnetic field strength in the billet, and let $u : \Omega \times [0,T] \to \mathbb{R}$ denote the temperature in the billet. The 2D Solenoidal model reads: find (H, u) such that

$$\begin{aligned}
-\mathrm{div}(\sigma^{-1}(u)\nabla H) + i\omega\mu(u,H)H &= 0 && \text{in } \Omega \times (0,T), && \text{(5.1a)}\\
H &= H_0 && \text{on } \partial\Omega \times (0,T), && \text{(5.1b)}\\
\rho(u)C_p(u)\frac{\partial u}{\partial t} - \mathrm{div}(\kappa(u)\nabla(u)) &= \frac{1}{2\sigma(u)}|\nabla H|^2 && \text{in } \Omega \times (0,T), && \text{(5.1c)}\\
\kappa(u)\frac{\partial u}{\partial n} + \alpha(|u|^3 u - u_{\text{amb}}^4) + \beta(u - u_{\text{amb}}) &= 0 && \text{on } \partial\Omega \times (0,T), && \text{(5.1d)}\\
u(\cdot,0) &= u_0 && \text{in } \Omega. && \text{(5.1e)}
\end{aligned}$$

Here, as introduced in Chapter 3, $\sigma(\cdot)$, $\mu(\cdot,\cdot)$, $\kappa(\cdot)$, $\rho(\cdot)$, and $C_p(\cdot)$ are strictly positive, bounded, and Lipschitz functions representing the electrical conductivity, magnetic permeability, thermal conductivity, material density, and specific heat capacity, respectively. The positive constants ω, u_{amb}, α, and β represent the angular frequency of the current, the ambient temperature, the radiation coefficient, and the convective coefficient, respectively. Note that in realistic scenarios, ω, u_{amb}, α, and β could be functions rather than constants.

In this model, (5.1a) is a complex quasi-static approximation for the magnetic field H, we have prescribed the total current data via the Dirichlet boundary condition (5.1b), and we assume that hysteresis is negligible. See Section 4.2.1 for a more detailed discussion on these assumptions.

In the literature, some numerical approximations for the Solenoidal model were implemented when (5.1a) was instead a time-dependant parabolic equation. One such approximation was implemented by Clain et al. (1993), who approximated in space using $\mathbb{P}_1$ elements and approximated in time using a Crank-Nicholson scheme. However, in order to accurately capture the magnetic frequency, very small time-steps were needed ($\Delta t \leq 10^{-6}\,\mathrm{s}$), which is an exceedingly small time-step. The authors resolved the model on two time levels for the magnetic field and the temperature to save some computational cost, but nevertheless it was prohibitively expensive.

A similar implementation was studied by Chaboudez et al. (1994), where voltage was prescribed instead of current. This was generally easier to measure but more difficult to implement in the code (see Section 3.3.1). They extended the results from Clain et al. (1993) by allowing the temperature to exceeded the Curie point. Generally, the steep discontinuity in $\mu(\cdot,\cdot)$ at Curie point causes issues with convergence in numerical schemes. To resolve this, the authors used a 'smoothed' $\mu(\cdot,\cdot)$ to help with convergence and, again, used very small time-steps. Additionally, they also used a fitting algorithm to find the optimal parameters α, β, and voltage to match the experimental data. Other authors proposed a predictor-corrector time-stepping scheme to accurately capture the model's behaviour around the Curie point (see, e.g. Massé, Morel, and Breville (1985)). It is noticeable that not many recent references are available for the Solenoidal model. This might be because, in more recent years, there has been more interest in the Axisymmetric model.

5.2.2 Axisymmetric 2D Model

The Axisymmetric model is well suited for configurations that are rotationally symmetric, and can capture temperature differences due to gaps in the coils, can resolve short billets, and can capture behaviour at corners. Therefore, it is considered more useful in industrial settings and thus attention has been given to implementing realistic axisymmetric approximations.

To define the Axisymmetric model, let $\breve{\Omega}$ be the axisymmetric domain defined in Section 3.4, with $\breve{\Omega}_0$, $\breve{\Omega}_{air}$ and $\breve{\Omega}_1, \ldots, \breve{\Omega}_m$ denoting the billet, air, and coil subdomains, respectively. Let $A : \breve{\Omega} \times [0,T] \to \mathbb{C}$ denote the magnetic potential in the whole domain, and let $u : \breve{\Omega}_0 \times [0,T] \to \mathbb{R}$ denote the temperature in the billet. Then the problem reads: find (A, u) such that, for $k = 0, \dots, m$,

$$\begin{aligned}
-\frac{\partial}{\partial r}\left(\frac{1}{\mu(u,A,r,z)r}\frac{\partial(rA)}{\partial r}\right) - \frac{\partial}{\partial z}\left(\frac{1}{\mu(u,A,r,z)}\frac{\partial A}{\partial z}\right) & \\
+ i\omega\sigma(u,r,z)A &= \frac{\sigma(u,r,z)}{r}C_k && \text{in } \breve{\Omega}_k \times (0,T), && (5.2a) \\
\frac{\partial}{\partial r}\left(\frac{1}{\mu(u,A,r,z)r}\frac{\partial(rA)}{\partial r}\right) + \frac{\partial}{\partial z}\left(\frac{1}{\mu(u,A,r,z)}\frac{\partial A}{\partial z}\right) &= 0 && \text{in } \breve{\Omega}_{air} \times (0,T), && (5.2b) \\
\frac{\partial(rA)}{\partial r} + A &= 0 && \text{on } \breve{\Gamma}^a_r \times (0,T), && (5.2c) \\
\frac{\partial(rA)}{\partial z} &= 0 && \text{on } \Gamma^a_n \times (0,T), && (5.2d) \\
A &= 0 && \text{on } \breve{\Gamma}^a_d \times (0,T), && (5.2e) \\
\rho(u)C_p(u)\frac{\partial u}{\partial t} - \frac{1}{r}\frac{\partial}{\partial r}\left(r\kappa(u)\frac{\partial(ru)}{\partial r}\right) - \frac{\partial}{\partial z}\left(\kappa(u)\frac{\partial u}{\partial z}\right) &= \frac{\omega\sigma(u)|A|^2}{2}, && \text{in } \breve{\Omega}_0 \times (0,T), && (5.2f) \\
\kappa(u)\frac{\partial u}{\partial n} + \alpha(|u|^3 u - u^4_{\text{amb}}) + \beta(u - u_{\text{amb}}) &= 0 && \text{on } \breve{\Gamma}^u_r \times (0,T), && (5.2g) \\
\kappa(u)\frac{\partial u}{\partial n} &= 0 && \text{on } \breve{\Gamma}^n_r \times (0,T), && (5.2h) \\
u(\cdot, 0) &= u_0 && \text{in } \breve{\Omega}_0. && (5.2i)
\end{aligned}$$

The material properties $\kappa(\cdot), \rho(\cdot)$, and $C_p(\cdot)$ are the thermal conductivity, material density, and specific heat capacity and, since these material properties are defined in the billet domain only, they are exactly the same as the Solenoidal model. The material properties $\mu(\cdot,\cdot,\cdot,\cdot)$ and $\sigma(\cdot,\cdot,\cdot)$ are the magnetic permeability and electrical conductivity and are defined over the whole domain. Therefore, these functions depend on (r, z).

Using a prescribed voltage, Chaboudez et al. (1997) built an axisymmetric approximation for (5.2). They showed that for a non-ferromagnetic material (i.e. when $\mu(\cdot,\cdot,\cdot,\cdot)$ is a constant in each domain), a finite element approximation with an implicit time-scheme could produce result that were within an acceptable tolerance of experimental data.

As with the Solenoidal model, we could also use a time-dependent parabolic approximation for A. This was done so by Fisk et al. (2022), where, similar to Clain et al. (1993), they used two different time scales for the magnetic potential and the temperature. A similar case was studied by Drobenko, Hachkevych, and Kournyts'kyi (2007), where displacement currents were not neglected and a time-dependent parabolic equation was used to solve a magnetic field vector equation.

The model (5.2) has also been extended to include more realistic physical effects. For example, Bay et al. (2003) solved an time-dependent parabolic problem in an axisymmetric domain, and included mechanical thermal effects (i.e. heat expansion), and a moving domain. They also included non-linear effects of μ, although the experiments stayed below the Curie point.

The numerical model by Chaboudez et al. (1997) was extended by Bermúdez et al. (2007b) to allow a phase change within the magnetic material which was held by a crucible. This phase change is important in induction heating applications where melting plays a key role, for example, in silicone purification. This work was extended by Bermúdez et al. (2009) to include a coupling with a hydrodynamic model to account for melting and mixing due to Lorentz forces generated within the molten material. This was extended further by Bermúdez et al. (2011), where they included a non-local radiation boundary condition from non-convex domains, and also allowed the possibility of a moving mesh.

An alternative method to solve the Axisymmetric model is to use a hybrid method that uses the Boundary Element Method (BEM) and the FEM. This method involves solving the PDEs on the boundary of the domain instead of over the whole domain. This method was implemented for the axisymmetric model by Bermúdez et al. (2007a), where they used a setup with a crucible and a phase change like in Bermúdez et al. (2007b). They argued that the absence of a mesh makes an extension to moving conductors more feasible, however, they found that the CPU time for this method was several orders of magnitude larger than an equivalent FEM that produced the same results. The mixed BEM/FEM method was also implemented for the 3D case by Wanser, Krahendbuhl, and Nicolas (1994), where they also found it to be prohibitively expensive. The BEM formulation, including hysteresis and a model for the microstructure of the ferromagnetic material, was studied by Rappaz and Świerkosz (1996), which they showed produced accurate results but led to multi-dimensional singular integrals and was extremely challenging to evaluate numerically. For these reasons, we choose to use a full FEM in our code.

In this Chapter, we describe, implement, and discuss results for the FEM code for the Solenoidal model and the Axisymmetric model. For the Solenoidal model we implement the BPM, which we proved in Chapter 4 is well-posed in convex domains and for non-Delaunay meshes. We compare the results from the codes to experimental data and an industrial software, and then show that the BPM produces more accurate results over non-Delaunay meshes.

5.3 Solenoidal Model

In order to define the FEM for the Solenoidal model we need to put (5.1) into its weak formulation. However, as discussed in detail in Section 3.3.3, taking the weak form of (5.1) in standard Sobolev spaces leads to an ill-posed problem. Therefore, we build our numerical scheme from the following weak form, restated from Section 3.3.3 for convenience, where we assume that all functions are 'regular enough' to make it well-defined:

Problem. Let u_0 be a sufficiently regular initial temperature, and let $[0,T] \subset \mathbb{R}$ be a time interval. The problem reads: find (H,u) 'regular enough' such that $\tilde{H} = H - H_\circ$, $\tilde{H}|_{\partial\Omega} = 0$ and for all $t \in (0,T)$,

$$(\sigma^{-1}(u)\nabla\tilde{H}, \nabla Q)_{\Omega,\mathbb{C}} + (i\omega\mu(u,|H|)\tilde{H}, Q)_{\Omega,\mathbb{C}} = (i\omega\mu(u,|H|)H_\circ, Q)_{\Omega,\mathbb{C}}, \tag{5.3a}$$

and

$$\begin{aligned}(\rho(u)C_p(u)u_t, v)_\Omega + (\kappa(u)\nabla u, \nabla v)_\Omega + \left(\alpha|u|^3u + \beta u, v\right)_{\partial\Omega} \\ = \left(\frac{|\nabla H|^2}{2\sigma(u)}, v\right)_\Omega + \left(\alpha u_{\text{amb}}^4 + \beta u_{\text{amb}}, v\right)_{\partial\Omega},\end{aligned} \tag{5.3b}$$

and

$$(u(0), z)_\Omega = (u_0, z)_\Omega, \tag{5.3c}$$

for all (Q,v) and z 'regular enough'.

Note that (5.3a) and (5.3b) are both non-linear equations, thus an iterative algorithm is needed to solve (5.3a) and (5.3b).

5.3.1 Total Current Data

We assume that the current going through the coil of wire is a given data. If this is known, then it is straightforward to incorporate this data into the Solenoidal model via the boundary condition for the magnetic field $H_\circ$. We find $H_\circ$ by calculating

$$H_\circ = \frac{nI}{L},$$

where n is the number of turns in the coil and L is the working length of the coil. In practice, it is difficult to measure the current I, as it requires breaking the circuit to measure the current flow. For this reason, in the experiments we use an Rogowski coil to calculate the voltage and frequency of the current, and manually calculate the current from this data. See Appendix A.2 for an example of this calculation. Another option is to use the voltage as the data in the weak formulation, but this is more difficult to implement numerically (see Section 3.3.1 for more details). For this reason, we choose to use the total current model.

5.3.2 Discretisation

Here we describe the FEM used to solve the Induction Heating Problem. We define two different methods to solve the heat equation: the standard Galerkin method and the BPM.

Let V_h be the piecewise linear real finite element space over Ω as defined in (2.15), and $V_{h,\mathbb{C}}$ be the piecewise linear complex finite element space over Ω as defined in (2.16). Let the time interval be $I = [0, T]$. We subdivide the time interval into N partitions $0 = t_0 < t_1 < ... < t_N = T$, denoting the subintervals $I_n := (t_{n-1}, t_n]$. Here we assume that the partition is uniform, that is we assume that $t_n - t_{n-1} = \Delta t$ for all n, where $n = 1, \ldots, N$. Define the function space

$$\begin{aligned} X_h := &\{\mathcal{Q}(x,t) : \forall\, n, \exists Q_h \in V_{h,\mathbb{C}} : \mathcal{Q}(\cdot,t) = Q_h, t \in I_n\} \\ &\times \{\boldsymbol{v}(x,t) : \forall\, n, \exists v_h \in W_h : \boldsymbol{v}(\cdot,t) = v_h, t \in I_n\}. \end{aligned}$$

This means that on each time interval X_h is equivalent to $V_{h,\mathbb{C}} \times V_h$. Indeed, X_h is piecewise constant in time and hence discontinuous. Let $H_h^n := H_h(t_n)$ and $u_h^n := u_h(t_n)$. Using this finite element space, we propose the following implicit-explicit (IMEX) scheme for the Solenoidal model. We elect to use this scheme because it is cheaper, faster and more accurate than a fully implicit one. First, we propose iterative schemes to solve the non-linear equations (5.3a) and (5.3b).

Magnetic Field Discretisation

We use a fixed-point iteration to solve the magnetic field equation, as detailed in Algorithm 1 below.

Algorithm 1 (Non-Linear Magnetic Field). Let u_h^{n-1} and H_h^{n-1} be given. Set $H_h^i = H_h^{n-1}$. Set $\omega_d \in (0,1]$ and set `tol` to be the error tolerance. Then the algorithm reads:

1. Find $\hat{H}_h$ such that $\hat{H}_h - \tilde{H}_h = H_\circ$, $\tilde{H}_h \in V_{h,\mathbb{C}}$ and

$$(\sigma^{-1}(u_h^{n-1})\nabla \tilde{H}_h, \nabla Q_h)_{\Omega,\mathbb{C}} + (i\omega\mu(u_h^{n-1}, H_h^i)\tilde{H}_h, Q_h)_{\Omega,\mathbb{C}} = (i\omega\mu(u_h^{n-1}, H_h^i)\tilde{H}_h, Q_h)_{\Omega,\mathbb{C}} \quad (5.4)$$

   for all $Q_h \in V_{h,\mathbb{C}}$.

2. Calculate $H_h^{i+1} = H_h^i + \omega_d(\tilde{H}_h - H_h^i)$.

3. Repeat steps 1-2 until $\|H_h^i - H_h^{i+1}\|_{0,\Omega,\mathbb{C}} \leq$ `tol`.

If $\mu(\cdot,\cdot)$ does not depend on H, then (5.4) becomes a linear equation, and thus can be solved with one iteration.

Temperature Discretisation with Standard Galerkin

We also use a fixed-point method to solve the temperature equation using the standard Galerkin method, detailed below in Algorithm 2.

Algorithm 2 (Non-Linear Temperature). Let u_h^{n-1} and H_h^n be fixed and known, set $\omega_d \in (0,1]$ and set `tol` to be the error tolerance. Set $u_h^i = u_h^{n-1}$. The algorithm reads:

1. Find $\tilde{u}_h \in W_h$ such that

$$\begin{aligned}\left(\rho(u_h^{n-1})C_p(u_h^{n-1})\tilde{u}_h, v_h\right)_\Omega + \Delta t\left(\kappa(u_h^i)\nabla\tilde{u}_h, \nabla v_h\right)_\Omega \\ + \Delta t\left(\alpha|u_h^i|^3\tilde{u}_h + \beta\tilde{u}_h, v_h\right)_{\partial\Omega} \\ = \left(\rho(u_h^{n-1})C_p(u_h^{n-1})u_h^{n-1}, v_h\right)_\Omega + \Delta t\left(\frac{|\nabla H_h^n|^2}{2\sigma(u_h^{n-1})}, v_h\right)_\Omega \\ + \Delta t\left(\alpha u_{\text{amb}}^4 + \beta u_{\text{amb}}, v_h\right)_{\partial\Omega},\end{aligned} \tag{5.5}$$

   for all $v_h \in W_h$.

2. Calculate $u_h^{i+1} = u_h^i + \omega_d(\tilde{u}_h - u_h^i)$.

3. Repeat steps 1-2 until $\|u_h^i - u_h^{i+1}\|_{0,\Omega} \leq \texttt{tol}$. Return $u_h^n := u_h^{i+1}$ as the solution.

We have elected to use the fixed-point method and a Backward Euler (BE) method since we have multiple non-linear terms.

Temperature Discretisation with BPM

In this Section we describe the algorithm that solves the time-dependent heat equation using the BPM. To define this, we first need to write a different discrete problem for the heat equation. First, recall that for a function $v_h \in W_h$, we define $(v_h)^k \in W_h^k$ to be

$$(v_h)^k := \sum_{i=1}^{M} \max\{0, \min\{v_h(\boldsymbol{x}_i), k\}\},$$

and $v_h^{-k} = v_h - (v_h)^k$. Given u_h^{n-1}, we solve the problem: find $u_h^n \in W_h$ such that

$$\begin{aligned}\left(\rho(u_h^{n-1})C_p(u_h^{n-1})\frac{(u_h^n)^k - u_h^{n-1}}{\Delta t}, v_h\right)_\Omega + \Big(\kappa((u_h^n)^k)\nabla(u_h^n)^k, \nabla v_h\Big)_\Omega \\ + \Big(\alpha|u_h^n|^3(u_h^n)^k + \beta(u_h^n)^k, v_h\Big)_{\partial\Omega} \\ + s((u_h^n)^{-k}, v_h) = \left(\frac{1}{2\sigma(u_h^{n-1})}|\nabla H_h^n|^2, v_h\right)_\Omega + \left(\alpha u_{\text{amb}}^4 + \beta u_{\text{amb}}, v_h\right)_{\partial\Omega}\end{aligned} \tag{5.6}$$

for all $v_h \in W_h$. We take $(u_h^n)^k$ as the solution for the problem. Here, k is chosen to be appropriately high, and will be explicitly stated in the examples of applications of the BPM that follow in this Chapter.

Following the work by Amiri, Barrenechea, and Pryer (2025), we adapt the BPM presented in Section 2.6 for a time-dependent problem. We define the stabilised mass-lumping term $s(\cdot,\cdot)$ as

$$s(v_h, w_h) := \alpha \sum_{i=1}^{N} \left(\|\kappa\|_{0,\infty,\omega_i} + \frac{\mathfrak{h}(\boldsymbol{x}_i)^2}{\Delta t} \right) v_h(\boldsymbol{x}_i) w_h(\boldsymbol{x}_i).$$

Since (5.6) is non-linear we use a modified Richardson iteration to solve for u_h^n. We follow the approach by Amiri, Barrenechea, and Pryer (2025), and design the algorithm to solve (5.6) as the following.

Algorithm 3 (BPM temperature). Let u_h^{n-1} and H_h^n be known and fixed. Choose $\omega_d \in (0,1]$ and set `tol` to be the error tolerance. Initialise the algorithm with $u_h^i = u_h^n$. Then the algorithm reads:

1. Find $u_h^{i+1} \in W_h$ such that

$$\begin{aligned}
&(\rho(u_h^{n-1})C_p(u_h^{n-1})u_h^{i+1}, v_h)_\Omega + \Delta t(\kappa(u_h^i)\nabla u_h^{i+1}, \nabla v_h)_\Omega + \Delta t(\alpha|u_h^i|^3 u_h^{i+1} + \beta u_h^{i+1}, v_h)_{\partial\Omega} \\
&= (\rho(u_h^{n-1})C_p(u_h^{n-1})u_h^{i}, v_h)_\Omega + \Delta t(\kappa(u_h^i)\nabla u_h^{i}, \nabla v_h)_\Omega + \Delta t(\alpha|u_h^i|^3 u_h^{i} + \beta u_h^{i}, v_h)_{\partial\Omega} \\
&\quad + \omega_d \Big(F^n(v_h) - \Big[(\rho(u_h^{n-1})C_p(u_h^{n-1})(u_h^i)^k, v_h)_\Omega + \Delta t(\kappa(u_h^i)\nabla (u_h^i)^k, \nabla v_h)_\Omega \\
&\qquad + \Delta t(\alpha|u_h^i|^3 (u_h^i)^k + \beta (u_h^i)^k, v_h)_{\partial\Omega} + \Delta t s((u_h^i)^{-k}, v_h) \Big] \Big), \qquad (5.7)
\end{aligned}$$

   where

$$\begin{aligned}
F^n(v_h) &= \big(\rho(u_h^{n-1})C_p(u_h^{n-1})u_h^{n-1}, v_h\big)_\Omega \\
&\quad + \left(\frac{|\nabla H_h^n|^2}{2\sigma(u_h^{n-1})}, v_h \right)_\Omega + \big(\alpha u_{\mathrm{amb}}^4 + \beta u_{\mathrm{amb}}, v_h\big)_{\partial\Omega}. \qquad (5.8)
\end{aligned}$$

2. Repeat step 1 until $\|u_h^i - u_h^{i+1}\|_{0,\Omega} \leq \texttt{tol}$.

3. Return $u_h^n := (u_h^{i+1})^k$ as the solution.

In cases where the mesh satisfies the appropriate conditions, then the Galerkin method provides a solution that respects the bounds of the problem, thanks to the DMP. In such a case, the BPM stops after one iteration and both methods coincide.

Coupled loop

Finally, we define a coupled loop that gives us a solution (H_h, u_h) that numerically solves (5.3) within a given tolerance.

Algorithm 4 (Coupled Galerkin/BPM). Let u_h^0 and H_h^0 be given, and set $u_h^j = u_h^{n-1}$ and $H_h^j = H_h^{n-1}$. Set $\omega_d \in (0,1]$ and set `tol` to be the error tolerance. For every $n = 1, \dots, N$:

1. Using H_h^j and u_h^j find H_h^{i+1} using Algorithm 1.
2. Using H_h^{j+1} and u_h^j find u_h^{i+1} using Algorithm 2 or 3, accordingly.
3. Repeat 1-2 until $\|H_h^{j+1} - H_h^j\|_{0,\Omega,\mathbb{C}} \leq \texttt{tol}$ and $\|u_h^{j+1} - u_h^j\|_{0,\Omega} \leq \texttt{tol}$.
4. Return the solutions as H_h^n and u_h^n.

The final solution is $(H_h, u_h) \in X_h$ where on every time interval $H_h(t_n) = H_h^n$ and $u_h(t_n) = u_h^n$.

We choose to implement an adaptive scheme that takes into account changes in material properties. On one hand, if changes in the material properties only incur a small change in H, Algorithm 4 can be skipped as the right-hand side of (5.3b) does not significantly change. On the other hand, near the start of the induction heating process, the temperature changes significantly in a short space of time, and near the Curie point the material properties are very sensitive to small changes in temperature. Thus, we only invoke the coupled algorithm (Algorithm 4) if the change in the material properties is large enough. More specifically, for a given p percentage, we invoke Algorithm 4 if

$$\frac{|\sigma(u_h^n(\boldsymbol{x}_i)) - \sigma(u_h^{n-1}(\boldsymbol{x}_i))|}{\sigma(u_h^{n-1}(\boldsymbol{x}_i))} > p\% \quad \text{or}$$

$$\frac{|\mu(u_h^n(\boldsymbol{x}_i), H_h^n(\boldsymbol{x}_i)) - \mu(u_h^{n-1}(\boldsymbol{x}_i), H_h^{n-1}(\boldsymbol{x}_i))|}{\mu(u_h^{n-1}(\boldsymbol{x}_i), H_h^{n-1}(\boldsymbol{x}_i))} > p\%$$

for all nodes $\boldsymbol{x}_i$.

A flowchart of the algorithm is shown in Figure 5.1.

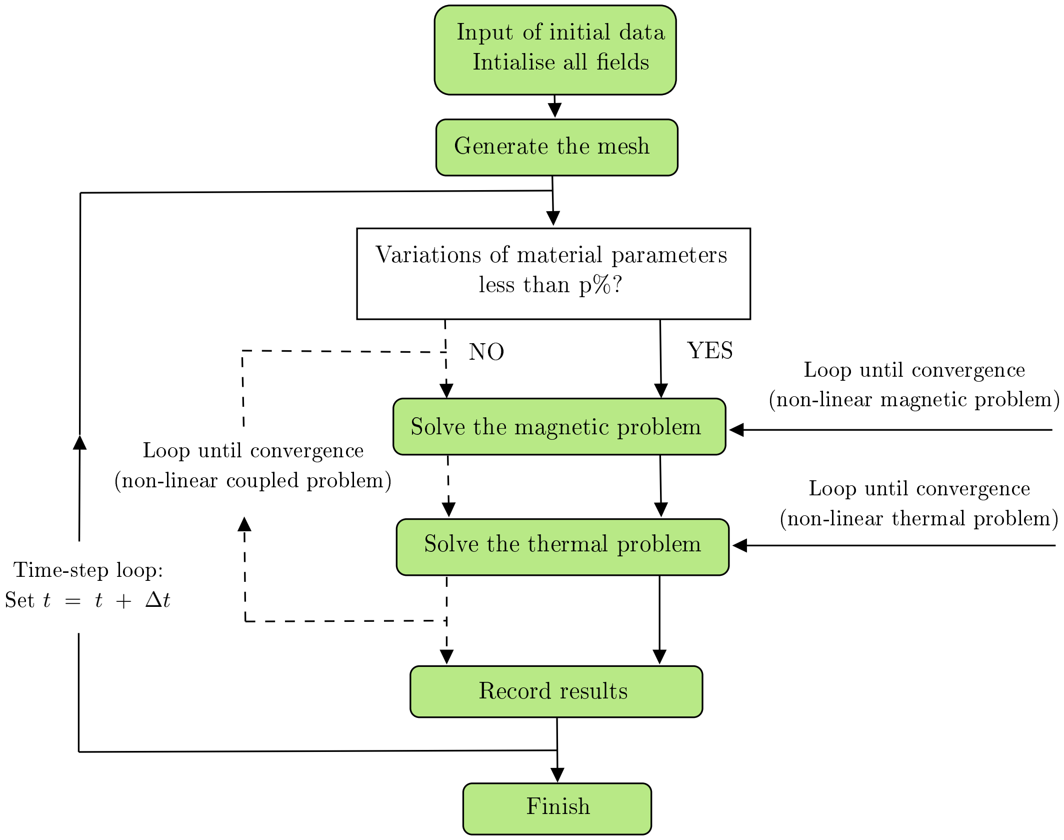

Figure 5.1: Flowchart of algorithm for the Solenoidal model.

It is worth highlighting that in order to accurately capture the skin-effect, in the majority of numerical models, an anisotropic mesh is used to conserve the number of elements needed. Now, if the domain is not rectangular or circular, imposing an anisotropic mesh can generate non-Delaunay elements, which we have seen can cause problems with the accuracy of the standard Galerkin FEM. We propose that one solution to this problem is to use the BPM, which we will explicitly show is more accurate than the standard Galerkin FEM under these mesh conditions in Section 5.6, and discuss a realistic setting with non-Delaunay meshes in Section 5.8. An alternative method to resolve this problem could be to implement an adaptive mesh algorithm on a standard Delaunay meshes. This would still require an extremely refined mesh around the boundary when the skin-effect is most severe, but an adaptive mesh could help to minimise the cost.

5.4 Axisymmetric Model

In this Section we discuss the numerical implementation of the Axisymmetric model (5.2). For reasons we discuss later, we set $\mu(\cdot,\cdot,\cdot)$ to only depend on u, r, and z, so that it does not depend on A. The weak formulation is as follows, restated from Section 3.4.3 for convenience:

Problem. Given constants $C_k \in \mathbb{C}$, an initial condition $u_0 \in L^2_r(\Omega)$, and a time interval $[0,T] \subset \mathbb{R}$, find $(A,u) \in L^2([0,T];\tilde{H}^1_r(\Omega;\mathbb{C})) \times L^2([0,T];\tilde{H}^1_r(\Omega) \cap L^5(\breve{\Gamma}^u_r))$ such that $A = 0$ on Γ^a_d and for all $t \in (0,T]$:

$$\begin{aligned}\int_{\breve{\Omega}} \left(\frac{1}{\mu(u,r,z)r} \frac{\partial(rA)}{\partial r} \frac{1}{r} \frac{\partial(r\overline{Q})}{\partial r} + \frac{1}{\mu(u,r,z)} \frac{\partial A}{\partial z} \frac{\partial \overline{Q}}{\partial z} \right) r \,\mathrm{d}r \,\mathrm{d}z \\ + \int_{\breve{\Omega}} i\omega\sigma(u,r,z) A\overline{Q}\, r \,\mathrm{d}r \,\mathrm{d}z + \int_{\breve{\Gamma}^a_r} \frac{1}{\mu(u,r,z)} A\overline{Q} \,\mathrm{d}z \\ = \sum_{k=1}^{m} \int_{\breve{\Omega}_k} \sigma(u,r,z) C_k \overline{Q} z \,\mathrm{d}r \,\mathrm{d}z,\end{aligned} \tag{5.9a}$$

for all $Q \in \tilde{H}^1_r(\Omega;\mathbb{C})$, and

$$\begin{aligned}\int_{\breve{\Omega}_0} \rho(u) C_p(u) \frac{\partial u}{\partial t} v\, r \,\mathrm{d}r \,\mathrm{d}z + \int_{\breve{\Omega}_0} \kappa(u) \nabla u \cdot \nabla v\, r \,\mathrm{d}r \,\mathrm{d}z + \int_{\breve{\Gamma}^u_r} (\alpha |u|^3 u + \beta u) v\, r \,\mathrm{d}z \\ = \int_{\breve{\Omega}_0} \frac{|\omega\sigma(u)A|^2}{2\sigma(u)} v\, r \,\mathrm{d}r \,\mathrm{d}z + \int_{\breve{\Gamma}^u_r} (\alpha u^4_{\mathrm{amb}} + \beta u_{\mathrm{amb}}) v\, r \,\mathrm{d}z \quad (5.9\mathrm{b}) \\ \int_{\breve{\Omega}_0} u(0) w\, r \,\mathrm{d}r \,\mathrm{d}z = \int_{\breve{\Omega}_0} u_0 w\, r \,\mathrm{d}r \,\mathrm{d}z\end{aligned}$$

for all $v \in \tilde{H}^1_r(\Omega) \cap L^5(\breve{\Gamma}^u_r)$ and $w \in L^2_r(\Omega)$.

The different subdomains consisting of the billet, the coils, and the air are distinguished in the model by the functions $\sigma(\cdot,\cdot,\cdot)$ and $\mu(\cdot,\cdot,\cdot)$, which vary over the domain $\breve{\Omega}$.

5.4.1 Total Current Data

In order for (5.9) to be physically meaningful we need to prescribe the state of the current flowing through the wire into the variational form. In this case, as in the Solenoidal model, we assume that we know the current intensity, rather than the voltage, as this is slightly more straightforward to include into the model.

The current data is incorporated in the model via the constants C_k, which can be thought of as Lagrange multipliers. The idea is to make the computed current intensities coincide with the prescribed ones. To compute the constants C_k, we use the same method as Bermúdez et al. (2007b), who cite Klein and Philip (2002). The method to compute these constants is shown in Algorithm 5 below.

Algorithm 5 (Calculating the constants (C_k)). Set $C_k = \delta_{i,k}$.

1. Set $C_0 = 0$ (in the conductor).
2. For every $i = 1, \ldots, k$ (iterate over the coils):
    (a) Set $C_i = \delta_{ik}$, $k = 1, \ldots, m$.
    (b) Solve equation (5.3a) to obtain A^i.
    (c) Compute
    $$\tilde{I}_k^i = \int_{\Omega_k} \sigma \left(\frac{C_k}{r} - i\omega A^j \right) drdz, \qquad k = 1, \ldots, m,$$
3. Compute the constants C_k as the solution of the linear system
    $$\sum_{i=1}^{m} \tilde{I}_k^i C_i = I_k, \qquad k = 1, \ldots, m.$$
    where I_k is the intensity going through the connected component Ω_k.
4. Compute A by solving (5.3a) with these constants C_k.

We also introduce a scale factor to the Lagrange multiplier constants C_k in order for the model to accurately match the experiments (similar to work by Chaboudez et al. (1997)).

5.4.2 Discretisation

Similar to the Solenoidal model, we use a Backward Euler method to discretise in time. We denote by $\breve{V}_{h,\mathbb{C}}$ and $\breve{V}_h$ the complex and real piecewise linear polynomial spaces over

$\breve{\Omega}$, respectively, and by $V_{h,\mathbb{C}}$ and V_h the complex and real piecewise linear polynomial spaces over $\breve{\Omega}_0$, respectively.

We define $A_d := A|_{\Gamma_r^u}$. This will be the Dirichlet boundary condition for the magnetic potential. For the heat equation we solve the problem in $\breve{\Omega}_0$. We define the function space

$$\begin{aligned}\breve{X}_h := \{&\mathcal{Q}(x,t) : \forall\, n, \exists Q_h \in \breve{V}_{h,\mathbb{C}} : \mathcal{Q}(\cdot,t) = Q_h, t \in I_n\}\\ &\times \{\boldsymbol{v}(x,t) : \forall\, n, \exists v_h \in \breve{V}_h : \boldsymbol{v}(\cdot,t) = v_h, t \in I_n\},\end{aligned}$$

where I_n is the same temporal discretisation as in the Solenoidal Section. The discrete formulation is as follows:

Problem. Given complex constants C_k, $k = 1, \dots, m$, and an initial magnetic potential A_h^0 and initial temperature u_h^0, find a pair $(A_h^n, u_h^n) \in X_h$ such that $A_h^n = 0$ on Γ_d^a, $A_h^n = A_d$ on Γ_r^a, and for $n = 1, \dots N$,

$$\begin{aligned}\int_{\breve{\Omega}} \left(\frac{1}{\mu(u_h^{n-1}, r, z) r} \frac{\partial (r A_h^n)}{\partial r} \frac{1}{r} \frac{\partial (r \overline{Q}_h)}{\partial r} + \frac{1}{\mu(u_h^{n-1}, r, z)} \frac{\partial A_h^n}{\partial z} \frac{\partial \overline{Q}_h}{\partial z} \right) r \, \mathrm{d}r \, \mathrm{d}z&\\ + \int_{\breve{\Omega}} i\omega\sigma(u_h^{n-1}, r, z) A_h^n \overline{Q}_h \, r \, \mathrm{d}r \, \mathrm{d}z + \int_{\breve{\Gamma}_r^a} \frac{1}{\mu(u_h^{n-1}, r, z)} A_h^n \overline{Q}_h \, \mathrm{d}z&\\ = \sum_{k=1}^{m} \int_{\breve{\Omega}_k} \sigma(u_h^{n-1}, r, z) C_k \overline{Q}_h \, \mathrm{d}r \, \mathrm{d}z&\end{aligned} \tag{5.10}$$

and

$$\begin{aligned}\int_{\breve{\Omega}_0} \rho(u_h^{n-1}) C_p(u_h^{n-1}) \frac{u_h^n - u_h^{n-1}}{\Delta t} v_h \, r \, \mathrm{d}r \, \mathrm{d}z + \int_{\breve{\Omega}_0} \kappa(u_h^n) \nabla u_h^n \cdot \nabla v_h \, r \, \mathrm{d}r \, \mathrm{d}z&\\ + \int_{\breve{\Gamma}_r^u} (\alpha |u_h^{n-1}|^3 u_h^n + \beta u_h^n) v_h \, r \, \mathrm{d}z = \int_{\breve{\Omega}_0} \frac{1}{2} \omega \sigma(u_h^{n-1}) |A_h^n|^2 v_h \, r \, \mathrm{d}r \, \mathrm{d}z&\\ + \int_{\breve{\Gamma}_r^u} (\alpha u_{\mathrm{amb}}^4 + \beta u_{\mathrm{amb}}) v \, r \, \mathrm{d}z&\end{aligned} \tag{5.11}$$

for all $(Q_h, v_h) \in \breve{V}_{h,\mathbb{C}} \times V_h$.

Since (5.10) is linear in A_h^n, it can be solved directly. The temperature equation

(5.11) is non-linear and hence it is solved using Algorithm 6, detailed below.

Algorithm 6 (Non-Linear Temperature). Let u_h^{n-1} and A_h^n be fixed and known, set $\omega_d \in (0,1]$ and set `tol` to be the error tolerance. Set $u_h^i = u_h^{n-1}$. The algorithm reads:

1. Find $\tilde{u}_h \in \breve{V}_h$ such that

$$\begin{aligned}\int_{\breve{\Omega}_0} \rho(u_h^{n-1})C_p(u_h^{n-1})\tilde{u}_h v_h \, r \,\mathrm{d}r\,\mathrm{d}z + \Delta t \int_{\breve{\Omega}_0} \kappa(u_h^i)\nabla\tilde{u}_h \cdot \nabla v_h \, r\,\mathrm{d}r\,\mathrm{d}z \\ + \Delta t \int_{\breve{\Gamma}_r^u} (\alpha|u_h^i|^3\tilde{u}_h + \beta\tilde{u_h})v_h \, r\,\mathrm{d}z = \int_{\breve{\Omega}_0} \rho(u_h^{n-1})C_p(u_h^{n-1})u_h^{n-1}v_h \, r\,\mathrm{d}r\,\mathrm{d}z \\ + \Delta t \int_{\breve{\Omega}_0} \frac{1}{2}\sigma(u_h^{n-1})|A_h^n|^2 v_h \, r\,\mathrm{d}r\,\mathrm{d}z + \Delta t \int_{\breve{\Gamma}_r^u} (\alpha u_{\mathrm{amb}}^4 + \beta u_{\mathrm{amb}})v_h \, r\,\mathrm{d}z, \quad (5.12)\end{aligned}$$

   for all $v_h \in \breve{V}_h$.

2. Calculate $u_h^{i+1} = u_h^i + \omega_d(\tilde{u}_h - u_h^i)$.
3. Repeat steps 1-2 until $\|u_h^i - u_h^{i+1}\|_{0,\breve{\Omega}_0} \leq$ `tol`.
4. Return $u_h^n := u_h^{i+1}$ as the solution.

Then the coupled algorithm is shown in Algorithm 7.

Algorithm 7 (Axisymmetric Coupled Galerkin). Let u_h^0 and A_h^0 be given, and set $u_h^j = u_h^{n-1}$ and $A_h^j = A_h^{n-1}$. Set $\omega_d \in (0,1]$ and set `tol` to be the error tolerance. For every $n = 1, \ldots, N$:

1. Find A_h^n by directly solving (5.10).
2. Using A_h^{j+1} and u_h^j find u_h^{i+1} using Algorithm 6.
3. Repeat 1-2 until $\|A_h^{j+1} - A_h^j\|_{0,\Omega,\mathbb{C}} \leq$ `tol` and $\|u_h^{j+1} - u_h^j\|_{0,\Omega} \leq$ `tol`.
4. Return the solutions as A_h^n and u_h^n.

The final solution is $(A_h, u_h) \in \breve{X}_h$ where on every time interval $A_h(t_n) = A_h^n$ and $u_h(t_n) = u_h^n$.

A flowchart of the algorithm is shown in Figure 5.2. Note that similar to the Solenoidal code, we also implement a method that is adaptive with the material properties.

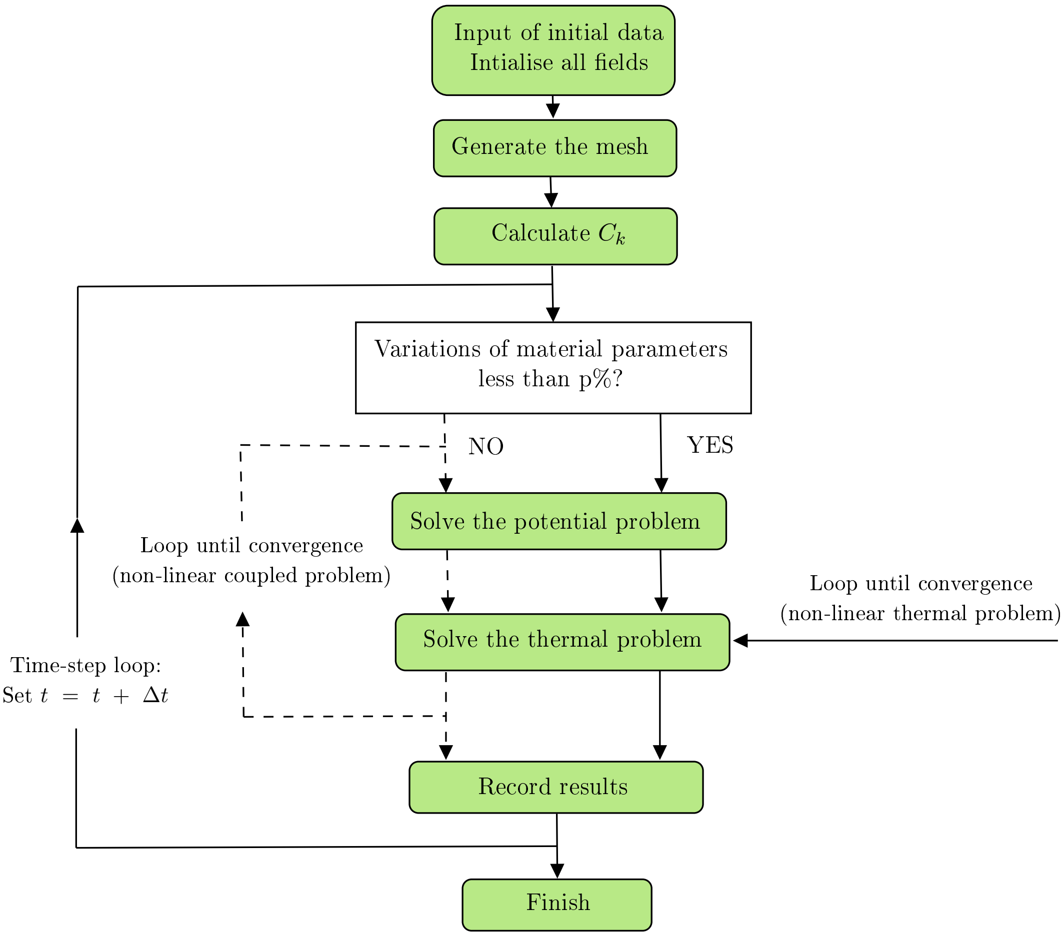

Figure 5.2: Flowchart algorithm for the Axisymmetric model.

5.5 Numerical Implementation with `FEniCSx`

We have chosen to build the code using the open-source computing platform `FEniCSx` (Baratta et al. 2023; Scroggs et al. 2022b; Scroggs et al. 2022a; Alnaes et al. 2014) as it offers a high-level `Python` interface to write efficient FEM code. `FEniCSx` consists of four core internal components, which are: the overarching `Python`/`C++` finite element package `DOLFINx`; `UFL` (Unified Form Language), the language for writing variational forms; `FFCx` (`FEniCSx` Form Compiler), an intermediary code translating `UFL` forms into `C` code; and `Basix`, a library for evaluating finite element basis functions. `FEniCSx` also natively supports geometry and mesh generations through the open source library `GMSH` (Geuzaine and Remacle 2009) through `GMSH`'s `Python` API, which is used to generate the geometries and meshes in this project. It also provides an interface for `PETSc` (Abhyankar et al. 2020; Abhyankar et al. 2021; Balay et al. 1997) via `petsc4py` (Dalcin et al. 2011), which is a suite of linear algebra structures and solvers.

The `UFL` package used in `FEniCSx` is a language for defining discrete variational formulations that are similar to the pen-and-paper notation. This way, the user has full control over the variational form, function spaces, and solver methods used in the code. A snippet of the code written for Algorithm 2 is shown in Listing 5.1, which illustrates the `FEniCSx` code with the `UFL`.

Listing 5.1: Example section of `FEniCSx` code solving one time-step of the heat equation. Note that this has been slightly modified for clarity as in the code this is a method in the TemperatureSolver `Python` Class.

```python
V = functionspace(domain, ("CG", 1)) # P1 Continuous Galerkin
u_k = Function(V, name="u_k")  # new function
u_k.x.array[:] = u_old.x.array # dofs equal to previous timestep
u_kplus = Function(V, name="u_kplus") # new function

max_iterations = 100
tol = 1e-6 # tolerance
w = 0.5 # damping paramter

u = TrialFunction(V) # trial function object
v = TestFunction(V)  # test function object

for j in range(max_iterations):

    a = (rho(u_old, V) * Cp(u_old, V) * inner(u, v) * dx
    + dt * inner(kappa(u_k, V) * grad(u), grad(v)) * dx
    + dt * alpha * inner(u_k**3 * u, v) * ds
    + dt * beta * inner(u, v) * ds) # bilinear form

    L = (rho(u_old, V) * Cp(u_old, V) * inner(u_old, v) * dx
    + dt * alpha * inner(u_amb**4, self.v) * ds
    + dt * beta * inner(u_amb, self.v) * ds
    + dt * inner(f, v) * dx) # linear form

    problem = petsc.LinearProblem(a, L, petsc_options={"ksp_type": "preonly", "pc_type": "lu"})
    u_tilde = problem.solve() # solve linear system
    u_kplus.x.array[:] = u_k.x.array + w * (u_tilde.x.array - u_k.x.array) # fixed point
    error = my_errors(domain, u_kplus - u_k)[0] # calculate L2 error

    if error < self.tol:
        print(f"The Backward Euler fixed point solver has converged after {j+1} iterations")
        break
    elif j == max_iterations - 1:
        print(’Fixed point solver has not converged’)

    u_k.x.array[:] = u_kplus.x.array # update
u_n.x.array[:] = u_k.x.array[:] # update for new time-step
```

All simulations of the `FEniCSx` code were run on a Lenovo X13 Thinkpad, which was equipped with an AMD Ryzen 7 PRO processor, a Radeon 780M Graphics card, 32 GB RAM, and 447 GB memory. We installed `FEniCSx` version 0.9.0 with complex number support, which was accessed through a WSL. Post-processing and visualisation was done in `Paraview` version 6.0.0 (Ahrens, Geveci, and Law 2005).

The overall structure of the code to solve both Induction Heating Problems is shown in Figure 5.3. First, all external modules are imported in, which includes native `FEniCSx` modules such as `DOLFINx`, the mesh generation software `GMSH`, and the linear algebra library `petsc4y`. We also import 5 modules that have been locally written by the author:

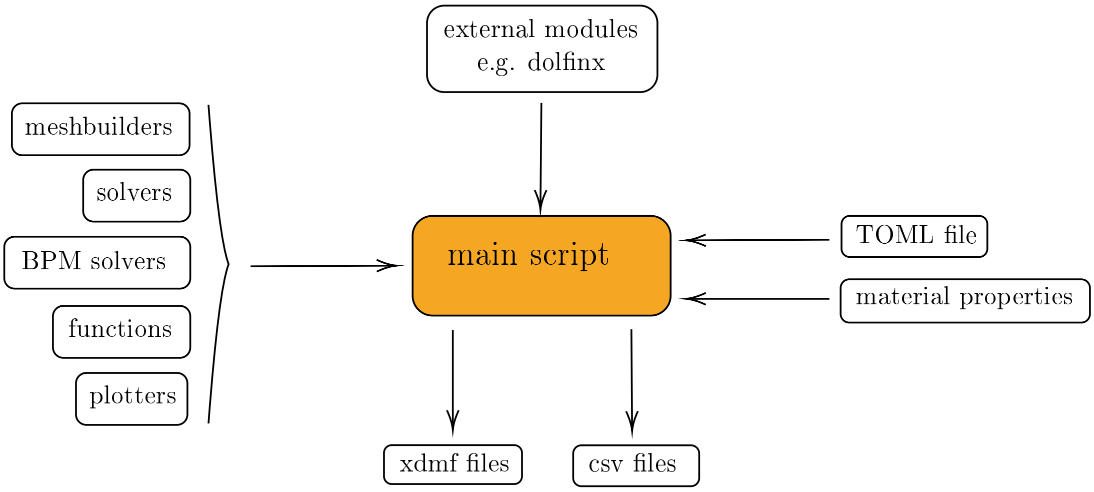

Figure 5.3: The structure of the `FEniCSx` code.

- `meshbuilders`: classes of meshes for induction heating simulation built using `GMSH`,
- `solvers`: variational forms and solvers for the PDEs representing induction heating,
- `BPM solvers`: variational forms and solvers using the BPM for the PDEs representing induction heating,
- `functions`: miscellaneous functions such as finding nodes in a mesh, writing functions to file, and calculating percentage change of material properties,

- `plotters`: functions for plotting results using `matplotlib`.

We use a `TOML` (Tom's Obvious Minimal Language) file to set configuration parameters for the code, e.g.: billet geometry, mesh parameters, solver methods, etc. The code is designed so that only the `TOML` file should need to be modified to run a new simulation. We also import material properties, which are piecewise polynomial functions that have been derived offline from `CSV` data. More details about the material properties are in Section 5.7.2. Finally, the code outputs some `XDMF` files that can be used for post-processing in `Paraview` and some `CSV` files for the temperature of the billet at points with coordinates specified in the `TOML` file. An example `TOML` file can be found in Appendix A.3, and the full induction heating code can be found in the Github Repository by MacKenzie (2025).

For all simulations, unless otherwise stated, we choose to solve the linear systems using a LU factorisation. We set all damping parameters to 0.5, the magnetic field tolerance to 10^{-8} and temperature and coupled tolerances to 10^{-6}. However, first we verify that the `FEniCSx` code behaves as expected by checking that it converges to a known solution.

5.6 Manufactured Solutions

In this Section we numerically verify the that Solenoidal `FEniCSx` code converges to a manufactured solution and that the Axisymmetric `FEniCSx` code converges to an analytic solution.

5.6.1 Solenoidal `FEniCSx` Code Manufactured Solution

For the manufactured solutions test, we artificially generate right-hand sides for (5.1) by plugging in a known solution. Then, any algorithm that solves (5.1) should recover an approximation to the known solution. This way, we can verify that the algorithm converges by finding convergence rates under successively refined approximations. Using this method, we validate the `FEniCSx` code for the Solenoidal model.

We consider a simplified case where the material properties $\kappa(\cdot)$, $\sigma(\cdot)$, $\mu(\cdot,\cdot)$, α, β, and ω are set equal to 1. Let $\Omega = (0,1) \times (0,1)$ be the unit square with boundary $\partial\Omega$. The simplified problem reads: find H and u such that

$$-\Delta H + iH = f_H \qquad \text{in } \Omega, \tag{5.13}$$

$$\frac{\partial u}{\partial t} - \Delta u = |\nabla H|^2 + f_u \qquad \text{in } \Omega. \tag{5.14}$$

Setting $u_{\text{amb}} = 0$, the boundary conditions are

$$H = H_\circ \quad \text{on } \partial\Omega,$$

$$\frac{\partial u}{\partial \boldsymbol{n}} + u + u^4 = g \text{ on } \partial\Omega.$$

For this manufactured solution, we set $H_{ex} = 2 + \sin(\pi x)\sin(\pi y)$, $H_\circ = 2$, $u_{ex} = e^t e^x \sin(\pi y)$, and $g = \frac{\partial u_{ex}}{\partial \boldsymbol{n}} + u_{ex} + u_{ex}^4$. We generate artificial right-hand sides by setting

$$f_H = -\Delta H_{ex} + i\omega H_{ex},$$

and

$$f_u = \frac{\partial u_{ex}}{\partial t} - \Delta u_{ex} - |\nabla H_{ex}|^2.$$

Using this data, we expect that the `FEniCSx` code converges to the exact solutions H_{ex} and u_{ex}.

Since (5.13) is independent of u, we use can Algorithm 1 to solve for H directly. Therefore, convergence of the numerical solution to the exact solution will verify Algorithm 1. We also verify convergence rates for (5.14), and consider both Algorithm 2, for the standard Galerkin method, and Algorithm 3, for the BPM. We test for spatial convergence over a sequence of increasingly refined uniform meshes and also test for temporal convergence over a sequence of increasingly small time-steps. We repeat this test over non-Delaunay meshes. Let us call the numerical magnetic field solution H_h, the numerical standard Galerkin temperature solution u_h^{GAL}, and the numerical BPM solution u_h^{BPM}. For the BPM, we chose $k = 50$, so that the solution u_{ex} is within the bounds for all t that we considered.

For the first test we verify spatial convergence. In order to minimise the errors due to the temporal discretisation, we use a small time-step of $\Delta t = 10^{-5}$ and run Algorithm 2 and 3 for 10 time-steps with a final time of $T = 10^{-4}$. We calculate the error at T over a sequence of uniform meshes with $h = 0.1$, 0.05, 0.025, 0.0125 and 0.00625. For the second test, to verify rates for the temporal convergence, we fix a uniform mesh with $h = 0.0125$, then compare the error after a longer length of time $T = 5$ for 1, 2, 4, 8, and 16 time-steps. The results for both tests are shown in Figure 5.4.

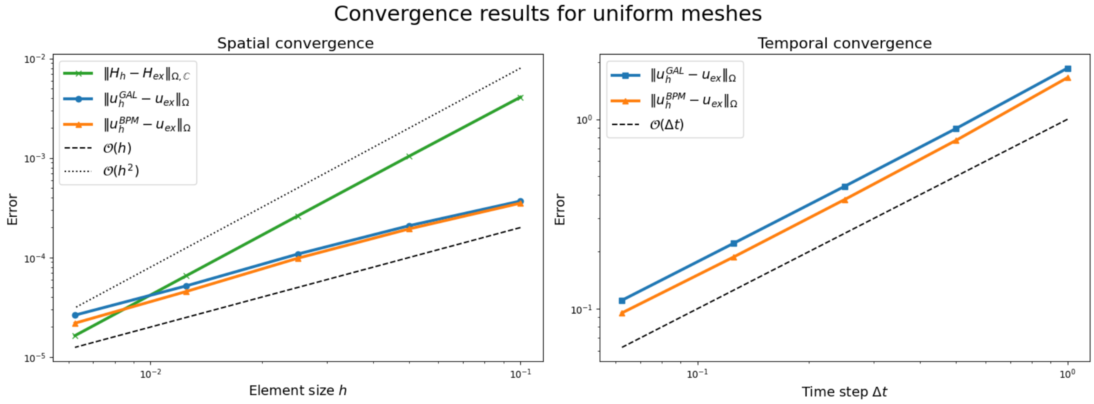

Figure 5.4: (a) $L^2(\Omega)$ errors between H_h and H_{ex}, and u_h^{GAL}, u_h^{k} and u_{ex} at final time $T = 10^{-4}$ after 10 time-steps over a sequence of uniform meshes. (b) $L^2(\Omega)$ errors between u_h^{GAL}, u_h^{BPM} and u_{ex} for a fixed uniform mesh with $h = 0.0125$ at final time $T = 5$ for increasingly small time-steps.

We can see that in Figure 5.4 (a), H_h converges to H_{ex} at a second order rate, which is the expected spatial convergence rate for $\mathbb{P}_1$ finite elements. It seems that both u_h^{GAL} and u_h^{BPM} converge at a first order rate in space, which is possibly due to the non-linear radiation boundary condition leading to a sub-optimal convergence. Additionally, the BPM provides, for this example, solutions that are closer to the exact solution than the standard Galerkin method. In Figure 5.4 (b) we see that u_h^{GAL} and u_h^{BPM} converge to u_{ex} at a first order rate in time which is the expected rate for a Backward Euler scheme, and again we see a slightly lower error for the u_h^{BPM}.

We also compare convergence rates when we use non-Delaunay meshes. We use the same meshes that are used in Section 4.7.2 and are illustrated in Figure 4.2. Here, we take a sequence of meshes with 9, 17, 33, 65, and 129 elements on each side of the unit square, which has corresponding $h = 0.1111$, 0.05882, 0.03030, 0.01539 and 0.007752 (4 sig.fig.). For the temporal discretisation we use the mesh with $h = 0.01539$. The results are shown in Figure 5.5

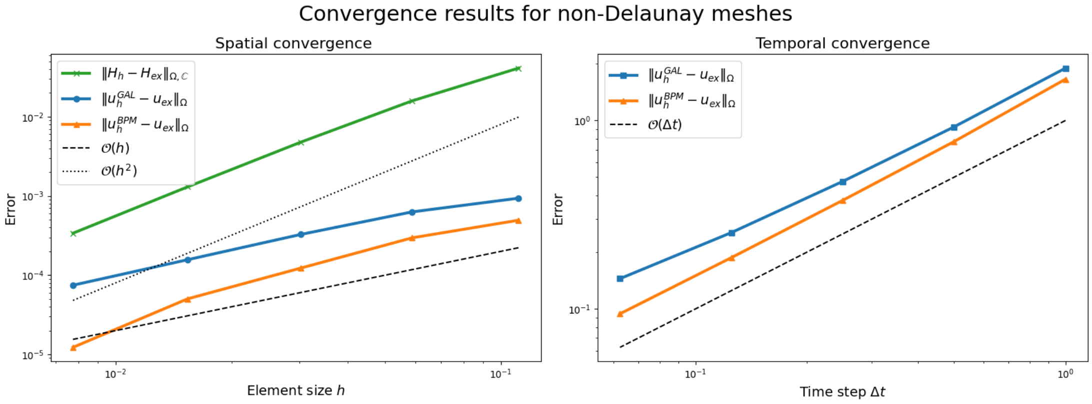

Figure 5.5: (a) $L^2(\Omega)$ errors between H_h and H_{ex}, and u_h^{GAL}, u_h^k and u_{ex} at final time $T = 10^{-4}$ after 10 time-steps over a sequence of non-Delaunay meshes. (b) $L^2(\Omega)$ errors between u_h^{GAL}, u_h^{BPM} and u_{ex} for a fixed non-Delaunay mesh with $h = 0.01539$ at final time $T = 5$ for increasingly small time-steps.

First of all, we see in Figure 5.5 (a) that a non-Delaunay mesh causes H_h and u_h^{GAL} to have much higher errors than a uniform mesh. We also see that u_h^{BPM} is significantly more accurate than u_h^{GAL}: indeed, for the finest mesh, u_h^{BPM} is an order of magnitude more accurate than u_h^{GAL}. This advantage is also seen in Figure 5.5 (b). This suggests that even for smooth solutions, applying the BPM to (5.14) leads to more accurate solutions than the standard Galerkin method, which is promising when we consider extending to more complicated problems.

5.6.2 Axisymmetric `FEniCSx` Code Analytical 1D Solution

Here we consider a 1D problem to verify the Axisymmetric `FEniCSx` code for the magnetic potential A by solving (5.10). We follow the example by Bermúdez et al. (2007b), and refer the reader to that paper for more details on the derivation.

Let us consider an infinite cylinder surrounded by an extremely thin coil, which is modelled as a continuous single coil with uniform current intensity. A diagram of the setup in 2D is shown in Figure 5.6. Here, r_1 is the radius of the billet, r_2 is the position of the infinitely thin coil, and r_3 is the boundary of the air domain.

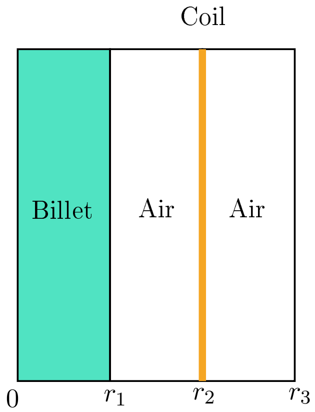

Figure 5.6: Diagram of the 1D simplification of the Axisymmetric domain. Here, r_1 is the radius of the billet, r_2 is the position of the infinitely thin coil, and r_3 is the boundary of the air domain.

In this test, we assume that the material properties are constant, and in the billet we take typical values for C42-MOD micro-alloyed steel. So in the air domain, we set $\sigma = 0$ and $\mu = \mu_0 = 2\pi \times 10^{-7}$, which is the magnetic permeability of free space. In the billet domain, we set $\sigma = 5.91 \times 10^6$, and set $\mu = 259.47\mu_0$.

Let the solution be denoted as A, and let us denote

$$\begin{aligned} A_1 &= A|_{(r_0,r_1)}, \\ A_2 &= A|_{(r_1,r_2)}, \\ A_{ext} &= A|_{(r_2,r_3)}. \end{aligned}$$

Then the Axisymmetric equations reduce to the problem: find A such that

$$\begin{aligned} \frac{1}{\mu}\frac{d}{dr}\left(\frac{1}{r}\frac{d(rA_1)}{dr}\right) + i\omega\sigma A_1 &= 0 && \text{if } r_0 < r < r_1, \\ \frac{1}{\mu_0}\frac{d}{dr}\left(\frac{1}{r}\frac{d(rA_2)}{dr}\right) &= 0 && \text{if } r_1 < r < r_2, \\ \frac{1}{\mu_0}\frac{d}{dr}\left(\frac{1}{r}\frac{d(rA_{ext})}{dr}\right) &= 0 && \text{if } r_2 < r. \end{aligned}$$

This is equipped with the boundary conditions

$$\begin{aligned} &A_1(r) \text{ is bounded } \text{ as } r \to 0, \\ &A_{ext}(r) = \mathcal{O}\left(\frac{1}{r}\right) \text{ as } r \to \infty, \end{aligned}$$

and the interface conditions

$$\begin{aligned} A_1(r_1) &= A_2(r_1), \\ A_2(r_2) &= A_{ext}(r_2), \\ \frac{1}{\mu}\frac{1}{r}\frac{d(rA_1)}{dr}(r_1) &= \frac{1}{\mu_0}\frac{1}{r}\frac{d(rA_2)}{dr}(r_1), \\ \frac{1}{\mu_0}\frac{1}{r}\left(\frac{d(rA_1)}{dr} - \frac{d(rA_2)}{dr}\right)(r_2) &= I, \end{aligned}$$

where I is the current intensity per unit length in the induction coil. It was shown by Bermúdez et al. (2007b) that this has an exact solution, namely

$$A_{ex} = \begin{cases} \alpha_1 \mathcal{I}_1(r) & 0 \leq r \leq r_1, \\ \frac{1}{2}\mu_0 \alpha_2 r + \beta_2/r & r_1 \leq r \leq r_2, \\ \beta_{ext}/r & r_2 \leq r, \end{cases}$$

where $\gamma_j = \sqrt{i\omega\sigma_j\mu_j}$, $\mathcal{I}_1$ and $\mathcal{K}_1$ are modified Bessel functions of the first kind and second kind, respectively, and

$$\begin{aligned} \gamma_1 &= \sqrt{i\omega\sigma\mu}, \\ \alpha_2 &= I, \\ \alpha_1 &= \mu_0 r_1 \alpha_2 / \mathcal{I}_1(\gamma_1 r_1) + r_1 \gamma_1 \mathcal{K}_1(\gamma_1 r_1), \\ \beta_2 &= r_1(\alpha_1 \mathcal{I}_1(\gamma_1 r1) - \frac{1}{2}\mu_0 r_1 \alpha_2), \\ \beta_{ext} &= r_2(\frac{1}{2}\mu_0 r_2 \alpha_2 + \beta_2/r_2). \end{aligned}$$

Since the solution is not ‘smooth’ we do not expect optimal convergence for this problem. We set $r_0 = 0.00001$ to avoid complications due to the singularity. The results are shown in Figure 5.7.

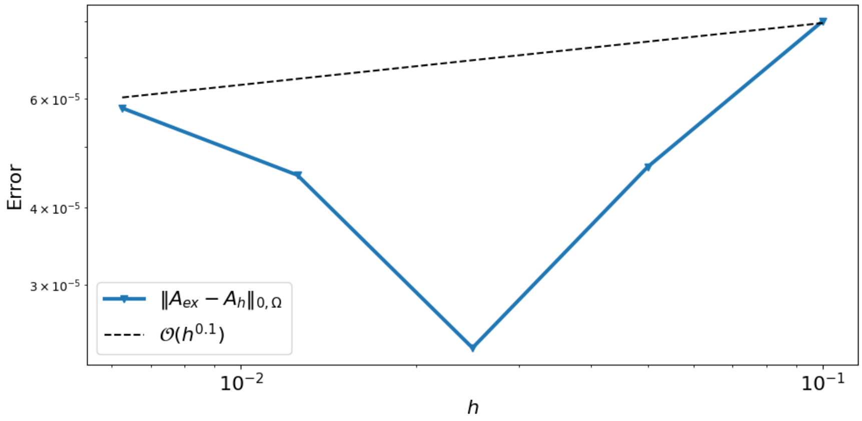

Figure 5.7: Convergence results for the Axisymmetric code for the magnetic potential A.

As we can see, we do not have optimal convergence. Indeed, the results show that when h gets smaller than ≈ 0.025, the error increases. This is possibly due to the fact that the solution is not smooth, or because the Bessel function is extremely sensitive near $r = 0$.

5.7 Comparison to Experimental Data

In this Section, we compare experimental data to output from the Solenoidal `FEniCSx` code, the Axisymmetric `FEniCSx` code, and a popular engineering FEM software, `DEFORM` (2023). We find that Solenoidal and Axisymmetric `FEniCSx` codes both produce favourable results within an acceptable tolerance.

5.7.1 Experiment Setup

In order to verify and compare the Solenoidal and Axisymmetric `FEniCSx` codes, a series of experiments were conducted by me at the AFRC. For these experiments, a small billet was subjected to heating by induction and the temperature of the billet was recorded during the heating process. Two different coil sizes were used: a large one and a small one. A photograph of the setup using the large coil can be seen in Figure 5.8.

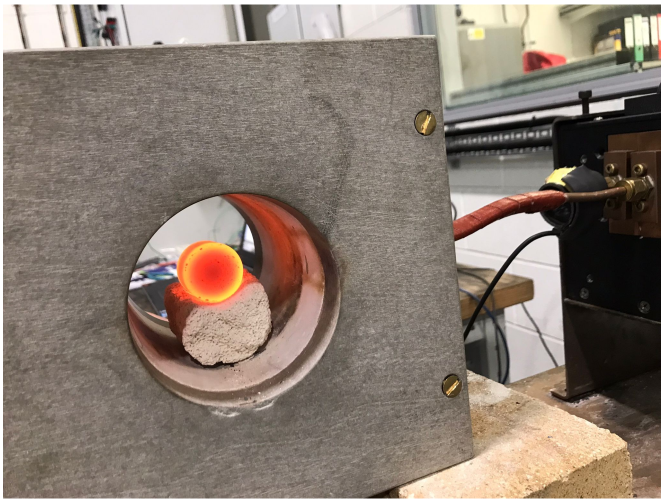

Figure 5.8: Setup of the induction heating experiment with the large coil: a small workpiece is supported by a refractory material at the centre of a coil of copper wire, which was encased in refractory cement.

As seen in Figure 5.8, the copper coil was encased in a non-conductive refractory cement that could withstand high temperatures. The billet was supported by a refractory material so that it was situated at the centre of the copper coils. The coil was connected to an Ambrell Ekoheat 15 kW induction heating system, which was the appliance for configuring the voltage and frequency of the alternating current in the coils. The temperature was measured at two positions using thermocouples that were inserted into small holes in the billet (see Figure 5.9). The temperature of the thermocouples were logged on a TC-08 Picolog, and the voltage and frequency of the alternating current were recorded using a Rogowski coil and a passive amplifier. The data from the Picolog and the Rogowski coil were logged onto a laptop.

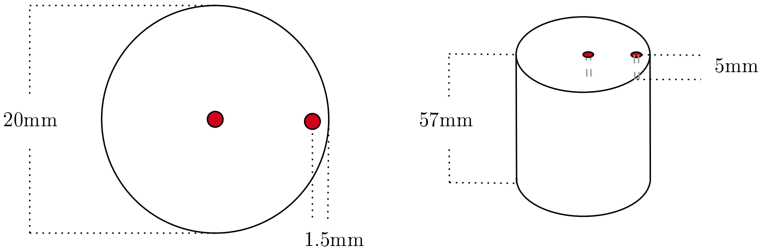

Figure 5.9: Geometry of the C42-MOD micro-alloyed steel billet.

The first experiment was carried out using the inductor with the smaller diameter.

An axisymmetric diagram of the induction heating setup is shown in Figure 5.10, where the measurements of the coil are shown. We have also highlighted four points on the billet: A, on the upper surface; B in a corner; C, at the centre; and D, at the surface. In the experiments, only the temperature at points A and B were measured using thermocouples, but we will use temperature profiles at points C and D when we compare the Axisymmetric `FEniCSx` code to output from the `DEFORM` software.

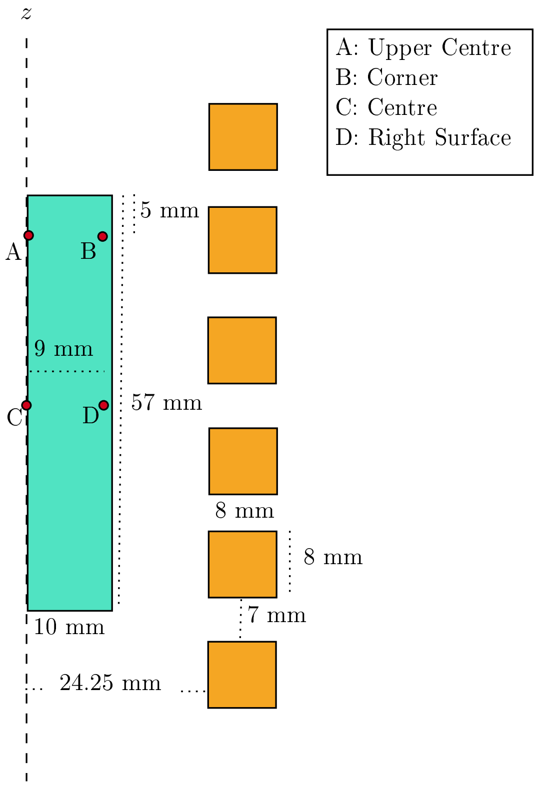

Figure 5.10: Axisymmetric diagram of the induction heating experimental setup. The temperature at points A and B are measured in the experiment, and we highlight points C and D to compare with the software `DEFORM`.

Table 5.1 shows the geometrical properties of the induction heating setup.

In this experiment, the voltage was set to 200 V and was configured to generate a 417 A current inside the inductor. The system was switched on for 60 seconds, and then switched off. We modelled the current as a step function which is shown in Figure 5.11.

The total current in the coil can be calculated from the frequency and voltage data logged by the Rogowski coil. In general, even if the system is configured to have a

Geometrical data for the experiment.	
Billet length:	57 mm
Billet radius:	10 mm
Air length:	400 mm
Air radius:	200 mm
Coil ID:	24.25 mm
Coil separation:	15 mm
Coil diameter:	8 mm

Table 5.1: Geometrical properties for the experiment.

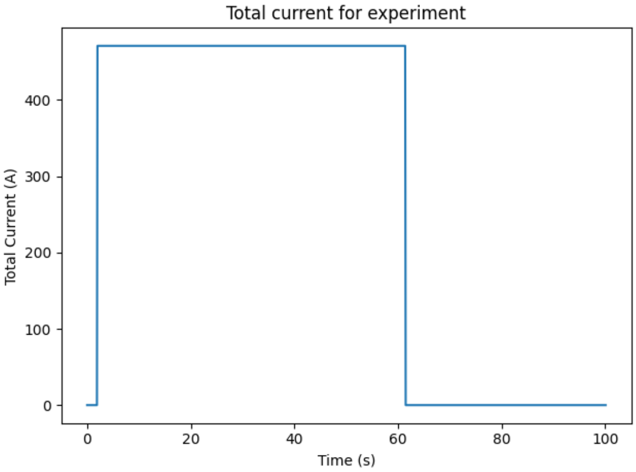

Figure 5.11: The current is set to 471 A if $2 \leq t \leq 62$, and the current is zero otherwise.

constant total current, there will still be some variation in the current. Therefore, ideally, the total current should be calculated directly from the measured frequency and voltage. An example of this calculation this is shown in Appendix A.2. However, for simplicity, we assume a step function is a good approximation for this simulation.

5.7.2 Material Properties

The cylindrical billet that we used in the setup was made from C42-MOD micro-alloyed steel. The data for the material properties used in this code comes from the software `JMatPro` (Saunders et al. 2003). To build functions that represent the material properties that change with temperature, we import the data from `JMatPro` as a `CSV` file, where each data-point represents the value of the property at a specific temperature.

The goal is to build analytical functions that accurately represent the data using the fewest conditions possible in order to maximise computational efficiency, since analytical expressions are much faster to evaluate than calculating a piecewise linear interpolant at every node and every time-step.

Using the data we use the `Python` module `sklearn` to build a piecewise polynomial function that approximates the data. First, we split the data into groups with the same trend. We then use a function from `sklearn` to find the optimal polynomial approximation using least-squares regression for all polynomial degrees up to 5. We choose the lowest degree polynomial approximation that has a maximum pointwise error of 1.2%, and an average error of 0.2%. If none of these approximations come within our chosen error tolerance, we split that group again, and repeat. We do this for all groups in the data. For example, the function used to approximate $\mu(\cdot)$ uses three groups and is written as follows:

$$\mu(u) = \begin{cases} 0.017328u + 0.000326u^2 + 6.059843 \times 10^{-8}u^3 + 259.831175 & \text{if } u \leq 720, \\ -10.744186u + 8198.813953 & \text{if } 720 < u \leq 763, \\ 1 & \text{if } 763 < u. \end{cases}$$

By constructing the functions in this way, we avoid using an expensive linear interpolation since there are many data-points. A graph of all material properties data and their corresponding approximated functions is shown in Figure 5.12.

We should take note of the steep discontinuities in the data, especially for the magnetic permeability $\mu(\cdot)$, as we can see in the graph of magnetic permeability in Figure 5.12. This discontinuity occurs when the material reaches the Curie point at $\approx$ 730°C, when the material becomes demagnetised. We also see a couple of discontinuities in the specific heat capacity $C_p(\cdot)$. The first spike is at the Curie point, and the second spike occurs at the melting point of the material at $\approx$ 1350°C. At these spikes, the term $\rho(\cdot)C_p(\cdot)$, which is the coefficient of the time derivative of the heat equation, is large in comparison to other terms and generates a decrease in the rate of change of temperature. Physically, this corresponds to the energy being used for magnetic or

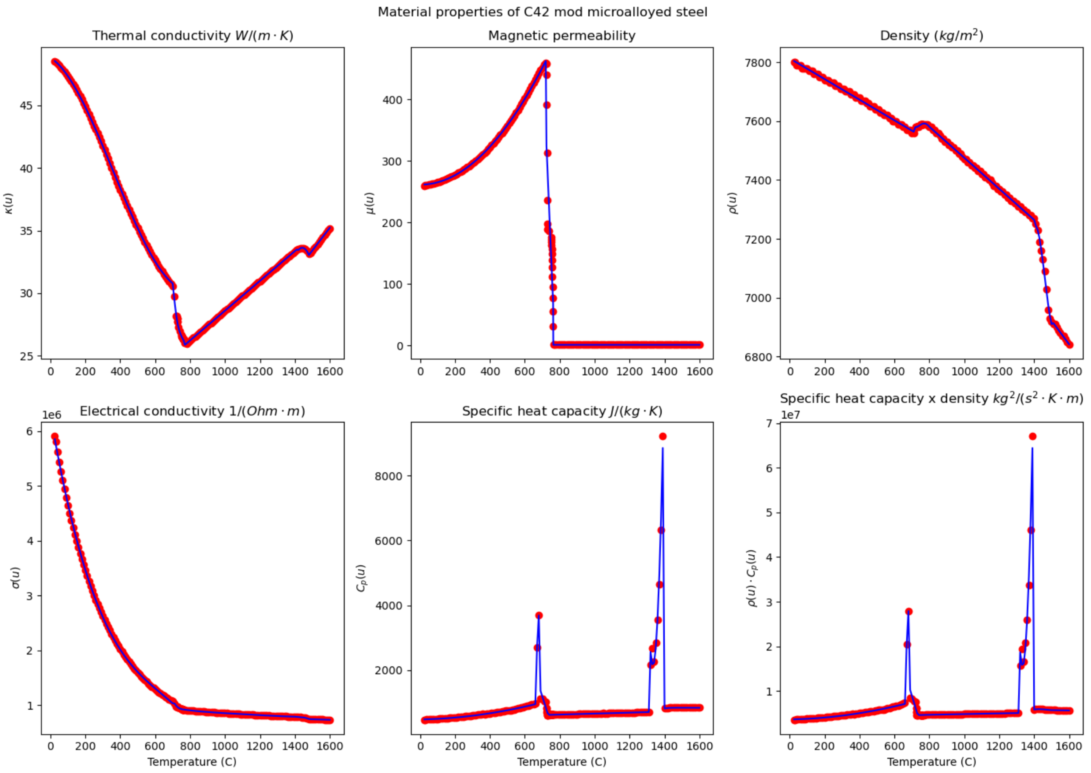

Figure 5.12: Material properties for C42-MOD micro-alloyed steel. The red dots represent the data imported from `JMatPro`, and the blue line represents the piecewise polynomial approximation.

structural phase-change, as opposed to heating the material. In our simulation we will not go above the melting point of the material, but we will go above the Curie point.

We also have the option of using a magnetic permeability that depends on the magnetic field H as well as the temperature u. The data for this function also comes from `JMatPro`. Since there are relatively fewer datapoints than in the 1D magnetic permeability data, for simplicity we use a linear interpolator from the `Python` library `scipy` to construct a 2D function. The function can be seen in Figure 5.13. We can still see a steep discontinuity when the temperature reaches the Curie point, and $\mu(\cdot, 0)$ corresponds to $\mu(\cdot)$ in Figure 5.12.

Note that alloys are difficult to find material properties for, since slight variations in material composition can correspond to large changes in properties. This can be another source of error between the model output and experimental data.

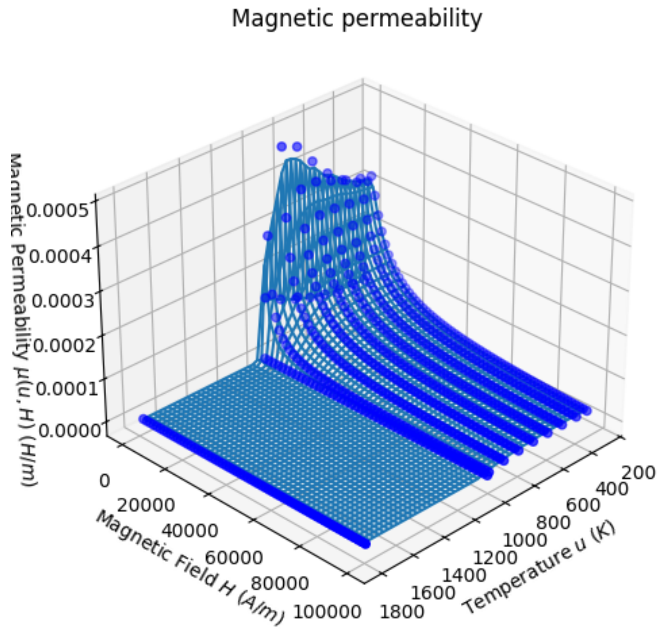

Figure 5.13: The non-linear property $\mu(u, H)$ for C42-MOD micro-alloyed steel. The blue dots are the data imported from `JMatPro`, and the mesh is the corresponding piecewise linear function that approximates the data.

5.7.3 Solenoidal `FEniCSx` Code

In order to run the Solenoidal `FEniCSx` code, we first need to construct a mesh. We design an anisotropic mesh that is refined such that the length of an element on the boundary is $1/4$ of the skin-depth, so that the model can accurately capture the boundary layer in the magnetic field. The mesh that we use is shown in Figure 5.14, which has a skin-depth of $16.6\,\mu\mathrm{m}$. This mesh has 9120 elements and 4561 degrees of freedom. For the time dependent model, a comparison is made between the temperature evolution at point A and point B. Note that since the Solenoidal `FEniCSx` code approximates the induction heating setup as an infinitely long element and coil, the model output would more likely correspond to the temperature at points C and D.

The results comparing the experimental data to the standard Galerkin FEM and the BPM are shown in Figure 5.15 and Figure 5.16, respectively. We take $k = 1700\,\mathrm{K}(\approx 1427\,^{\circ}\mathrm{C})$ to be higher than the melting point of C42-MOD micro-alloyed steel, as the temperature in the experiments do not go above the melting point and we want to

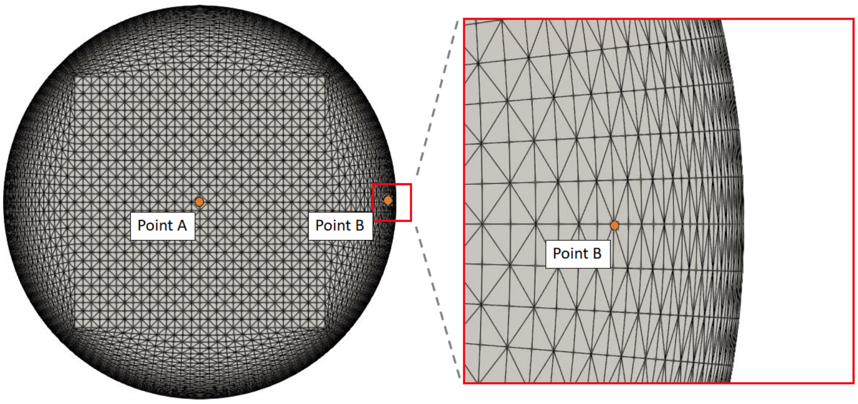

Figure 5.14: Mesh for the Solenoidal model.

Parameter	**Value**	**Parameter**	**Value**
Time-step Δt	0.1 s	Percentage tolerance p	5 %
Final time T	100 s	Coupled tolerance `ctol`	10^{-6}
Time current active	8 s	Magnetic tolerance `mtol`	10^{-8}
Current I	471 A	Temperature tolerance `ttol`	10^{-6}
Coupled max iterations `cmax`	20	Coupled damping ω_c	0.5
Magnetic max iterations `mmax`	20	Magnetic damping ω_m	0.5
Temperature max iterations `tmax`	50	Temperature damping ω_t	0.5
Convective coefficient β	10	Radiation coefficient α	4.54×10^{-8}

Table 5.2: Configuration parameters for the Solenoidal `FEniCSx` code for comparing the model to experimental data with a C42-MOD micro-alloyed steel billet.

guarantee that k is high enough. We choose to allow $\mu(\cdot,\cdot)$ to depend on H as well as u. Both models take 1 h 20 min to run on the laptop. The configurations for the fixed-point algorithms, and the values for α and β, are shown in Table 5.2.

Overall, the results produced by the standard Galerkin method and the BPM exhibit very similar qualitative behaviours to the experimental result, and produce results which are within acceptable tolerance (10-15% error) of the experimental results.

Indeed, the conductor heats up faster on the boundary than in the interior due to the skin-effect. Once the temperature reaches approximately 1050 K, there is a large decrease in the rate of change of temperature in both the experimental and model results, due to the Curie point being reached. See Figure 5.17 for the temperature distribution and magnetic field strength before and after the Curie point. Additionally, once the voltage is switched off at $t = 60$, there is a decrease in the temperature at the boundary which is seen in both the experimental data and in the simulation. Finally, both the model and experimental data temperature decay slowly, and point A becomes hotter than point B.

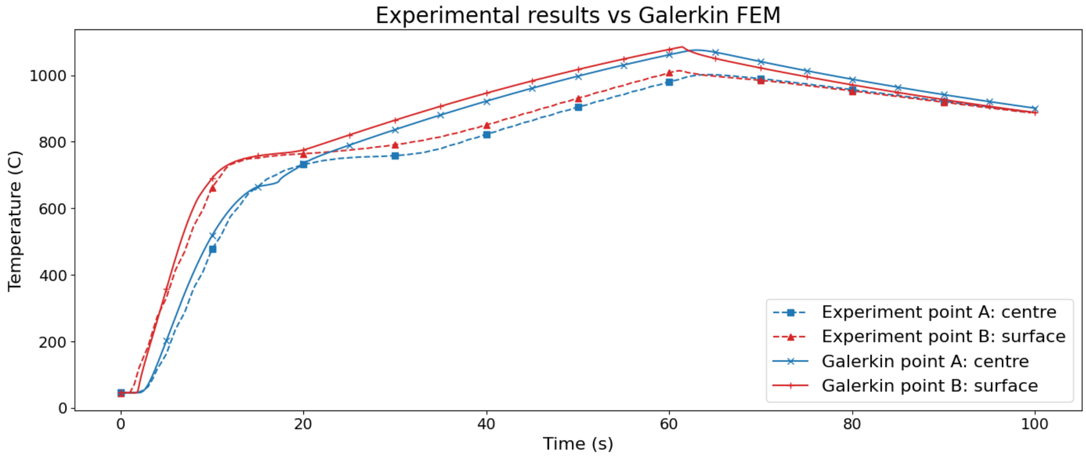

Figure 5.15: Comparison between the standard Galerkin model and the experimental data at points A and B.

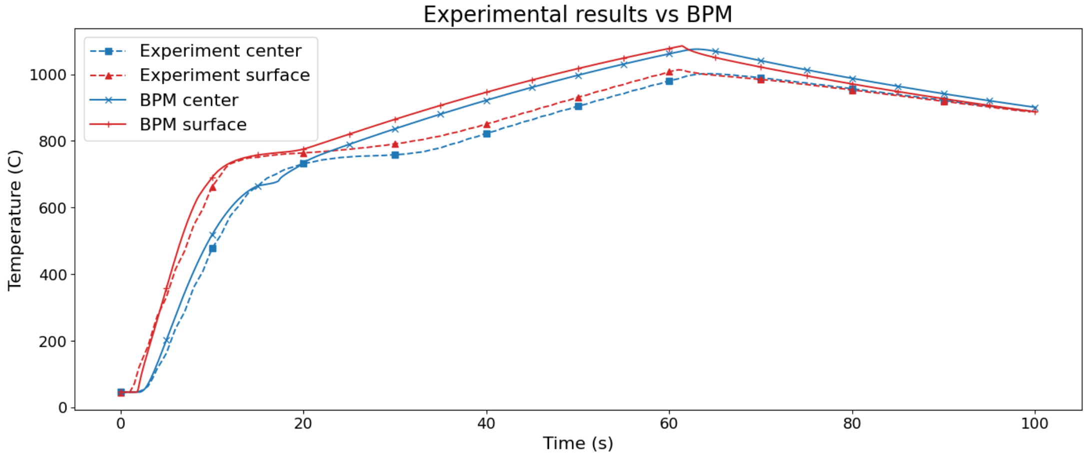

Figure 5.16: Comparison between the BPM and the experimental data at points A and B.

The errors between the experimental data and the model can be explained by the fact that the Solenoidal `FEniCSx` code is best suited to modelling the temperature in a long billet, and the temperature at the thermocouples was measured 5 mm from the end of the billet. Mismeasurements within the physical experiment itself can also be a major source

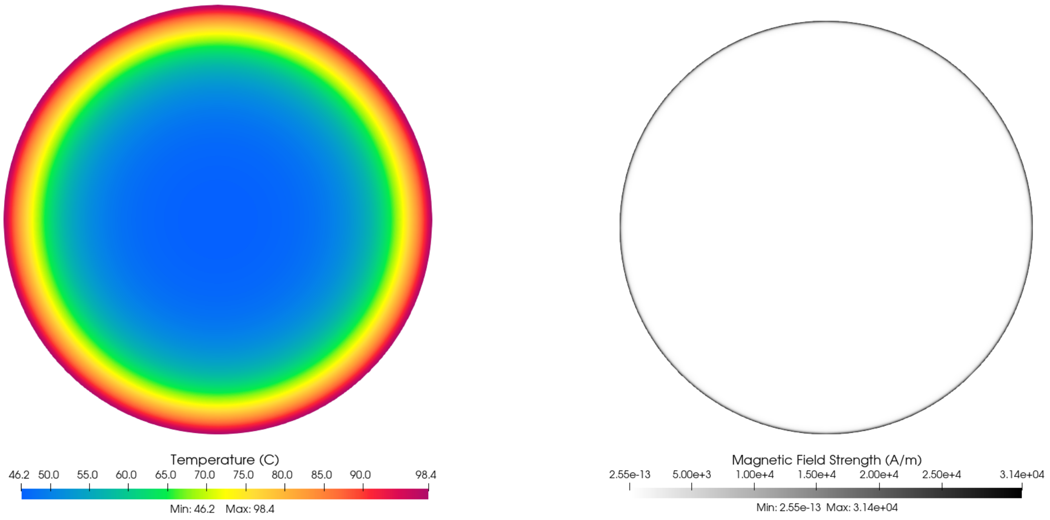

(a) Temperature at $t = 0.4$.

(b) Magnetic Field strength at $t = 0.4$.

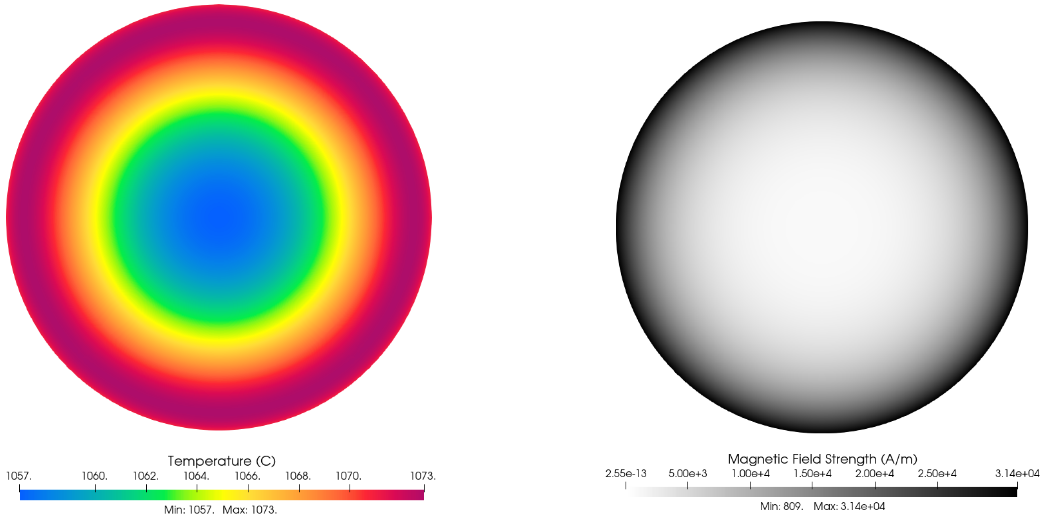

(c) Temperature at $t = 60$.

(d) Magnetic Field Strength at $t = 60$.

Figure 5.17: Temperature and magnetic field strength for the Solenoidal model at $t = 0.4$ in (a) and (b), respectively, and at $t = 60$ in (c) and (d), respectively. Note the marked increase in skin-depth at from (b) to (d).

of errors. As for errors within the model, we note that the code is very sensitive to $\mu(\cdot,\cdot)$ and perhaps the approximation of $\mu(\cdot,\cdot)$ is too coarse. Additionally, the model struggles to converge near the Curie point. This is a common problem that is highlighted in the literature, for example Clain (1994), Chaboudez et al. (1997), and Bay et al. (2003) do not go beyond the Curie point for this reason. Other methods to improve convergence at the Curie point include using a specialist algorithm (Chaboudez et al. 1994), or by using extremely small time-steps in a parabolic magnetic field equation (Drobenko, Hachkevych, and Kournyts'kyi 2007; Fisk et al. 2022). Additionally, Chaboudez et al. (1994) note that the behaviour of the model is highly sensitive to the radiation coefficient α so that could be another source of error.

Nevertheless, these results demonstrate that, despite being a relatively simple model, an implementation of the Solenoidal `FEniCSx` code using the standard Galerkin method or the BPM is capable of producing accurate and reliable results for induction heating that extend beyond the Curie point.

5.7.4 Axisymmetric `FEniCSx` Code and Industrial Software

In this Section we compare experimental data to the Axisymmetric `FEniCSx` code and an engineering FEM software: `DEFORM` (2023). This is one of the FEM software most widely used in industrial settings to analyse metal forming and heat treatment, and has been used by researchers and companies for over 20 years. In particular, `DEFORM` is one of the primary software used at the AFRC for the simulation of heat treatment and forging, and has been used in multiple projects for AFRC industrial members such as Bifrangi, Rolls-Royce, and Aubert & Duval. Here we use `DEFORM Multiple Operation v14.0.2`.

First, we design a mesh for the Axisymmetric `FEniCSx` code. For a fair comparison, we design a mesh that is comparable in size to the mesh constructed in `DEFORM` (see Figure 5.18 for the full mesh, and Figure 5.19 for a closer view of the mesh around the billet). Since `DEFORM` can only use quadrilateral meshes in 2D, we elect to do the same for the Axisymmetric mesh. The local size of the elements are specified to be the same in each mesh, with a larger size in the air domain, and a smaller size within a box around the coils and billet. Similar to the Solenoidal `FEniCSx` code, the mesh in the billet has a boundary layer in order to capture the skin-effect (see Figure 5.19).

We highlight that the `DEFORM` mesh actually consists of four different meshes (for the billet, coils, air around the billet, and air around the coils). As such there are hanging nodes in the `DEFORM` mesh, which can be seen more readily in Figure 5.19(a). The data and flux transfer over the mesh boundaries is dealt with internally in `DEFORM`

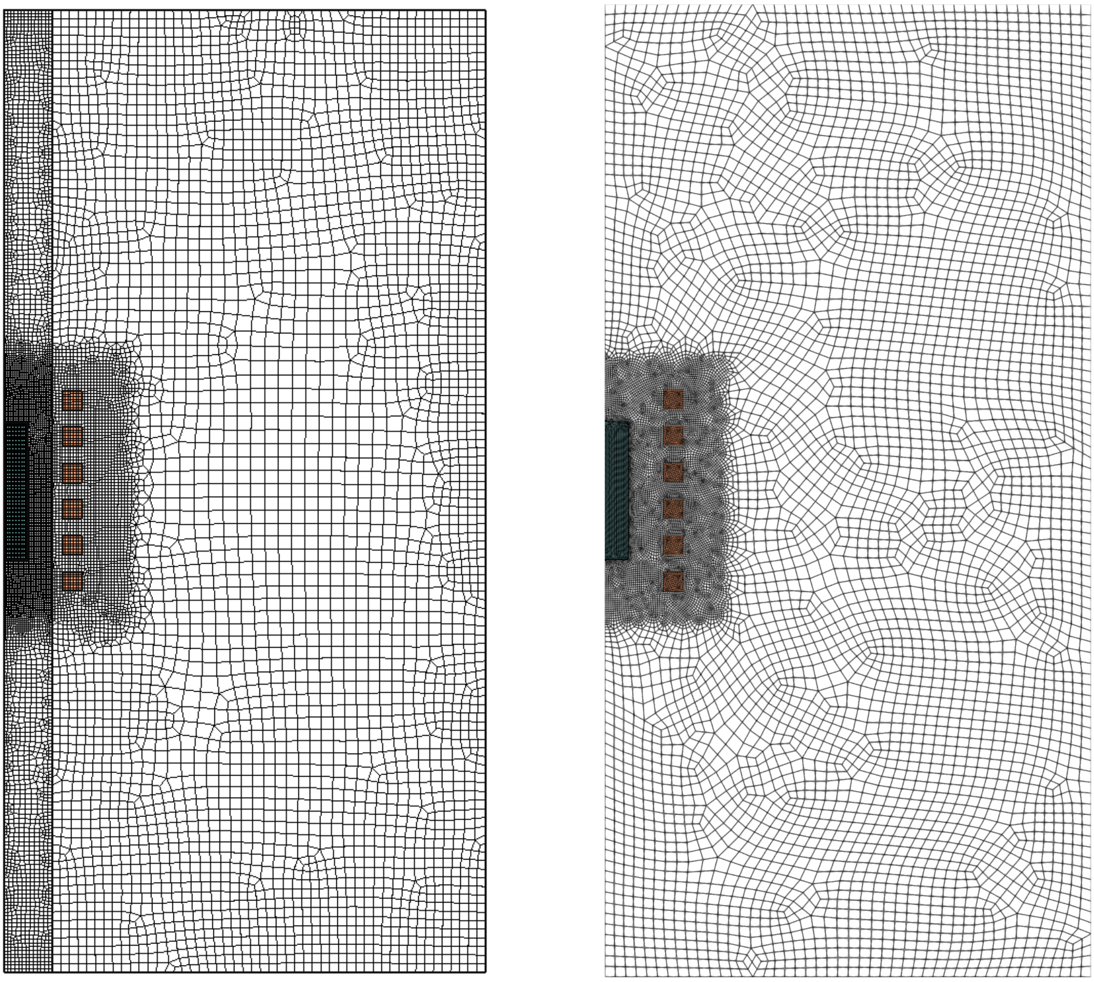

(a) `DEFORM` mesh.

(b) `FEniCsx` mesh.

Figure 5.18: Comparison between `DEFORM` mesh and `FEniCSx` mesh. Quadrilateral elements are used and the `FEniCSx` mesh is explicitly configured to have elements the same size as the `DEFORM` mesh.

through a specific ‘contact tab’. We investigated the possibility of importing the `DEFORM` mesh into `FEniCSx`, but since `FEniCSx` does not allow hanging nodes, this would require re-interpolating nodal values to create a mesh with no hanging nodes, or manually constructing a function that allows data transfer onto separate meshes. Therefore, we thought it was reasonable to simply define a new mesh with the same element properties as the `DEFORM` mesh.

For this test we use $\mu(\cdot)$ that only depends on temperature. The main reason is that we do not have any data for the magnetic permeability function $\mu_A(\cdot, \cdot)$ that depends

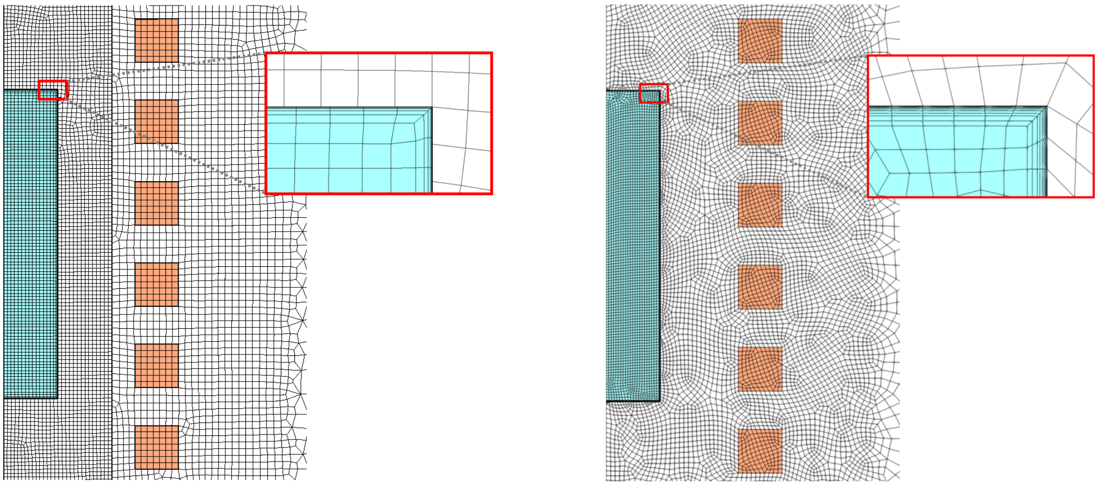
(a) `DEFORM` mesh close up.

(b) `FEniCSx` mesh close up.

Figure 5.19: Comparison between `DEFORM` mesh and the `FEniCSx` mesh. A boundary layer is present at the edge of the billet. Note that `DEFORM` meshes contain hanging nodes at the edges of different subdomains: this is why we could not use this mesh in the `FEniCSx` code.

on the magnetic potential A. It is possible to construct this function $\mu_A(\cdot,\cdot)$ from $\mu(\cdot,\cdot)$ depending on H. However, recall that since

$$A = \text{curl } \mathbf{B} \quad \Rightarrow \quad A = \text{curl } \{\mu(u, |\mathbf{H}|)\mathbf{H}\}.$$

This implies that

$$\mu_A(u, A) = \mu_A\left(u, \ \text{curl } \{\mu(u, |\mathbf{H}|)|\mathbf{H}|\}\right),$$

so $\mu_A(\cdot,\cdot)$ depends on the curl of the scalar field $\mu(u, |\mathbf{H}|)\mathbf{H}$. If $\mu(u, |\mathbf{H}|)$ is already a coarse approximation, then this will likely induce large errors in the approximation. Indeed, we implemented this in Axisymmetric `FEniCSx` code but found that the code struggled to converge. Furthermore, the same behaviour also occurs in `DEFORM`, so in this software they recommend using $\mu(\cdot)$ for this reason. Therefore, we choose to use $\mu(\cdot)$ to depend only on temperature.

A visualisation of the output of the code for the initial values of magnetic potential and the magnetic field in the whole domain is shown in Figure 5.20. This shows what we would expect: the magnetic potential is highly concentrated around the coils and

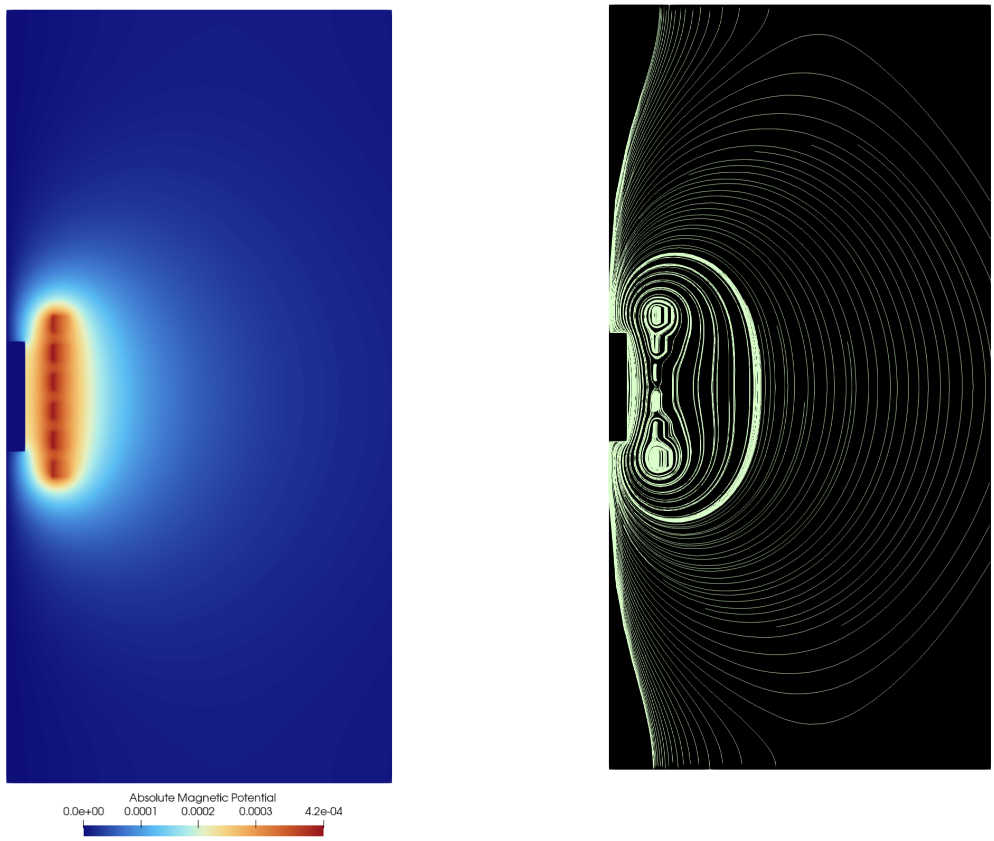

(a) Magnitude of the magnetic potential A.

(b) Streamlines of the magnetic field H.

Figure 5.20: Initial magnetic potential and corresponding streamlines for the Axisymmetric `FEniCSx` code.

penetrates only a small amount into the billet (equal to the skin-depth), so the billet can be readily seen in Figure 5.20 (a) and Figure 5.20 (b). The square coils produce streamlines that are tightly concentrated between the coils and the billet. Note that unlike the Solenoidal model, the magnetic potential will not be constant on the boundary of the billet but will vary in the geometry. It also seems that square coils produce large variation of magnetic potential concentration along the billet boundary, so we expect that the temperature distribution will not be even along the boundary.

The code was run using the same configuration as the Solenoidal `FEniCSx` code, detailed in Table 5.2. We take 471 A as the current for the model, which in `DEFORM` translates to a current density of 7.36 A/mm^2. `DEFORM` takes 1 min 41 s to run and uses 217 adaptive time-steps, and the Axisymmetric `FEniCSx` code takes about 2 h 12 min to run and uses 1000 uniform time-steps. Evidently, the Axisymmetric `FEniCSx` code could be made more efficient, so some potential ways of doing this are to move the mesh generation offline, to use adaptive time-stepping schemes, adaptive meshing, adaptive damping parameters, or to simply run it on a more powerful machine. We should note that when temperature in `DEFORM` reaches the Curie point, the solver does not converge, and it stops after a maximum of 200 iterations.

The results comparing the temperature evolution at point A and point B in the Axisymmetric `FEniCSx` code to the temperature measured in the experiment are shown in Figure 5.21. The results show the correct qualitative behaviour with the temperature overestimated with an error of about 15 %. Indeed, if we compare the experimental results to the same result run in `DEFORM` (see Figure 5.22), we see that `DEFORM` actually underestimates the temperature at a slightly higher error rate.

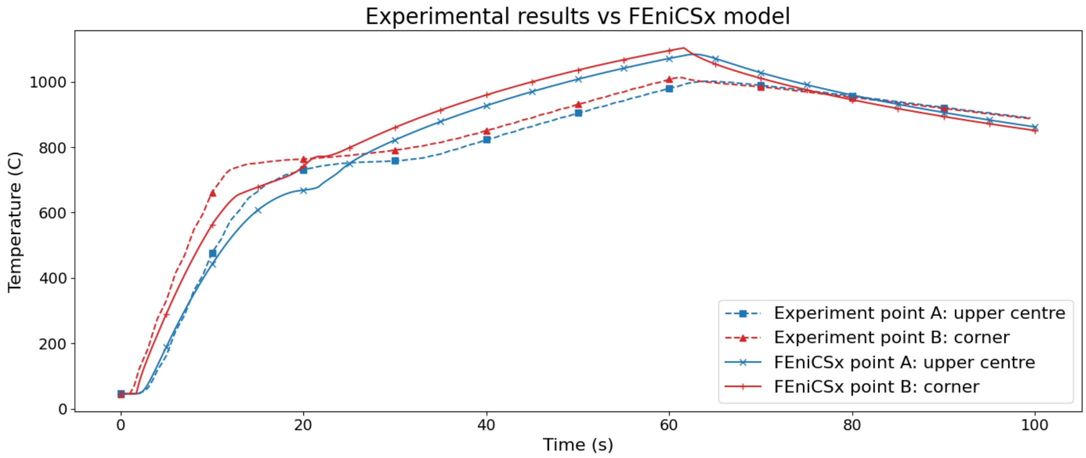

Figure 5.21: Experimental results compared to output from the Axisymmetric `FEniCSx` code.

In Figure 5.23, we compare the output of the `FEniCSx` code and `DEFORM` at the four separate points. The overall behaviour matches very well, although the rate of change at the start of the simulation for the `DEFORM` code is higher. In both sets of results, we see that the surface temperature sharply increases once it reaches about 650 °C, which is due to the Curie point being reached. However, we see in the `FEniCSx` code that at high temperatures, the corner is the hottest part of the billet.

The comparison between the `FEniCSx` code and the `DEFORM` software can be more

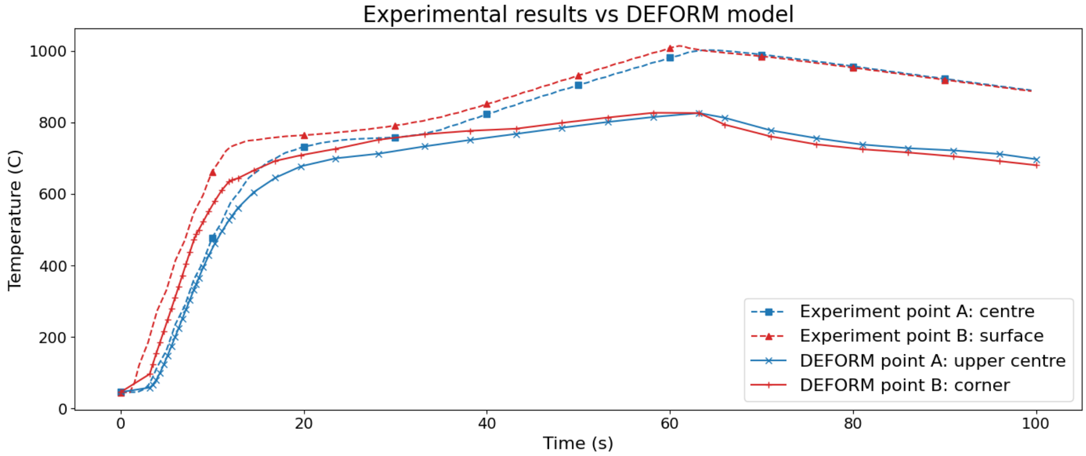

Figure 5.22: Experimental results compared to output from the `DEFORM` software.

readily seen in Figure 5.24 and Figure 5.25. Comparing these two sets of results, it seems that they are an excellent match. In Figure 5.24 (a) and 5.25 (a), the skin-effect is easily seen, and both models have reached a maximum temperature of about 100 °C. We can see in (b) that after about 5 seconds, the temperature had increased by about 500 °C, so both models were able to accurately capture the magnitude of the rapid temperature increase near the surface of the billet. In (c) a hotspot has been generated due to the temperature at that part of the billet reaching the Curie point. Both models have produced this hotspot within 2 seconds of each other. At 14.4 seconds in (d), both simulations have produced three hotspots due to variations of the magnetic potential along the boundary of the billet. In (e), at $t = 60$ we have reached the end of the heating process and the billet has reached its maximum temperature. Finally, at $t = 100$ in (f), the billet has been allowed to cool for 40 seconds and so we can see the heat loss on the surface of the billet.

We need to mention the heating at the corners in Figure 5.25 (e). It is well known that Maxwell's equations solved in domains with corners produce results that are not in the correct function spaces, so one might assume that the heating at the corners is a numerical artefact. However, it has been observed that spurious heating at the corners is a physical occurrence in induction heating simulations. Therefore, the results from the Axisymmetric `FEniCSx` code correspond better to the physical process of induction

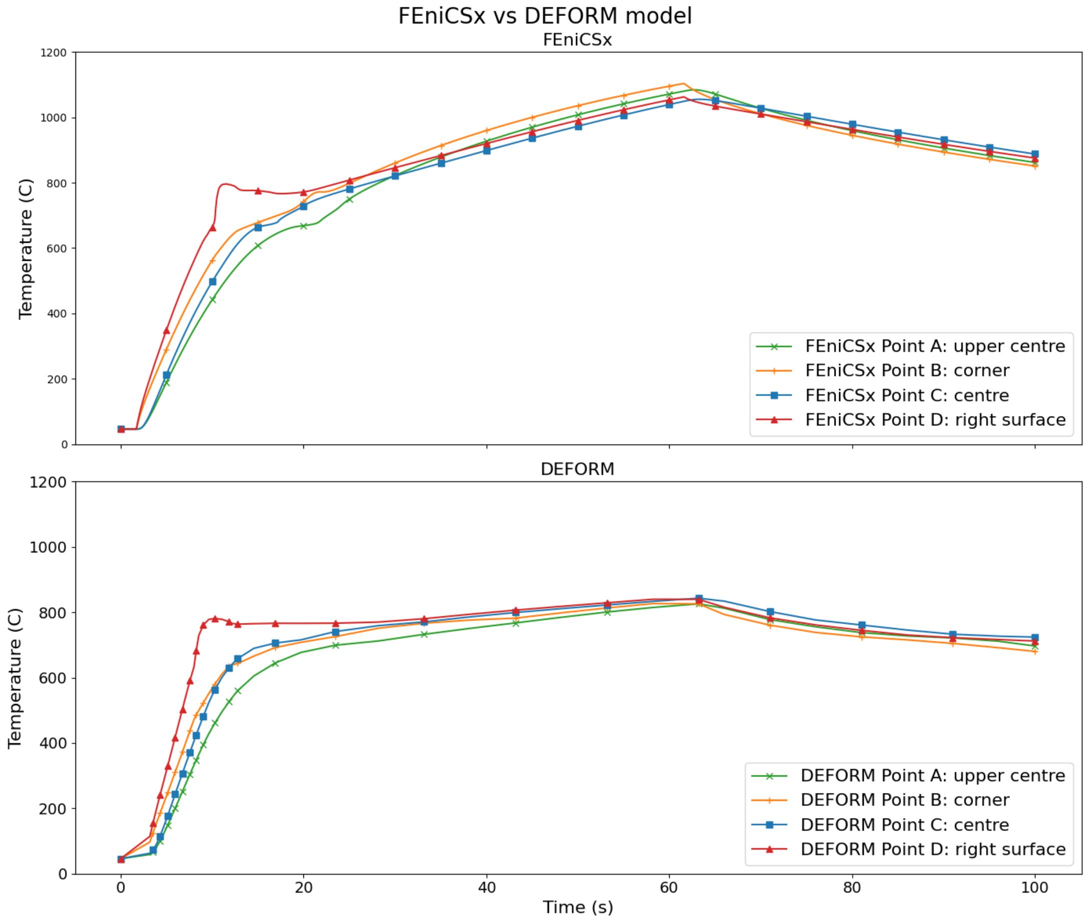

Figure 5.23: Temperature at points A, B, C and D for the Axisymmetric `FEniCSx` code and `DEFORM` software. There is a large difference in temperature between the two codes after the Curie point.

heating than the results in `DEFORM` (Figure 5.24).

5.8 Non-Convex Domain with Non-Delaunay Anisotropic Mesh

In this final Section, we consider the Solenoidal model where the billet is non-convex and is solved over a non-Delaunay anisotropic mesh. See Figure 5.26 for measurements of the domain and the corresponding mesh. The purpose of this Section is to illustrate the new results from Chapter 4 in a real-world application, namely, that the BPM works

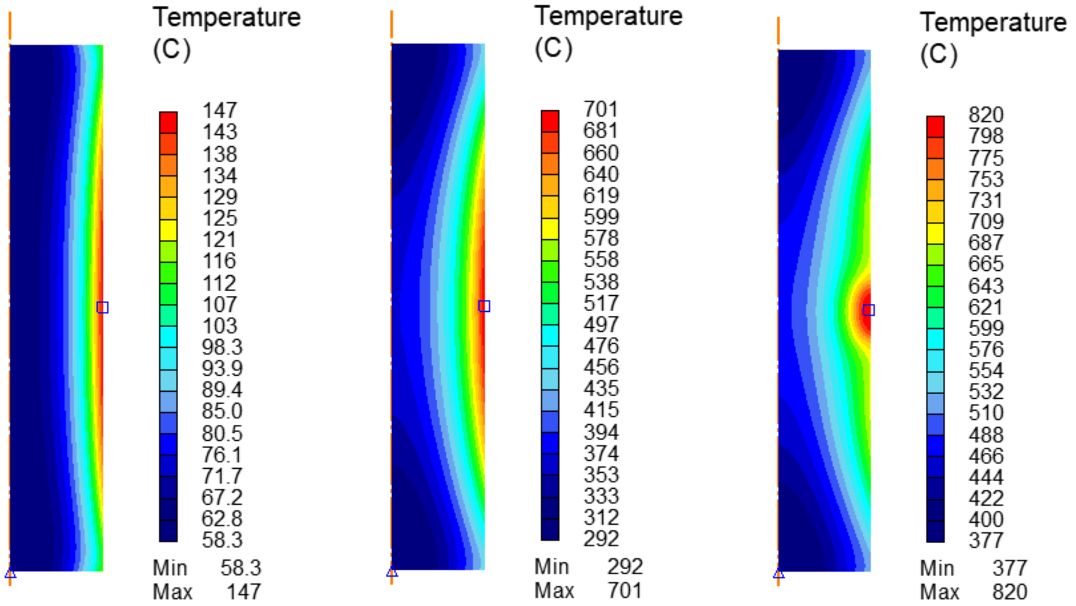

(a) $t = 3.189$ (b) $t = 7.573$ (c) $t = 9.032$

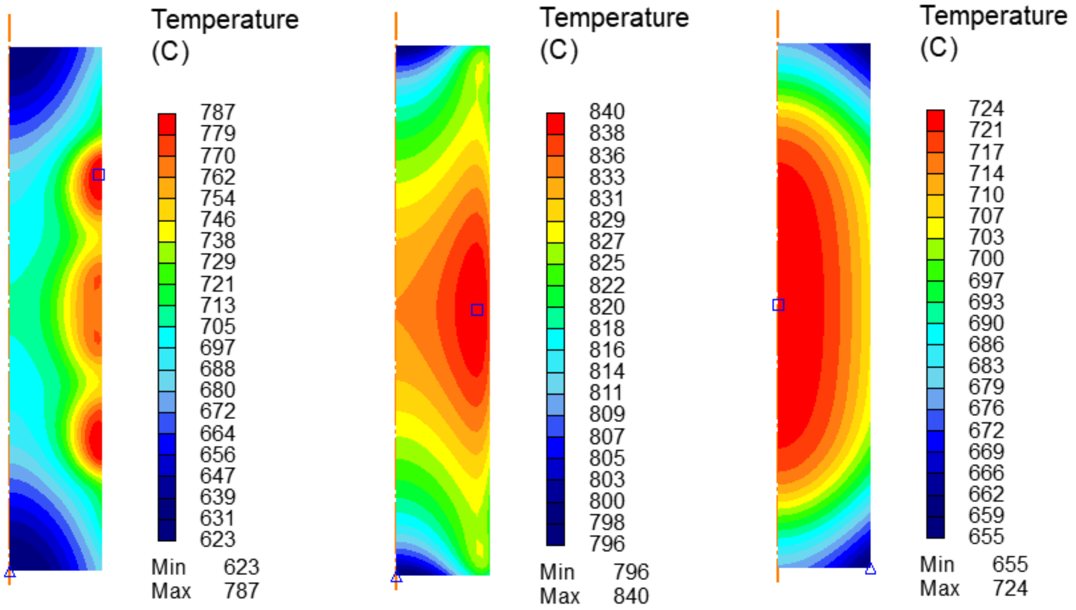

(d) $t = 16.901$ (e) $t = 58.195$ (f) $t = 100$

Figure 5.24: Results from `DEFORM` at 6 different times.

for non-Delaunay meshes on non-convex domains with realistic industrial parameters. We note that the results in Chapter 4 apply to the Dirichlet problem: the results in this Section suggest that these convergence proofs might extend to the temporal problem

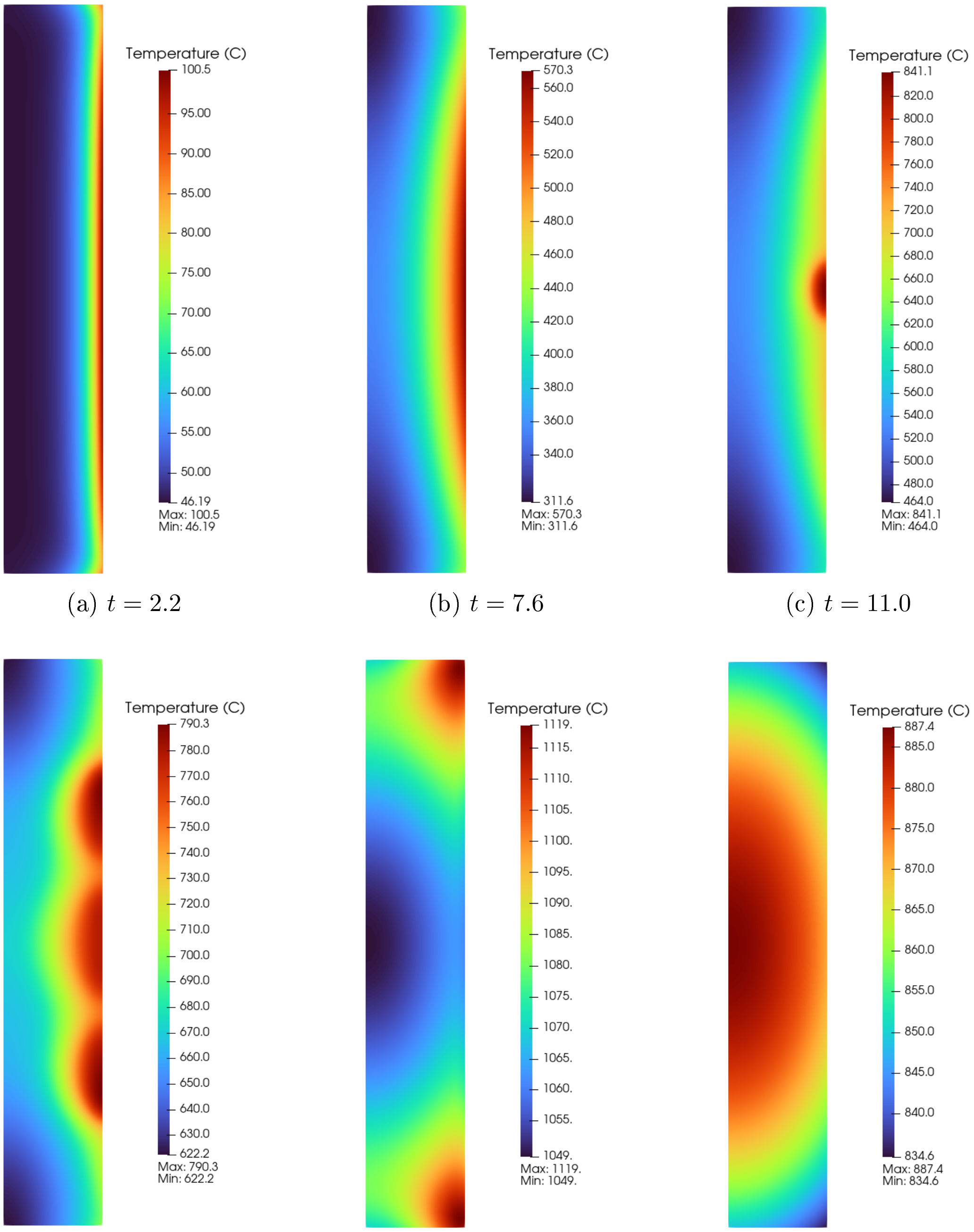

(a) $t = 2.2$ (b) $t = 7.6$ (c) $t = 11.0$

(d) $t = 16.4$ (e) $t = 62.0$ (f) $t = 100$

Figure 5.25: Results from the `FEniCSx` code at 6 different times.

with radiation boundary conditions with data relating to natural coefficients.

In this Section, we also show that the BPM can provide better results than the standard Galerkin method in certain scenarios when the standard Galerkin method

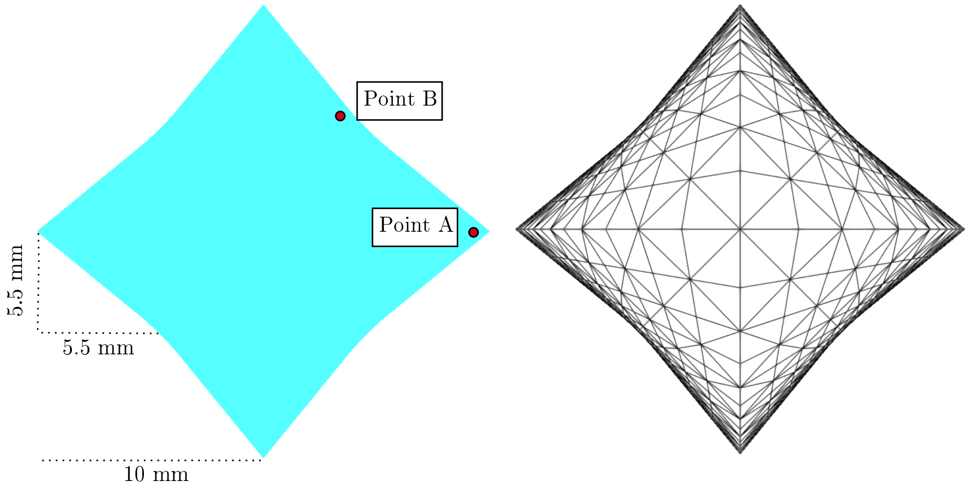

Figure 5.26: Illustration of non-convex domain and corresponding non-Delaunay mesh. This mesh has 4761 nodes and 9248 elements.

Parameter	Value	Parameter	Value
Time-step Δt	1 s	Percentage tolerance p	5 %
Final time T	15 s	Coupled tolerance `ctol`	10^{-6}
Time current active	8 s	Magnetic tolerance `mtol`	10^{-8}
Current I	471 A	Temperature tolerance `ttol`	10^{-6}
Coupled max iterations `cmax`	10	Coupled damping ω_c	0.9
Magnetic max iterations `mmax`	10	Magnetic damping ω_m	0.5
Temperature max iterations `tmax`	10	Temperature damping ω_t	0.9
Convective coefficient β	10	Radiation coefficient α	4.54×10^{-8}

Table 5.3: Configuration parameters for the non-convex experiment with C42-MOD micro-alloyed steel.

produces spurious oscillations in the solution.

For this artificial experiment, we use C42-MOD micro-alloyed steel and corresponding material properties. We use the same coil and current intensity as in Section 5.7, but the current is switched off after 10 seconds of the runtime. See Table 5.3 for all the properties used in the setup. We elect to use a large time-step to try to generate instabilities in the method. We also set the maximum iterations to be 10 for all fixed-point loops, and set the coupled and temperature damping parameter to be 0.9, in order to converge at a faster rate but also to amplify the non-convergence of the algorithm.

The temperature at points A and B at each time-step are plotted in Figure 5.27 for both the standard Galerkin method and for the BPM. We can see that the standard

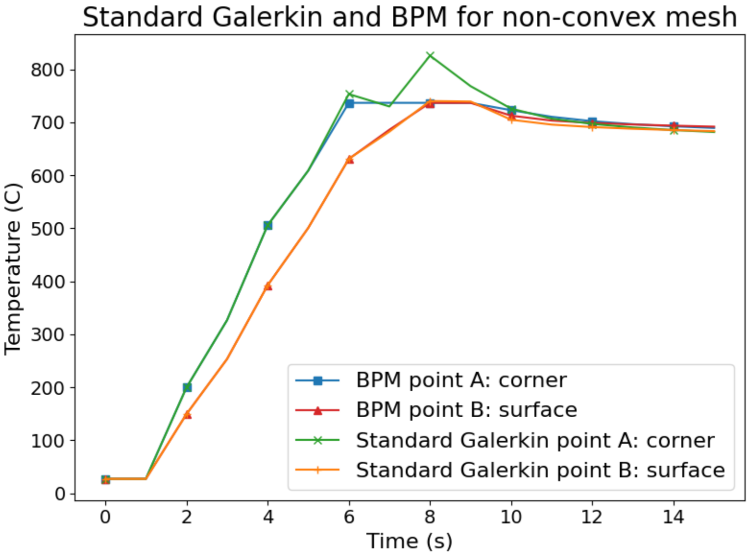

Figure 5.27: Results comparing the standard Galerkin method and the BPM on a non-convex domain. Here we set $k = 736.85\,°\mathrm{C}$ in the BPM.

Galerkin method exhibits some instability near the Curie point, and we get some spurious oscillations at the corner of the billet. However, by choosing $k = 1010\,\mathrm{K}$ ($736.85\,°\mathrm{C}$) in the BPM we can avoid these spurious oscillations, and obtain a much smoother and realistic solution. For the parts of the simulation where there are no numerical oscillations, the BPM and the standard Galerkin solution produce the same results. The choice of k was found by running the standard Galerkin method with a more refined time-step, finding the maximum value of temperature in the simulation, and setting k equal to that maximum.

Figure 5.28 illustrates the difference between the temperature distributions of the standard Galerkin solution and the BPM at the point of highest instability. We can see that the standard Galerkin solution has much higher temperatures at the corners, whereas the BPM is constrained. However, looking at Figure 5.29, a few seconds later, after the current has been switched off, we can see that the BPM produces a temperature distribution that is higher. This suggests that the standard Galerkin solution with higher temperature at $t = 8$ was indeed a numerical artefact, and is causing undershoots in the temperature distribution at later times.

We finish by commenting that although it is clear from this experiment that un-

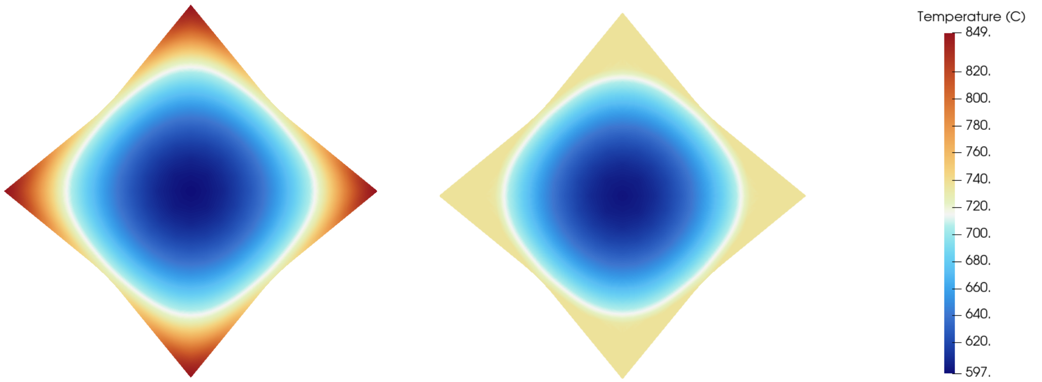

(a) Galerkin solution $t = 8$.

(b) BPM solution at $t = 8$.

(c) Temperature scale.

Figure 5.28: Comparison between the standard Galerkin method and the BPM at $t = 8$.

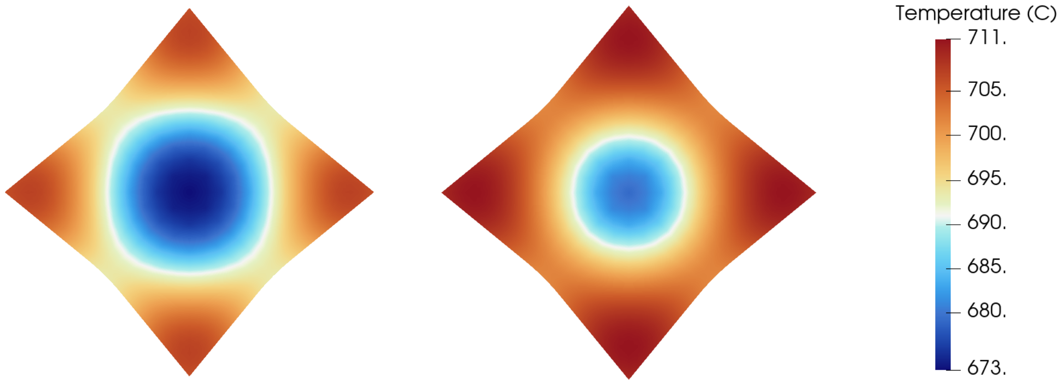

(a) Galerkin solution $t = 11$.

(b) BPM solution at $t = 11$.

(c) Temperature scale.

Figure 5.29: Comparison between the standard Galerkin method and the BPM at $t = 11$.

wanted numerical oscillations can be suppressed by the BPM, it is heavily dependent on the choice of the parameter k, the point where the solution is truncated. Too low a choice of k, and the entire solution would be suppressed and this would induce a non-physical solution. Therefore, in order to use the BPM effectively, we need to know how to make an educated choice for k. Nevertheless, this experiment is a proof of concept that the BPM could be used in realistic induction heating applications in cases where there are spurious oscillations due to irregular meshes.

5.9 Discussion

In this Chapter we considered the numerical implementation of the Induction Heating Problem using three different `FEniCSx` codes. We considered the standard Galerkin FEM and the new BPM for the Solenoidal model, and a standard Galerkin FEM for the Axisymmetric model. We numerically verified convergence rates for the Solenoidal codes, and found that for domains with irregular (non-Delaunay) meshes, the BPM is much more accurate than the standard Galerkin FEM. We also compared these codes to experimental data and compared the Axisymmetric `FEniCSx` code to output from `DEFORM`, a popular FEM software used in engineering modelling. We found that all codes produced results that were within an acceptable tolerance to the experimental data, and that the Axisymmetric `FEniCSx` code produced results that were closer to the experiments than `DEFORM`. We also found that `FEniCSx` and `DEFORM` produced very similar temperature distributions throughout the simulation. Furthermore, the Axisymmetric `FEniCSx` code managed to produce heating at the corners, which is what is seen in practice, but is not seen in the industrial software.

Fundamentally, for the Solenoidal model, we have shown that the BPM is just as accurate as the standard Galerkin FEM for realistic induction heating setups, and we have shown that it is more accurate when the mesh is non-Delaunay. Therefore, the BPM should be considered as a serious option to solve the Solenoidal model, due to the fact that it is robust over the shape of the mesh. This is one key takeaway from this Chapter.

For the Axisymmetric model, we have built a code in `FEniCSx` which is able to produce results that are comparable to, and even improve upon, results produced by the industrial software `DEFORM`. Although the scope of `DEFORM` is much larger, as it can simulate many different engineering scenarios, the internal workings of `DEFORM` are inaccessible to the user, as the software is accessed via a graphical interface. In the specific case of axisymmetric induction heating that we have studied here, the Axisymmetric `FEniCSx` code could be used by engineers alongside `DEFORM` as an open-source option that allows access to the numerical methods used in the code.

Chapter 6

Conclusions, Discussion, and Future Work

In this Thesis, we explored the analysis and implementation of FEMs for 2D Induction Heating Problems. In this short chapter, we summarise the main results and discuss possible future directions for the work in this Thesis.

Following a short introduction in Chapter 1, the background material was presented in Chapter 2. In particular, we highlighted the issue of posing a weak form of a PDE with a right-hand side in $L^1(\Omega)$. We also introduced BPM and justified why this method is well suited to this problem. Chapter 3 described the physics of induction heating and derived the 3D problem from Maxwell's equations. The assumptions and simplifications leading to the Solenoidal Induction Heating Problem and Axisymmetric Induction Heating Problem were also discussed.

The first new results appeared in Chapter 4, where we analysed a simplified stationary Solenoidal Induction Heating Problem with Dirichlet boundary conditions. We proved existence of solutions to the coupled problem, extending results by Clain and Touzani (1997a) by allowing non-convex polygonal domains. This proof of existence relied on showing that the right-hand side of the heat equation was more regular than in $L^1(\Omega)$ and using methods inspired from existing literature on the Thermistor Problem (Holst et al. 2010; Jensen and Målqvist 2012). We proved that the standard Galerkin FEM converged to an exact solution under the assumption that the family of meshes was quasi-uniform. A first, partial result on how to avoid this condition on the mesh was to use the BPM. In fact, we proved convergence for the decoupled problem where, fundamentally, we have avoided the need to use the discrete inf-sup condition (4.20), which is valid only if the mesh is quasi-uniform. This proof relied on the fact that the BPM solution satisfied a variational inequality, and thus corresponded to the projection of the exact solution onto a closed convex subset of the solution space. Numerical experiments verified these results, and showed: that a BPM for a heat equation with a non-physical bound converged to a projection of the exact solution onto the closed convex subset; that the BPM produced results that were superior to the standard Galerkin method for solutions with boundary layers on non-Delaunay meshes; and that the method converged to a solution of the full coupled Induction Heating Problem.

A first clear extension could be to try to prove convergence of the BPM for the coupled Dirichlet problem. We have seen numerical evidence in Section 4.7 that supports the idea of convergence of the BPM for the coupled system, and the case for the BPM could be enhanced if there was a proof for this result. Additionally, we have proven existence of solutions to the coupled Dirichlet problem, so another extension to this work could be to prove similar results with a Neumann boundary condition, a Robin boundary condition, or a radiation boundary condition.

Going further, another development could be to study non-convex domains where there is non-localised radiative heating, i.e., where there is radiative heat transfer between different parts of the surface. This is a situation commonly seen in industry, for example, when heating a hollow cylindrical billet. There has been some analysis considered for the heat equation (e.g. Druet (2009) and Druet (2010)), but to our knowledge no analysis has been attempted for the coupled problem.

For the sake of completeness, it would be desirable to prove uniqueness of solutions to the coupled Induction Heating Problem. However, we have seen in the literature that even the simpler Thermistor Problem does not have a proof for uniqueness of solution unless strict *a-priori* assumptions are made on the data, coefficients for the PDE, and regularity of the solution. Therefore, we expect that this would be quite a difficult extension to investigate.

Another ambitious extension could be to try to prove results without using the additional regularity due to the coupling, and instead to write the weak formulation as the renormalised solution, seen for a Poisson problem with $L^1(\Omega)$ data in Casado-Díaz et al. (2007). This was a possibility that was considered during this project, and more details and discussions about this method can be found in the Appendix A.1.

In Chapter 5 we implemented a realistic finite element code for the Solenoidal model and the Axisymmetric model using the FEM software `FEniCSx`. In this Chapter, we described three numerical codes in detail: the standard Galerkin `FEniCSx` code for the Solenoidal model, the BPM `FEniCSx` code for the Solenoidal model, and the Axisymmetric `FEniCSx` code for the Axisymmetric model. We numerically verified convergence rates for these codes using a method of manufactured solutions and by comparing to an analytical solution. We showed in these tests that the BPM is more accurate then the standard Galerkin method for non-Delaunay meshes.

We found that the Solenoidal codes produced results that were close to experimental data. Crucially, we found that the BPM produces more accurate results for a non-convex domain with non-Delaunay meshes. This is the main contribution of the numerical part of this Thesis: the BPM is a relatively new method and we were able to implement it to such a level that it produced results close to experimental data. The Axisymmetric `FEniCSx` code produces results that are also comparable to experimental data, and when comparing the results to the industrial software `DEFORM`, we found that it was extremely close to the results from `DEFORM` and exhibited similar temperature distributions. Moreover, the `FEniCSx` code captured the heating at the corners that is seen in the physical setting, but is not seen in `DEFORM`.

There are also a range of improvements that the code could be given. First, the code could be made more efficient by using an adaptive time-stepping scheme, or even an adaptive damping parameter. We could also employ an adaptive meshing, which would be particularly useful once the skin-depth increases as fewer elements would be needed to accurately resolve the skin-effect. Another option to look into is to consider how to adapt the code so it can be run on parallel processors - something that `FEniCSx` is capable of doing.

Finally, the current plan, as requested by the industrial partners, is to publish the code to make it available for engineers to use. Therefore, future work will include: updating the code to make it more user friendly, making sure it is robust under testing, and writing a user manual. If this is done, then the new results for this recently developed BPM will be used in an industrial setting.

Appendix A

Appendix

In this Appendix we present the concept of renormalised solutions, describe on how to incorporate voltage input into the code, and present an example `TOML` file code.

A.1 Renormalised Solutions

As a part of this Thesis, we investigated the possibility of applying the BPM to a renormalised solution of a Poisson problem. The idea was to extend results by Casado-Díaz et al. (2007), who prove that the standard Galerkin method converges to the renormalised solution under *very* strict conditions on the mesh, and use the BPM to prove convergence without any conditions on the mesh. If this could be proven for the Poisson problem, then this could pave the way to apply it to an Induction Heating Problem in the future.

Now let us introduce the renormalised solution. Consider the Poisson problem: given an open and bounded domain $\Omega \subset \mathbb{R}^d$, $d \geq 2$, find u such that for $f \in L^1(\Omega)$:

$$\begin{aligned} -\Delta u &= f \qquad \text{in } \Omega, \\ u &= 0 \qquad \text{on } \partial\Omega. \end{aligned} \tag{A.1}$$

The weak formulation is: find u in $H_0^1(\Omega)$ such that for all v in $H_0^1(\Omega)$:

$$\int_\Omega \nabla u \cdot \nabla v \ \mathrm{d}\boldsymbol{x} = \int_\Omega f v \ \mathrm{d}\boldsymbol{x}. \tag{A.2}$$

Since $f \in L^1(\Omega)$ this formulation is not well-defined. To get around this, a naïve approach could be to simply require $u \in C^\infty(\Omega)$, $v \in C^\infty(\Omega)$. Since V_h is not contained in $C^\infty(\Omega)$, we cannot use a FEM. Another naïve approach could be to take $u \in L^1(\Omega)$, $v \in L^\infty(\Omega)$. This would make the right-hand side of (A.2) well-defined, and the FEM would also be contained within this space. However, since neither $L^1(\Omega)$ nor $L^\infty(\Omega)$ are Hilbert spaces, existence and uniqueness cannot be guaranteed by the Lax-Milgram Lemma (Theorem 2.4.10) or by the BNB Theorem (Theorem 2.4.11).

A solution suggested by Casado-Díaz et al. (2007) is to redefine the weak formulation of (A.1) completely using the definition by Bénilan et al. (1995). First, define the truncation function $T_k(s)$, $k > 0$ as

$$T_k(s) = \begin{cases} s & \text{if } |s| \le k \\ \frac{s}{|s|}k & \text{if } |s| > k \end{cases}, \tag{A.3}$$

and recall the standard Galerkin solution u_h is the unique element in V_h such that for all $v_h \in V_h$,

$$\int_\Omega \nabla u_h \cdot \nabla v_h \, \mathrm{d}\boldsymbol{x} = \int_\Omega f v_h \, \mathrm{d}\boldsymbol{x}. \tag{A.4}$$

Then the new weak formulation is as follows:

Definition A.1.1 (Renormalised solution)**.** Let $S(\cdot) \in C_c^1(\mathbb{R})$ with $\operatorname{supp} S \subset [-k, k]$. A function $u \in L^1(\Omega)$ is called a *renormalised solution* of (A.1) if $\forall k > 0$, $T_k(u) \in H_0^1(\Omega)$, $\lim_{k\to\infty} \frac{1}{k} \int_\Omega |\nabla T_k(u)|^2 \, dx = 0$, and u is the solution to

$$\int_\Omega \nabla T_k(u) \cdot \nabla (vS(u)) \, \mathrm{d}\boldsymbol{x} = \int_\Omega f v S(u) \, \mathrm{d}\boldsymbol{x},$$

for all $v \in L^\infty(\Omega) \cap H_0^1(\Omega)$.

Now consider the FEM discretisation. It has been shown by Casado-Díaz et al. (2007) that if every inner angle of every element is acute (i.e. not larger than $\pi/2$), then for $1 \leq p < 2$,

$$\begin{aligned} u_h &\to u && \text{strongly in } W_0^{1,p}(\Omega) && \text{as } h \to 0 \\ \forall k > 0, \quad \Pi_h(T_k(u_h)) &\to T_k(u) && \text{strongly in } H_0^1(\Omega) && \text{as } h \to 0. \end{aligned}$$

We aimed to get a similar result but without any restrictions on the shape of the elements in the triangulation. A potential solution we suggested was to use the BPM, since this method does not depend on the shape of the mesh. This method assumes a-priori that u is bounded by $[0, k]$ for some $k > 0$ and we define

$$u_h^k := \sum_{i=1}^{N} \max(0, \min(u_h(x_i), k))\phi_i$$

and

$$u_h^{-k} := u_h - u_h^k.$$

Then our solution is u_h^k, where u_h is the unique solution of

$$\int_\Omega \nabla u_h^k \cdot \nabla v_h \, \mathrm{d}\boldsymbol{x} + s(u_h^{-k}, v_h) = \int_\Omega f v_h \, \mathrm{d}\boldsymbol{x}. \tag{A.5}$$

for all $v_h \in V_h$, where $s(\cdot, \cdot)$ is defined in Section 4.6. We attempted to show that for all $1 \leq p < 2$,

$$u_h^k \to u \text{ strongly in } W_0^{1,p}(\Omega) \text{ as } h \to 0 \text{ and } k \to \infty.$$

This is similar to the result we proved in Theorem 4.6.3. Unfortunately, we were not able to prove this, but we were able to gather some numerical evidence, and we demonstrate the results from one test here.

Let Ω be the unit square. By taking a logarithmic function that is only in $H^1(\Omega)$, computing its gradient, and squaring it, we obtain a function that is only in $L^1(\Omega)$. For this experiment we choose

$$
\begin{aligned}
f &= \left(\frac{d}{dx}\log\sqrt{(x-0.5)^2+(y-0.5)^2}\right)^2 \\
&= \frac{(x-0.5)^2}{((x-0.5)^2+(y-0.5)^2)^2}.
\end{aligned}
$$

Note that this function has a singularity at $(0.5, 0.5)$.

Then, we solve the Poisson problem with the right-hand side f defined as above. To test for convergence, we find the exact solution by truncating the singularity in f *very* high (at 10^6), and set the exact solution to be the Galerkin solution on an extremely refined mesh ($\approx 2\times 10^6$ elements), and we truncate the solution at $k = 10$. We compared the solution of a truncated standard Galerkin method with the solution of the BPM over a non-Delaunay mesh.

In Figure A.1 we see the results from the comparison between BPM solution u_h^k, and the truncated standard Galerkin solution $T_k(u_h)$, where in both cases $k = 10$. This test provides some numerical evidence that perhaps the BPM converges to a truncated solution when imposing non-physical bounds. In particular, it shows that for this problem with a right-hand side in $L^1(\Omega)$ only, and when solving over non-Delaunay meshes, the BPM provides a more accurate approximation than a truncated standard Galerkin

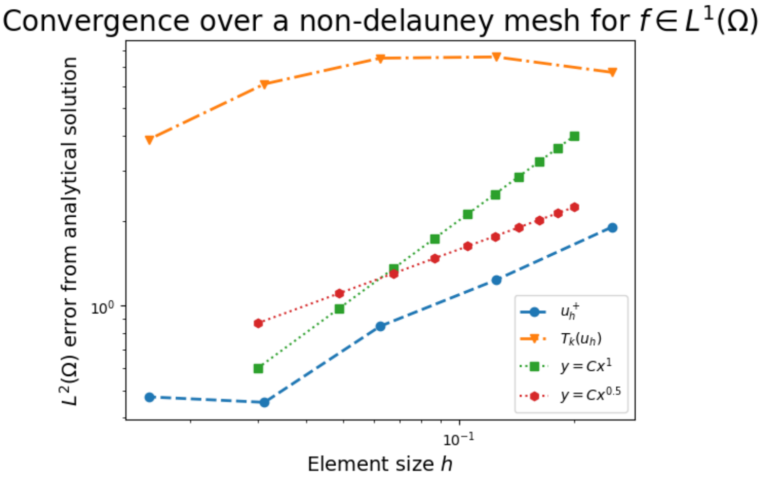

Figure A.1: Comparison between BPM solution and truncated standard Galerkin solution with right-hand side in $L^1(\Omega)$ over non-Delaunay meshes.

solution.

A.2 Incorporating Voltage Input

While performing the experiments at the AFRC, we recorded the voltage data using a Rogowski coil. In Section 5.7 we assumed that the current data could be accurately represented by a step function, but another way to obtain the current data is to process the voltage data directly within the code. This can lead to a more accurate representation of the current over the length of the experiment. In this Section, we use the data gathered from one of our experiments to explain how we processed the voltage data within the `FEniCSx` code.

To account for the high frequency of the current, the voltage was recorded every 0.000 001 s by the Rogowski coil and the output was stored in a `CSV` file. The resulting `CSV` file was extremely large in size ($>$ 1 GB), and was so large that it could not be opened on the laptop. Clearly, this needed to be modified to be more accessible and to extract the data about the frequency and current from the data.

First, the data was split into ‘chunks’ of 10^6 `CSV` rows. The first chunk was split into 1000 rows, and we used the `scipy` module `signal` to construct a dataframe with the peak and frequency for this small section. The mean of the peaks and frequency were calculated and appended to a `numpy` array. This process was repeated for the whole chunk and then successively for each chunk after until the whole data file had been processed. The result was a dataset of the averaged voltage and the frequency which is significantly smaller in size than the original `CSV` file. See Figures A.2 and A.3 for the pre-processed averaged voltage output of the experiment.

There is not a straightforward linear relationship between the voltage, frequency, and the current. In order to obtain the current from the voltage and frequency, we use a conversion table which is shown in Table A.1 (courtesy of the AFRC).

Therefore, using Table A.1, we can find the current I by calculating

$$I = 1000 C_f V.$$

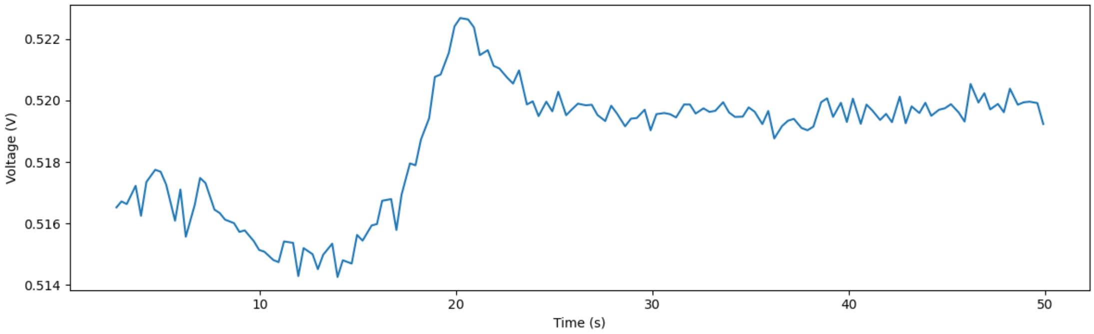

Figure A.2: Averaged voltage for non-zero current.

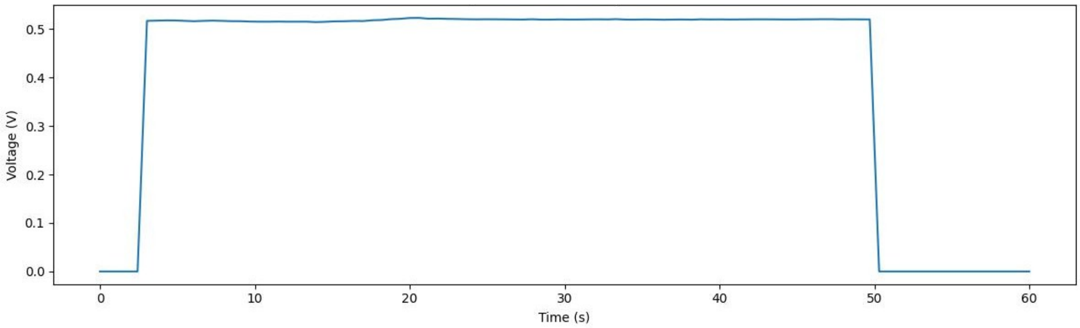

Figure A.3: Averaged voltage for the full simulation.

Frequency f Hz	Ratio $\mathrm{kA\,V^{-1}}$ (C_f)
60	0.113
100	0.177
200	0.346
500	0.681
1,000	0.890
2,000	0.976
5,000	1.011
10,000	1.011
20,000	1.013
50,000	1.019
100,000	1.009
150,000	1.003
200,000	1.000
500,000	0.807
1,000,000	0.397

Table A.1: Table of ratio factors for calculating current from voltage and frequency. This table comes from calibration of the Rogowski coil directly from the manufacturer.

The resulting current for the experiment is shown in Figure A.4. Note, in particular, that the output is similar to a step function, which justifies out approximation in Section 5.7.

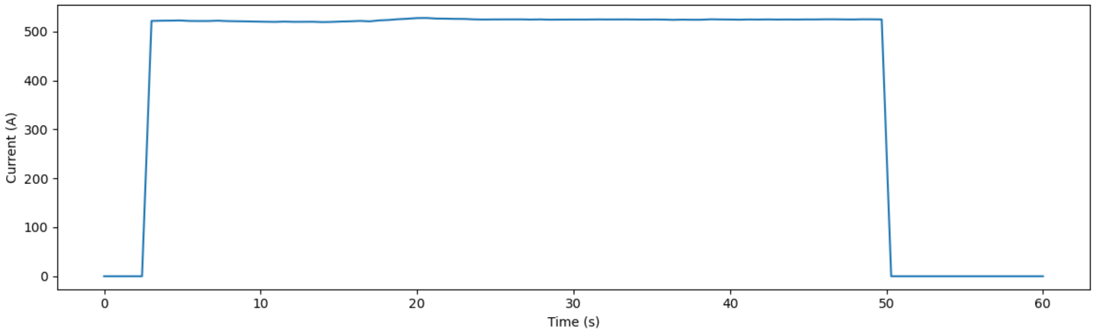

Figure A.4: Current for the full simulation.

A.3 Example `TOML` file

Listing A.1: The TOML file used in Section 5.7.

```
[geometry]
billet_radius = 0.01 # 10mm billet radius
billet_length = 0.057 # 57mm billet length
coil_radius = 0.02425 ##24.25 inner diameter
coil_center_separation = 0.015 # 15mm between coil centres
working_length = 0.09 # 90mm working length
wire_radius = 0.004 # 4mm wire radius for square
air_radius = 0.2 # 200mm air radius
air_length = 0.4 # 400mm air length
no_turns = 6 # number of turns in the coil

[mesh]
mesh_name = "DEFORM_mesh"
type = "quad" # triangle or quad
lc = 0.009 # 9mm max diameter of mesh size
lc_in_box = 0.0018 # 1/5 lc max
lc_in_coil = 0.0024 # 1/5 wire diameter
lc_in_billet = 0.001 # 1mm max diameter in billet
box_radius = 0.05 # refined box radius around billet and coil
box_length = 0.11 # refined box length around billet and coil
boundary_layer_thickness = 0.0005 # thickness of boundary layer
boundary_layer_ratio = 2 # ratio between two consecutive mesh sizes perpendicular to boundary
nx = 31 # number of nodes on side of Solenoidal model
ratio = 0.90 # ratio of square within circle in Solenoidal model
mesh_builder = "generate_circular_mesh" # function to generate the mesh

[material]
properties = "M1_PROPERTIES" # C42 Mod microalloyed steel properties
emmisivity = 0.8 # material emmisivity used to calculate alpha
```

```
beta = 10 # convective coefficient

[setup]
experiment_name = "DEFORM_experiment"
f = 95294  # frequency of alternating current (Hz)
coords_rz = {centre = [0.0001, 0.0], upper_surface = [0.0001, 0.0235], right_surface = [0.0085, 0.0], corner = [0.0085, 0.0235]}
coords_xy = {centre = [0, 0], surface = [0, 0.085]} # coordinates of the points
n_points_rz = 4 # number of points for Axisymmetric model
n_points_xy = 2 # number of points for Solenoidal model

[data]
temperature_data_file = "../data/csv_files/temperature_experiment_3_modified.csv"
#voltage_data_file     = "../data/csv_files/20240313-0003.csv" # optional

[time]
t = 0 # start time
dt = 0.1 # timestep
nt = 1000 # number of steps
tol = 1e-6  # tolerance criteria for the coupled loop
utol = 1e-6 # tolerance criteria for inner temperature loop
mtol = 1e-8 # tolerance criteria for inner magnetic field loop
ptol = 0.05 # percentage tolerance allowed for changes in parameters sigma and mu
max_iterations_coup = 20 # maximum iterations allowed for the coupled loop
max_iterations_temp = 50 # maximum iterations allowed for the temperature loop
max_iterations_magn = 20 # maximum iterations allowed for the magnetic field loop
w_coup = 0.5 # damping coefficient for the coupled loop
w_temp = 0.5 # damping coefficient for the temperature loop
w_magn = 0.5 # damping coefficient for the magnetic field loop


[solvers]
u_solver_method_xy = "solve_be" # temperature solver for Solenoidal model
u_solver_method_rz = "solve_be_rz" # temperature solver for Axisymmetric model
H_solver_method    = "solve_nonlinear" # nonlinear magnetic field solver for Solenoidal model
H_solver_temp      = "solve" # linear magnetic field solver for Solenoidal model
A_solver_method    = "solve_nonlinear_wholedomain" # nonlinear magnetic potential solver for Axisymmetric model
using_bpm = false # if set to true, use BPM in temperature for Solenoidal model

[constants]
T_AMB = 300.15 # ambient room temperature (K) - 25 degrees C
T_INIT = 319.15 # initial temperature (K) - 44 degrees C
SB_CONSTANT = 5.67e-8 # Stefan-Boltzman constant
SIGMA = 5.911563017e6 # electrical conductivity
MUR = 259.47 # relative magnetic permeability
```

Bibliography

(STFC), Scientific Forming Technologies Corporation (2023). *DEFORM (Design Environment for FORMing)*. Computer Program. URL: `https://www.deform.com/`.

Abhyankar, S., M. F. Adams, S. Balay, J. Brown, P. Brune, K. Buschelman, L. Dalcin, A. Dener, V. Eijkhout, W. D. Gropp, D. Kaushik, M. G. Knepley, D. A. May, L. C. McInnes, R. T. Mills, T. Munson, K. Rupp, P. Sanan, B. F. Smith, S. Zampini, H. Zhang, and H. Zhang (2021). *PETSc Users Manual*. Report. Argonne National Laboratory. URL: `https://www.mcs.anl.gov/petsc`.

Abhyankar, S., M. F. Adams, S. Balay, J. Brown, P. Brune, K. Buschelman, L. Dalcin, A. Dener, V. Eijkhout, W. D. Gropp, D. kaushik, M. G. Knepley, D. A. May, L. C. McInnes, R. T. Mills, T. Munson, K. Rupp, P. Sanan, B. F. Smith, S. Zampini, H. Zhang, and H. Zhang (2020). *PETSc Web page*. Generic. https://www.mcs.anl.gov/petsc.

Adams, R. A. and J. J. F. Fournier (2003). *Sobolev Spaces*. 2nd. Vol. 140. Pure and applied mathematics. Elsevier/Academic Press.

Ahrens, J., B. Geveci, and C. Law (2005). *ParaView: An End-User Tool for Large Data Visualization*. Elsevier.

Akrivis, G. and S. Larsson (2005). "Linearly implicit finite element methods for the time-dependent joule heating problem". In: *BIT. Numerical Mathematics* 45.3, pp. 429–442.

Alnaes, M. S., A. Logg, K. B. Ølgaard, M. E. Rognes, and G. N. Wells (2014). "Unified Form Language: A domain-specific language for weak formulations of partial differential equations". In: *Association for Computing Machinery. Transactions on Mathematical Software* 40.

Amiri, A., G. R. Barrenechea, E. H. Georgoulis, and T. Pryer (2025). *A nodally bound-preserving composite discontinuous Galerkin method on polytopic meshes.* arXiv: `2510.02094 [math.NA]`. URL: `https://arxiv.org/abs/2510.02094`.

Amiri, A., G. R. Barrenechea, and T. Pryer (2025). "A nodally bound-preserving finite element method for time-dependent convection–diffusion equations". In: *J. Comput. Appl. Math.* 470, p. 116691. ISSN: 0377-0427. DOI: `10.1016/j.cam.2025.116691`.

Balay, S., W. D. Gropp, L. C. McInnes, and B. F. Smith (1997). *Efficient Management of Parallelism in Object Oriented Numerical Software Libraries.* Birkhauser Press.

Baratta, I. A., J. P. Dean, J. S. Dokken, M. Habera, J. S. Hale, C. N. Richardson, M. E. Rognes, M. W. Scroggs, N. N. Sime, and G.N. Wells (2023). "DOLFINx: The next generation FEniCS problem solving environment," in: *Preprint.* DOI: `doi.org/10.5281/zenodo.10447666`.

Barrenechea, G. R., E. H. Georgoulis, T. Pryer, and A. Veeser (2024). "A nodally bound-preserving finite element method". In: *IMA Journal of Numerical Analysis* 44.4, pp. 2198–2219.

Barrenechea, G. R., V. John, and P. Knobloch (2024). "Finite Element Methods Respecting the Discrete Maximum Principle for Convection-Diffusion Equations". In: *SIAM review* 66.1, pp. 3–88.

— (2025). *Monotone Discretizations for Elliptic Second Order Partial Differential Equations.* Vol. 61. Computational Mathematics. Springer.

Bay, F., V. Labbe, Y. Favennec, and J. L. Chenot (2003). "A numerical model for induction heating processes coupling electromagnetism and thermomechanics". In: *International Journal for Numerical Methods in Engineering* 58.6, pp. 839–867.

Bénilan, P., L. Boccardo, T. Gallouët, R. Gariepy, M. Pierre, and J. Vázquez (1995). "An L^1-Theory of existence and uniqueness of solutions of nonlinear elliptic equations." In: *Analli della Scuola Normale Superiore di Pisa - Calsse di Sciebnze* 22, pp. 241–273.

Bensoussan, A., J. L. Lions, and G. Papanicolau (1978). *Asymptotic Analysis for Periodic Structures.* Vol. 5. Elsevier.

Bermúdez, A., D. Gómez, M. C. Muñiz, and P. Salgado (2007a). “A FEM/BEM for axisymmetric electromagnetic and thermal modelling of induction furnaces”. In: *International Journal on Numerical Methods in Engineering* 71.7, pp. 856–878.

— (2007b). “Transient numerical simulation of a thermoelectrical problem in cylindrical induction heating furnaces”. In: *Advances in Computational Mathematics* 26.1-3, pp. 39–62.

Bermúdez, A., D. Gómez, M. C. Muñiz, P. Salgado, and R. Vázquez (2009). “Numerical simulation of a thermo-electromagneto-hydrodynamic problem in an induction heating furnace”. In: *Applied numerical mathematics* 59.9, pp. 2082–2104.

Bermúdez, A., D. Gómez, M. C. Muníz, and R. Vázquez (2011). “A thermo-electrical problem with a nonlocal radiation boundary condition”. In: *Mathematical and computer modelling* 53.1, pp. 63–80.

Bermúdez, A., D. Gómez, R. Rodríguez, and P. Venegas (2015). “Numerical analysis of a transient non-linear axisymmetric eddy current model”. In: *Computational and Applied Mathematics* 70.8, pp. 1984–2005.

Bermúdez, A., D. Gómez, P. Salgado, R. Rodríguez, and P. Venegas (2013). “Numerical solution of a transient nonlinear axisymmetric eddy current model with nonlocal boundary conditions”. In: *Mathematical Models and Methods in Applied Sciences* 23.13, pp. 2495–2521.

Bermúdez, A., C. Reales, R. Rodríguez, and P. Salgado (2010). “Numerical analysis of a finite-element method for the axisymmetric eddy current model of an induction furnace”. In: *IMA journal of numerical analysis* 30.3, pp. 654–676.

Bermúdez, A., R. Rodríguez, and P. Salgado (2002). “A finite element method with Lagrange multipliers for low-frequency harmonic Maxwell equations”. In: *SIAM Journal on Numerical Analysis* 40.5, pp. 1823–1849.

Boccardo, L. and T. Gallouët (1989). “Nonlinear elliptic and parabolic equations involving measure data”. In: *Journal of Functional Analysis* 87.1, pp. 149–169.

Brenner, S. C. and L. R. Scott (2008). *The mathematical theory of finite element methods.* 3rd. Vol. 15. Texts in Applied Mathematics. 3rd ed. Springer.

Brezis, H. (2011). "Functional analysis, Sobolev spaces and partial differential equations". In.

Brouwer, L. E. J. (1912). "Über Abbildungen von Mannigfaltigkeiten". In: *Mathematische Annnalen* 71, pp. 97–115.

Casado-Díaz, J., T. Chacón Rebollo, V. Girault, M. Gómez Mármol, and F. Murat (2007). "Finite elements approximation of second order linear elliptic equations in divergence form with right-hand side in L^1". In: *Numerische Mathematik* 105.3, pp. 337–374.

Céa, J. (1964). "Approximation variationnelle des problèmes aux limites". In: *Annales de l'institut Fourier* 14.2, pp. 345–444.

Chaboudez, C., S. Clain, R. Glardon, D. Mari, J. Rappaz, and M. Swierkosz (1997). "Numerical modeling in induction heating for axisymmetric geometries". In: *IEEE Transactions on Magnetics* 33.1, pp. 739–745.

Chaboudez, C., S. Clain, R. Glardon, J. Rappaz, M. Swierkosz, and R. Touzani (1994). "Numerical modelling of induction heating of long workpieces". In: *IEEE Transactions on Magnetics* 30.6, pp. 5028–5037.

Ciarlet, P. G. and P. A. Raviart (1973). "Maximum principle and uniform convergence for the finite element method". In: *Computer methods in applied mechanics and engineering* 2.1, pp. 17–31.

Cimatti, G. (1988). "A bound for the temperature in the thermistor problem". In: *IMA journal of applied mathematics* 40.1, pp. 15–22.

— (1989). "Remark on existence and uniqueness for the thermistor problem under mixed boundary conditions". In: *Quarterly of applied mathematics* 47.1, pp. 117–121.

— (1992). "Existence of weak solutions for the nonstationary problem of the Joule heating of a conductor". In: *Annali di matematica pura ed applicata* 162.1, pp. 33–42.

Cimatti, G. and G. Prodi (1987). "Existence results for a nonlinear elliptic system modelling a temperature dependent electrical resistor". In: *Annali di matematica pura ed applicata* 152.1, pp. 227–236.

Clain, S. (1994). "Analyse mathématique et numérique d'un modèle de chauffage par induction". Thesis.

Clain, S., J. Rappaz, M. Swierkosz, and R. Touzani (1993). "Numerical Modeling of Induction Heating for Two-Dimensional Geometries". In: *Mathematical Models and Methods in Applied Sciences* 3.6, pp. 805–822.

Clain, S. and R. Touzani (1997a). "A Two-dimensional Stationary Induction Heating Problem". In: *Mathematical Methods in the Applied Sciences* 20.9, pp. 759–766.

— (1997b). "Solution of a two-dimensional stationary induction heating problem without boundedness of the coefficients". In: *Mathematical Modelling and Numerical Analysis* 31.7, pp. 845–870.

Dal Maso, G., F. Murat, L. Orsina, and A. Prignet (1999). "Renormalized solutions of elliptic equations with general measure data". In: *Annali Della Scuola Normale Superiore de Pisa* 28.4, pp. 741–808.

Dalcin, L., P. Kler, R. Paz, and Cosimo A. (2011). "Parallel Distributed Computing using Python". In: *Advances in Water Resources* 34.9, pp. 1124–1139.

Dall'Aglio, A. (1996). "Approximated solutions of equations with L^1 data. application to the H-convergence of quasi-linear parabolic equations". In: *Annali di matematica pura ed applicata* 170.1, pp. 207–240.

Dautray, R. and J. L. Lions (2000). *Mathematical analysis and numerical methods for science and technology: Volume 2 Functional and Variational Methods*. Springer.

Develey, G. (2000). *Chauffage par induction électromagnétique: principes*. Online Database.

Drobenko, B., O. Hachkevych, and T. Kournyts'kyi (2007). "A mathematical simulation of high temperature induction heating of electroconductive solids". In: *International Journal of Heat and Mass Transfer* 50, pp. 616–624. ISSN: 0017-9310.

Druet, P-É. (2009). "Weak solutions to a stationary heat equation with nonlocal radiation boundary condition and right-hand side in L^p $(p \geq 1)$". In: *Mathematical methods in the applied sciences* 32.2, pp. 135–166.

Druet, P. É. (2010). "Weak solutions to a time-dependent heat equation with nonlocal radiation boundary condition and arbitrary p-summable right-hand side". In: *Applications of Mathematics* 55.2, pp. 111–149.

Ern, A. and J. Guermond (2021a). *Finite Elements II - Galerkin Approximation, Elliptic and Mixed PDEs.* 1st 2021. Vol. 73. Texts in Applied Mathematics. Springer.

Ern, A. and J. L. Guermond (2004). *Theory and practice of finite elements.* Vol. 159. Applied Mathematical Sciences. Springer-Verlag.

— (2021b). *Finite elements I - Approximation and interpolation.* Vol. 72. Texts in Applied Mathematics. Springer.

Facchinei, F. (2003). *Finite-dimensional variational inequalities and complementarity problems.* eng. Springer series in operations research. New York: Springer. ISBN: 9780387955803.

Fisk, M., M. Ristinmaa, A. Hultkrantz, and L. Lindgren (2022). "Coupled electromagnetic-thermal solution strategy for induction heating of ferromagnetic materials". In: *Applied mathematical modelling* 111, pp. 818–835.

Fonseca, I. and G. Leoni (2007). *Modern Methods in the Calculus of Variations: L^p Spaces.* Monographs in Mathematics. Springer.

Gallouët, T. and R. Herbin (1994). "Existence of a solution to a coupled elliptic system". In: *Applied Mathematical Letters. An International Journal of Rapid Publication* 7.2, pp. 911–925.

Geuzaine, C. and J. F. Remacle (2009). "Gmsh: A 3-D finite element mesh generator with built-in pre- and post-processing facilities". In: *International Journal for Numerical Methods in Engineering* 79.11, pp. 1309–1331.

Gilbarg, D. and N. S. Trudinger (1998). *Elliptic partial differential equations of second order.* Springer.

Grisvard, P. (2011). *Elliptic Problems in Nonsmooth Domains.* Vol. 24. Monographs and studies in mathematics. Pitman.

Hiptmair, R. and O. Sterz (2005). "Current and voltage excitations for the eddy current model". In: *International Journal of Numerical Modelling: Electronic Networks, Devices and Fields* 18.1, pp. 1–21.

Holst, M. J., M. G. Larson, A. Målqvist, and R. Söderlund (2010). "Convergence analysis of finite element approximations of the Joule heating problem in three spatial dimensions". In: *BIT. Numerical Mathematics* 50.4, pp. 781–795.

Howison, S. D., J. F. Rodrigues, and M Shillor (1993). “Stationary Solutions to the Thermistor Problem”. In: *Journal of Mathematical Analysis and Applications* 174, pp. 573–588.

Inc, ANSYS (2025). *Ansys Academic Research Mechanical, Coupled Field Analysis Guide*. Generic. URL: `https://www.ansys.com`.

Jensen, M. and A. Målqvist (2012). “Finite element convergence for the Joule heating problem with mixed boundary conditions”. In: *Bit Numerical Mathematics* 53.2, pp. 475–496.

Jensen, M., A. Målqvist, and A. Persson (2022). “Finite element convergence for the time-dependent Joule heating problem with mixed boundary conditions”. In: *IMA Journal of Numerical Analysis* 42.1, p. 199.

Jerison, D. and C. E. Kenig (1995). “The Inhomogeneous Dirichlet Problem in Lipschitz Domains”. In: *Journal of Functional Analysis* 130.1, pp. 161–219.

Jiles, D. C. and D. L. Atherton (1986). “Theory of ferromagnetic hysteresis”. In: *Journal of magnetism and magnetic materials.* 61.1-2, pp. 48–60.

Kinderlehrer, D. and G. Stampacchia (2000). *An introduction to variational inequalities and their applications.* Vol. 31. Classics in applied mathematics. Society for Industrial and Applied Mathematics.

Klein, O. and P. Philip (2002). “Correct voltage distribution for axisymmetric sinusoidal modeling of induction heating with prescribed current, voltage, or power”. In: *IEEE Transactions on Magnetics* 38.3, pp. 1519–1523.

Kresin, G. I. and V. G. Maz’ya (1993). “Criteria for validity of the maximum modulus principle for solutions of linear strongly elliptic second order systems”. In: *Potential Analysis* 2.1, pp. 73–99.

Loula, A. F. D. and J. Zhu (2001). “Finite element analysis of a coupled nonlinear system”. In: *Comput. Appl. Math* 20, pp. 321–339.

— (2006). “Mixed finite element analysis of a thermally nonlinear coupled problem”. In: *Numerical Methods for Partial Differential Equations. An International Journal* 22.1, pp. 180–196.

MacKenzie, K. (2025). *Induction Heating.* Computer Program. URL: `https://github.com/Katie795/induction_heating`.

Målqvist, A. and T. Stillfjord (2017). "Finite element convergence analysis for the thermoviscoelastic Joule heating problem". In: *Bit Numerical Mathematics* 57.3, pp. 787–810.

Massé, P., B. Morel, and T. Breville (1985). "A finite element prediction correction scheme for magneto-thermal coupled problem during curie transition". In: *IEEE Transactions on Magnetics* 21.5, pp. 1871–1873.

Mbehou, M. (2018). "The theta-Galerkin finite element method for coupled systems resulting from microsensor thermistor problems". In: *Mathematical Methods in the Applied Sciences* 41.4, pp. 1480–1491.

Parietti, C. and J. Rappaz (1998). "A quasi-static two-dimensional induction heating problem. Part I: modelling and analysis." In: *Mathematical Models and Methods in Applied Sciences* 8.6, pp. 1003–1021.

— (1999). "A quasi-static two-dimensional induction heating problem. Part II: numerical analysis." In: *Math Models and Methods in Applied Sciences* 9.9, pp. 1333–1350.

Rannacher, R. and R. Scott (1982). "Some optimal error-estimates for piecewise linear finite-element approximations". In: *Mathematics of Computation* 38.158, pp. 437–445.

Rappaz, J. and M. Świerkosz (1996). "Mathematical Modelling and Numerical Simulation of Induction Heating Processes". In: *Applied Mathematics and Computer Science* 6.2, pp. 207–221.

Raviart, P. A. and J. M. Thomas (1992). *Introduction à l'analyse numérique des équations aux dérivées partielles.* Collection mathématiques appliquées pur la maîtrise sous la direction de P. G. Ciarlet et J. L. Lions. Masson.

Renardy, M. and R. C. Rogers (2004). *An introduction to partial differential equations.* 2nd. Vol. 13. Texts in applied mathematics. 2nd ed. Springer-Verlag.

Roubíček, T. (2013). *Nonlinear partial differential equations with applications.* 2nd. Vol. 153. International Series of Numerical Mathematics. Birkhäuser.

Rudnev, V. I., R. L. Cook, D. L. Loveless, and M. R. Black (1997). *Induction Heat Treatment, Basic Principles, Computation, Coil Construction, and Design Consideration.* Marcel Dekker, Inc.

Saunders, N., Z. Guo, Li, A. P. Miodownik, and J. P. Schille (2003). "Using JMatPro to model materials properties and behavior". In: *The Journal of The Minerals, Metals and Materials Society (TMS)* 55, pp. 60–65.

Scott, L. R. and S. Y. Zhang (1990). "Finite-element interpolation of nonsmooth functions satisfying boundary-conditions". In: *Mathematics of Computation* 54.190, pp. 483–493.

Scroggs, M. W., I. A. Baratta, C. N. Richardson, and G. N. Wells (2022a). "Basix: a runtime finite element basis evaluation library". In: *Journal of Open Source Software* 7.73.

Scroggs, M. W., J. S. Dokken, C. N. Richardson, and G. N. Wells (2022b). "Construction of arbitrary order finite element degree-of-freedom maps on polygonal and polyhedral cell meshes". In: *ACM Transactions on Mathematical Software* 48.2, 18:1–18:23.

Süli, E. (2020). *Lecture Notes on Finite Element Methods for Partial Differential Equations.* Generic.

Tiihonen, T. (1997). "Stefan-Boltzmann Radiation on Non-convex Surfaces". In: *Mathematical Methods in the Applied Sciences* 20.1, pp. 47–57.

Touzani, R. and J. Rappaz (2014). *Mathematical Models for Eddy Currents and Magnetostatics: With Selected Applications.* Scientific Computation. Springer.

Wanser, S., L. Krahendbuhl, and A. Nicolas (1994). "Computation of 3D induction hardening problems by combined finite and boundary element methods". In: *IEEE Transactions on Magnetics* 30.5, pp. 3320–3323.

Zhu, J., X. Yu, and A. F. D. Loula (2011). "Mixed discontinuous Galerkin analysis of thermally nonlinear coupled problem". In: *Computer methods in applied mechanics and engineering* 200.13, pp. 1479–1489.